HZDR-001

ANNUAL REPORT 2010

INSTITUTE OF RADIOCHEMISTRY

HZDR

HELMHOLTZ
ZENTRUM DRESDEN
ROSSENDORF

Annual Report 2010

Institute of Radiochemistry

Editors:
Prof. Dr. G. Bernhard

Editorial staff:
Dr. H. Foerstendorf
Dr. A. Richter
Dr. K. Viehweger

HZDR

HELMHOLTZ
ZENTRUM DRESDEN
ROSSENDORF

Contact

Cover picture

Monitoring (reactive) fluid flow in geological material by means of Positron Emission Tomography (PET) is the unique feature of the Reactive Transport Division at the Research Site Leipzig of the HZDR. This so called GeoPET method has been developed in the course of the last about 10 years and provides four-dimensional images of colloidal and/or fluid flow transport processes in porous geologic media with unprecedented quality.

The cover picture illustrates a typical installation procedure, where a rock core, contained inside of an acrilyc glass column, is inserted into the ClearPET™ scanner.

Dear reader,

THE ANNUAL REPORT 2010 OF THE INSTI-
tute of Radiochemistry marks the begin-
ning of a new series of Scientific Reports
edited by the Helmholtz-Zentrum Dresden-
Rossendorf (HZDR), formerly known as For-
schungszentrum Dresden-Rossendorf. Since
January 1, 2011, the HZDR is a member of the
Helmholtz Association of German Research
Centers. This is not without reason, for the
HZDR fits well with the Helmholtz Association,
regarding the center's research structure that is
based on four research programs: Advanced
Electronic Materials, Cancer Research, Nuclear
Safety Research and Research with Photons,
Neutrons and Ions.

There have already been close cooperations in
the past with the Helmholtz Association. As far
as the HZDR's Institute of Radiochemistry is
concerned, researchers have been collaborating,
for instance, with the Forschungszentrum Jülich,
the Helmholtzzentrum München – German Re-
search Center for Environmental Health and the
Karlsruhe Institute of Technology in the German
competence network for radiation research
(Kompetenzverbund Strahlenforschung). Col-
laborations of this kind are likely to be enhanced
by the fact that the HZDR is now a member of
the Helmholtz Association.

The Institute of Radiochemistry forms one pillar
of the Nuclear Safety Research program of the
HZDR. As becomes visible in this Annual Re-
port, researchers are studying the behavior and
transport of long-lived radionuclides in biologi-
cal and geological systems, thus contributing to
the quest for permanent nuclear disposal sites.

I wish you a pleasant read!

Prof. Dr. Roland Sauerbrey
Scientific Director

Preface

AT THE BEGINNING OF 2011, THE FORMER Forschungszentrum Dresden-Rossendorf (FZD) was fully integrated into the Helmholtz Association, as Helmholtz-Zentrum Dresden-Rossendorf (HZDR). Therefore, the present Annual Report 2010 of the Institute of Radiochemistry (IRC) is published as the first HZDR-Report.

The Institute of Radiochemistry is one of the six Research Institutes of this centre. IRC contributes to the research program "Nuclear Safety Research" in the "Research Field of Energy" and performs basic and applied research in radiochemistry and radioecology. Motivation and background of our research are environmental processes relevant for the installation of nuclear waste repositories, for remediation of uranium mining and milling sites, and for radioactive contaminations caused by nuclear accidents and fallout. Because of their high radiotoxicity and long half-life the actinides are of special interest.

In 2010, about 100 scientists, technicians, PhD-, diploma-, master-, and bachelor students were working at the IRC. Promotion of young scientists is an important requirement to ensure that the competence and excellent scientific results of radiochemistry will be maintained in the future. We accomplished many new scientific results in the past year, which are presented in about 50 scientific articles published in peer-reviewed international journals.

Following a recommendation of the German Council of Science and Humanities (Wissenschaftsrat) the Division of Georadiochemistry of the Institut für Interdisziplinäre Isotopenforschung, Leipzig, was integrated into the IRC as the division "Reactive Transport" at the beginning of 2010. An important enhancement of our research in the field of metal transport in the environment is in evidence.

Only a few research results published in this Annual Report can be highlighted in this preface.
We were very successful in the determination of formation and structures of various uranium, americium, and curium complexes with relevant organic and inorganic ligands. First results about the dependency of uranium(VI) complexation with small organic ligands at elevated temperatures were achieved. We gained new insights in the mechanisms of luminescence quenching of uranyl complexes by density functional theory calculations.
Bacteria, algae, and fungi can influence the mobilization or immobilization of heavy metals in water and soils. We strengthened our research on the behavior of biofilms in uranium contaminated sites.
To describe the aqueous transport of actinides and other long-lived radionuclides the dominating processes on the liquid/solid interfaces must be considered. Interesting results about the sorption and surface complexation of different metals (long-lived radionuclides) during interaction with various mineral surfaces, and colloids were achieved. Substantial progress was made on knowledge about the visualization and quantification of fluid flow in salt rock formations by using Positron Emission Tomography.

Furthermore, we can report that our own radiochemical experimental facilities – the radiochemistry lab at the Rossendorf Beamline at ESRF and our different laser-spectroscopic and microscopic systems are continuously working on a high quantitative and qualitative level. This instrumentation is essential for the excellent scientific results obtained by the researchers of the IRC and by scientists from external institutions.

I would like to thank the visitors, German and international ones, for their interest in our research and for their participation in the institute seminars. We would also like to thank our scientific collaborators and the visiting scientists for coming to Dresden-Rossendorf in 2010 to share their knowledge and experience with us. We continue to strongly encourage the collaborations and visits by scientists in the future. Special thanks are due to the Executive Board of the Forschungszentrum Dresden-Rossendorf, the Ministry of Science and Arts of the State Saxony, the Federal Ministry of Education and Research, the Federal Ministry of Economics and Technology, the Deutsche Forschungsgemeinschaft, the European Commission, and other organizations for their support.

Prof. Dr. Gert Bernhard
Director of the Institute of Radiochemistry

Contents

PART II – LONG-LIVED RADIONUCLIDES AT PERMANENT DISPOSAL SITES

PUBLICATIONS

SCIENTIFIC ACTIVITIES

PERSONNEL

ACKNOWLEDGEMENTS

INDEX OF AUTHORS

LONG-LIVED RADIONUCLIDES IN

BIOSYSTEMS

Detection of uranium(IV) by LIPAS in biologic relevant samples

G. Geipel, S. Drewitz, K. Viehweger

The reduction of uranyl by quercetin in 50% methanol at pH 5.8 and 7.0 under inert gas conditions was observed due to the formation of uranium(IV), the most stable reduced uranium species. Uranium(IV) was detected by using laser-induced photoacoustic spectroscopy (LIPAS) [1].

Uranium(IV) can be detected exploiting its spectroscopic properties at low concentrations by laser-induced methods. As fluorescence of uranium(IV) can only be excited with wavelength in the UV region, this method is not applicable for samples containing other components with strong absorption properties in the same wavelength region. Alternatively, uranium(IV) can be determined by its absorption properties in the visible range around 650 nm. Laser-induced photo-acoustic spectroscopy provides the possibility to reach detection limits of about two orders of magnitude lower compared to conventional UV-vis measurements. The structure of quercetin is shown in Fig. 1.
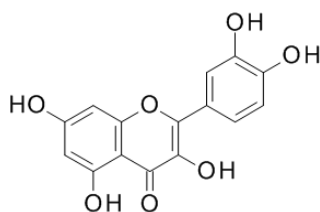
Fig. 1. Structure of quercetin.

EXPERIMENTAL. The set up of laser-induced photo-acoustic spectroscopy is described elsewhere [2]. Additionally, we used the thermostated cuvette holder (Quantum northwest, USA) to keep the temperature in the cuvette constant at 283 K. For the studies of the reduction of uranium(VI) by quercetin, 100 µM U(VI) solutions were treated with 500 µM quercetin in 50% methanol. The experiments were carried out in a glove box under inert gas conditions. The ionic strength was set to 0.1 M $NaClO_4$. The pH of the samples was adjusted to 5.8 and 7.0, respectively. After one day the amount of formed uranium(IV) was determined by using LIPAS.

RESULTS. The redox potential of quercetin is pH dependent and can be described by equation (1), where the potential is given in mV and measured against Standard Hydrogen Electrode (SHE).

$$E = (823 \pm 17) - (69 \pm 3) \cdot pH \qquad (1)$$

In these solutions, uranium may be additionally stabilized by complex formation with quercetin. We determined the formation constant by UV-vis spectroscopy. The formation constant for

$$C_{15}H_5O_7^{5-} + 3H^+ + U^{4+} \leftrightarrow U(C_{15}H_8O_7)^{2+} \qquad (2)$$

was assigned to be $\log K = 49.26 \pm 0.18$ compared to the stability constant of the analog complex with uranium(VI) $\log K = 41.4 \pm 0.4$ [3]. This stabilizes the formed uranium(IV) as well as the solubility of uranium(IV) will be increased.

The laser-induced photo-acoustic measurements show clearly the formation of uranium(IV) already after one day of contact (Fig. 2). The amount of formed uranium
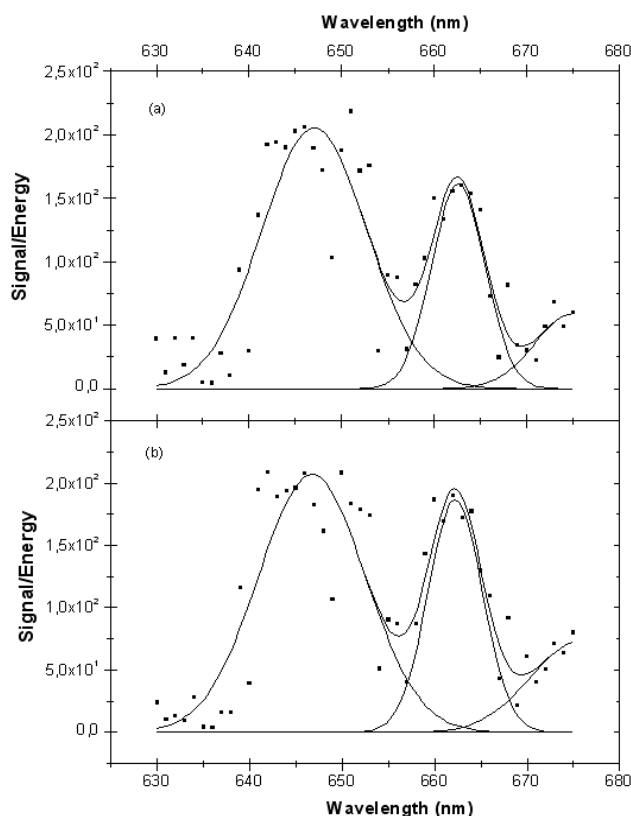
Fig 2: U(IV) formation determined by LIPAS, (a) sample containing 100 µM uranium(VI) and 500 µM quercetin and (b) reference sample containing 10 µM uranium(IV) and 500 µM quercetin. The spectra were processed by Gaussian deconvolution.

Tab. 1: Results of the peak fit procedure.

Wavelength [nm]	Peak area	
	Sample 100 µM UO_2^{2+}/500 µM quercetin	Reference 100 µM U^{4+}
646	66.5	62.2
663	26.5	28.7

was determined by comparison of the peak area of the main absorption bands at 647 nm and 662 nm (Tab. 1). The results of the laser-induced spectroscopy show that about 10% of the uranium(VI) were reduced under the applied experimental conditions. Additional analytical methods like TTA-extraction as well as absorption measurements after addition of arsenazo-III were used to confirm the reduction of uranium(VI). These experiments resulted in the formation of up 5% uranium(IV). Due to more working steps it can not be excluded that uranium(IV) is already partly reoxidized.

[1] Drewitz, S. (2010) Diploma thesis, Dresden University of Technology, Dresden.
[2] Geipel, G. et al. (1998) *Radiochim. Acta.* **82**, 59-63.
[3] Viehweger, K. et al. (2009) *Report FZD-511*, p. 41.

Model spectra of organic phosphate-U(VI) and sulfurU(VI) complexes: a study of P k-edge and S k-edge XANES

B. Li, H. Foerstendorf, J. Raff, J. Rothe,[1] K. Dardenne[1]

[1]Institute of Nuclear Waste Disposal, Karlsruhe Institute of Technology, Karlsruhe, Germany

In this study, model spectra were set up using phosvitin-U(VI), DMSO-U(VI), and sulfate-U(VI) for phosphate-, sulfoxide-, and sulfate-U(VI) complexes, respectively. Spectra features were found to represent the U(VI) complexation.

Phosphorylation of serine threonine and tyrosine, oxidation of methionine and sulfation on the sugar residues are common post translational modifications to proteins or other bioligands. In the study of protein-U(VI) interaction at a molecular level, those functional groups are often hard to be detected by many spectroscopic methods because of their rather low concentrations to other functional groups. Meanwhile, P/S k-edge XANES are ideal spectroscopic methods to detect the upper functional groups and their complexation form with U(VI).

EXPERIMENTAL. The phosvitin-U(VI) complexes were prepared as described in [1]. The $UO_2(DMSO)_5(ClO_4)_2$ crystal was prepared from UO_3 and $HClO_4$ was dissolved in hot triethyl orthoformate, followed by addition of DMSO. The yellow precipitate was filtered and washed with diethylether. The Sulfate-U(VI) complex was prepared by desolving UO_3 in equal molar H_2SO_4. The crystal was determined to be $UO_2SO_4 \cdot 2.5H_2O$ using XRD (data not shown).

The ground dried samples were applied on a Kapton tape for the XANES measurement. The phosphor and sulfur k-edge XANES spectra were recorded in fluorescence mode with 50 mbar N_2 in sample compartment at room temperature. The energy was calibrated within range of ± 0.5 eV. The ionization potential was defined for P k-level and S k-level as 2,140 eV-2,180 eV and 2,450 eV-2,500 eV, respectively. The spectra were averaged with minimum three spectra. The pre- and post-edge correction and other data analysis were carried out using Athena of IFEFFIT's sixpack program (CARS, USA).
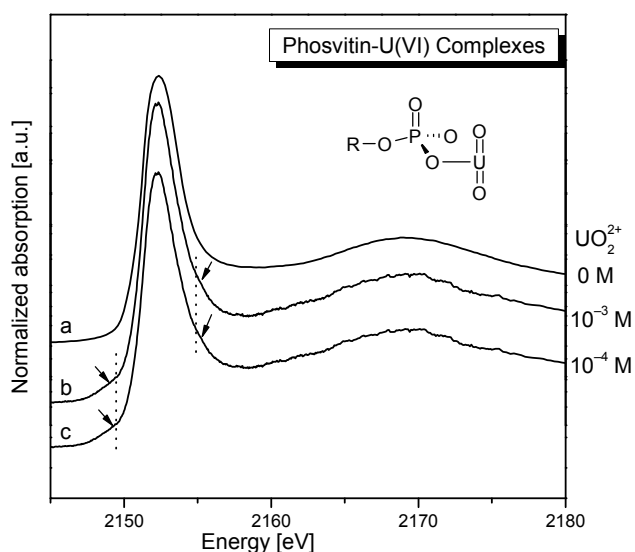
Fig. 1: Phosphor k-edge XANES spectra of phosvitin U(VI) complexes with diferent initial U(VI) concentration: 0 M (a), 10^{-3} M (b) and 10^{-4} M (C).
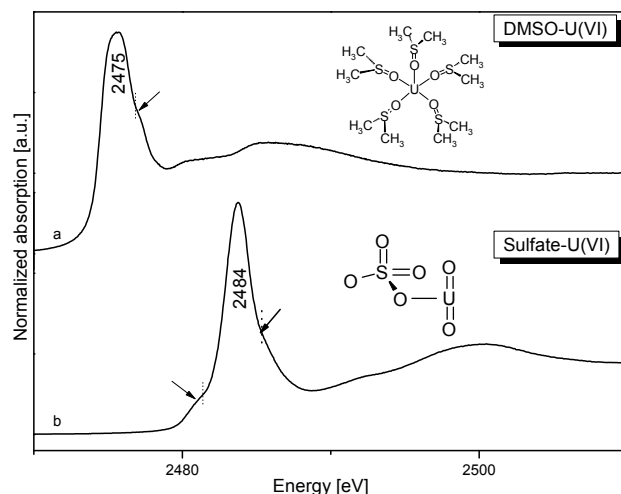
Fig. 2: Sulfur k-edge XANES spectra of DMSO-U(VI) and sulphate-U(VI) complexes.

RESULTS. Figure 1 shows a comparison of P K-edge XANES spectra of phosvtin and its U(VI) complexes with two different initial U(VI) concentrations. In general, all the spectra show the white line at 2152.4 eV, and the O-oscillation at 2169.4 eV. No difference has been observed between the spectra of samples with different initial U(VI) concentrations, although different U(VI) complexes were suggested from the IR spectra [1]. Nevertheless, a characteristic pre-edge feature and a continuum resonance have been found only on both spectra of phosvitin U(VI) complexes (arrows in Fig 1b and c). The pre- and post-edge features locate about −3 eV and 2.5 eV from the edge, respectively. Similar pre-edge structures were reported from $Fe_3(PO_4)_2$ [2] and $LiFePO_4$ [3].

Figure 2 shows the sulfur k-edge XANES spectra of $UO_2(DMSO)_5(ClO_4)_2$ and $UO_2SO_4 \cdot 2.5H_2O$ crystals. Compared with the spectrum of DMSO [4], the DMSO-U(VI) complex presents a shift of the edge and the shoulder from 2473.5 eV to 2475 eV and from 2475 eV to 2477 eV (shown by an arrow on Fig. 2a), respectively. On the spectrum of Sulfate-U(VI), the edge shift from 2482 eV [5] to 2484 eV, and a pre-edge structure −3 eV and post-edge structure +1 eV to the edge have been also observed (shown by an arrow on Fig. 2b).

[1] Li, B. et al. (2010) *J. Inorg. Biochem.* **104**, 718-725.
[2] Yoon, W.S. et al. (2006) *Electrochem. Solid St.* **9**, A415-A417.
[3] Jenkins, G.N. et al. (1988) *Philos. Mag. B* **58**, 271-283.
[4] Damian, E. et al. (2005) *Physica Scripta* **T115**, 1077-1079.
[5] Fleet, M.E. et al. (2005) *Can. Mineral.* **43**, 1811-1838.

U(VI) complexes with phosphorylated amino acid (P-Serine & P-Tyrosine): an ATR FT-IR study

S. Brüning, B. Li, H. Foerstendorf

For a better understanding of the complexation between U(VI) and phosphorylated proteins, e.g. phosvitin, P-serine (P-Ser) and P-tyrosine(P-Tyr) (Fig. 1), the most frequently phosphorylated residues on proteins, were used to complex with U(VI) in aqueous solution at pH 4. U(VI) complexation via the phosphate group was determined by IR spectroscopy. Complexation via the α-carboxylic group can be ruled out.
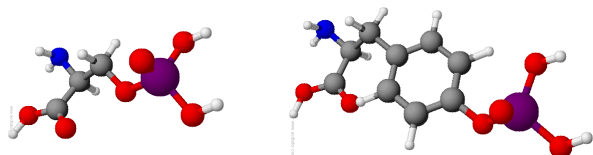
Fig 1: Balls and stick model of phosphoserine and phosphotyrosine.

EXPERIMENTAL. The condition of all the batch experiment is fixed to 1 mM uranium(VI), with 0.1 M NaCl at pH 4. The concentration of amino acid was varied to reach different ratios of functional group to U(VI). The infrared spectra were recorded at a Bruker Vertex 80/v FT-IR spectrometer equipped with an ATR accessory and a flow cell. Each single beam spectrum was averaged from 256 scans. Difference spectra were calculated by subtracting ligand spectra from spectra of the U(VI)-amino acid complexes.

RESULTS. Generally, the spectra of phosphorylated amino acid-U(VI) complexes show bands in the spectral regions around 1600-1350, 1250-950, 950-880 cm^{-1} representing the vibrational modes of carboxyl, phosphate and uranyl groups, respectively.

The complexation of the uranyl ion via the phosphate group of P-Ser becomes evident in the spectrum shown in Fig. 2b where great changes are observed only in the spectral region of the phosphate groups. In comparison to the spectrum representing the change of the protonation

Fig. 3: ATR FT-IR difference spectra of U(VI)-P-Tyr complexes with various U:P concentration ratios: 1 : 1 (B), 1 : 0.1 (C). The difference spectrum of aqueous phosphotyrosine solutions within pH 8 – pH 4 is shown as a reference (A).

state of P-Ser (Fig. 2a) the shifts of the bands additionally reflect this complexation behavior. The $v_{as}(UO_2)$ mode is observed at 908 cm^{-1} which is bathochromatically shifted compared with the uranyl speciation without ligands under the same conditions [1]. No changes are observed in the carboxyl region. With an increasing U:P ratio (Fig. 2C), $v_{as}(UO_2)$ mode appears at 961 and 925 cm^{-1} representing the a domination of uncomplexed U(VI) species. However, the pattern of bands in the phosphate region demonstrates the presence of the phosphate-U(VI) complexes. The respective UO_2 band is obviously hidden under those of the dominating uncomplexed U(VI) species. In addition, the two bands at around 1530 and 1456 cm^{-1} were determined to derive from the unbound U(VI), which is in agreement of TRLFS results recorded under the same experimental conditions [2].

Similar results are obtained with the P-Tyr ligand (Fig. 3). The complexation of the actinide ion occurs via the phosphate group. The spectral differences observed with the P-Tyr ligand are tentatively explained by a specific impact of the benzene ring on the U(VI) complexation.

[1] Müller, K. et al. (2008) *Inorg. Chem.* **47**, 10127-10134.
[2] Koban, A. et al. (2007) *J. Inorg. Biochem.* **101**, 750-757.

Fig. 2: ATR FT-IR difference spectra of U(VI)-P-Ser complexes with various U:P concentration ratios: 1 : 1, (B) 1 : 0.1 (C). The difference spectrum of aqueous phosphoserine solutions pH 8 − pH 4 is shown as a reference (A).

Unusual structural arrangement of the tetrapeptide glycyl-L-glutamyl-L-phosphoseryl-L-leucine

K. B. Heine, J. K. Clegg,[1] K. Fairweather,[1] K. Jolliffe,[1] K. Gloe,[2] T. Henle,[2] G. Bernhard

[1]Synthetic Organic Chemistry, School of Chemistry, University of Sydney, Australia; [2]Department of Chemistry and Food Chemistry, Dresden University of Technology, Dresden, Germany

The crystal structure of the tetrapeptide is characterized by two crystallographically different molecules. In the packing these molecules are connected by a complicated intermolecular hydrogen bonding network, including the phosphate residues, NH and OH functions and co-crystallized water.

Biologically active receptors, like peptides and proteins, which are able to bind d-block and f-block elements are of great interest for the understanding of their interactions in biological and natural systems. During our studies, we were able to characterize the crystal structure of a phosphopeptide for the first time. Crystal structures of small unphosphorylated peptides are already known [1].

EXPERIMENTAL. Glycyl-L-glutamyl-L-phosphoseryl-L-leucine (Fig. 1) was obtained as described before [2]. A colourless needle like crystal for X-ray analysis was removed from methanolic solution and used directly for the X-ray study. The structures were determined on a Bruker APEXII-FR591 diffractometer at 150(2) K and refined by using SAINT, XPREP [3], WinGX [4] and SADABS [5].
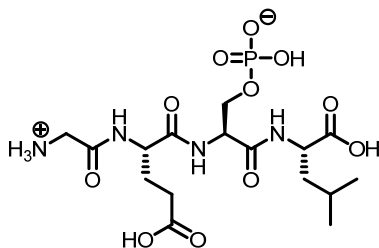
Fig 1: Glycyl-L-glutamyl-L-phosphoseryl-L-leucine.

RESULTS. The basic unit contains two crystallographically different molecules (one containing P1, the other containing P2), with one of them showing a disorder of the L-leucine side chain (Fig. 2).

Between the two peptide molecules, three water mole-
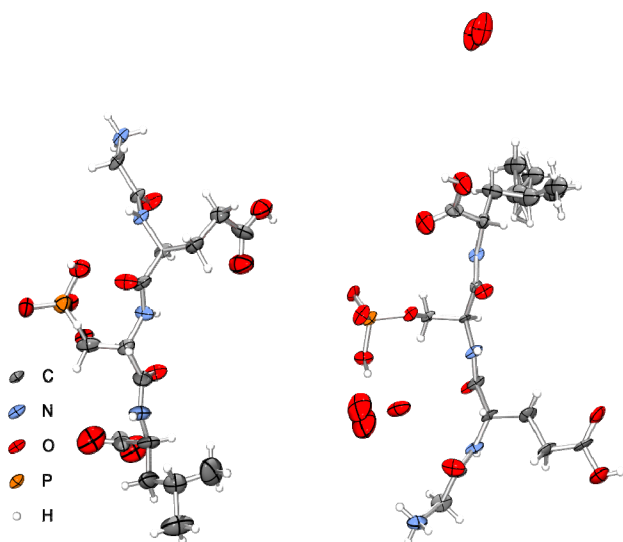
Fig. 2: Molecular structure of glycyl-L-glutamyl-L-phosphoseryl-L-leucine as ellipsoid plot with 50% probability.
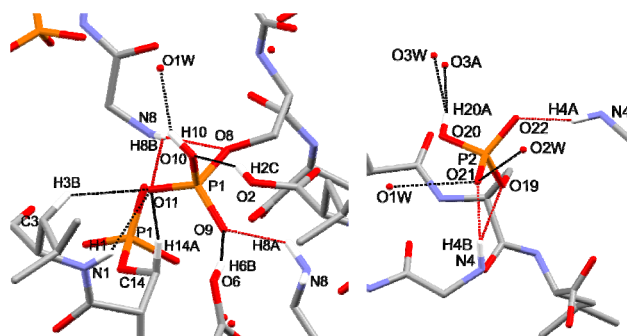
Fig. 3: Hydrogen bonds involving the phosphate groups containing P1 (left) and P2 (right) with the interactions to the N-termini given in red stippled lines (water, disordered atoms and hydrogen atoms not involved in interactions are omitted for clarity).

cules can be found, two of them are highly disordered. Four peptide molecules are situated in one unit cell. They can be divided into two pairs, which are linked by two moderate hydrogen bonds while within one pair only one weak interaction is present. Additionally, moderate hydrogen bonds between the backbones are observed. Because of the packing, interactions of the backbones occur along the crystallographic b-axis, whereby the P1 and P2 molecules alternate.

The two phosphate groups of the P1 and P2 molecules show different hydrogen bonding schemes. The group of P1 acts as a single H-bond donor but six times as an acceptor whereas the group of P2 is a five-fold acceptor and a single donor, if the disorder of O3W/O3A is considered (Fig. 3).

The hydrogen bonding scheme where the N-terminus of one molecule is connected to the C-terminus of one or more other molecules is commonly observed in crystal structures of peptides [1,6]. In contrast to the so-called head-to-tail chains, in our case "head-to-phosphate chains" have been observed. Each phosphate group binds two other peptide molecules (N8-H8A···O9, N8-H8B···O8 and N8-H8B···O11 for P1-phosphate; N4-H4A···O22; N4-H4B···O19 and N4-H4B···O21 for P2-phosphate; Fig. 3).

A network is built by those head-to-phosphate interactions in which water is co-crystallized in tight channels. There are no interactions between the water molecules themselves.

[1] Görbitz, C.H. (2010) *Acta Crystallogr. Sect. B-Struct. Sci.* **66**, 84–93.
[2] Schreppel, K. et al. (2009) *Report FZD-530*, p. 12.
[3] Bruker Inc. (1995) *SMART, SAINT and XPREP. Area detector control and data integration and reduction software.* Bruker Analytical X-ray Instruments Inc., Madison, Wisconsin, USA.
[4] Farrugia, L.J. (1999) *J. Appl. Cryst.* **32**, 837-838.
[5] Blessing, R.H. (1995) *Acta Crystallogr. Sect. A* **51**, 33-38.
[6] Vijayan, M. (1988) *Prog. Biophys. Mol. Biol.* **52**, 71–99.

Influence of the variation of process parameters on the cultivation of microaerophilic microorganisms

M. Suhr, M. Dudek, S. Kutschke, K. Pollmann, J. Raff

Gram-positve lactic acid bacteria like the used obligatory heterofermentative *Lactobacillus* sp. play an important role in food microbiology and in the protein biochemistry. These kinds of bacteria are microaerophile and tolerant to different media. The experiments show that there is an important influence of process parameters such as the ventilation of air and pH-value on the growth of the bacteria and the total protein concentration and especially to the expression of S-layer proteins.

S-layer proteins are widespread proteins and represent the outer cell envelope of many eubacteria and archaea. The paracrystalline protein lattice features different strain-depended geometrical structures. The proteins once isolated exhibit the ability to form lattices on different kinds of interfaces as well as a high metal binding capacity that opens a wide spectrum of applications. They can be used as ion traps, molecular sieves and as templates for the synthesis of catalytic nanoparticles [1]. Therefore, it is necessary to find the optimal process parameters for a reproducible cultivation of bacterial biomass and to reach a high yield of S-layer proteins. The *Lactobacillus* S-layers are different from *Bacillus* strains in their size, primary structure, pI value and are used for comparison with S-layers of our isolates.

EXPERIMENTAL. *Culture medium and growth conditions*. *Lactobacillus hilgardii* B706 from the Institute of Microbiology and Wine Research, Johannes Gutenberg University, Mainz, was cultivated in defined medium composed of 10 g tryptone, 10 g meat extract, 5 g yeast extract, 10 g glucose, 1 g tween®, 80.2 g K_2HPO_4, 5 g NaAc, 2 g $(NH_4)_2$citrate, 0.2 g $MgSO_4$, and 0.05 g $MnSO_4$ per liter. The medium was sterilized at 121 °C for 30 min. After the addition of glucose, pH was adjusted to 6.6-6.8 with 1 M NaOH at 30 °C. The inoculum (60 mL) was incubated at 30 °C for 48 h and added to the fermentation broth.
Extraction of S-Layer-proteins and SDS-Page. Cells were harvested after 48 h and washed with buffer (50 mM TRIS, 3 mM NaN_3, 1mM $MgCl_2$, pH 7.5). After centrifugation (12,400 g, 20 min, 4 °C) proteins were extracted as described in [2]. The proteins were analyzed by SDS-Page using a 10% acrylamide separating gel.

RESULTS. *Online* and *offline* measurements (Fig. 1) proved the influence of the different aeration (0.0, 0.1, and 0.3 L/min for fermentation 1, 2 and 3, respectively) on the growth of bacteria within the first 28 h of cultivation. The achieved optical densities (OD_{620nm}) after this period were 1.95 (OD1), 6.36 (OD2) and 1.17 (OD3). In the second stage of the cultivation, after 28 h, changes of pH (fermentation 2) or air flow (fermentation 3) were induced, whereas the parameters in fermentation 1 were kept constant over 48 h. In fermentation 3, after readjusting the air flow to 0.1 L/min, the bacteria grew much faster than with a higher ventilation. These data support the results obtained from fermentation 2, where the cell density after 28 h is higher than in the other fermentations after 48 h. In addition to aeration, the influence of
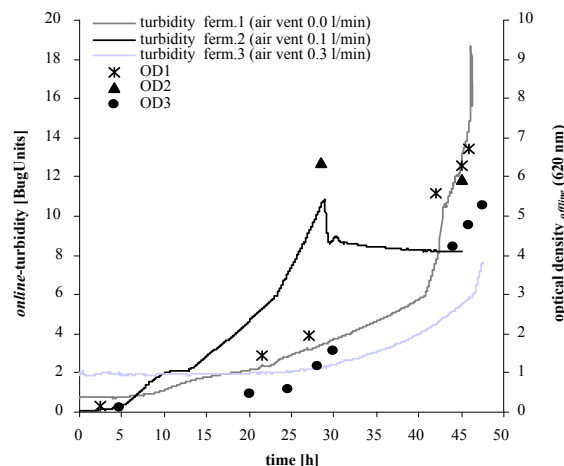
Fig. 1: Growth phases from the fermentations of *Lactobacillus hilgardii* B706. *Online*-turbidity measurements via BugEye 2100, *offline* optical density at 620 nm.

changes of pH on bacterial growth was studied. The adjustment to pH 6.5 (fermentation 2) revealed that the bacteria prefer a lower pH of 4.5-5.1 for the optimal growth. Microsopic images demonstrate that the aciduric cells form short chains depending on pH.
The total protein amount (Fig. 2, left) agrees with the *online* data of fermentation 2. The highest protein concentration is reached within 28 h with a constant air flow of 0.1 L/min and an acidic pH. This trend in fermentation 2 can be also observed in biomass (dry weight) and in optical density. An increase of pH or ventilation leads to the stagnation of growth and does not increase the protein yield.
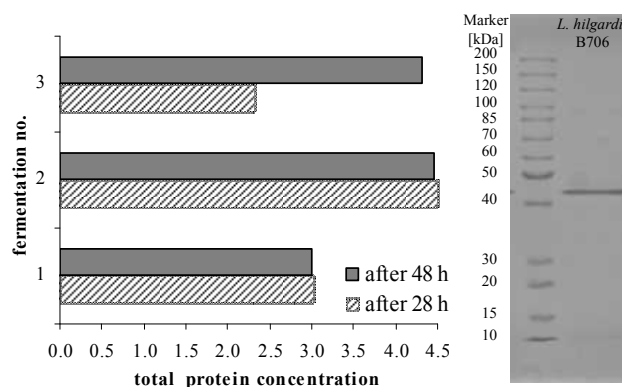
Fig. 2: Total protein concentration of the fermentations at 28 h and 48 h (left); SDS-Page, protein band of *L. hilgardii* B706 at about 45 kDa after isolation (right).

The success of the isolation of S-layer-proteins was controlled by SDS-Page. The specific protein band was found at ~45 kDa (Fig. 3, right) which is in accordance with the values for *Lactobacillus* S-Layer described in [3]. In addition, S-layer proteins could be extracted from the harvested biomass by using the chaotropic salt lithium chloride with a yield of almost 100%.

[1] Sleytr, U.B. et al. (2001) *Prog. Surf. Sci.* **68**, 231-278.
[2] Lortal, S. et al. (1992) *J. Gen Microbiol.* **138**, 611-618.
[3] Dohm, N. (2010) Diploma thesis, Johannes Gutenberg University, Mainz.

Secretion monitoring via S-layer-Xylanase fusion protein

R. Münch, F. Lederer, K .Pollmann

Escherichia coli **is one of the best studied micro-organisms and the most widely used host in genetic engineering. The heterologous expression of surface layer (S-layer) proteins in** *E. coli* **BL21(DE3) caused a drastic morphological change from typical single cell structure to a filamentous cell structure. Surprisingly the expressed S-layer proteins were coevally found in the periplasm and the supernatant of the growing** *E. coli* **which is generally known as a poor secretor. In this study the colorimetric detectable xylanase was fused to S-layer-fragments. The presence of these fusion proteins in diverse cell fractions was detected by the monitoring of xylanase activity. This method demonstrates the secretion of heterologously expressed S-layer proteins.**

The intestinal bacterium *Escherichia coli* is well studied and new findings about these bacteria are rare. Typical *E. coli* single cells are rod-shaped with a size of 1.1-1.5 µm × 2.0-6.0 µm. The heterologous expression of the silent S-layer protein SllB of *Lysinibacillus sphaericus* JG-A12 induces drastic morphological changes of the *E. coli* host cells. After induction of the S-layer expression with IPTG, *E. coli* formed filaments of > 100 µm in length instead of rod-shaped single cells [1]. The S-layer expressing *E. coli* cultures reached a high optical density and cells showed a high viability as well as strong expression of S-layer proteins. The S-layer proteins were found in the periplasm and in the supernatant of S-layer expressing *E. coli*. These results point to a mechanism mediating the transport of S-layer proteins in *E. coli*, which is not identified yet. In the present study we fused the enzyme xylanase that can be detected by colorimetric assays [2] to S-layer proteins in order to analyse the secretion process. For this investigation we isolated different protein fractions and analyzed the occurrence of xylanase. In addition, we checked the intactness of the S-layer expressing *E. coli* cells by analysing the presence of β-galactosidase that is exclusively found in the cytoplasm. Results of these analyses demonstrate a secretion of recombinant S-layer proteins to the medium.

EXPERIMENTAL. S-layer-Xylanase expressing *E. coli* were harvested in the exponential and in the stationary growth phase after 5, 20, 27 and 46 hours. The supernatant was concentrated, the periplasmic cell fraction was isolated by osmotic shock treatment and the cytoplasmic cell fraction was isolated with BugBuster protein extraction reagent. The presence of S-layer proteins in the 3 different protein fractions was checked by analyzing the activity of xylanase (Fig. 1). Each cell fraction was treated with the heteropolysaccharide xylan. Afterwards the reducing character of the xylanase-released sugars was used to reduce the 3,5-dinitrosalicylic acid to 3-amino-5-ni-trosalicylic acid accompanied by a color change of yellow to orange. Furthermore the β-D-galactosidase activity in each protein fraction was analyzed (Fig. 2).

RESULTS. The S-layer-Xylanase protein is dominantly found in the cytoplasm of *E. coli* (Fig. 1). Coevally the S-layer concentration increases in the periplasm and in the supernatant while cells stay intact as shown by β-galacto-

xylanase assay
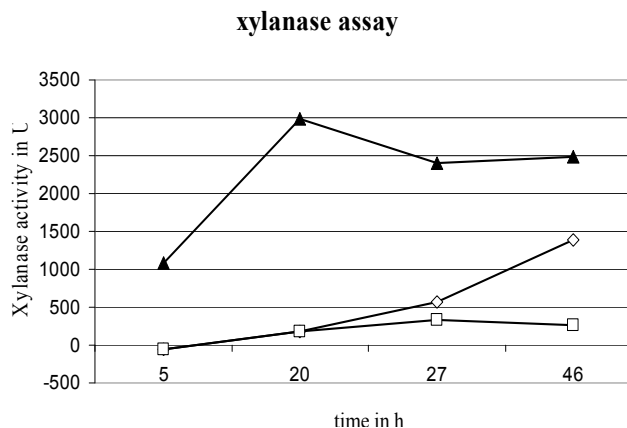
Fig. 1: Xylanase activity in the supernatant (◊) the periplasmic (□) and the cytoplasmic (▲) protein fractions at different points of time. The supernatant was concentrated, periplasmic proteins were isolated by osmotic shock of the cell pellet, and the cytoplasmic proteins were isolated by treatment with BugBuster Protein extraction reagent.

galactosidase assay
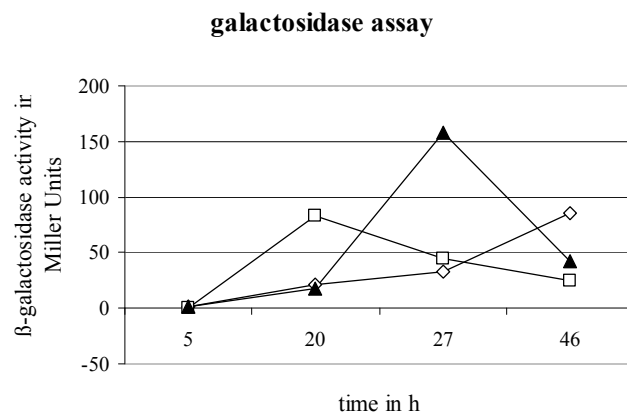
Fig. 2: β-Galactosidase activity in the supernatant (◊), the periplasmic (□) and the cytoplasmic (▲) protein fractions at different points of time. The supernatant was concentrated, periplasmic proteins were isolated by osmotic shock of the cell pellet, and the cytoplasmic proteins were isolated by treatment with BugBuster Protein extraction reagent.

sidase assays (Fig. 2). These results indicate a transport of the proteins that is not caused by cell damage.

DISCUSSION. *E. coli* is generally a poor secretor. However, the S-layer expressing strain *E. coli* BL21 secretes these proteins first to the periplasm and later to the medium. The secretion process itself is actually not identified but the findings raise new questions regarding the secretory pathway in one of the best studied microorganism.

[1] Lederer, F. et. al. (2010) *Microbiology* **156**, 3584-3595.
[2] Williams, J.F. (1989) *BioTechniques* **7**, 762-769.

Recombinant S-layer production induces disordered cell division in *E. coli* filaments

F. Lederer, T. Günther, J. Raff, K. Pollmann

***Escherichia coli* is one of the best studied micro-organism and the most widely used host in genetic engineering. The heterologous expression of surface layer (S-layer) proteins in *E. coli* BL21 (DE3) caused a drastic morphological change from typical single cell structure to a filamentous cell structure. Analyses of the mechanism of filament formation with DAPI-DNA stain showed long DNA-fibres that cross the filaments. The recombinant S-layer production seems to affect a disordered cell division of *E. coli*. Our results give a new insight in the morphology and the cell division process in *E. coli* induced by recombinant proteins.**

The intestinal bacterium *Escherichia coli* is the best studied microorganism and new findings about these bacteria are rare. Typical *E. coli* single cells are rod-shaped with a size of 1.1-$1.5\,\mu m \times 2.0$-$6.0\,\mu m$. Recently, the heterologous expression of the S-layer protein SllB of the uranium mining waste pile isolate *Lysinibacillus sphaericus* JG-A12 in *E. coli* BL21, which is used as a host, draw new attention on effects of recombinant protein production on the cell morphology of these microorganisms. Recombinant S-layer producing *E. coli* BL21 were grown at room temperature with IPTG. Filaments of $> 100\,\mu m$ in length were formed in the exponential growth phase while in the stationary growth phase the cells started to form tube-like structures leaving single cells [1]. AFM, TEM, SDS-PAGE and IR-spectroscopic analyses indicated that tubes are stable, exhibit a height of 75 nm and are composed of multiple layers of outer membranes stabilized by S-layer proteins. In the present study, the mechanism which is responsible for the tube formation was further analyzed. We stained the DNA in cells and filaments of GFP/S-layer expressing *E. coli* using DAPI reagent. Results of these analyses give new information with respect to DNA and protein arrangement inside the cells.

EXPERIMENTAL. The silent S-layer protein gene *sllB* of *Lysinibacillus sphaericus* JG-A12 was cloned as PCR product in the vector pET-30 Ek/LIC [2], fused with the green fluorescent protein gene *gfp* and heterologously expressed in *E. coli* Bl21(DE3) [1]. The gene expression was induced by addition of IPTG. The *E. coli* cells were harvested at the end of the stationary growth phase and washed in Tris-buffered saline (TBS, pH 7.5). To stain the GFP/S-layer expressing *E. coli* the cells were treated with 3% DAPI-DNA staining solution in the dark for 10 min. Subsequently, the cells were washed again with TBS.
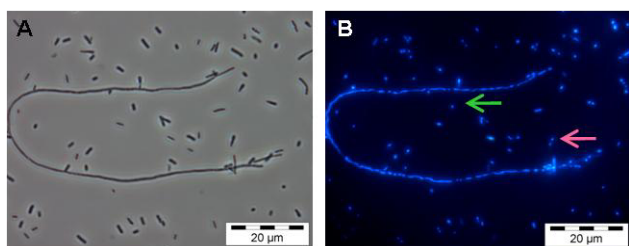
Fig. 1: Light microscopic images of S-layer expressing *E. coli* BL21 (DE3) in phase contrast mode (A) and visualized with the fluorescence microscopic filter U-MNU (B) of DAPI-stained DNA within cells and filaments. The green arrow marks DNA of *E. coli* single cells in the beginning and the pink arrow marks DNA of *E. coli* single cells in the final stage of the cell division.
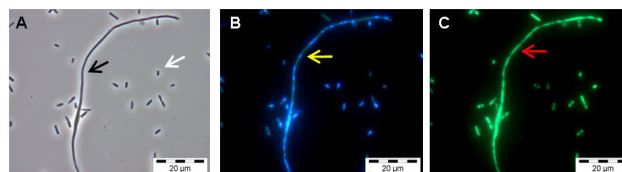
Fig. 2: Fluorescence microscopic images of GFP-coupled S-layer expressing *E. coli*. The phase contrast image shows a long filament (black arrow) next to *E. coli* single cells (white arrow) (**A**). Image **B** shows DNA stained with DAPI stain. The yellow arrow marks a DNA cluster next to unstained (DNA-free) cell areas. Image **C** shows the presence of the GFP-coupled S-layer protein. The red arrow marks the former "DNA-free" cell area that exhibit strong GFP fluorescence.

Light microscopic images of the cells and tubes were taken with an Olympus BX61 microscope in phase contrast mode and with the fluorescence filters U-MNU (DAPI) and U-MNIBA (GFP).

RESULTS. The microscopic analyses of GFP/S-layer expressing *E. coli* cells in phase contrast mode demonstrate that the cells form very long filaments showing dark and bright areas. In addition to the filaments, single cells of *E. coli* are found that possess a typical cell division behaviour. Staining with DAPI reagent shows that the *E. coli* single cells concentrate the complete DNA in the centre of the cells in the beginning cell division process (Fig. 1B, green arrow). At the end of the cell division process the divided cells possess two DNA-clusters at the reverse poles (Fig. 1B, pink arrow). Coevally, the long filaments that are found in the sample possess unusual long DNA-fibres that cross the whole filament (Fig. 1B). In a later stage these DNA-fibres split into shorter fibres that cross the single cells (Fig. 2B). The "DNA-free" areas contain a high amount of GFP-fusion protein as shown by microscopic images using a GFP-fluorescent filter (Fig. 2C).

DISCUSSION. The recombinant S-layer production in *E. coli* induces the formation of stable filaments and tubes. The huge amount of recombinant S-layer protein seems to interfere with the cell division while a lower protein amount in *E. coli* single cells ensure a normal cell division. It can be assumed that the number of plasmids is responsible for the effects. However, the underlying mechanism is still not characterized in detail.

[1] Lederer, F. et. al. (2010) *Microbiology*, **156**, 3584-95.
[2] Pollmann, K. et al. (2007) *Appl. Microbiol. Biotechnol.* **75**, 1079-1085.

Detection of a Fluorescence Resonance Energy Transfer (FRET) between two fluorescence dyes linked to S-layer proteins of *Lysinibacillus sphaericus* JG-A12

U. Weinert, K. Pollmann, J. Raff

S-layer proteins are the outermost cell envelope of numerous bacteria and almost all archaea. Their ability to self assembly in aqueous solution and on surfaces qualifies them as matrix for the construction of sensory layers. As part of such layers, two fluorescence dyes with the potential to initiate a FRET were coupled to the S-layer protein of *L. sphaericus* JG-A12. By using two different methods it could be verified that a FRET exist between these two proteins bound fluorescence dyes.

EXPERIMENTAL. The bacterial isolate *Lysinibacillus sphaericus* JG-A12 was grown over night at room temperature in Nutrient Broth medium (6 g/L, Mast Group Ltd., Merseyside, UK). S-layer proteins were isolated according to the protocol in reference [1]. S-layer proteins were modified at their carboxylic groups with the two fluorescence dyes Hilyte488 (green) and Hilyte555 (red) hydrazides in molar ratio of 3 : 1. The unspecific coupling was carried out with 20 mM of 1-ethyl-3-(3-dimethyl-aminopropyl) carbodiimide (EDC) as crosslinker which initiates an amid bond between a carboxylic and an amino group. All experiments were carried out in a 50 mM phosphate buffer at pH 5.6.

Fluorescence and lifetime measurements were performed in order to detect FRET. Fluorescence measurements (FluoroMax, Koyoto, Japan) were carried out at an excitation wavelength ($\lambda_{exc.}$) of 500 nm. Emission spectra were taken in range of 520 to 600 nm. The modified S-layer proteins were digested with trypsin, in order to interrupt a potential FRET in a molar ratio of 1 : 1 and time resolved fluorescence spectra were recorded. Lifetime measurements were performed with time-correlated single-photon counting (TCSPC) using the QM-40 system with Q-25 lifetime option (Birmingham, USA). An LED at 460 nm was used as excitation source and the emission was measured at 520 nm.

RESULTS. *Fluorescence measurements.* S-layer proteins were modified with a donor (Hilyte488) and acceptor (Hilyte555) fluorescence dye. Furthermore, two samples were modified with either Hilyte488 or Hilte555 and used as reference. Time resolved fluorescence measurements over two hours were performed in order to monitor the digestion of the proteins with trypsin.

Figure 1 shows the emission maxima of the FRET pair Hilyte488 and Hilyte555 and their corresponding reference over time. It can be clearly seen that the acceptor fluorescence decreases significantly during digestion in comparison to its reference sample, where only Hilte555 is bound to the protein. The emission of Hilyte488 remains nearly constant in both cases.

The measured data indicate that a previous FRET is interrupted, because the fluorescence dyes that were initially neighbored are located on different protein fragments after digestion. In result, the acceptor fluorescence decreases clearly due to the lack of energy transfer from the donor dye.

Lifetime measurements. Two samples were prepared which were coupled with either Hilyte488 or Hilyte488 and Hilyte555 as donor/acceptor pair. It is expected that
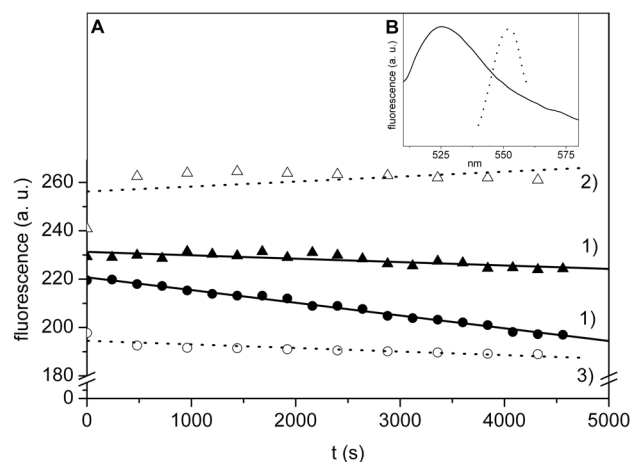
Fig. 1: (A) Time dependent fluorescence of the the S-layer proteins ($\lambda_{exc.}$ = 500 nm), The S-layer proteins were modified with (1) FRET pair Hilyte488/Hilyte555 at an emission of either 527 nm (▲) or 565 nm (●), with (2) Hilyte488 at an emission of 527 nm (△), and with (3) Hilyte555 at an emission of 565 nm (○) in presence of the protease trypsin. (B) Emission spectra of Hilyte488 (solid line; $\lambda_{exc.}$ = 500 nm) and excitation spectra of Hilyte555 (dashed line) with an emission wavelength of 565 nm.

the lifetime of the fluorescence of the donor Hilyte488 is decreased, if FRET occurs between the two dyes as compared to the unquenched lifetime of Hilyte488. The table shows the lifetime of Hilyte488 in both samples. It can be clearly seen that the fluorescence lifetime of the donor is decreased in the presence of the acceptor dye. These results indicate that a FRET occurs between Hilyte488 and Hilyte555.

Tab. 1: Lifetime of fluorescence donor dye Hilyte488 with (FRET) and without the influence of acceptor (no FRET); LED with an excitation wavelength of 460 nm and emission wavelength at 520 nm was used for detection.

Sample	Lifetime [ns]
no FRET	1.2 ± 0.1 (31%)
	4.3 ± 0.04 (69%)
FRET	0.23 ± 0.1 (78%)
	3.5 ± 0.08 (22%)

Fluorescence decays were fitted with 2-exponential model function using the nonlinear least squares minimization with iterative reconvolution. The amplitude-averaged lifetimes were also calculated.

Both methods prove the occurrence of a FRET between Hilyte488 and Hilyte555 when coupled to the S-layer protein by EDC crosslinking. In further experiments the FRET will be optimized and used as part of a biosensing layer where S-layer proteins serve as a matrix for the binding of various functional molecules.

[1] Raff, J. et al. (2003) *Chem. Mater.* **15**, 240-244.

Interactions of U(VI) with cell and SlaA-layer ghosts of *Sulfolobus acidocaldarius*

T. Reitz, M. Merroun,[1] A. Rossberg, S. Selenska-Pobell

[1]Departamento de Microbiologia, Universidad de Granada, Granada, Spain

We demonstrate that the main ligands involved in U(VI) binding by *Sulfolobus acidocaldarius* DSM 639 in the range of the physiological pH optimum for the growth of the strain (pH 1.5 and 3) are located on the cytoplasma membrane and not on the SlaA-layer enveloping its cells. At moderate acidic conditions, (pH 4.5 and 6) the purified SlaA-layer binds U(VI) *via* carboxylic groups.

Populations of the acidothermophilic archaeon *S. acidocaldarius* were demonstrated to persist and even to propagate in acidic environments such as coal and heavy metal mining wastes [1, 2]. The cells of this organism are covered by a detergent-resistant proteinaceous S-layer, called SlaA [3]. The extreme stability of the SlaA-layer to high temperature, proteases, and detergents allows isolation and purification of empty SlaA-layer ghosts with the shape of the cells. This allowed us to clearly demonstrate that, in contrast to the S-layers of bacteria, recovered from similar habitats, which possess high uranium binding capability, the SlaA-layer of *S. acidocaldarius* is not implicated in uranium binding at highly acidic conditions and binds only low amounts of uranium at moderate acidic conditions. The main role in uranium binding at both pH conditions plays the phosphate groups of the cytoplasma membrane. At moderate acidic conditions, however, the carboxylic groups of some associated with the cytoplasma membrane proteins are also implicated in the uranium complexation.

EXPERIMENTAL. The *S. acidocaldarius* cell and SlaA-layer ghosts were prepared and purified by using the procedure of Grogan *et al.* [4]. The protein content of the two kinds of ghosts was analyzed by using denaturing sodium dodecyl sulphate polyacrylamide gel electrophoresis (SDS-PAGE) according to [5]. The cell and the SlaA-layer ghosts were treated with uranyl nitrate as described earlier [6] and their sorption activity was compared to those published for the whole cells by the same authors.

RESULTS. The two studied cell envelope fractions, the cell ghosts and the SlaA-layer ghosts had a translucent appearance under microscope, indicating that they were
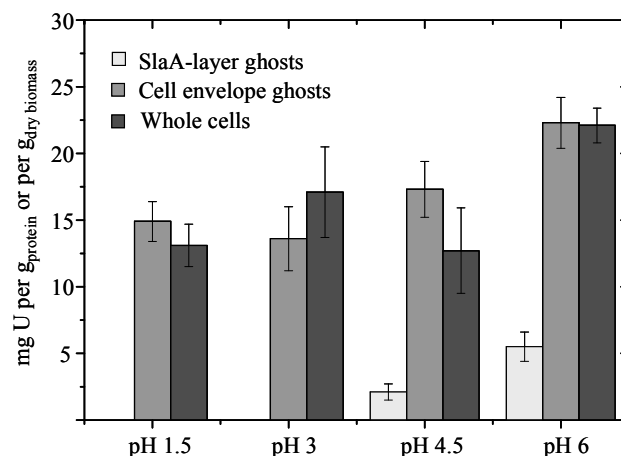
Fig. 2: U(VI) binding capacities of the cell and the SlaA-layer ghosts compared to the whole cells of *S. acidocaldarius* at different pH values (biomass concentration was 0.5 ± 0.05 mg).

free of cellular compounds (not shown). They both possessed the shape and the size of the whole cells, perceptibly due to the presence of the outermost SlaA-layer, obviously responsible for the shape and mechanical stability of the cells of the studied organism.

The protein content of the two cell envelope fractions was checked by using denaturing SDS-PAGE. As shown in Fig. 1, only one band is present in the lane containing the purified SlaA-layer ghosts. The molecular mass of about 150 kDa is well in line with those obtained in former studies [3]. As anticipated, the same protein band was observed in the sample prepared from the cell envelope ghosts (Fig. 1, lanes 2 and 3). In addition, several further protein bands are present in the cell ghost's fraction. The most prominent of these additional bands has a molecular mass of about 60 kDa which corresponds to those of the SlaB protein [3] anchoring the SlaA protein to the cytoplasma membrane. The rest of the protein bands most likely represent integral membrane proteins.

As evident from the results presented in Fig. 2 the SlaA-ghost do not bind detectable amounts of U at pH 1.5 and 3.0 and rather low amounts at pH 4.5 and 6.0. TRLF and XAS analyses revealed that the carboxylic groups of the SlaA are implicated in this binding [7]. The uranium binding capability of the cell ghosts, however, is almost the same as those of the whole cells. This indicates that the S-layer of the studied thermo acidophilic archaeon plays a very limited role in the protection of the cells of the strain against uranium. This is in contrast to the case of bacterial S-layers studied up to date.

[1] Groudev, S. et al. (1991) *FEMS Microb. Rev.* **11**, 261-267.
[2] Marsh, R. et al. (1983) *FEMS Microbiol. Lett.* **17**, 311-317.
[3] Veith, A. *et al.* (2009) *Mol. Microbiol.* **73**, 58-72.
[4] Grogan, D.W. *et al.* (1996) *J. Microbiol. Methods* **26**, 35-41.
[5] Laemmli, U.K. (1970) *Nature* **227**, 680-685.
[6] Reitz, T. *et al.* (2010) *Radiochim. Acta* **98**, 248-257.
[7] Reitz, T. (2011) Thesis, in preparation.
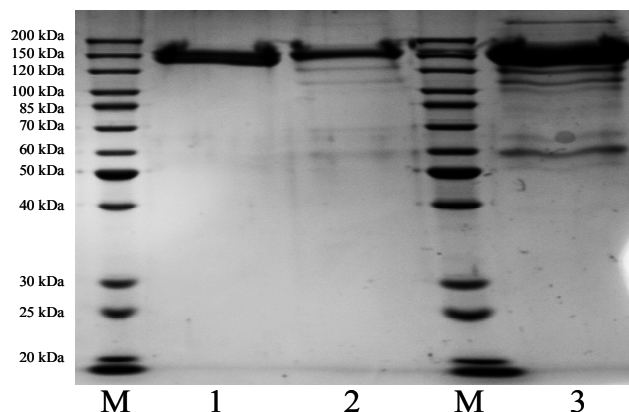
Fig. 1: SDS-PAGE protein gel stained with colloidal Coomassie Briliant Blue G-250. (1) 15 µg of the SlaA-layer ghosts; (2) 10 µg of the cell envelope ghosts; (3) 30 µg of the cell envelope ghosts; (M) protein marker - Pageruler[TM] SM0661.

Fabrication of highly ordered magnetic bio-Au nanoclusters by using SlaA-layer ghosts of *Sulfolobus acidocaldarius* as a template

T. Reitz, T. Herrmannsdörfer,[1] M. Merroun,[2] A. Geissler, S. Selenska-Pobell

[1]Dresden High Magnetic Field Laboratory, HZDR, Dresden, Germany; [2]Departamento de Microbiologia, Universidad de Granada, Granada, Spain

We demonstrate that the surface layer SlaA of the archaeon *Sulfolobus acidocaldarius* is an excellent matrix for preparation of bio-Au nanoclusters. The archaeal bio-Au nanoparticles are significantly bigger than those formed on the *B. sphaericus* JG-A12 S-layer. Moreover, in contrast to *B. sphaericus* bio-Au and to Au as a bulk noble metal, the archaeal bio-Au nanoparticles possess unique magnetic properties.

The regularly structured paracrystalline surface layers (S-layers) of prokaryotic microorganisms are promising biological templates for production of metal nanoclusters for biotechnological applications. Formerly we have demonstrated that the S-layers of some *Bacillus sphaericus* strains can effectively bind noble metals and can be used for preparation of palladium, platinum, and gold nanoclusters by using different reduction agents [1,2] or electron beam [3].

In this work, Au-nanoclusters were produced on the extremely stable (against high temperatures, acidity, proteases, and mechanic stress) S-layer of the acidothermophilic archaeon *Sulfolobus acidocaldarius*. One additional important characteristic feature of this S-layer, called recently SlaA [4], is the presence of the sulfur containing amino acid cysteine in its primary structure. This is in contrast to the above mentioned bacterial S-layers and is of great importance for the effective binding and deposition of Au cations.

EXPERIMENTAL. The SlaA was purified by using the procedure of Grogan et al. [5]. The purified SlaA-layer fraction was treated initially with tetrachloroauric(III) acid solution as described in [2]. Afterwards, the deposited Au(III) cations were reduced to Au(0) by using dimethylaminoborane. The localization and the size of the bio-Au nanoparticles were studied by using Transmission Electron Microscopy (TEM) combined with EDX. The magnetic properties of the bio-Au were measured by using a SQUID magnetometer.

RESULTS. Figure 1 presents a TEM micrograph of the bio-Au nanoclusters distributed on the SlaA-layer of the studied archaeon and the EDX analysis of one particular cluster. The size of the nanoparticles is about 3 nm and they are associated with sulfur atoms. As demonstrated by SQUID magnetometry the studied gold nanoparticles are paramagnetic and possess a magnetic moment of order 0.1 μ_B/Au atom (Fig. 2). No magnetic properties were observed for the Au-nanoparticles formed on the S-layer of the above mentioned *B. sphaericus* S-layer which contains no sulfur.

We suggest that the sulfur atoms are possibly contributing to the observed magnetic properties of the bio-Au. However, the number of sulfur atoms implicated in the Au complexation is extremely low (only a few atoms per nano-particle). On the other hand, the size of the nanoparticles formed on the archaeal SlaA-layer is significantly bigger (about 3 nm) in comparison to those formed on the bacterial S-layer (less then 1 nm). The size difference in
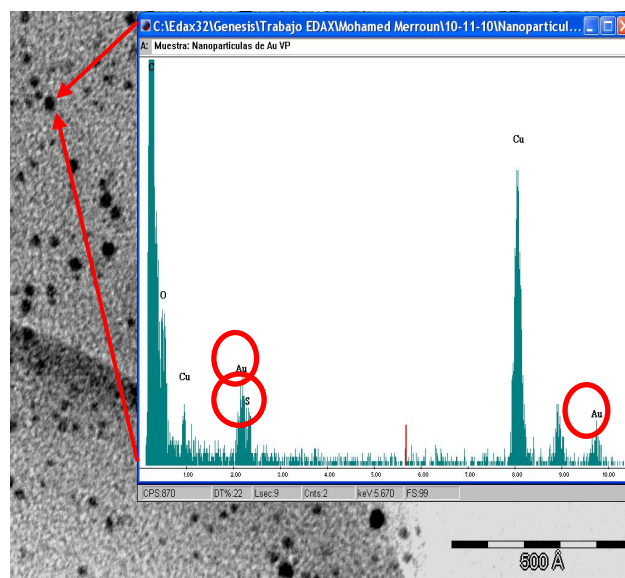
Fig. 1: Bio-Au nanoparticles formed on the SlaA-layer of *Sulfolobus acidocaldarius*.
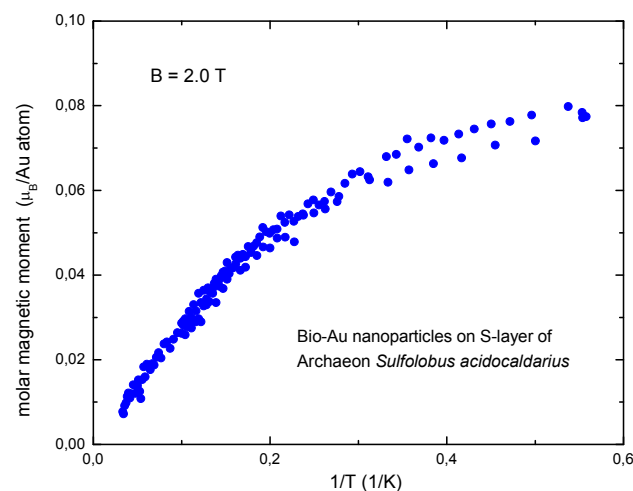
Fig. 2: Paramagnetism of Bio-Au nanoparticles formed on the SlaA-layer of *Sulfolobus acidocaldarius*.

the two kinds of nanoparticles can be explained by the different size of the pores of the two S-layer lattices, where the initial deposition of the metal cations occurs. The archaeal SlaA-layer possesses p3 lattice symmetry and significantly larger pores [4] then the bacterial S-layer which has P4 symmetry [1,2]. The size of the Au-nanoclusters may play also a role for their magnetic properties.

Efforts to understand the reasons for the observed unexpected magnetic behavior of the newly constructed bio-Au-nanoparticles are in progress.

[1] Fahmy, K. et al. (2006) *Biophys. J.* **91**, 996-1007.
[2] Merroun, M. et al. (2007) *Mater. Sci. Eng. C-Mater. Biol. Appl.* **27**, 188-192.
[3] Wahl, R. et al. (2001) *Adv. Mater.* **13**, 736-740.
[4] Veith, A. et al. (2009) *Mol. Microbiol.* **73**, 58-72.
[6] Grogan, D.W. (1996) *J. Microbiol. Methods* **26**, 35-41.

S-layer protein from *Lysinibacillus sphaericus* JG-A12 as a matrix for Au(III) sorption and Au nanoparticle formation

U. Jankowski, M. Merroun,[1] S. Selenska-Pobell, K. Fahmy

[1]Departamento de Microbiologia, Universidad de Granada, Granada, Spain

The strain *Lysinibacillus sphaericus* JG-A12, isolated from the uranium mining site at Haberland, Saxony (Germany), accumulates radionuclides and toxic metals through binding to its surface layer (S-layer). We show by Fourier-transform infrared (FT-IR) spectroscopy that upon Au(III) binding and the subsequent reductively induced formation Au-nanocluster formation, the S-layers becomes resistant to acid denaturation. Side chain carboxylates respond little to metallization and pH, indicating a hydrophobic environment in the Au-treated samples. EXAFS spectra agree with the metallic Au-Au distance but the reduced coordination number indicates that the Au-nanoclusters do not exceed ~2 nm. Thus, the S-layer of *L. sphaericus* JG-A12 provides a biotemplate for efficient Au-nanocluster formation in an acid-resistant matrix and independently of cysteins [1].

Bacterial surface layers (S-layers) are common surface structures in many bacteria and archaea and have attracted attention by their potential for a variety of biotechnological applications [2] including the growth of metal nanoclusters within their two-dimensional paracrystalline protein lattice [3]. Here, we have studied the formation of gold nanoclusters using the S-layer of *L. sphaericus* JG-A12 as a template. The strain had been isolated from an uranium mining waste pile (Haberland, Saxony, Germany) and binds various metals, including high amounts of uranium [4].

EXPERIMENTAL. S-layers were prepared [5] and incubated in a solution of 3 mM $Au^{(III)}$ (from $HAuCl_4$) for 72 h followed by dialysis against H_2O. Nanoparticles were formed by reduction with dimethylamineboran (DMAB). FTIR absorption spectra were measured by attenuated total reflectance (ATR) at 2 cm^{-1} resolution using a nitrogen-cooled MCT-detector. Gold L_{III}–edge X-ray absorption spectra of dried S-layers were collected at the Rossendorf Beamline at the European Synchrotron Radiation Facility (ESRF), Grenoble (France) according to described procedures [5]. A metallic Au foil and a solution of 3 mM $HAuCl_4$ pH 3 were used as reference compounds.
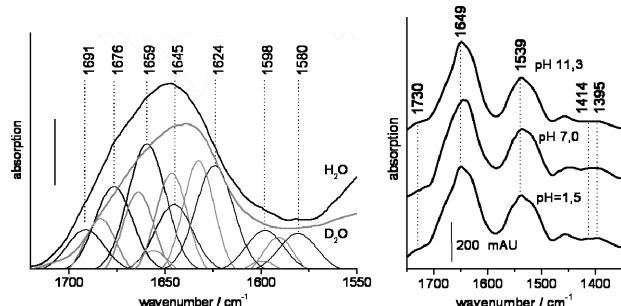
Fig .1: IR spectra of Au-bound S-layers. *Left:* S-layer loaded with Au(III) in H_2O (black) and D_2O (gray) and decomposed in Gaussian/Lorentzian bands (halftones corresponding to original spectra). Scale bar: 100 mAU. *Right:* pH-sensitive IR absorption of the S-layer with Au-nanoparticles formed after reduction with DMAB.
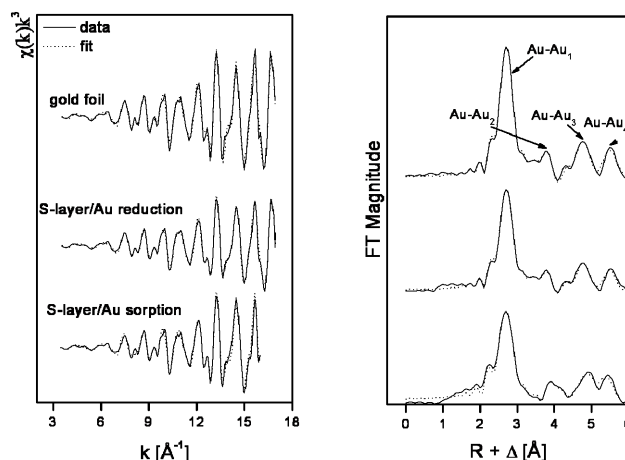
Fig. 2: k^3-weighted EXAFS spectra for the Au-loaded S-layer protein after and before addition of DMAB and for Au foil as a gold reference compound.

RESULTS. Au-treated S-layers of *L. sphaericus* JG-A12 (Fig. 1, left) show an amide-I absorption indicative of predominant β-sheets supported by the typical additional high frequency carbonyl modes (1680-1690 cm^{-1}). Large contributions from random structure between 1650 and 1620 cm^{-1} are inferred from the frequency down shifts upon H/D exchange. This resembles the normal and Pd(II)-bound S-layer for which secondary structure has been analyzed in detail [5]. Reductive Au-nanocluster formation causes a slight upshift of the amide-I absorption (Fig. 1, right) compatible with increased random structures. The pH dependence of the antisymmetric stretching mode at ~1560 cm^{-1} with Au(III) is much weaker than in the Pd(II)-bound state and already at alkaline pH the symmetric carboxylate stretching (1350-1450 cm^{-1}) resembles that obtained with untreated S-layers only at pH < 4, indicating partially protonated carboxyl side chains in Au-treated samples at pH 7 in agreement with the positive feature in the 1720-1730 cm^{-1} range (COOH carbonyl). This similarity between Au(III)-bound and nanocluster-carrying S-layer suggests 1) an intrinsic reducing property, 2) Au(III)/Au(0) seem to induce the hydrophobic burial of Asp and Glu side chains, thereby, destabilizing their ionized states. Figure 2 shows gold L_{III}-edge EXAFS spectra of the S-layers in the presence and absence of DMAB together with those of Au foil. In both samples, metallic Au is present with interatomic distances (2.87 ± 0.02 Å) comparable to those in Au foil but with reduced coordination number in the first shell (10.8 ± 2.0 Å), evidencing the formation of ~2 nm-sized particles (using the cubic FM3-M structure of metallic gold). In agreement with the FT-IR results, Au(0) formation can occur already in the absence of DMAB.

[1] Jankowski, U. et al. (2010) *Spectr.-Int. J.* **24**, 177-181.
[2] Sara, M. et al. (2005) *J. Nanosci. Nanotechnol.* **5**, 1939-1953.
[3] Pollmann, K. et al. (2006) *Lett. Appl. Microbiol.* **43**, 39-45.
[4] Pollmann, K. et al. (2006) *Biotechnol. Adv.* **24**, 58-68.
[5] Fahmy, K. et al. (2006) *Biophys. J.* **91**, 996-1007.

Coupling of anti-thrombin aptamers to S-layer proteins for sensory applications

N. Müller, U. Weinert, J. Raff, K. Pollmann

Surface-layer proteins are structure proteins forming a paracrystalline lattice on a nanometer scale. They are self assemble in aqueous solution, at interfaces or on surfaces. Additionally, S-layer proteins possess a high amount of modifiable functional groups. All these characteristics make them highly attractive for nanotechnological applications. One approach is the design of a sensory device with the help of S-layer proteins, aptamers and fluorescence dyes for the detection of analytes in aqueous solutions. In this work, a model aptamer is coupled to the S-layer protein in order to prove the functionality in such a system. The aptamer is specific for thrombin and SDS-PAGE was used to investigate the affinity for binding the enzyme.

Aptamers are single stranded DNA or RNA oligonucleotides [1] which are specific for one analyte. Thereby the binding is realized by its three dimensional structure [2]. In comparison to antibodies aptamers are more stable, easier to handle and smaller in size [3]. In this current work, an anti-thrombin aptamer (AT-aptamer) is used as receptor [4].

EXPERIMENTAL. The isolate *Lysinibacillus sphaericus* JG-A12 was grown over night at room temperature in Nutrient Broth medium (6 g/L, Mast Group Ltd., Merseyside, UK). S-layer proteins were extracted according to the protocol in reference [5]. The AT-aptamer was purchased with a SH-group at its 5' end and with fluorescence dye TAMRA at its 3' end. The coupling of S-layer proteins with AT-aptamer was realized with the heterologous crosslinker p-maleimidophenyl isocyanate (PMPI). PMPI possesses an isocyanate group and a maleimide group. In a first step, the crosslinker is linked to the hydroxy group of the S-layer protein, and in a second step, the AT-aptamer is coupled to the protein by its SH-group. Therefore, 0.5 mg S-layer proteins were resuspended in 90 μL 50 mM phosphate buffer (pH 6.7) and 10 μL PMPI, solved in DMSO, was added to S-layer suspension to a final concentration of 10 μg mL^{-1}. The reaction solution was incubated for 30 min, the modified S-layer proteins centrifuged, selectively resuspended, the AT-aptamer added in a molar ratio of 1 : 5000 (aptamers to S-layer proteins) and incubated over night at 4 °C. The modified S-layer protein was washed several times to remove unbound aptamer.

In order to check for functionality of the linked AT-aptamer, affinity measurements with human thrombin were performed. Thrombin was added to the sample in a final concentration of 0.36 μM and the solution was allowed to stay for 4 h at 4 °C. The modified S-layer proteins were centrifuged at 12,400 g for 60 min at 4 °C in order to remove not attached thrombin. Both supernatant and functionalized S-layer proteins were analyzed by SDS-PAGE.

RESULTS. The success of coupling of aptamers to the S-layer proteins was proven by fluorescence measurements (data not shown). After successful binding of the AT-aptamer to the protein the samples were incubated with thrombin. Not linked thrombin was removed by centrifugation and supernatants and pellets were analyzed by
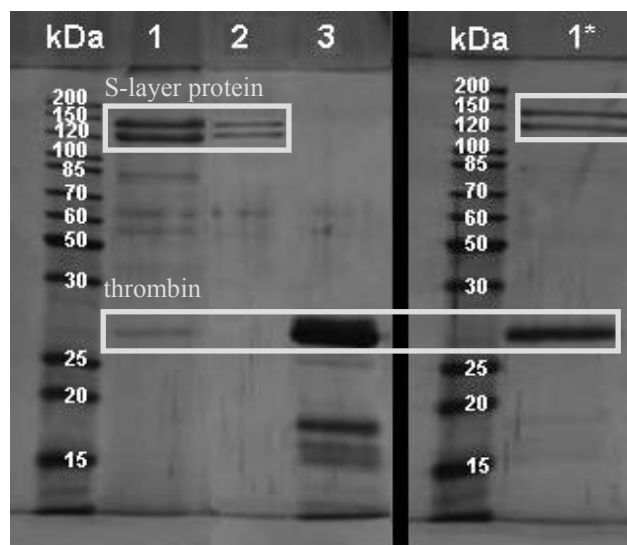
Fig. 1: SDS-PAGE of S-layer proteins modified with AT-aptamer and after incubation with thrombin; (1) S-layer protein modified with AT-aptamer and attached thrombin, (2) S-layer protein, (3) thrombin, (1*) supernatant after centrifugation.

SDS-PAGE (Fig. 1). Lane 3 presents thrombin with its significant band at approx. 25 kDa. The S-layer protein is shown in lane 2 and it can be seen that no band occurs at 25 kDa. There are two bands visible in the range of 120 to 150 kDa which both represent the S-layer protein (native and fragmented protein). Lane 1 demonstrates the thrombin binding to the linked AT-aptamer. A band at 25 kDa can be clearly identified which represents thrombin (Fig. 1). During sample preparation for SDS-PAGE thrombin was released from the aptamer because of the denaturing conditions. Hence, thrombin and the modified S-layer protein are visible as distinct bands on the SDS gel. The last lane in Fig. 1 (lane 1*) shows the supernatant of the binding experiment. There are also bands visible in the range of 120 to 150 kDa and at 25 kDa, representing again the S-layer protein and thrombin. S-layer protein is also present in the supernatant, because there is an equilibrium between the protein polymers and monomers in solution.

The presented results demonstrate that aptamers can be linked to S-layer proteins without losing their functionality, thus proving the feasibility of the first essential step in the construction of a sensory layer. The next step will be the modification of S-layer proteins with both, aptamers and fluorescence dyes.

[1] Ellington, A.D. et al. (1990) *Nature* **346**, 818-822.
[2] Stoltenburg, R. et al. (2005) *Anal. Bioanal. Chem.* **383**, 83-91.
[3] Mairal, T. et al. (2008) *Anal. Bioanal. Chem.* **390**, 989-1007.
[4] Bock, L.C. et al. (1992) *Nature* **355**, 564-566.
[5] Raff, J. et al. (2003) *Chem. Mater.* **15**, 240-244.

Influence of S-layer proteins on the crystallization of ZnO

K. Pollmann, A. Marquard, J. Raff

ZnO particles were prepared using two different synthesis methods at different temperatures with and without S-layer proteins. XRD and SEM analyses demonstrated a strong influence of the protein on crystallinity and morphology of formed ZnO particles.

Different peptides and proteins have been used for the synthesis of composite materials consisting of the biological compound and an inorganic compound such as ZnO. These materials may exhibit enhanced properties such as superior mechanical stability or photocatalytic activity. The adsorption of ZnO, kinetics of ZnO-formation, crystallinity and morphology of ZnO crystals depends on the isoelectric point, size, shape and chemical composition of the proteins [1]. In the present study, we investigated the influence of S-layer proteins on ZnO formation using two different synthesis methods. These materials can be used for the development of photocatalytically active surfaces. The formation of two-dimensional arrays via self-assembling makes the S-layer proteins highly attractive for the development of thin composite films.

EXPERIMENTAL. S-layer proteins of *Lysinibacillus sphaericus* were isolated as described previously [2]. In the first method, ZnO particles were synthesized by incubation of 10 mg S-layer in 20 mL 20 mM $ZnCl_2$, pH 8.0, at 22 °C, 37 °C, or 50 °C. ZnO was synthesized by the addition of 25% NH_3 and subsequent washing with deionized H_2O [3]. In the second method [1], ZnO particles were synthesized by the addition of 10 mg S-layer to a solution of 50 mL 30 mM Tris-buffer at pH 8.0. ZnO formation was started by the addition of $Zn(NO_3)_2(H_2O)_6$ to a final concentration of 20 mM. The solutions were incubated at 22 °C, 37 °C, or 50 °C for 6 h. ZnO synthesized in the presence and absence of S-layer proteins was characterized using XRD (D8 theta-theta diffractometer in Bragg-Brentano geometry) and SEM (S-4800, Hitachi).

Tab. 1: Influence of proteins on ZnO formation from $Zn(NO_3)_2(H_2O)_6$: formation of precipitates and crystallinity.

Incubation temperature	With S-layer protein, 4 h incubation	Without protein, 4 h incubation
22 °C	Crystalline ZnO, crystallite size 14.4 nm	Clear solution
37 °C	Crystalline ZnO, crystallite size 12.2 nm	Crystalline ZnO; size 12.6 nm
50 °C	Crystalline ZnO, crystallite size 13.3 nm	Crystalline ZnO; size 18.4 nm

RESULTS. When using $Zn(NO_3)_2(H_2O)_6$ as Zn source, a white fluffy precipitate was formed in all protein samples immediately after addition of the nitrate (Tab. 1).Without protein, a fine white precipitate was formed only at higher temperatures. When using $ZnCl_2$ as Zn source, a precipitate was formed in all samples (Tab. 2).
Composition and crystallinity of the formed precipitates were analyzed by XRD. In all protein samples, the analyses demonstrated the formation of crystalline ZnO. Sizes of the crystallites depended on the chosen method and ranged between 10.6 and 14.4 nm. In comparison, crystalline ZnO of a crystallite size of 12.6 nm was formed

Tab. 2: Influence of proteins on ZnO formation from $ZnCl_2$: formation of precipitates and crystallinity.

Incubation temperature	With S-layer protein	Without protein
22 °C	Crystalline ZnO, crystallite size 15.6 nm	Amorphous
37 °C	Crystalline ZnO, crystallite size 16.3 nm	Amorphous
50 °C	Crystalline ZnO, crystallite size 15.0 nm	Crystalline ZnO, size 16.2 nm

without protein when using $Zn(NO_3)_2(H_2O)_6$ as Zn source (Tab. 1). From a $ZnCl_2$ solution, crystalline ZnO was formed only at a temperature of 50 °C (Tab. 2).
The morphology of the ZnO composites was studied by SEM. The images demonstrate a significant influence of proteins on the morphology of ZnO particles. ZnO particles produced without proteins using $Zn(NO_3)_2(H_2O)_6$ showed a donut-like morphology of a size of 12-16 µm. These particles were composed of ZnO sheets of a size of about 400 to 800 nm. In comparison, in the presence of S-layers the formed ZnO particles were significant smaller (4-8 µm) and were enclosed by the proteins (Fig. 1b).
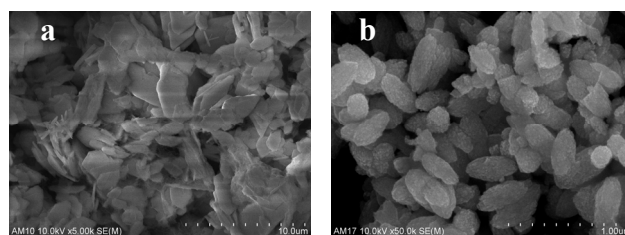
Fig. 2: SEM of ZnO precipitated from $ZnCl_2$ at 37 °C without protein (a), and in the presence of S-layer (b).

Similarly, precipitates produced from $ZnCl_2$ without protein showed the formation of sheets of different sizes (Fig. 2a). In comparison, oval ZnO-particles were formed from the same solution in the presence of proteins (Fig. 2b).
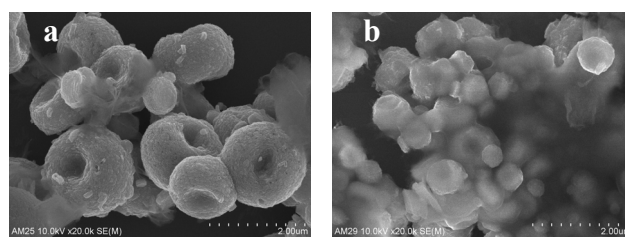
Fig. 1: SEM of ZnO precipitated from $Zn(NO_3)_2(H_2O)_6$ at 37 °C without protein (a), and in the presence of S-layer (b).

CONCLUSIONS. The results clearly demonstrate the influence of the proteins on ZnO formation, crystallinity, size and morphology of particles.

[1] Bauermann , L.P. et al. (2007) *Int. J. Mat. Res.* **98**, 879-883.
[2] Raff, J. (2002) *Report FZR-358.*
[3] Pollmann, K. et al. (2009) *Report FZD-511*, p. 27 .

S-layer based catalytic hollow spheres

T. Günther, C. Steiniger, J. Raff, K. Pollmann

The development of new catalytic materials is one branch of continuing research originating in the investigation of interactions of heavy metals with bacterial surface layers. Their high binding capacity for palladium and platinum and their regular structure makes them suitable for the formation of nanocatalysts. Simple and cheap methods were developed to prepare hollow polyelectrolyte capsules which were subsequently coated with recrystallizing S-layer proteins. The coating technique was optimized on polyelectrolyte coated flat substrates [1]. The S-layer recrystallization on these surfaces was monitored by AFM. The steps of the capsule preparation were checked by AFM and SEM. The complexation of metals was quantified by ICP-MS. Catalytic activity was tested by Cr(VI) reduction.

EXPERIMENTAL. Templates were prepared by precipitating calcium carbonate in the presence of polystyrenesulfonate (PSS) as described [2]. Polyelectrolyte shells on these templates were prepared by the LbL method [3] using five to seven alternating polyelectrolyte layers of polyallylaminehydrochloride (PAH) and PSS. The coating started with PAH. The calciumcarbonate core was dissolved by adding 3 M HCl. After washing, the S-layer proteins were recrystallized on the outer surface of the hollow spheres by using the method described in [4] at an altered pH of 8.0. The spheres were loaded with Pd-nanoparticles by three hours incubation of the templates with 2 mM K_2PdCl_4 solved in phosphate buffer pH 5.4, followed by washing and subsequent reduction of the bound palladium with dimethylaminoborane. For AFM and SEM analyses 20 µL of the sample suspensions were placed on a cleaned wafer and dried at 70°C for at least 2 hours. AFM was done in AC mode using a silicon cantilever (1 N/m, 75 kHz). The catalytic Cr(VI) reduction was done as described elsewhere [5].

RESULTS. The hollow spheres that were used as templates had an average size of 5 to 7 µm and a narrow size distribution as shown in Fig. 1-A. A seven layer shell has a thickness of about 70 nm after solving the core as determined by AFM (Fig. 1-B). The completely composed spheres are shown in the SEM image Fig. 1-C. With the S-layer coating metal binding could be doubled from 30 mg/ml to 60 mg/ml compared to uncoated spheres. On flat surfaces the S-layer form a monolayer of 10 nm height in water. The swollen polyelectrolyte layers are five to ten times thicker than in dried condition [6]. This means that the walls of the capsules are 350 to 700 nm thick. The small protein layer can bind more metal than the 35 to 70 times thicker polyelectolyte layer. First experiments addressing catalytic activity were promising compared to palladium powder as reference catalyst. The reduction of 1.74 mmol Cr(VI) by 0.1 mg Pd nanoparticles bound on capsules was completed (99%) within 2 min. Palladium powder was used as reference material. Only 17% of the Cr(VI) was reduced after 10 min.
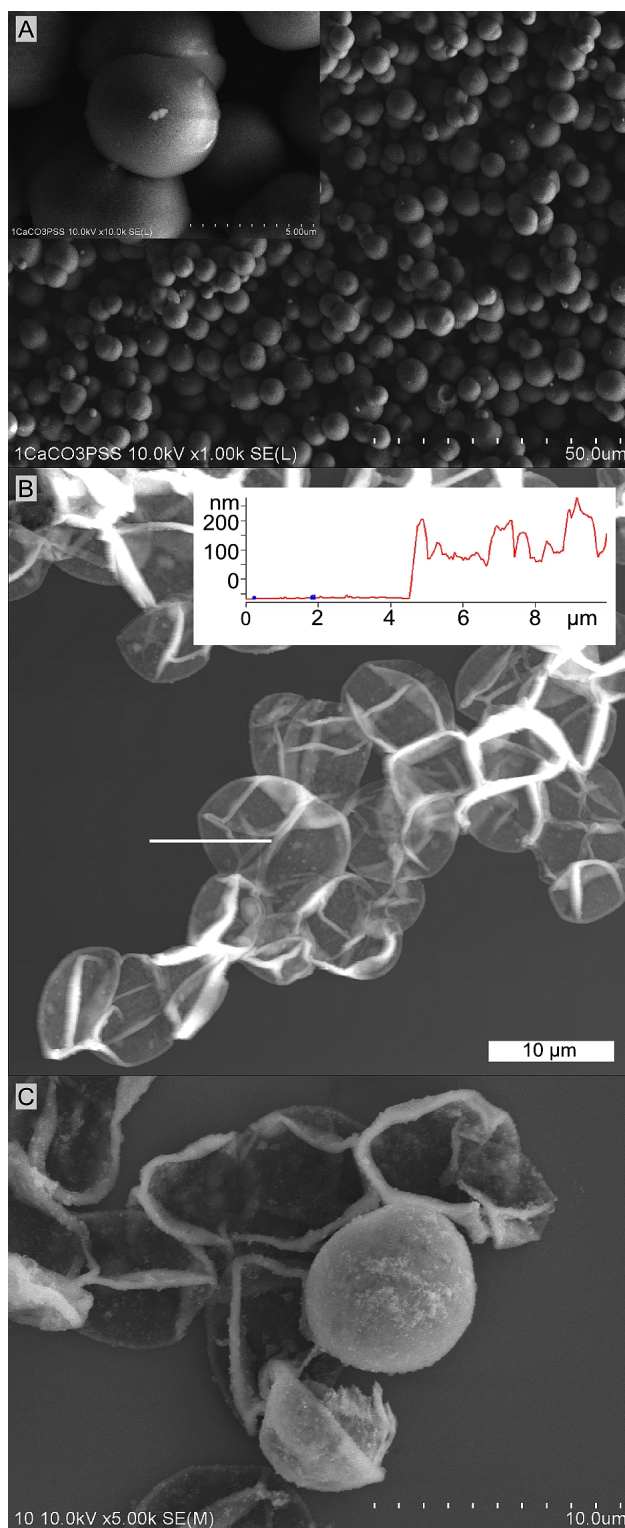
Fig. 1: A – SEM image of dried calcium carbonate templates at silicon
B – AFM height image of hollow capsules after dissolution of the template (embedded height plot corresponds to the line)
C – SEM image of the ready to use catalytic microspheres dried at silicon support

[1] Günther, T. et al. (2009) *Report FZD-530*, p. 23.
[2] Jiang, Y. et al. (2009) *J. Mater. Chem.* **19**, 9068–9074.
[3] Decher, G. et al. (1997) *Science*. **277**, 1232-1237.
[4] Györvary; E.S. et al. (2003) *J. Microsc.*, **212**, 300–306.
[5] Mabbett, A.N. et al. (2002) *Biotechnol. Bioeng.* **79**, 389-397.
[6] Cornelsen, M. et al. (2010) *Macromolecules* **43**, 4300-4309.

Impact of uranium on the cellular glutathione pool in canola (*Brassica napus*) cell suspensions

K. Viehweger, G. Geipel

Uranium (U) as a redox-active heavy metal can cause various redox imbalances in plant cells. Measurements of the cellular glutathione/glutathione disulfide (GSH/GSSG) by HPLC after cellular U contact of canola cell suspensions (*Brassica napus*) revealed an interference with this essential redox couple. Using the Nernst equation, it was possible to calculate the half-cell reduction potential of 2GSH/GSSG [1].

EXPERIMENTAL. Canola cell suspensions were sequentially fractionated obtaining the cytoplasmic fraction. Proteins were subsequently precipitated by acetone and the SH- and NH_2 functionalities in the remained supernatant were tagged either by monobromobimane (MBB) or 2,4-dinitrobenzol (DNFB, Sanger reagent) and detected by reversed phase HPLC measurements.

RESULTS. The cellular GSH remained constant within the first 6 hours of contact with 10 µM U (Fig. 1A). Afterwards, the tripeptide dropped down even on the half of the initial amount after 24 hours. In contrast, 50 µM U induced a strong increase of GSH up to the 5 fold of the initial level (Fig. 1A).

The level of GSSG was raised up to 5 fold in the presence of U compared with the respective initial values (Fig. 1B). However, this starting level was reached after 24 hours again.

In contrast to 10 µM U, 50 µM U caused a drastic increase of GSH. Such high U concentrations apparently induced the formation of ROS and free radicals. U is a redox-active heavy metal which can directly generate ROS *via* Fenton like reactions and the Haber-Weiss cycle. The detoxification of ROS is GSH consuming and generates GSSG. U triggered the accumulation of cellular GSSG (Fig. 1B).

These changes in glutathione status induced cellular redox imbalances. Another expression for these imbalances is the altered half-cell reduction potential of the couple 2GSH/GSSG. This can be calculated using an adapted Nernst equation (Eq.1).

$$E = -267 \text{ mV} - \frac{59.1}{2} \log \frac{2\left[GSH\right]}{\left[GSSG\right]} \text{ mV; at 25 °C, pH 7.4}$$

(Eq. 1)

Moderate U concentrations (10 µM) shifted the cellular redox environment towards more oxidizing conditions due to elevated GSSG levels whereas higher U concentrations (50 µM) enhanced the reducing capacity of the cell (Fig. 2) due to a more pronounced increase of GSH. Such different defense reactions induced by lower and higher concentrations of biotic or abiotic stress are well known. The enhanced reducing capacity in the case of 50 µM U can be attributed to an elicitation of hypersensitive response.

Fig. 1: Absolute concentrations of GSH (A) and GSSG (B). Data are means of 3 independent experiments for each U concentration, SD ± 0.9 for GSH and SD ± 0.3 for GSSG. Asterisks denote significant differences between controls and U treatments (two-way ANOVA; *** p < 0.001; ** p < 0.01; * p < 0.05).
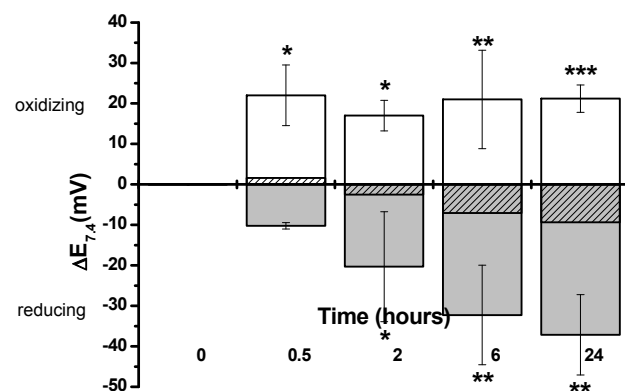
Fig. 2: Development of the half-cell reduction potential of 2GSH/GSSG calculated using Eq. 1 and the values from Fig. 2. Open columns represent addition of 10 µM U, filled columns 50 µM U and hatched columns the control.

CONCLUSIONS. The cellular redox balance in suspension cells of canola was impaired by contact with U. Two different, U concentration dependent defense pathways can be postulated: a specific after contact with lower U concentrations and an unspecific induced by higher concentrations, respectively.

[1] Viehweger, K. et al. (2011) *Environ. Exp. Bot.*, submitted.

Interaction of U(VI) with fungal cells

A. Günther, J. Raff

Different strains of fungi have a high potential for the uptake of heavy metals and actinides such as uranium. They are used as model organisms to obtain access to unknown uranium uptake mechanisms and binding forms in living cells. Selected *Schizophyllum commune* strains, namely 4-39 and 12-43, bind high amounts of U(VI) on the cell surface and inside the cells at pH 5 and 6 (ICP-MS, REM). The first spectroscopic investigations (TRLFS) of formed uranyl complexes show that organic and inorganic phosphate groups are mainly responsible for the binding of U(VI).

EXPERIMENTAL. *Schizophyllum* cells were cultivated in an organic liquid full medium. The biomass was harvested and washed with mineral medium. For sorption experiments, the fungal biomass was resuspended (300 mg dry weight/L) in uranium containing mineral medium in a concentration range from $2 \cdot 10^{-6}$ M to $4 \cdot 10^{-4}$ M at pH 4, 5, 6, and 7 at room temperature. After 24 hours the cells were separated from the medium by filtration and washed with 0.1 M NaClO$_4$. The cells were used for REM measurements and investigations applying TRLFS and EXAFS.

RESULTS. Figure 1 shows the uranium binding capacities as a function of initial uranium concentrations and pH value of the *Schizophyllum* strain *4-39* as an example.

At uranium concentrations up to 50 mg/L, the fungal biomass shows comparable binding capacities independent on pH value. At higher initial uranium concentrations, clearly higher binding capacities were obtained, ranging from 230 to 280 mg/g dry weight at pH 5 and 6. These values correspond to 65 to 80% bound uranium under the given experimental conditions. At pH 4 and 7 only 140 mg/g dry weight was bound by fungal cells corresponding to 40% of the initial amount of uranium in the medium.

As demonstrated by scanning electron microscopy (see Fig. 2), fungal cells are highly transparent. The light deposits on the cell's surface (a) and inside the cells (b) are uranium containing accumulates (EDX analysis not shown).

The luminescence spectra of such fungal biomass demonstrate a significant bathochromic shift of the emission

Fig. 2: SEM picture of a uranium containing fungal sample; [U(VI)] = $8 \cdot 10^{-5}$ M, pH 5.

bands of the U(VI) species in comparison to the signals of the U(VI) species in the initial solutions. The results are independent of the fungal strain and pH value at constant biomass and uranium concentration. With increasing U(VI) concentration in the initial solution, the luminescence emission signals of U(VI)-fungi species are shifted to longer wavelengths (Fig. 3). Furthermore, different fluorescent species in different amounts are formed. The emission bands of U(VI)-fungi species are in the range of bands of several uranyl phosphates. At low uranium concentrations, the uranium is mainly bound to organic phosphate groups (example [1]). At higher uranium concentrations, the binding of uranium to inorganic phosphates groups (example [2]) is getting more and more important. This means a mixture of uranium complexes with organic and inorganic phosphate has been formed. The latter can be explained by a progressive biomineralization process. In addition, the dominant role of the phosphate groups in the uranium binding on/in the fungal biomass was also confirmed by EXAFS investigations.
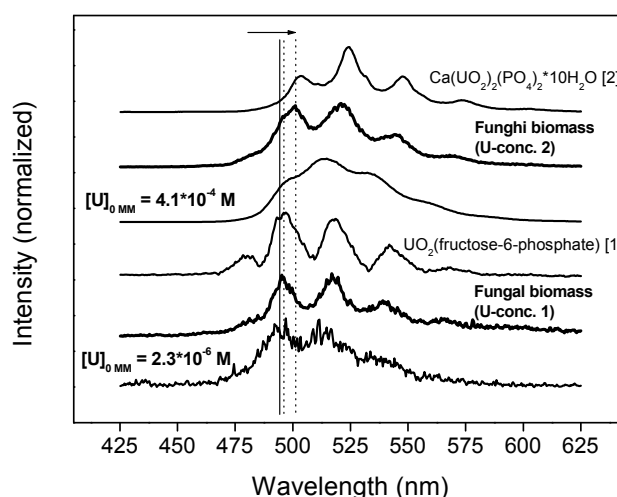
Fig. 3: U(VI) luminescence spectra of fungal cells in comparison to the spectra of initial solutions at pH 5 and reference spectra.

Fig. 1: U(VI) binding capacities of *Schizophyllum 4-39*.

[1] Koban, A. et al. (2004) *Radiochim. Acta* **92**, 903-908.
[2] Geipel, G. et al. (2000) *Radiochim. Acta* **88**, 757-762.

Interaction of U(VI) with the Äspö strain *Pseudomonas fluorescens*

L. Frost, H. Moll, G. Bernhard

The investigated Äspö isolate can accumulate large amounts of U(VI), up to 540 mg/g dry biomass at an initial [U(VI)] of 138 mg/L and pH 6.0. The accumulation is strongly pH-dependent. Using time-resolved laser-induced fluorescence spectroscopy (TRLFS) it was shown that in the cell pellets as well as the supernatants U(VI) is bound *via* phosphate and/or carboxylic groups. With increasing pH hydroxide additionally can be attached to the surface-bound U(VI).

Microbes occur ubiquitously in nature, significantly affecting the migration behavior of actinides. The investigated subsurface groundwater strain *Pseudomonas fluorescens* has been isolated from the Äspö site, Sweden [1]. The interaction of U(VI) with *P. fluorescens* was studied in terms of the metal accumulation capability of the cells in dependence on $[U(VI)]_{init}$, [dry biomass] and pH. TRLFS was applied to investigate the U(VI) binding form at the cell surface and in the supernatants at different pHs.

EXPERIMENTAL. *P. fluorescens* CCUG 32456A was cultivated in NB medium. Cells were harvested in the mid-exponential growth phase and washed in 0.1 M $NaClO_4$. Culture purity was ensured by light microscopy and *in situ* PCR with subsequent RFLP. U(VI) accumulation experiments were carried out with a $UO_2(ClO_4)_2$ stock solution and in 0.1 M $NaClO_4$ at constant pH varying (a) $[U]_{initial}$ from 0.4 to max. 138 mg/L and (b) [dry biomass] from 0.05 to 0.6 g/L. Unless varied, [U(VI)] was set to $1 \cdot 10^{-4}$ M and [dry biomass] to 0.2 g/L. Investigated pH values were 4.0, 6.0, 7.0 and 8.0 for (a) and only 6.0 for (b). After 48 h U(VI) contact, the cells were centrifuged and supernatants analyzed regarding [U(VI)] with ICP-MS. Supernatants and washed cell pellets were investigated using TRLFS with a setup as described in [2].

RESULTS. Figure 1 illustrates the strong pH dependence of the U(VI) sorption by *P. fluorescens*. At pH 6, at maximum sorption, the cells accumulate 5 times as much U(VI) as at pH 4 at $[U(VI)]_{init}$ of 138 mg/L. Investigating the U(VI) accumulation in dependence on [dry biomass], an asymptotic behaviour of the sorption can be observed (Fig. 2). Because always a fraction of U(VI) remains in solution, the release of cellular ligands leading to UO_2^{2+} mobilization can be assumed. Using ion-exchange chromatography a significant release of inorganic phosphate was determined. TRLFS was applied to determine the

Fig. 2: Accumulated U(VI) vs. dry biomass concentration at an initial [U(VI)] of $1 \cdot 10^{-4}$ M and pH 6.0.
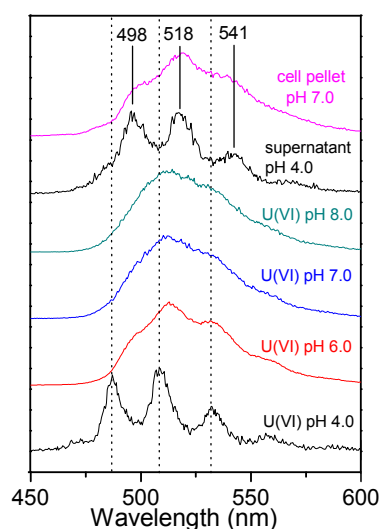
Fig. 3: Exemplary luminescence spectra of U(VI) in cell pellet and supernatant in comparison to those of U(VI) reference solutions.

U(VI) speciation. Since all measured supernatants plus the cell pellets at pH 4 and 6 showed similar spectra, and also the spectra of the cell pellets at pH 7 and 8 were similar, Fig. 3 only depicts representative spectra. All obtained spectra are significantly red-shifted compared to the reference spectra. Comparing the main emission bands of U(VI) in the supernatant at pH 4 to the literature [3], a coordination of U(VI) by phosphate groups is suggested. An additional coordination via carboxylic groups [4] is probable. Comparing both representative spectra, a pH dependence of the U(VI) speciation at the cell surface is noticeable. Nevertheless the characteristic main emission band at 518-519 nm is preserved, although here a very broad UO_2^{2+} hydroxide-like spectrum is observable indicating additional hydroxide attached to the surface-bound U(VI). Potentiometric titrations are in progress to determine the pK_A values and the site densities of the cell envelope's functional groups. This is necessary for a detailed discussion of formed U(VI) surface species.

[1] Pedersen, K. et al. (1997) *FEMS Microbiol. Rev.* **20**, 399-414.
[2] Frost, L. et al. (2011) *Radiochim. Acta*, accepted.
[3] Panak, P. et al. (2000) *Radiochim. Acta* **88**, 71-76.
[4] Barkleit et al. (2009) *Dalton Trans.* **27**, 5379-5385.

Fig. 1: U(VI) accumulation in dependence on $[U]_{init}$ in 0.1 M $NaClO_4$.

Fast and reliable bacterial diversity assay of Opalinus Clay samples collected from the Mont Terri underground laboratory

V. Bachvarova, S. Selenska-Pobell

In this work we studied the differences in the bacterial community in the inner and surface part of an Opalinus Clay sample collected from the Mont Terri Rock Laboratory using the Ribosomal Intergenic Spacer Amplification (RISA) approach. Using the same method we observed shifting in the bacterial community of the inner part of clay sample caused by two weeks long treatment with R2A medium under anaerobic conditions. In contrast to this result, the uranium and NaClO$_4$ treatments of the surface sample caused no visible changes in bacterial community.

Studies on microbial diversity in extreme environments foreseen for radioactive waste repositories is of great interest because microorganisms can interact with radionuclides and heavy metals using different mechanisms. Crucial moments in such studies are the methods applied for the recovery of total DNA from the environmental samples and those used for estimation of the microbial diversity. In the current work we describe a reliable method for monitoring the changes in bacterial community in Opalinus Clay samples from the Mont Terri Rock Laboratory as a result of different treatments.

EXPERIMENTAL. The Opalinus Clay core samples used in this study were collected in April 2009 from the borehole BHT-1 of the Mont Terri Rock Laboratory.

In order to distinguish the indigenous clay bacteria from any contaminants, which might be introduced into the core samples during the drilling, we analyzed two parallel samples – one containing material from the inner part of the core (MT-2) and a second one – from the surface part (MT-2-SF). To study the response of the natural bacterial community to different treatments we studied one R2A medium treated sample from the inner part of the core (MT-2-R2A), and two core surface samples, MT-2-SF + U and MT-2-SF + NaClO$_4$, treated with $1 \cdot 10^{-6}$ M solution of U(VI) and 0.1 M NaClO$_4$, respectively. To recover total DNA from the Opalinus Clay we used a method described previously [1] with small modifications. This method gives a chance to vary in a great attitude volume of the samples and all the solutions used. This is very important in consideration to the low density of the bacterial community in this 180 million year old clay formation.

Due to the tight binding of the DNA to the clay particles, DNA recovery from clay samples is especially difficult [2]. In order to increase the efficiency of the DNA extraction by alkaline cells lysis at 70 °C, this step was performed four times. To increase the total DNA yield, the elution step was preformed twice with additional volume from the elution buffer. Due to the expected low yield, the recovered DNA was dissolved finally in 25-30 µl TE buffer, pH 8.

For quick and reliable estimation of the bacterial community structure the Ribosomal Intergenic Spacer Amplification (RISA) approach was used as described earlier, using the primer pair 16S$_{969F}$-23S$_{130R}$ [1].

RESULTS. The RISA approach applied to the samples studied in this work gave a chance to obtain very basic
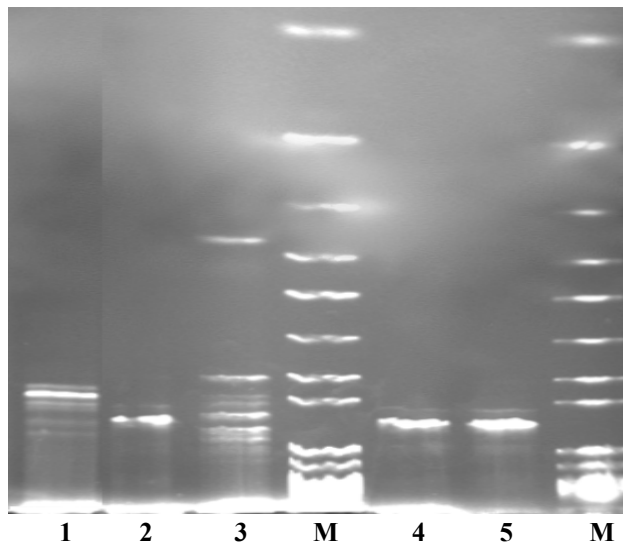
Fig. 1: RISA analysis of the samples: (1) MT-2; (2) MT-2-SF; (3) MT-2-R2A; (4) MT-2-SF+U, and (5) MT-2-SF+NaClO$_4$; (M) 1 kb Plus DNA Ladder (Invitrogen).

but interesting information about the bacterial community structure in the Opalinus Clay.

As evident from the results presented in Fig. 1 the RISA patterns obtained for the MT-2-SF sample did not match with those of the MT-2 sample. This result indicates that the core surface sample is occupied by bacteria not or barely presented in the parallel sample MT-2 from the inner part of the core. With other words, to analyze clay material from the inner part of the core was a helpful idea to avoid contaminants which might penetrate into the core during the sampling. Applying RISA to the R2A medium treated sample MT-2-R2A we obtained very different profile that indicates shifting in the bacterial community structure due to the addition of nutrients.

Interestingly, the RISA profiles of the MT-2-SF, MT-2-SF + U and MT-2-SF + NaClO$_4$ samples showed no differences between each other. It seems that the bacterial groups present in this part of the core were not or were very weakly influenced by the U(VI) and NaClO$_4$ treatments. This possibly is due to the short term of the treatments, the low concentrations of the added U(VI) and NaClO$_4$, and to the lack of nutrients. Further studies will give more complete information about the bacterial groups presented in the Mont Terri Opalinus Clay and those which were positively stimulated by the treatments.

[1] Selenska-Pobell, S. et al. (2001) *Antonie Van Leeuwenhoek* **79**, 149-161.
[2] Kweku, K.Y. et al. (2009) *Appl. Environ. Microbiol.* **75**, 6017-6021.

Uranium sorption in surface water from the Gessenwiese test site by *Chlorella vulgaris*

M. Vogel, A. Günther, J. Raff

Surface water from Gessenwiese test site was used to test the capability of living and dead *Chlorella* cells to remove uranium naturally occurring in mining related water. The sorption experiments showed that living cells removed up to 13% and dead cells up to 31% of the uranium in the surface water. Speciation calculation suggested the free uranyl ion to be mainly responsible for the interaction with the biomass.

From previous studies with *Chlorella vulgaris* it is known, that these algae are able to sorb significant amounts of uranium from artificial solutions under laboratory conditions [1,2]. The aim of this study was to test the capability of *Chlorella* cells to remove uranium from natural occurring mining related water. For this purpose, surface water from Gessenwiese test site located at the former uranium mining area near Ronneburg (Thuringia) was chosen.

EXPERIMENTAL. The surface water from Gessenwiese test site was analyzed regarding its composition before and after sterile filtration (Tab. 1). The results were used for speciation calculation with the computer program EQ 3/6 [3] using the NEA database [4]. Sorption experiments were carried out with sterile filtered surface water with the measured uranium concentration of 1.6 µM and a pH of 3.9 ± 0.1. Living and heat killed (by autoclaving) *C. vulgaris* cells were incubated in surface water with a biomass concentration of 0.5 g algae$_{dry\ weight}$/L. The uranium sorbed onto the biomass was measured after 5 min, 48 h and 96 h. For that, the cells were separated from the water by centrifugation (10 min, 10,000 g) and the uranium amount remaining in the supernatant was measured by ICP-MS. The viability of the living cells was verified by plating diluted algae samples on agar plates and counting the number of colony forming units.

Tab. 1: Composition of surface water from Gessenwiese test site after sterile filtration.

Parameter	Concentration [mM]	Parameter	Concentration [mM]
Na	0.43	Co	0.04
K	0.08	As	$< 1.3 \cdot 10^{-5}$
Mg	26.42	Cd	$4.0 \cdot 10^{-4}$
Ca	8.06	Pb	$1.1 \cdot 10^{-5}$
Al	1.53	U	$1.6 \cdot 10^{-3}$
Si	0.72	Cl	2.41
Ni	0.19	NO_3^-	0.07
Cu	0.01	PO_4^{2-}	$< 5.0 \cdot 10^{-3}$
Fe	0.01	SO_4^{2-}	45.39
Zn	0.04	$CO_3^{2-}/$	0.07
Mn	1.35	HCO_3^-	

RESULTS. The uranium speciation in the surface water with a natural uranium concentration of 1.6 µM at pH 3.9 ± 0.1 is dominated by the uranyl sulfates $UO_2SO_4(aq)$ with 66.2% and $UO_2(SO_4)_2^{2-}$ with 18%. The free uranyl ion UO_2^{2+} accounts for 14.3%.
Sorption experiments with living and dead *Chlorella* biomass showed that in both cases only a small amount of uranium could be removed by the algae from the surface
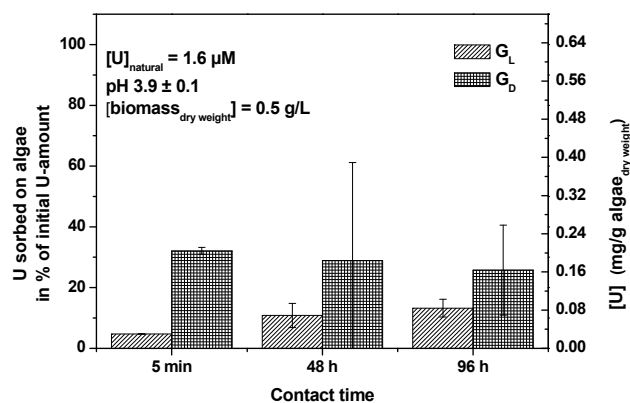
Fig. 1: Uranium sorbed on living and dead *Chlorella*-cells from surface water of Gessenwiese test site. G$_L$: living algae; G$_D$: dead algae.

water of Gessenwiese test site (Fig. 1). Living cells sorbed 13% of the dissolved uranium from surface water which corresponds to 84.8 µg U/g algae$_{dry\ weight}$. Dead Chlorella cells sorbed 31%, which equates to 205.6 µg U/g algae$_{dry\ weight}$. The fact that dead cells sorbed more uranium than living ones is already known from previous studies in a mineral medium (pH 4.4-7.0) under laboratory conditions [2]. The results indicate that living cells are able to influence binding of uranium actively or passively. The number of living cells remained constant over the whole investigation period of 96 h. Considering the calculated uranium speciation in surface water, it is obvious that the uranium is bound preferably as UO_2^{2+} [5]. The role of the uranyl sulfate species for the interaction with the algae cells could not be estimated. It is obvious that especially the dead cells had removed additional uranium species besides the free uranyl ion. The pH value also influences the sorption properties of algae biomass. At the given pH of 3.9 the competition for binding sites on the algae cell surface between the uranyl species and protons is greater than at higher pH values. A pH-range between 5−7 was described to be the best for uranium sorption by *C. regularis* [6].

Summarizing, most of the uranium in natural surface water from Gessenwiese test site was not bound by *C. vulgaris* independently from the cell status of the algae.

[1] Günther, A. et al. (2008) *Biometals* **21**, 333-341.
[2] Vogel, M. et al. (2010) *Sci. Total Environ.* **409**, 385-396.
[3] Wolery, T.J. (1992) *Report UCRL-MA-110662* part 1.
[4] Guillaumont, R. et al. (2003) *Update on the chemical thermodynamics of uranium, neptunium, plutonium, americium and technetium,* Elsevier, Amsterdam.
[5] Nakajima, A. et al. (1979) *Agr. Biol. Chem.* **43**, 625-629.
[6] Horikoshi, T. et al. (1979) *Agr. Biol. Chem.* **43**, 617-623.

Eukaryote diversity of biofilms in acidic, uranium-contaminated water from the "Gessenhalde" (Ronneburg/Eastern Thuringia)

I. Zirnstein, E. Krawczyk-Bärsch, T. Arnold, I. Röske[1]

[1]Institute of Microbiology, Dresden University of Technology, Dresden, Germany

The eukaryote diversity of biofilms growing in a creek of the former uranium leaching dump "Gessenhalde" as algae mat were investigated by light microscopy and by constructing 18S rDNA clone libraries. The water of the creek is characterized by related concentrations of sulfate, uranium and a low pH of pH 3.3-4.5. The eukaryote communities of the biofilms were dominated by the filamentous green algae *Microspora sp.* and *Klebsormidium sp*.

EXPERIMENTAL. The biofilm samples of 2010 were taken in a creek of a former uranium leaching dump of the WISMUT GmbH near Ronneburg (Thuringia, Germany). The biofilms occur as thick algae mats forming filamentous stream biofilms. The pH values of the water varied seasonally between 3.3 and 4.5. The uranium concentration is ranging seasonally between 75 and 291 ppb ($\sim 1 \cdot 10^{-6}$ and $6 \cdot 10^{-6}$ M) [1].The eukaryote diversity of the biofilm samples was analyzed by extracting the total DNA using the NucleoSpin®Soil Kit (Marchery-Nagel) followed by 18S-rDNA-PCR using the primer 515F and 1209R [2]. Molecular analysis of the Eukaryote community: Amplification was performed for 30 cycles with an annealing temperature of 55 °C using the 5'-Prime MasterMix from Eppendorf. The purified amplified 18S rDNA fragments were cloned into *E. coli* (chemical competently TOP 10 F') using the pMBL T/A Cloning Kit (Genaxxon BioScience) following the manufacturers' recommendations. The recombinant clones (230 clones of biofilm samples) were selected by blue-white colony selection. Representative clones were selected for sequencing to enable the phylogenetic classification of the predominant eukaryotic populations. The high-quality sequences were compared to sequences available in the non-redundant nucleotide database in the National Center or Biotechnology data base using BLASTN.

Another method to characterize the eukaryote diversity was the microscopic study of the biofilm samples. Different species of eukaryote communities were analyzed using light microscopy.

RESULTS AND DISCUSSION. The molecular and microscopic characterization of the eukaryote diversity (Fig. 2) of the biofilm samples shows a wide spectrum of free living eukaryote microorganisms, like the filamentous green algae *Microspora* and *Klebsormidium* as the dominant eukaryotes (Fig. 1). Numerous studies show that green algae usually dominate acid habitats. Species of *Klebsormidium* and *Microspora* among others have all been noted previously in very low pH streams [3, 4] and are insensitive to changing environmental conditions [5]. Green algae like *Klebsormidium* and *Microspora* are present in every sample independent of the season, just like *Fungi* and *diatoms* like *Nitzschia sigma*. *Flagellates, Ciliates* and *Rotatoria* are present as representatives of the protozoa in minor amounts, according to the season of sampling. In addition, species of *Chrysophyceae, Amoebozoa, Gastrotricha* and protists were found. By light microscopy species of *Cryptophycaea* and *Heliozoa* were noted, too.
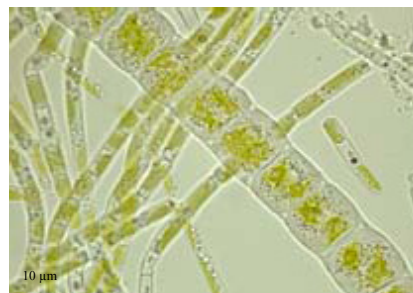
Fig. 1: Light microscopy image of the fila-mentary green algae *Microspora* (in front) and *Klebsormidium* (background).
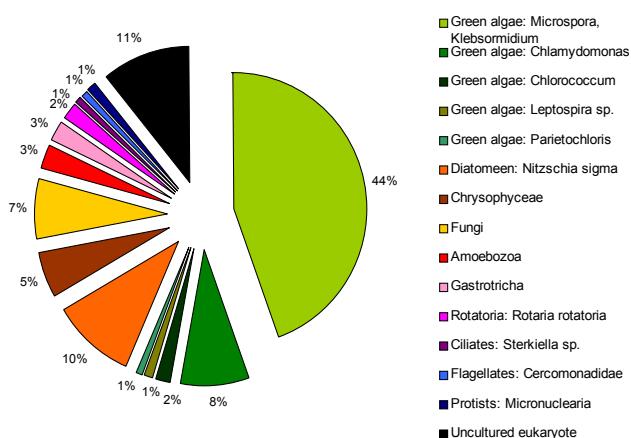
Fig. 2: Molecular analysis of Eukaryote diversity of the biofilms in the creek "Gessenhalde" identified on basis of the analyzed 18S rDNA-sequences.

The determined species tolerate the metals (e.g. uranium) in the water, using different mechanism to live in acid environments [6]. The growth of the detected eukaryotes in the biofilms is not effected by the prevalent concentration of uranium. Further external factors are pH, atmospheric precipitation, time of daily sunshine, dryness and temperature, which are limiting the growth.

In the present study, biomolecular and microscopic methods have been combined, showing that different methods are important to characterize the complete biodiversity of microorganisms. The determination of the eukaryote diversity in biofilms is necessary as well as the analysis of bacteria due to the fact that biofilms are representing a living community of microorganisms. Each of them is influencing the living conditions of the other participant as well as the migration of metals and pollutants in the environment.

[1] Baumann, N. et al. (2010) *Chem. Listy* **104**, S190.
[2] Baker, B.J. et al. (2009) *Appl. Environ. Microbiol.* **75**, 2192-2199.
[3] Verb, R.G. et al. (2001) *Aquat. Bot.* **71**, 93-107.
[4] Johnson, D.B. (1998) *FEMS Microbiol. Ecol.* **27**, 307-317.
[5] Rindi, F. et al. (2008) *J. Phycol.* **44**, 1529-1540.
[6] Meade, J.C. et al. (1989) *Mol. Biochem. Parasitol.* **33**, 81-91.

The ability of *Euglena mutabilis* to bioaccumulate uranium at low pH conditions

S. Brockmann,[1] T. Arnold, G. Bernhard

[1]Institute of Analytical Chemistry, Dresden University of Technology, Dresden, Germany

Euglena mutabilis **was studied regarding its ability to bioaccumulate uranium from acid solutions (pH 3 and 4). It was found that axenic cultures of this protozoan were able to immobilize more than 90% uranium from an initially** $1 \cdot 10^{-5}$ **M solution. Laser Induced Fluorescence Spectroscopic (LIFS) measurements indicate that the uranium bound in the cells or on the cell pellicle were attributed to** $UO_2(glycine)_2^{2+}$ **or uranium-ATP related complexes.**

Uranium mining was/is often carried out by leaching uranium ores with sulfuric acid generating acid mine drainage (AMD) waters with high uranium and other toxic heavy metal concentrations. To remove the uranium from these contaminated and mobile waters, many efforts have been undertaken including microbial approaches. In contrast to the well studied bacteria, little is known about the interactions of eukaryotes with uranium, as e.g. *Euglena* species. *Euglena mutabilis* is a eukaryotic microorganism which is often encountered in AMD environments and hence it is an ideal candidate for bioaccumulation processes. Thus, the aim of this study was to investigate the potential of *Euglena mutabilis* to bioaccumulate uranium in an AMD relevant pH range and to identify the immobilized uranium species by LIFS measurements.

EXPERIMENTAL. Cells of an axenic strain of *Euglena mutabilis Schmitz* were grown under sterile air supply in liquid medium. The cells were harvested by centrifugation (4,500 g, 4 °C, 10 min) when the culture reached a high cell density (observable by the intensive green color). The cell pellets were washed and subsequently resuspended (0.42 g *Euglena* dry weight/L) in sterile solutions containing $1 \cdot 10^{-5}$ M uranium in 3.48 g/L Na_2SO_4 adjusted to the pH of 3 and 4. The cells were left in contact to the uranium solutions for five days on a rocking shaker. After this time, the supernatant and the cells were separated by centrifugation. The uranium content in the solutions was analyzed by ICP-MS. Furthermore, LIFS measurements applying an excitation wavelength of 266 nm were performed to obtain information on the uranium speciation.

RESULTS. It was found that more than about 95% of the initially added uranium was removed from the solutions and bound to the cells. Tab. 1 lists the detailed results of the experiments. More than 5 mg uranium was bound per gram *Euglena* cell dry weight. Figure 1 shows the fluorescence spectra of the samples at pH 3. In contrast to the spectra from the uranium in the solutions, the spectra of the uranium bound in/on the cells are slightly shifted (about 2 nm) to longer wavelengths. The emission bands of the peak maxima from the recorded LIFS spectra are summarized in Tab. 2 together with some emission bands of uranium references.

Fig. 1: Fluorescence spectra of the samples at pH 3.

The aqueous uranium speciation in the initially added uranium solutions and in the solutions after 5 days of contact to the cells was dominated by UO_2SO_4 complexes. In contrast, the immobilized uranium in/on the *Euglena* cells were most likely attributed to $UO_2(glycine)_2^{2+}$ or U-ATP complexes.

This study demonstrates the potential of *Euglena* cells or its components to immobilize uranium with high effectiveness at low pH values. In future *Euglena* cells may turn out to be promising to be used as immobilization agents for uranium removal in AMD water treatments.

Tab. 1: Results of the bioaccumulation experiments.

		Bound uranium	
initial pH	final pH	initial amount [%]	*Euglena* dry weight [mg/g]
3.0	3.1	95.9 ± 0.7	5.4 ± 0.17
4.0	4.3	95.1 ± 0.1	5.3 ± 0.03

Tab. 2: Comparison of the LIFS-emission bands of the measured samples and references.

Sample		Emission bands measured samples [nm]					
		1	2	3	4	5	6
pH 3, Na₂SO₄	Init. sol.	477.5 ± 1.1	493.0 ± 0.2	513.7 ± 0.1	537.1 ± 0.2	562.5 ± 0.3	590.1 ± 1.1
	Sol. a.c.	476.5 ± 1.9	493.0 ± 0.5	513.9 ± 0.8	536.8 ± 0.6	561.6 ± 0.6	594.8 ± 1.9
	Euglena cells	478.5 ± 1.3	494.9 ± 0.5	516.0 ± 0.6	538.9 ± 1.6	564.6 ± 0.9	591.8 ± 1.9
pH 4, Na₂SO₄	Init. sol.	476.5 ± 0.4	492.8 ± 0.1	513.9 ± 0.1	537.2 ± 0.3	562.9 ± 0.3	591.3 ± 0.3
	Sol. a.c.		493.8 ± 0.8	514.7 ± 1.3	537.7 ± 1.4	563.5 ± 1.9	
	Euglena cells	477.3 ± 2.4	495.6 ± 0.8	517.3 ± 0.9	541.3 ± 1.2	564.4 ± 2.0	
		Emission bands references [nm]					
U-SO₄ [1]		477.5	492.8	514.1	537.5	563.0	590.1
U-ATP [2]		480.9	495.3	516.5	540.2	564.6	593.8
UO₂(gly)₂²⁺ [3]		478.7	495.3	516.7	540.6	565.0	594.4

Sol. a.c.: contact time with *Euglena* cells of 5 days, ATP: adenosine-triphosphate.

[1] Arnold, T. et al. (2011) *Geochim. Cosmochim. Acta,* submitted.
[2] Merroun, M.L. et al. (2003) *Biometals* **16**, 331-339.
[3] Günther, A. et al. (2007) *Polyhedron* **26**, 59-65.

Biofilms in uranium contaminated acidic mine drainage (AMD) waters and their influence on the mobilization of uranium

E. Krawczyk-Bärsch, T. Arnold, E. Eisbein,[1] V. Brendler

[1]Institute of Physical Chemistry, TU Bergakademie Freiberg, Freiberg, Germany

The underground uranium mine of the WISMUT GmbH near Königstein (Saxony, Germany) is currently in the process of being flooded. In the gallery of pit 390 at +50 m above sea level biofilms, dominated by acidophilic *Ferrovum myxofaciens* [1], are formed in the acidic mine drainage (AMD) water of $3 \cdot 10^{-5}$ M to $6 \cdot 10^{-5}$ M. Under ambient conditions biochemical processes, catalyzed by the microbes, inhibit an immobilization of uranium in the biofilms as well as in the AMD water. Laboratory experiments, simulating the first state of flooding of the uranium mine, showed the influence of the microbes on the acidification of the AMD water. Consequently, the formation of solid uranium minerals is inhibited as long as *Ferrovum myxofaciens* will be the dominant bacteria of the biofilms.

EXPERIMENTAL. Microsensor measurements were performed in-situ in the biofilms of the drainage channels by using a miniaturized platinum redox potential and pH electrode from Unisense (Denmark), each of them with a tip diameter of 10 μm. Additionally, biofilm samples were taken from the drainage channel and prepared for sensor measurements in the laboratory by positioning the biofilms in a self-constructed rectangular flow cell. AMD water from the channels was sampled for anions and cations analysis. The analytical data of the water was used for the calculation of the predominance fields of different uranium species in the pH-Eh diagram for the U-S-O-H-C system at 15 °C by using the geochemical speciation code "Geochemist´s Workbench" Version 8.0.8/ACT2 Version 8.0.8. In laboratory experiments, the first phase of flooding was simulated. The pH of the sampled AMD water was increased to a neutral pH by adding 1 M NaOH, while the water was pumped in a closed circle through the biofilm, which was positioned in the flow cell. The pH of the water was measured two times a day during 95 hours and was readjusted to 6.45-6.80 since it decreased permanently < 4. Redox potential and pH measurements were performed in the biofilm and in the AMD water after 20 and 95 hours, respectively.

RESULTS. The results of the microsensor measurements clearly show a difference between the redox potential and pH of the AMD water in comparison to the measured values in the biofilm. The redox potential inside the biofilm is approximately 200 mV higher than in the surrounding water. In general, this difference is important in respect to the migration behavior of uranium. The calculated theoretical predominance stability fields of the solid uranium species found in the AMD water under the ambient condition are shown in the constructed pH-Eh diagram (Fig. 1). The area of pH > 4.8 and Eh < 960 mV is defined by the stability field of the solid U(VI) mineral Uranophane [$Ca(UO_2)_2(SiO_3OH)_2 \cdot 5H_2O$]. Assuming reducing conditions, the formation of the U(IV) mineral Coffinite [$U(SiO_4)_{1-x}(OH)_{4x}$] is predicted in the area of pH > 0 and Eh < 300 mV. The plotted redox potential and pH values measured in the AMD water and in the biofilm appear in the area of aqueous solution (Fig. 1), indicating that an
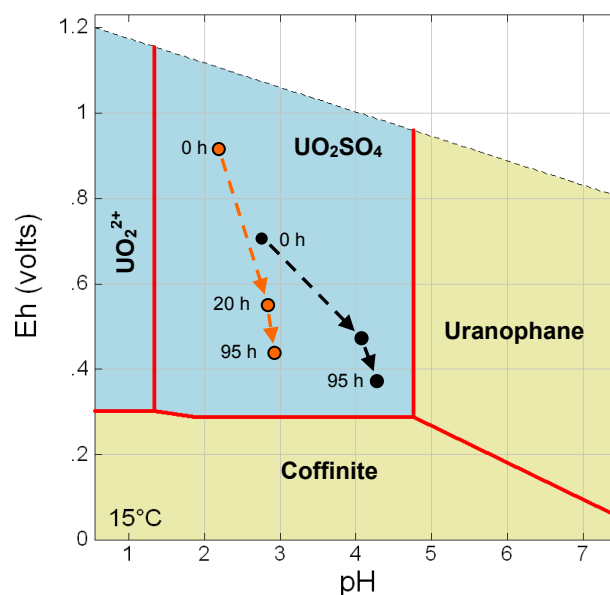
Fig. 1: pH-Eh diagram for U-S-O-H-C system at 15 °C. Eh and pH data correspond to the ambient condition measured in the AMD water (•) and within the biofilm (•).

aqueous uranium(VI) sulfate complex exists under these conditions in the biofilm as well as in the AMD water. In fact, the highly mobile aquatic uranium sulfate species $UO_2SO_{4(aq)}$ was determined in very recent TRLFS studies (data not shown).

The simulation of the first state of flooding of the uranium mine by neutralization of the AMD water reveals the influence of the *Ferrovum myxofaciens* dominated biofilm. Although the pH was adjusted to a neutral pH during 95 hours, the pH of the AMD water decreased permanently. It could be suggested that pH homeostatic mechanisms, e.g. active proton pumping and release of protons by efflux systems, are used by the microbes to maintain their living condition. The results of the microsensor measurements, which were performed after 20 and 95 hours, are found again in the area of aqueous solution (Fig. 1) with a trend towards the calculated predominance fields of uranium minerals. Consequently, bioremediation and immobilization of uranium will be delayed as along as *Ferrovum myxofaciens* will be the dominant bacteria of the biofilms. A substantial retention of uranium can be considered when basic changes of the geochemical conditions of the underground situation during a later phase of the flooding process will be adjusted with the consequence of a change of the microbial diversity due to anaerobe conditions.

[1] Brockmann et al. (2010) *J. Fluoresc.* **20**, 943-951.

Long-lived radionuclides at
PERMANENT DISPOSAL SITES

Advancements of GeoPET image quality as prerequisite for comparison of observation and simulation in reactive transport

J. Kulenkampff

Positron Emission Tomography (PET) is not only an important nuclear medical method but also ideally suited to observe the propagation of compounds, labeled with an appropriate PET-tracer, in dense material (GeoPET). However, image quality is impaired by strong absorption and scattering of the PET-photons.

The method of Positron Emission Tomography (PET) has been applied successfully for spatially resolved transport observations in rocks and soils since the foundation of the IIF, more than ten years ago [1]. The recent acquisition of a "preclinical PET-camera" ClearPET™ [2] enables the performance of tracer transport experiments with an appropriate spatial resolution and on a due time scale which is principally comparable to the results of *ab initio* computer simulations [3,4].

GeoPET observations of transport experiments in soils and rocks demonstrated a spatial resolution of nearly 1 mm (Fig. 1), but also showed significant degradation of image quality by artifacts. These artifacts (Fig. 2) considerably constrain the comparability with transport simulations on the pore scale, because the whole continuum of the specimen has to be considered (in contrast to selected compartments in biomedical research). Phantom experiments and simulations helped to find the causes of the artifacts and to derive correction methods.

EXPERIMENTAL. Custom made, different dense phantoms were filled with [18F]KF-solution (< 20 MBq) and scanned, and the resulting projection data and images were analyzed with respect to three image impairing effects:

- absorption of radiation,
- regional scattering effects (inhomogeneous background radiation field) (Fig. 3),
- blurring caused by scattering.

RESULTS. Compared to the conditions in biomedical PET-imaging, where scattering and absorption are frequently neglected, these effects have to be thoroughly considered here. Improper corrected projections cause image reconstruction artifacts, which are due to the iterative reconstruction method (STIR OSEM [5]) and the inhomogeneous geometrical sensitivity distribution of the scanner [6].

First, a method for absorption correction based on geometrical model of attenuation coefficients was developed, improvable with μCT density-imaging in future. Second, a detection and correction method for an inhomogeneous background field of pseudo-coincidences caused by strong sources in or out of the field of view (FOV) was developed. With these two corrections, the major error sources have been reduced considerably.

However, the effects of Compton-scattering are still disregarded, although scatter fractions > 50% were determined. Currently, Monte-Carlo simulations are conducted in order to develop proper correction methods, or even new model-based reconstruction algorithms [7].
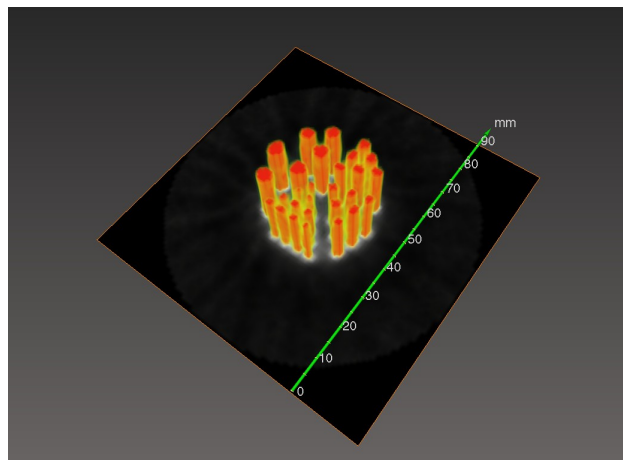
Fig. 1: Derenzo-like phantom with bores of 1 to 5 mm filled with [18F]KF-solution for testing resolution and signal-noise ratio.
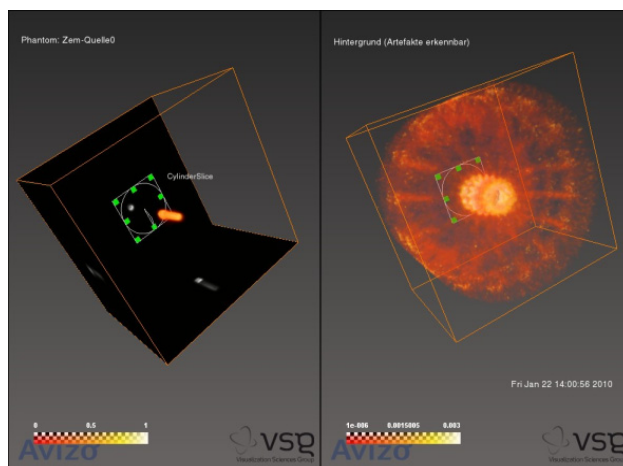
Fig. 2: Cylindrical cement phantom (circle) with central, tracer-filled bore (orange). Right: amplified activity scale uncovers low-level artifacts. Scattering causes out-of-object apparent activity and also corrupts the activity distribution within the object.
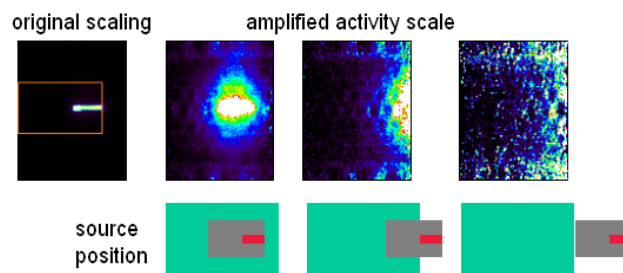
Fig. 3: Effect of inhomogeneous background radiation: upper pane: central slice, lower pane: position of FOV (green), sample (grey), and source (red). Such artifacts could be mistaken as diffusing front in transport experiments.

[1] Richter, M. et al. (2002) *Z. angew. Geol.* **46**, 101-109.
[2] Ziemons, K. et al. (2005) *Nucl. Instr. Meth. A* **537**, 307-311.
[3] Kulenkampff, J. et al. (2010) *EDGG* **242**, 95-97.
[4] Wolf, M. et al. (2010) *EDGG* **244**, 200-212.
[5] Weber, S. et al. (2006) *Nucl. Instr. Meth. A* **569**, 381-385.
[6] Gundlich, B. et al. (2007) *Nucl. Instr. Meth. A* **571**, 235-238.
[7] Zakhnini, A. et al. (2011) this report, p. 38.

Monte Carlo simulations of a ClearPET™: scatter and attenuation of gamma rays in various rock formations

A. Zakhnini, J. Kulenkampff, J. Lippmann-Pipke, U. Pietrzyk[1]

[1]Physics Department, University of Wuppertal, Wuppertal, Germany

We apply positron emission tomography (PET) in geosciences and visualize flow and transport process in various rock formations (GeoPET [1,2,3]). While this denser rock material requires more demanding and stronger corrections of scatter and attenuation of the gamma rays than in body tissue, it bears the chance of accomplishing a higher accessible resolution (≥ 1 mm). We suggest Monte Carlo simulations of our ClearPET™ camera (*raytest*®) as means for achieving this aim.

EXPERIMENTAL. The simulation of a typical experimental setup of GeoPET (3D) is conducted by means of the simulation software GATE (Geant4 Application for Tomograhic Emission [4], Open Gate Collaboration). It is based on the scripting language Geant4 [5] and allows for the simulation of various PET and SPECT systems in the field of nuclear medicine, the visualization of the detector and particle trajectories (Fig. 1), and the data storage for subsequent data analysis at different levels of detail and refinement. The user defines the geometry of the detector system, location and amount of the applied radiotracer (^{18}F, ^{124}I, ^{58}Co), the geometry and density of the various rock samples and finally the kind of physical interactions between gamma rays and sample material (TREE). The probabilities and the timing of the generation of primary particles of events, the tracking of particles through materials, the physical processes governing particle interactions (annihilation, Compton and Rayleigh scattering, multiple scattering, photo-electric effect and pair conversion) and the response of the detector components are simulated. The results of a simulation run are stored (ROOT file) and are further analyzed by means of C++ programs.

RESULTS. The simulation results enable to quantify the impact of certain parameters (sample material, kind of radionuclide, gantry diameter and energy window) on the fraction of unscattered, not randomly (true) coincidentally detected γ-particles that originate from the annihilation of ß$^+$ particles.

A high scatter fraction (e.g. 3% randoms, 23% trues, 74% scattered trues, predominantly multiple scatter, for a ^{18}F-line source in anhydrite, Fig. 1, left) is common for all PET-nuclides and rock formations though their values greatly differ. With selection of an appropriate energy windows the scatter fraction can be significantly reduced, e.g. from 0.74 (250-750 keV) to 0.48 (400-650 keV), accepting a corresponding loss of efficiency.

Of particular interest are the spatial distributions of the coincidences along the axis (Fig. 2). The profile of the unscattered trues (blue) shows significant counts only in *radial* direction from the axial alignment of the source (13-57 mm). In contrast, the profile of the scattered coincidences (Fig. 2, green) shows significant counts also in *axial* direction (−40-13 mm). The red contour line summarises both, the total and the unscattered trues and illustrates the particular importance of implementing scatter and attenuation correction algorithm in dense material: Uncorrected GeoPET images are systematically biased in
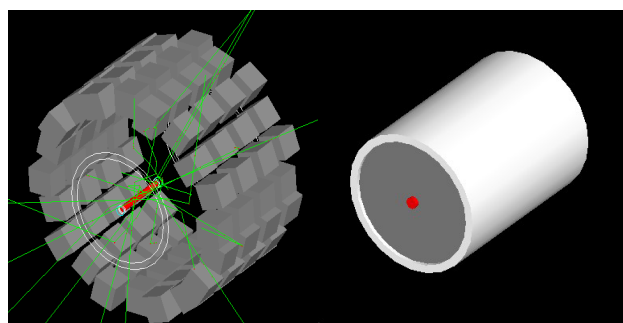
Fig. 1: Geometry of the GeoPET. *left*: gantry with 20x4 detector blocks (grey), source (red), γ-trajectories (green) and position of the liner; *right:* sample material (gray, length = 115 cm, OD = 80 mm) with axially positioned radiotracer (red, length = 44 mm, OD = 4.5 mm) and sample liner (white, thickness = 5 mm).
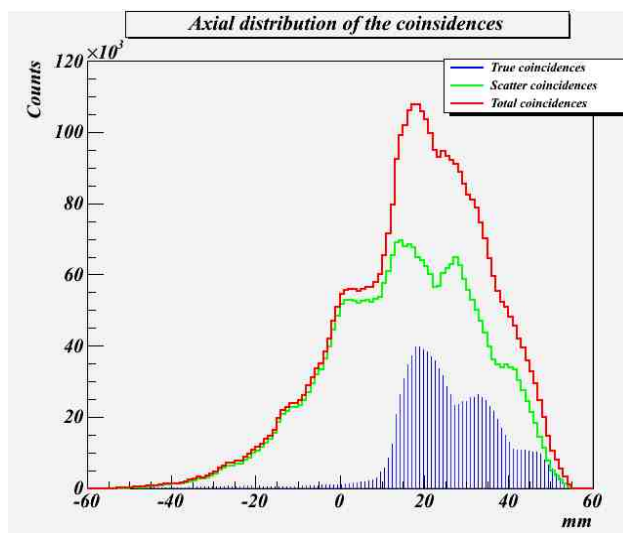
Fig. 2: Spatial distribution of the unscattered true (blue), scattered true (green) and total coincidences (red) along the axis of an anhydrite sample (total length: 115 cm). The ^{18}F source extends from 13 to 57 mm.

the 3 to 5 mm ahead of a tracer front, which could be severely misinterpreted.

[1] Richter, M. et al. (2002) *Proc. GeoProc. 2002*, 539-549.
[2] Gründig, M. et al. (2007) *Appl. Geochem.* **22**, 2334-2343.
[3] Kulenkampff, J. et al. (2008) *Phys. Chem. Earth* **33**, 937-942.
[4] Wolf, M. et al. (2010) *EDGG* **244**, 200-212.
[4] Jan, S. et al. (2004) *Phys. Med. Biol.* **49**, 4543-4561.
[5] Agnostinelli, S. et al. (2003) *Nucl. Instr. Meth. A* **506**, 250-303.

3D-visualization and quantification of fluid flow in salt rock formations by means of Positron-Emission-Tomography

M. Wolf, J. Kulenkampff, F. Enzmann,[1] M. Gründig, M. Richter, H. Mittmann, J. Lippmann-Pipke
[1]Institute of Geosciences, Johannes Gutenberg University, Mainz, Germany

Damages caused by abandoned historical potassium mining at Staßfurt (Saxony-Anhalt) have motivated a joint research project „*Dynamics of drowned and flooded salt mines and their overlaying rocks*" of ten co-operating universities, research facilities and companies, funded by the BMBF and coordinated by the BGR (Bundesanstalt für Geowissenschaften und Rohstoffe), in order to clarify causes, processes and effects of these damages [1]. The contribution of HZDR Research Site Leipzig (former IIF) were small scale laboratory experiments of processes and structures on drilling core samples from hydrologic relevant lithologies of that region in close collaboration with high resolution CT imaging and structure-controlled modeling conducted by colleagues from JGUM [2] in order to improve the comprehension of small scale fluid flow.

After about 10 years of in-house research and development of PET in geosciences the MiniPET camera (ClearPET™, *raytest*[®]) of the HZDR Research Site Leipzig allows in combination with advanced image reconstruction and correction algorithms the visualization of fluid flow in geologic material with a spatial resolution of 1.15 mm and a temporal resolution of about 1 min [3]. Flow behavior can be described with heterogeneous and process-dependent parameter distributions, like effective volume, permeability and dispersion rates. Process comprehension is particularly improved by matching PET data with Lattice-Boltzmann simulations (LBM) of the flow processes [4], which are based on high-resolution CT images of the internal structure of the same core samples. This matching is conducted with geostatistical methods and implies a scaling over several orders of magnitude.

EXPERIMENTAL. Drilling cores (length: 10-20 cm, diameters: 10 cm) from anhydrite, sandstone and rock salt formations of the Staßfurt salt dome were examined with flow-through experiments with highly saline solution and pressures between 0.1 and 5.0 kPa. Radiotracer impulses of [^{18}F]KF and [[124]I]KI with activities between 50 and 250 MBq were injected and in situ PET-measurements of the tracer propagation were conducted between several hours and several weeks, depending on sample permeability. Data sets were matched with CT data (Fig. 1) and LBM based particle tracking simulation data sets of the same samples.

RESULTS. PET turns out as an ideal method for direct quantitative spatiotemporal visualization of tracer transport in rocks on core scale. Matching of PET and CT data sets combines ongoing fluid flow processes with structure information (pore space, cleavages etc.), enables to observe the flow path topology, to determine the effective volume and frequently reveals fingering phenomena in fracture flow. The portion of the inner surface of the rock samples in contact with the mobile fluid – the reactive surface area – decreases with increasing localization of the transport paths and therefore considerably narrows the
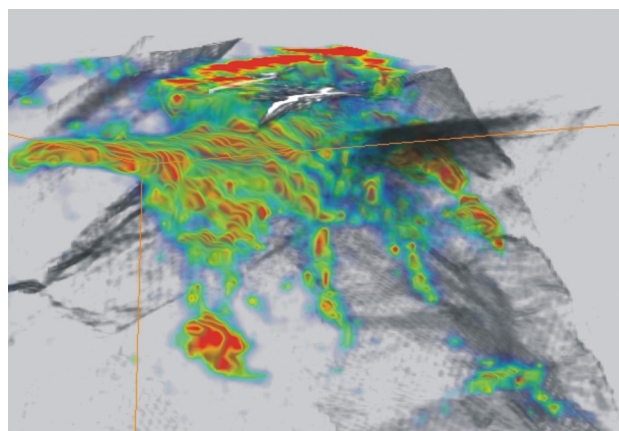
Fig. 1: Combination of PET (colored) and CT (grey, voids) data. Radio-labeled solution flows along a cleavage, showing distinct preferential flow (fingering).
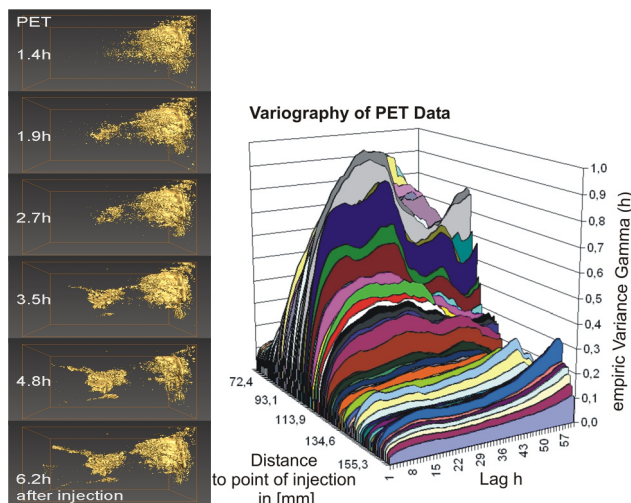
Fig. 2: Propagation of radiolabeled salt solution through a fractured halite core (left), geostatistics (3D-variography) to characterize the complex flow patterns (right).

potential of the inner rock surface for dissolution and sorption reactions. In combination with simulated data, the streaming velocity patterns could be quantified and turned out to be highly variable along distinct parts of the fractures. Local high flow velocities increase local solubility and cause widening of fracture cross sections that may lead to a self energizing mechanism of increasing flow velocities and flow rates in saline rock.

Due to the complex flow patterns and the different resolution of the data sets but especially to prepare future up-scaling techniques for the derived hydrologic parameters to the field scale a geostatistical approach via variography is preferred to compare measured and simulated data as it reveals scale independent similarities and differences in the flow patterns (Fig. 2).

[1] Gerardi, J. (2006) *Report BGR*, p. 79.
[2] Enzmann, F. et al. (2010) *EDGG* **244**, 213-224.
[3] Kulenkampff, J. et al. (2008) *Phys. Chem. Earth* **33**, 937-942.
[4] Wolf, M. et al. (2010) *EDGG* **244**, 200-212.

Water and gas migration in sandy clay buffer material: CT and GeoPET studies

M. Richter, J. Kulenkampff, M. Gründig, A. Seese,[1] J. Rüedi,[2] J. Lippmann-Pipke

[1]Clinic and Policlinic of Nuclear Medicine, University of Leipzig, Leipzig, Germany; [2]National Cooperative for the Disposal of Radioactive Waste (Nagra), Wettingen, Switzerland

Bentonite/sand mixtures are foreseen as sealing and buffer material for nuclear waste disposal sites in granitic formations. For model evaluation or prediction, time and spatially resolved experimental data on gas and water flow through such materials are mandatory. By jointly applying CT and GeoPET measurements we provide for the first time such measurement results of fluid flow in a bentonite/sand column.

For gas migration in water saturated clay/sand mixtures, the following different regimes are discussed [1]:
- conventional two phase flow in porous media,
- reversible formation of micro fractures opening up a new porosity exclusively for the gas flow,
- irreversible formation of macro fractures producing separate regions for gas und water flow.

Spatial characterization of flow patterns is generally not obtained by integral measurements of the gas flow through buffer material [2]. However, the combination of structural information by computer tomography (CT) [3] and flow investigation of PET is suggested to deliver new insights in the flow processes [4].

EXPERIMENTAL. The structure of a plexiglass column (inner diameter: 50 mm, length: 110 mm), filled with a 1 : 4 bentonite/sand mixture, was studied before and after its water saturation by CT (Biograph 16/Siemens). For column saturation, a water flow of 0.002 mL/min was applied for 20 d. Then a conservative PET tracer solution with $[^{58}Co](Co(CN)_6)^{3-}$ was injected with 0.001 mL/min for 42 d. The spatial tracer distribution was monitored by GeoPET (ClearPET™, raytest). After that, helium was injected with 20 bar pressure until breakthrough was observed, the tracer distribution was measured again to identify any flow paths (Fig. 1).

RESULTS. The density distribution (averaged over the column cross sections) before and after water saturation is calculated from CT (Fig. 2). This implies a nearly uniform water content along the column length and a suggested stationary flow. The density distribution in the cross section of the column material ranges between 1.5 and 1.7 g/cm³ (Fig. 3).
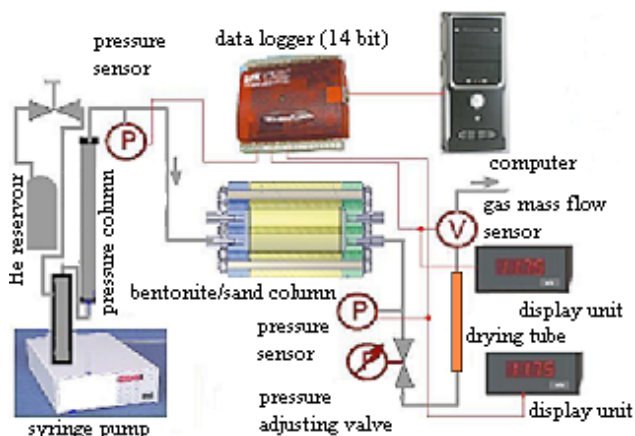
Fig. 1: Scheme of the set-up for the gas flow experiments.
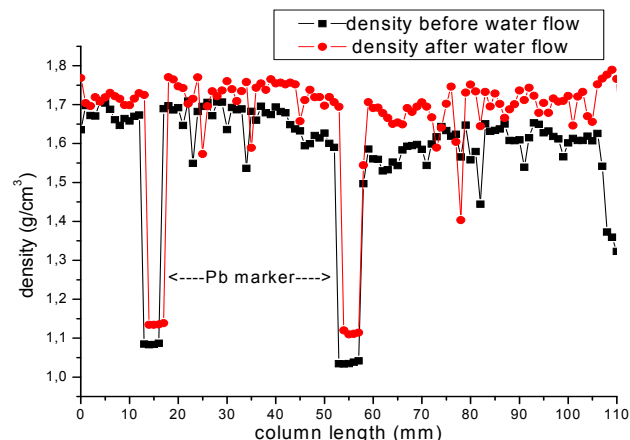
Fig. 2: Mean density distribution in the column cross sections.
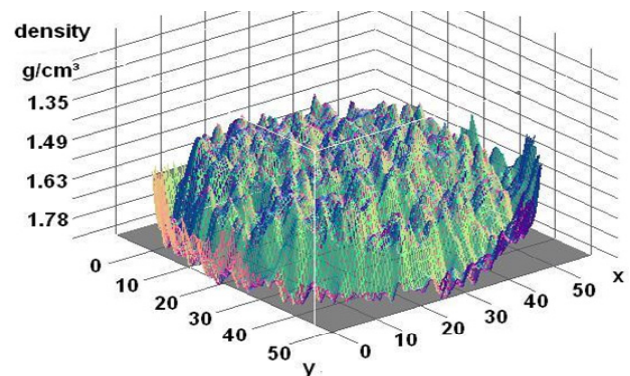
Fig. 3: Density distribution in the cross section 50 mm from the input.

The gas break-through proceeded very quickly at the input pressure of 20 bar. Gas was observed at the outlet after about 12 h. The comprehensive interpretation of the GeoPET images (Fig. 4) in respect to preferential flow paths is in progress.
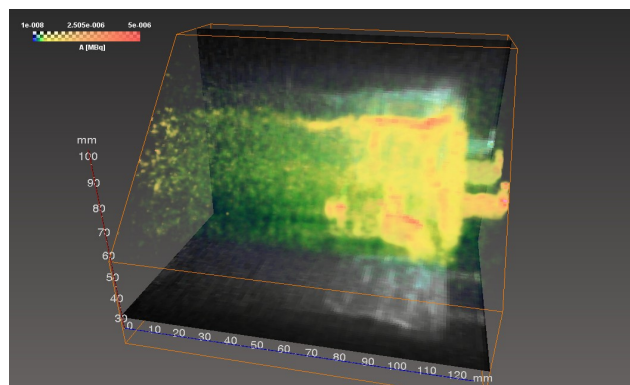
Fig. 4: PET image 42 days after the start of tracer injection.

[1] Hunter, F. et al. (2007) *SKB-Report* TR-07-09.
[2] Marschall, P. et al. (2005) *Oil & Gas Sci. Tech. Rev.* **60**, 121-139.
[3] Tanai, K., et al. (2006) *Mat. Res. Soc. Proc.* **932**, 73.
[4] Wolf, M. et al. (2010) *EDGG* **244**, 200-212.

The physico-chemical characterization of Belarusian soil contaminated after Chernobyl catastrophe

A. Ilyashuk,[1] S. Sachs, K. Schmeide, S. Weiß, A. Barkleit
[1]International Sakharov Environmental University, Minsk, Belarus

Physico-chemical characteristics of Belarusian soil, contaminated after the Chernobyl catastrophe have been determined and compared with literature data from 1996 [1]. It is shown that our results for pH (KCl), total organic carbon, total carbon content and loss on ignition at 1000 °C measurements are comparable to [1] and 0.3% of soil substance occurs in respirable particles (< 3-5 μm) with γ-activity ~ 4% (for Cs-137 and Eu-154) of total γ-activity of the soil sample.

The physico-chemical characterization of soil, contaminated with radionuclides is important for estimation of internal doses on human body due to intake of radionuclides by inhalational and peroral way.

EXPERIMENTAL. Six soil samples from two different places in the undisturbed fields of the area of Masany, Gomel district, Belarus (~ 10 km from Chernobyl power station, Ukraine) have been collected. The soil samples have been taken from three soil horizons (0-5, 5-10, 10-15 cm) in 2006 and 2009.

For characterization of the soil samples, pH (KCl), water content at 105 °C and loss on ignition at 1000°C have been determined according to [2]. Cation exchange capacity (CEC) was determined by compulsive exchange method [3]. The total organic carbon (TOC) and total carbon (TC) content have been analyzed with Multi N/C 2100 analyzer (Analytik Jena). The specific surface area (BET) of soil particles has been determined with SA 3100 analyzer (Beckman-Coulter). The activity of the soil samples has been determined with γ-spectrometry applying HPGe detector system (Ortec). Particle size distribution of the soil samples was determined with sieve analysis (Retsch; sieve diameters: 2 mm-20 μm) as well as with scanning electron microscopy (SEM) measurements (Hitachi S-4800). Elemental composition of soil particles was determined by energy dispersive X-ray spectrometry (EDX; Oxford Instruments) and inductively coupled plasma mass spectrometry (ICP-MS; Elan 9000, Perkin Elmer). In order to characterize organic matter of the soil it was isolated and fractionated (water soluble fraction, mobile humic acids (HA) and fulvic acids (FA), stable HA and FA and unhydrolyzed residue (humin)) according to [4]. The γ-activity and TOC content of the isolated fractions of soil organic matter have been determined.

RESULTS. Table 1 shows the physico-chemical characteristics of the soil samples gathered in 2006 and 2009 in comparison to literature data [1]. Results of γ-spectrometry of one soil sample (0-5 cm, 2006) are shown in Tab. 2. The radionuclides summarized in Tab. 2 contribute the highest γ-activity to the soil sample. Am-241 and Np-237 also represent α-emitters. That means a high radiation danger for people after incorporation.

Sieve analysis of the soil sample (0-5 cm, 2006) showed that 0.3% of soil substance occurs in particles < 20 μm. Results of γ-spectrometry of this fraction (< 20 μm) of the soil sample showed that it contains ~ 4% (for Cs-137 and

Tab. 1: Physico-chemical characteristics of the soil samples (average from samples of 3 soil horizons (0-5 cm, 5-10 cm, 10-15 cm)) collected in 2006 and 2009 in comparison to literature data.

	1996 [1]	2006	2009
pH (KCl)	5.5	3.9 ± 0.1	5.7 ± 0.1
CEC_{CE} [meq/100 g]	–	2.8 ± 0.3	4.1 ± 0.3
TOC [mg/g]	6.3	6.2 ± 0.5	8.2 ± 0.2
TC [mg/g]	8.6	6.3 ± 0.4	9.9 ± 0.6
TIC* [mg/g]	2.3	0.1	1.7
BET [m^2/g]	–	0.5	1.5
water content at 105 °C [%]	–	0.8 ± 0.01	2.0 ± 0.01
loss on ignition at 1000°C [%]	2.2	1.2 ± 0.01	2.8 ± 0.01

* TIC(total inorganic carbon) = TC − TOC.

Tab. 2: Results of γ-spectrometry of the soil sample, 0-5 cm, 2006.

Isotope	Activity [Bq/kg]	Uncertainty [%]
Cs-137	24000	8.4
Am-241	227	8.7
Np-237	86	15.4
Eu-154	45	7.9

Eu-154) of total γ-activity of the soil sample. SEM measurements showed that 95-98% of amount of the soil fraction < 20 μm have diameters < 3-5 μm. Therefore, they are respirable particles and most radiation hazardous for the human body. EDX and ICP-MS measurements showed a predominance of oxygen, aluminum and silicon in the elemental content of soil particles, which points to clay particles.

The results of the TOC content measurements of each isolated fraction of soil organic matter showed a decrease of the TOC content from the highest (0-5 cm) to the lowest soil horizon (10-15 cm). The TOC content in the fraction of mobile HA and FA (66% of all carbon in liquid fractions) is higher than in the water soluble (6%) and stable HA and FA (28%). Results of γ-spectrometry of the isolated fraction of a soil sample (0-5 cm, 2006) showed that < 1% of Cs-137 appears in the water soluble fraction, 18% in mobile HA and FA, 21% in stable HA and FA and 60% in unhydrolyzed residue (humin).

[1] Mironov, V. et al. (1998) *Research into parameters governing the behavior of radioelements in contaminated soil of the Chernobyl region, phase No.* 2, p. 49, *Report IRB-10.96/12,* Academy of Sciences of Republic of Belarus, Minsk, Belarus.
[2] Pansz, M. et al. (2006) *Handbook of soil analysis, mineralogical, organic and inorganic methods*, Springer, Berlin.
[3] Sumner, M.E. et al. (1996) *Methods of soil Analysis. Part 3. Chemical methods*, p.1201-1230, Soil Society of America, Madison, U.S.A.
[4] Kononova, M. et al. (1961) *Pochvovedenie* **10**, 75-87.

Double photoexcitation of 2*p* and 4*f* electrons in curium

C. Hennig, S. Skanthakumar,[1] L. Soderholm[1]

[1]Chemical Sciences and Engineering Division, Argonne National Laboratory, Argonne, IL, U.S.A.

The *L₃*-edge X-ray absorption spectrum of the aqua trivalent Cm ion in aqueous solution exhibits a double photoexcitation involving 2*p* and 4*f* electrons. The multielectron excitation occurs at 508.1 ± 10 eV [1].

Photoelectron excitations can be regarded in general as multielectron processes. They involve the total electron configuration of the excited atom including relaxation effects after the photoelectron ejection as well as multielectron excitations. A detailed analysis shows that the amplitude of the X-ray absorption fine structure is reduced by multielectron effects [2,3]. This is a consequence of the requirement that the total absorption cross section must remain unchanged regardless of the recovery processes. EXAFS analyses consider multielectron excitations through a *k*-dependent amplitude reduction factor $S_i(k)$. The resonances are especially intense for actinides in the trivalent and tetravalent oxidation states [4] but have also been observed in compounds containing actinides in their higher oxidation states [5-8]. The aim of this study is to extend the knowledge about mulitielectron excitations to higher actinides by determining the [2*p*4*f*] double-electron excitation energy of ₉₆Cm.

EXPERIMENTAL. EXAFS measurements were performed by using an aqueous solution of 0.523 M ^{248}Cm(III) in 1 M $HClO_4$. X-ray absorption spectra were collected at the Advanced Photon Source on beamline 12-BM-B.
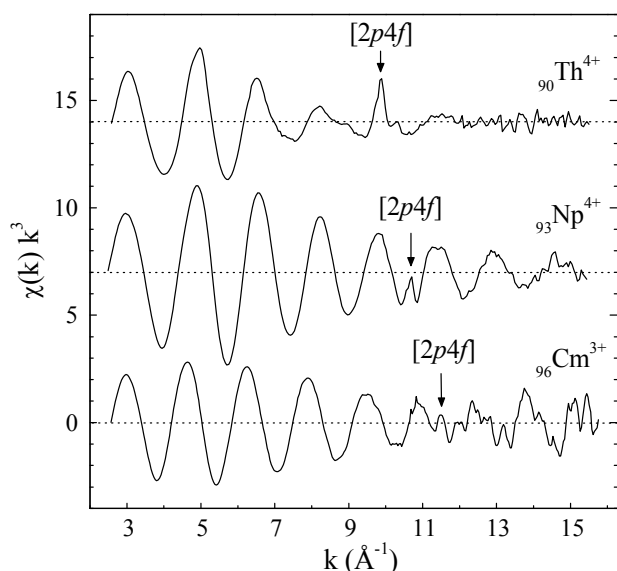
Fig. 1: Experimental *k³*-weighted extended X-ray absorption fine structure at the *L₃*-edge of Th⁴⁺, Np⁴⁺ and Cm³⁺. Arrows indicate the maxima of the [2*p*4*f*] double-electron excitations.

RESULTS. Figure 1 shows the *k³*-weighted L₃ edge EXAFS spectrum of the homoleptic aqua coordinated Cm³⁺ in aqueous solution together with the reference spectra of Th⁴⁺ and Np⁴⁺ taken from [4]. Arrows indicate the relatively sharp resonances of the [2*p*4*f*] double-electron excitations. The spectrum of Th⁴⁺ is obtained from strongly disordered amorphous Th oxyhydoxide silicate. Due to the disorder, the EXAFS amplitude is significantly damped, even at k ~ 9 Å⁻¹, and the multielec-

tron excitation is therefore well pronounced. The multielectron resonance of Np⁴⁺ aqua complex occurs in superposition with the intense sinusoidal EXAFS oscillation but is clearly visible due to the relative low noise level. The EXAFS from Cm³⁺ suffers from relatively high experimental noise. However, by following the EXAFS from low to high k values one can observe a sharp resonance followed by a fast increasing experimental noise level. The abruptness of this feature is an indicator that it is not a noise artifact. This resonance is interpreted as multielectron excitation. The Cm[2p4f] multielectron excitation occurs at E_S = 508.1 ± 10 eV.
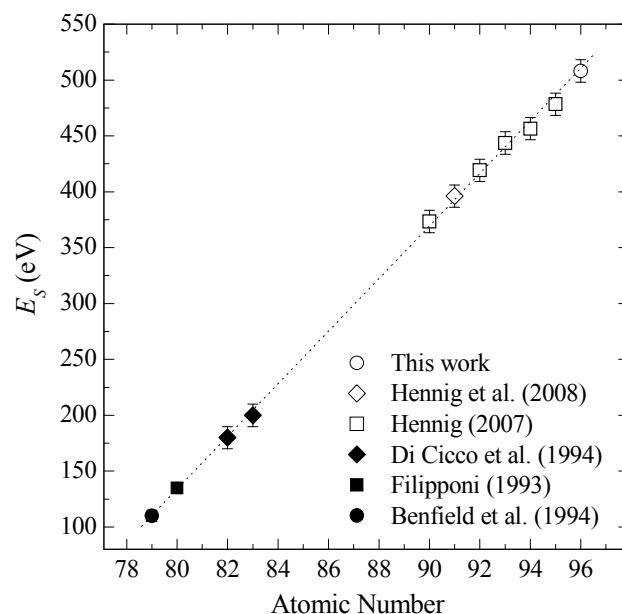
Fig. 2: Experimental energy E_S of Cm³⁺ in comparison with the published literature data of elements with atomic numbers $79 < Z < Z_{Cm}$.

The recent literature provides experimental data of [2p4f] double-electron excitations for several elements. Figure 2 summarizes the known [2*p*4*f*] double-electron excitation energies E_S for the elements with Z > 79. The highest [2*p*4*f*] energy determined so far is the one for Cm which follows the systematic trend of the earlier actinides [4,5] and the elements of the sixth period [9-11].

[1] Hennig, C. et al. (2010) *J. Electron Spectrosc. Relat. Phenom.* **180**, 17-20.
[2] Stern, E.A. et al. (1979) *Phys. Rev. Lett.* **42,** 1372-1375.
[3] Chaboy, J. et al. (1994) *Phys. Rev. B* **49,** 11652-11661.
[4] Hennig, C. (2007) *Phys. Rev. B* **75**, 035120.
[5] Hennig, C. et al. (2008) *Phys. Rev. B* **77**, 235102.
[6] Ikeda-Ohno, A. et al. (2008) *Inorg. Chem.* **47**, 8294-8305.
[7] Hennig, C. et al. (2007) *Inorg. Chem.* **46**, 5882-58892.
[8] Hennig, C. et al. (2009) *Inorg. Chem.* **48**, 5350-5360.
[9] Benfield, R.E. et al. (1994) *J. Phys.-Condens. Matter* **6**, 8429-8448.
[10] Filipponi, A. (1993) *Phys. Rev. A* **48**, 2098-2101.
[11] Di Cicco, A. et al. (1994) *Phys. Rev. B* **49**, 12564-12571.

Aqueous Cm(III) phosphate species investigated by TRLFS

H. Moll, V. Brendler, G. Bernhard

Two Cm(III)–phosphate complexes could be identified from TRLFS data, $CmH_2PO_4^{2+}$ and $CmHPO_4^+$, showing peak maxima at 599.6 and 600.8 nm, respectively. Based on the factor analysis of the emission data, the stability constants of the two complexes were calculated to be $\log \beta_{121} = 20.23 \pm 0.13$ and $\log \beta_{111} = 16.54 \pm 0.80$ at an ionic strength of 0.1 M ($NaClO_4$).

Phosphorous is ubiquitous in natural waters as ionic species. Studies concerning the speciation of actinides with ligands present in environmental systems are of great interest and importance. A-priori there is poor knowledge of the impact of phosphates on the Cm(III) speciation in environmental waters.

EXPERIMENTAL. The TRLFS experiments were performed under N_2 atmosphere at 25 °C. TRLFS spectra were recorded using a pulsed flash lamp pumped Nd:YAG-OPO laser system. Selected samples were ultra-filtrated through 1 kD to determine the influence of Cm(III)–phosphate colloids on the TRLFS results. Details on the experimental set-up and the sample preparation are summarized in [1].

RESULTS. An overview of the emission spectra of $2 \cdot 10^{-8}$ M Cm(III) in 0.1 M $NaClO_4$ measured in the phosphate system is presented in Fig. 1.
A detailed characterization of aqueous Cm(III)–phosphate species based on the changes of the intrinsic luminescence of Cm^{3+} was not reported before. At pH values < 3 (data not shown), the complex formation between Cm^{3+} and $H_2PO_4^-$ is accompanied by both a red shift of the emission maximum from 593.7 (Cm^{3+}) to 600 nm and an increase of the luminescence intensity. The spectroscopic speciation depicted an influence of *Cm(III)–phosphate species 1* at H_3PO_4 concentrations $\geq 3 \cdot 10^{-3}$ M and pH ≤ 3. In general, at $[H_3PO_4] \geq 0.005$ M and pH values between 4 and 6, a strong decrease of the luminescence intensity was observed. This can be interpreted by the precipitation of Cm(III)–phosphate phases or static quenching by the formation of Cm(III)–phosphate colloids. To avoid colloid formation and subsequent precipitation at pH 5 and 6, measurements using $2 \cdot 10^{-8}$ M Cm(III) were performed (see Fig. 1). The decrease of the luminescence emission band at 593.7 nm, Cm^{3+} ion, is accompanied by an in-

crease at 601 nm indicating the formation of *Cm(III)–phosphate species 2*. The program SPECFIT was used to extract the metal-ligand stability constants and the single component spectra. The variations observed in the emission data could be described by the following equilibria:
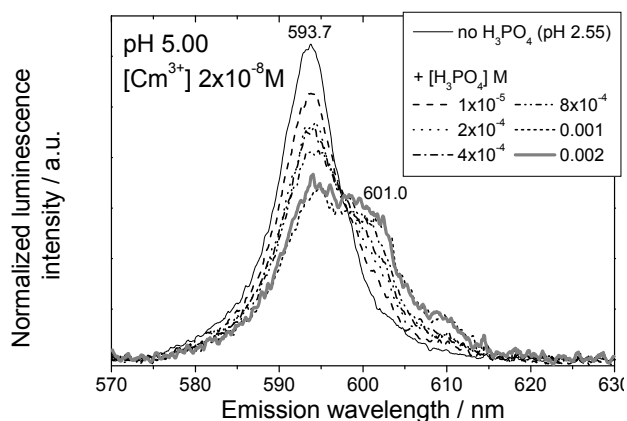
Cm(III)–phosphate species 1:
$$Cm^{3+} + 2H^+ + PO_4^{3-} \rightleftharpoons CmH_2PO_4^{2+} \; ; \log \beta_{121}$$

Cm(III)–phosphate species 2:
$$Cm^{3+} + H^+ + PO_4^{3-} \rightleftharpoons CmHPO_4^+ \; ; \log \beta_{111}$$
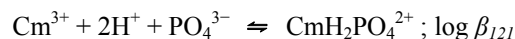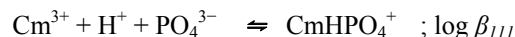
Formation constants were calculated to be $\log \beta_{121} = 20.23 \pm 0.13$ and $\log \beta_{111} = 16.54 \pm 0.80$ (after 1 kD ultra-filtration) at an ionic strength of 0.1 M, respectively [1]. The magnitude of the $\log \beta_{111}$ value is influenced by Cm(III)–phosphate colloid formation. These colloids are characterized by a broad emission maximum at 603.1 nm.
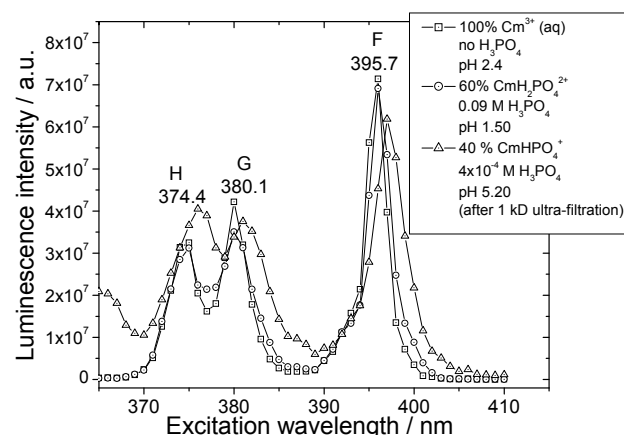
Fig. 2: Excitation spectra of $3 \cdot 10^{-7}$ M Cm(III) measured in the phosphate system at an ionic strength of 0.1 M ($NaClO_4$).

The excitation spectra measured in the Cm(III)–phosphate system are characterized by sharp, well-resolved absorption bands coming from intense transitions to the H-, G-, and F-states (see Fig. 2). The excitation spectra of $CmH_2PO_4^{2+}$ showed a slight red shift in combination with an increase in luminescence line widths of the G and F absorption bands, e.g. F band: 396.2 (2.82) nm compared with 395.7 (2.44) nm for Cm^{3+}. The differences were more pronounced in the excitation spectra of $CmHPO_4^+$. The main excitation band (F) of Cm^{3+} at 395.7 nm is shifted to 397.2 nm. The excitation spectra clearly support our conclusions drawn from the luminescence emission measurements concerning the speciation of aqueous Cm(III) in the phosphate system.
Our results demonstrate that aqueous Cm(III)–phosphate species can influence the geochemical behavior of Cm(III) at high phosphate concentrations ($\geq 5 \cdot 10^{-3}$ M) and acidic pH < 5.

[1] Moll, H. et al. (2011) *Radiochim. Acta.*, accepted.

Fig. 1: Luminescence spectra of $2 \cdot 10^{-8}$ M Cm(III) measured as a function of $[H_3PO_4]$ at pH 5.0.

Temperature dependence of Am(III)-pyromellitate complex formation studied by UV-vis spectroscopy

M. Müller, M. Acker,[1] A. Barkleit, S. Taut[1]

[1]Central Radionuclide Laboratory, Dresden University of Technology, Dresden, Germany

The complex formation of Am(III) with pyromellitic acid (1,2,4,5-benzenetetracarboxylic acid) was studied at different temperatures between 25 °C and 50 °C using UV-vis spectroscopy with a Liquid Waveguide Capillary Cell (LWCC). The reaction turned out to be slightly endothermic. Complex stability and thermodynamic data are presented.

The assessment of long term safety of nuclear waste disposal requires the understanding of migration behavior of radionuclides and hence, of the aquatic chemistry of actinides under specific conditions. Up to now, most of the available data are limited to 25 °C. Since radioactive decay is accompanied by a strong heat development, thermodynamic data are also needed for higher temperatures. Complex formation with organic and inorganic matter can significantly influence migration properties of radionuclides. Until now, little is known about the complex formation of Am(III) with organic molecules.

EXPERIMENTAL. For the determination of complex stability a spectrophotometric titration was performed. A stock solution of the ligand was added stepwise to an Am(III) solution ($5 \cdot 10^{-7}$ M), thus increasing pyromellitate concentration from 0 to 10^{-3} M. All experiments were performed under inert gas atmosphere (N_2) at temperatures between 25 °C and 50 °C. The ionic strength was adjusted to 0.1 M ($NaClO_4$) and the pH was kept constant at 5.0. The absorption of the sample was measured between 480 and 530 nm at each titration step. Stability constants of Am(III)-pyromellitate complexes were calculated from the spectra using the factor analysis program SPECFIT (version 3.0).

RESULTS. Figure 1 shows the absorption spectra of spectrophotometric titration of Am(III) with pyromellitic acid at pH 5.0 and T = 25°C. The Am(III) absorption band at 503 nm is strongly influenced by the chemical environment and thus, information on the speciation can be obtained. At all investigated temperatures we observe a slight red shift as well as an increase of absorption maximum with increasing ligand concentration, indicating complex formation. Complex stabilities were calculated from the spectra using temperature dependent protonation constants from potentiometric titration of pyromellitic acid. Considering the speciation of the ligand at pH 5.0 the formation of a deprotonated 1 : 1 complex can be assumed at all temperatures. Furthermore, the spectra indicate the occurrence of a second complex species. The complex stability of the 1 : 1 complex is in very good agreement with the literature value [1] and increases with increasing temperature (Tab. 1). The thermodynamic parameters enthalpy (ΔH) and entropy (ΔS) were determined from the temperature dependence of ln K using the Van`t Hoff equation (Fig. 2). Until now no literature data are available to compare with but the values are in the same scale as those reported for the analogue Eu(III) complex [2]. The enhancement of complex stability with increasing temperature might be due to a strengthening of ligand basicity and therefore, increasing negative charges
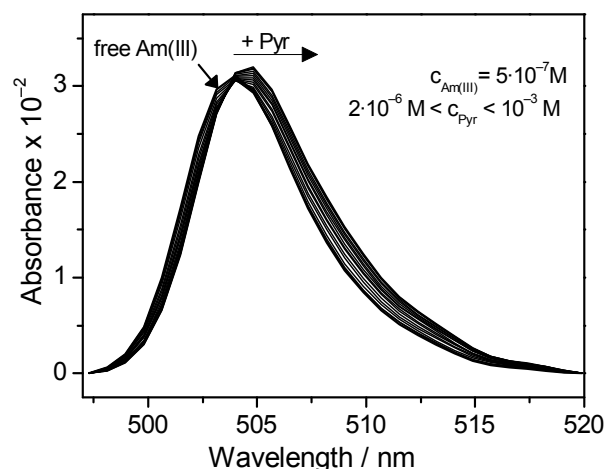
Fig. 1: UV-vis absorption spectra of Am(III) at pH 5.0 and 0.1 M $NaClO_4$ in dependence of ligand concentration.
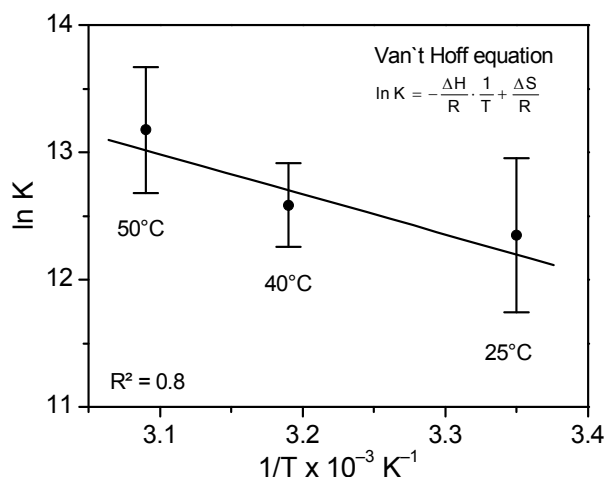
Fig. 2: ln K of AmL$^-$ complex formation as a function of temperature (Van`t Hoff Plot).

Tab. 1: Thermodynamic data for AmL$^-$ complex formation.

T [°C]	$\log \beta_{110}$	Ref.
25	5.42 ± 0.16	[1]
25	5.4 ± 0.3	this work
40	5.5 ± 0.1	this work
50	5.7 ± 0.2	this work
ΔH [kJ mol^{-1}]	26 ± 2; (18.5^*)	this work; ([2])
ΔS [J mol^{-1} K^{-1}]	189 ± 43; ($152 \pm 5^*$)	this work; ([2])

*for the analogue Eu(III)-complex.

experienced by the metal ion. It can be concluded that the formation of Am(III)-pyromellitate complex is endothermic and driven by entropy. Further investigations have to be done in order to determine the second complex species accurately.

[1] Barkleit, A. et al. (2011) *Spectroc. Acta Part A-Molec. Biomolec. Spectr.* **78**, 549-552.
[2] Barkleit, A. et al. (2010) *Report FZD-530*, p. 64.

First fluorescence spectroscopic investigation of Am(III) complexation with small organic ligands

A. Barkleit, G. Geipel, M. Acker,[1] S. Taut[1]

[1]Central Radionuclide Laboratory, Dresden University of Technology, Dresden, Germany

For the first time Am(III) complexation with carboxylic acids (pyromellitic acid (1,2,4,5-benzene-tetracarboxylic acid, BTC), lactic acid (Lac)) could be identified and characterized with time-resolved laser-induced fluorescence spectroscopy (TRLFS) at trace metal concentration.

Small organic molecules are to be found in pore water of clay mineral, a potential formation for a final nuclear waste disposal. They can influence the transport behavior of actinides. Additionally, they serve as model compounds for main functionalities of humic substances, which are ubiquitous in natural waters and soils and also affect the mobility of actinides. The potential influence of these molecules or fragments of actinide migration can be estimated with complex stability constants.

EXPERIMENTAL. TRLFS measurements of $2 \cdot 10^{-6}$ M (BTC) and $5 \cdot 10^{-6}$ M (Lac) Am^{3+} were carried out with a pulsed Nd:YAG-MOPO laser system, combined with a Spectrograph M270 and an ICCD camera system at an excitation wavelength of 503 nm, at pH 5.0 (BTC) and 6.0 (Lac), an ionic strength of 0.1 M ($NaClO_4$), 25 °C and 65 °C (only Lac). The ligand concentrations were varied from $1 \cdot 10^{-6}$ to $9 \cdot 10^{-5}$ M (BTC) and from $5 \cdot 10^{-4}$ to 0.1 M (Lac).

RESULTS. In the Am-BTC complex system the luminescence intensity of the $^5D_1-^7F_1$ transition at 691 nm increases with increasing ligand concentration (Fig. 1) [1]. In the Am-Lac system, we additionally observe a red shift of the emission maximum to 696 nm upon complexation (Fig. 2). A slope analysis on the basis of the modified logarithmic mass action law (Eq. 1) was carried out to determine the complex stoichiometry.

$$\log \frac{c[AmL_n^{(3-x)+}]}{c[Am^{3+}]} = n \times \log c[L] + \log K \qquad (1).$$

The concentrations of metal ion, ligand ([L]) and complex ($[AmL_n^{(3-x)+}]$) were calculated from mathematical deconvolution of the spectra. For BTC, the slope of 1.25 ± 0.11 indicates a predominant 1:1 complexation [1]. For Lac, the slope is near 1 up to 0.01 M Lac and rises up to about 3 with higher ligand concentration, indicating the formation of higher complexes (1:2, 1:3).

The initial luminescence lifetime of Am^{3+}(aq) of 23.5 ± 2.3 ns is in very good accordance with literature (23 ± 2 ns [2]). The number of the associated hydration water molecules in the inner coordination sphere can be calculated applying the empirical linear relationship given by Kimura et al. [3],

$$n(H_2O) \pm 0.5 = 2.56 \times 10^{-7} \times \tau^{-1} - 1.43 \qquad (2).$$

This yields 9.5 ± 0.5 water molecules for Am^{3+}(aq). For the Am-BTC 1:1 complex, the lifetime is prolonged due to complexation (exchange of water molecules by ligand molecules) to 27.2 ± 2.2 ns, corresponding to 8.0 ± 0.5 remaining water molecules. For the Am-Lac system, we observe a lifetime of 30.0 ± 1.1 ns (7.1 ± 0.5 H_2O) at

0.01 M Lac and 37.4 ± 0.9 ns (5.4 ± 0.5 H_2O) at higher ligand concentration (0.1 M Lac). These lifetimes and correspondent remaining water molecules also indicate a formation of complexes with higher stoichiometries (1:2, 1:3).

Complex stability constants were determined for the 1:1 complexes from the static spectra using the computer code SPECFIT to be $\log \beta_{110} = 5.42 \pm 0.16$ for the Am-BTC complex and 2.22 ± 0.13 (25 °C) and 2.35 ± 0.35 (65 °C) for the Am-Lac complex.
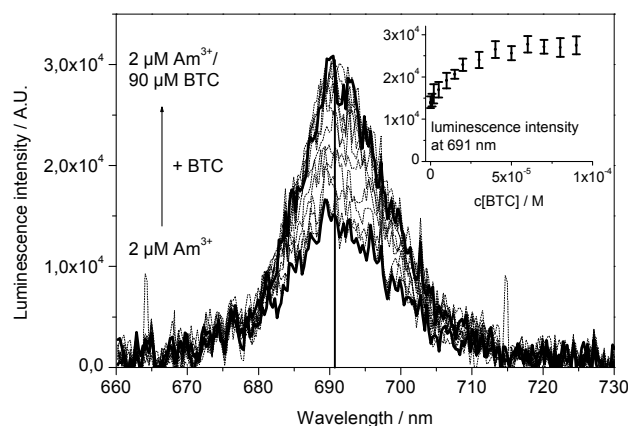
Fig. 1: Luminescence spectra of 2 μM Am^{3+} as a function of BTC concentration (1 μM - 90 μM BTC, pH 5.0, 0.1 M $NaClO_4$, 25 °C). Small insert: Luminescence intensity at 691 ± 1 nm in dependency of the BTC concentration.
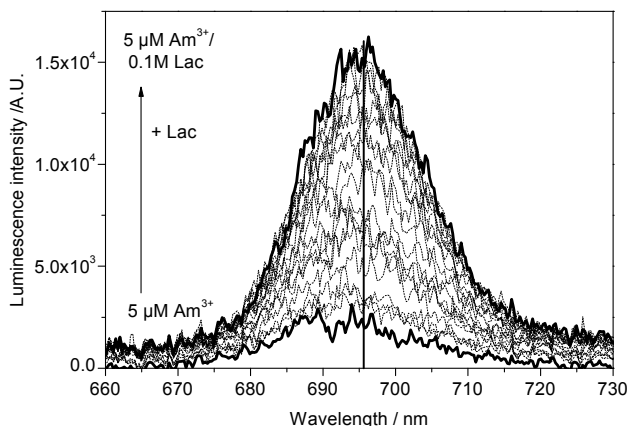

Fig. 2: Luminescence spectra of Am^{3+} as a function of lactate concentration (0.5 mM - 0.1 M Lac, pH 6.0, 0.1 M $NaClO_4$, 25 °C).

[1] Barkleit, A. et al. (2011) *Spectroc. Acta Pt. A-Molec. Biomolec. Spectr.* **78**, 549-552.
[2] Beitz, J. V. (1994) *J. Alloys Compd.* **207**, 41-50.
[3] Kimura, T. et al. (1998) *J. Alloys Compd.* **271**, 867-871.

UV-vis study of complexation of trivalent Am, Eu and Nd by tartaric acid at low metal concentrations

M. Acker,[1] M. Müller,[1] A. Barkleit, S. Taut[1]

[1]Central Radionuclide Laboratory, Dresden University of Technology, Dresden, Germany

For the first time, the complex formation of trivalent Am and the inactive analogues Eu and Nd with tartaric acid was studied by UV-vis spectroscopy using an Liquid Waveguide Capillary Cell (LWCC). The complexation is indicated by a small red shift of the absorption bands. The stability constants of two tartrate complexes (ML^{2+}, ML$_2^+$) and their optical absorption oscillator strengths P were calculated.

EXPERIMENTAL. The complex formation investigations were carried out as spectrophotometric titrations at 25 °C, at ionic strength of 0.1 M (NaClO$_4$) and pH range between 4 and 5. Small aliquots of a appropriate sodium tartrate solution were added to sample solutions with different initial metal concentrations (Nd: $2.5 \cdot 10^{-4}$ M, Am: 6 to $8 \cdot 10^{-7}$ M , Eu: 2.5 to $5 \cdot 10^{-4}$ M).

The absorption spectra were recorded with a fiber optics spectrometer (MCS601 Carl Zeiss Jena, Germany) coupled with a 2 m LWCC.[2] The recorded spectral ranges depend on the main absorption bands of the metal ions. All spectra were base line corrected and analyzed between 495 and 520 nm for Am, between 500 and 650 nm for Nd, and between 389 and 403 nm for Eu.

RESULTS. The absorption of lanthanide and actinide ions has hypersensitive transitions that are very sensitive to the coordination environment. Table 1 summarizes the measured transitions of Am, Nd, and Eu.

Tab. 1: The measured absorption transitions of Am, Nd, Eu.

metal ion	hypersensitive transition	wavelength [nm]	extinction [L mol^{-1} cm^{-1}]
Am	$^7F_0 \rightarrow {}^5L_6$	~503	380 [2]
Nd	$^4I_{9/2} \rightarrow {}^5G_{5/2}, {}^2G_{7/2}$	~575	7.20 [1]
Eu	$^7F_0 \rightarrow {}^5D_2$	~465	< 0.05
	$^7F_0 \rightarrow {}^5L_6*$	~394	2.77 [1]

* This transition is not hypersensitive.

The hypersensitive transition $^7F_0 \rightarrow {}^5D_2$ of Eu is very weak and it was only observable at higher Eu concentrations ($> 5 \cdot 10^{-4}$ M) in connection with a considerable complex formation with tartrate. Here a great rise of the absorption intensity by factor 11 at 20 fold excess of tartaric acid was observed. However, the extinction of this peak is too low for a reasonable analysis, so that the most intensive but not so sensitive peak at 394 nm was used. A red shift in the absorption spectra of the metal ions was observed with increasing ligand concentration (in Fig. 1 shown for Nd). An increase of intensity is reflected in the experimental optical oscillator strength (Tab. 2), expressed as integral of molar extinction coefficient and calculated by the equation given in [1, 4]. Tartrate complexes of Eu and Am show only a small increase of absorption intensity in comparison to the free metal ions: ~6 to 7% for 1:1 and ~ 12% for 1:2 complex compared to the Nd tartrate species with ~32% and ~87%, respectively.

The reaction of M(III) (M = Am, Eu, Nd) with tartaric acid can be formulated as follow:
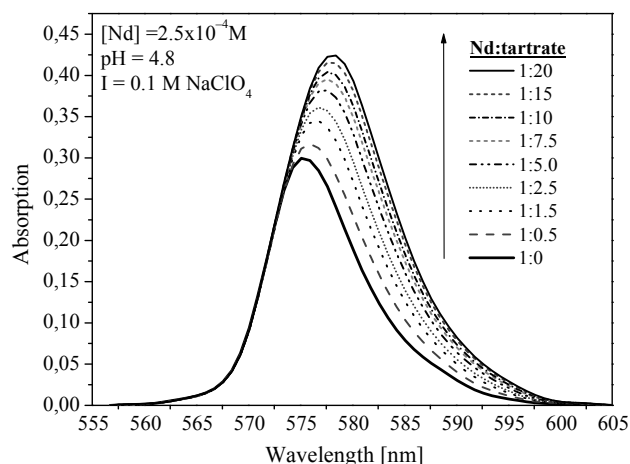
Fig. 1: UV-vis spectra of Nd as function of tartrate concentration.

$$x\,M^{3+} + y\,H^+ + z\,\text{tart}^{2-} \rightarrow M_x H_y \text{tart}_z^{(3x+y-2z)}$$
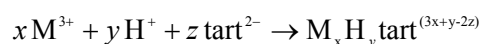
$$\text{with} \quad \beta_{xzy} = \frac{[M_x H_y \text{tart}_z^{(3x+y-2z)}]}{[M^{3+}]^x \cdot [H^+]^y \cdot [\text{tart}^{2-}]^z} \qquad (1)$$

The spectra were analyzed by deconvolution with Solver (Excel) and via slope analysis by using the logarithmic form of mass action law (eq. 1) to get the stoichiometric composition. Slopes near 1 and at higher ligand concentration near 2 were found, indicating a 1:1 and 1:2 complex. The stability constants (Tab. 2) were determined by the global analysis program SPECFIT/32 including the protonation constants of tartaric acid of pKa$_1$ = 3.95 and pKa$_2$ = 2.82 [5]. The obtained data are in good agreement with literature data [3]. Due to the similar ionic radii and chemical properties of Am, Nd and Eu differences between the formation constants are not expected. The differences are within the experimental errors.

Tab. 2: Absorption maxima, optical oscillator strength and complex stability constants of reaction of Am, Nd, Eu with tartrate.

Metal ion	Absorption maxima [nm] *Oscillator strength Px10^6*			log β_{xzy}, I = 0.1 M	
	M$_{free}$	1:1 complex	1:2 complex	log β_{110}*	log β_{120}*
Am	503.9 *485*	504.7 *521*	505.8 *542*	4.2 ± 0.2	7.1 ± 0.6
Nd	575.0 *9.4#*	576.7 *12.4*	578.4 *17.6*	4.1 ± 0.3	6.7 ± 0.4
Eu	394.0 *1.7#*	394.6 *1.8*	395.3 *1.9*	4.2 ± 0.3	7.3 ± 0.5

*error 2σ from repeated experiments, #values in agreement with [4].

[1] Carnall, W. T. (1979) *Handbook on the Physics and Chemistry of Rare Earths, Vol. 3,* p.172-208, North Holland, Amsterdam.
[2] Müller, M. et al. (2010) *Radioanal. Nucl. Chem.* **286**, 175-180.
[3] Rao, V.K. et. al (1987) *Inorg. Chim. Acta* **128**, 131-134.
[4] Carnall, W.T. (1968) *J. Chem. Physics*, **49**, 4412-4423.
[5] Barkleit, A. (2010) unpublished results.

How to evaluate mixed-valence Pu(III)–PuO$_2$ XANES/EXAFS spectra

R. Kirsch,[1,2] D. Fellhauer,[3] M. Altmaier,[4] V. Neck,[4] L. Charlet,[2] A. C. Scheinost[1]

[1]Institute of Radiochemistry, Helmholtz-Zentrum Dresden-Rossendorf, Dresden, Germany; [2]Earth and Planetary Science Department, University of Grenoble-I, Grenoble, France; [3]Institute for Transuranium Elements, Karlsruhe, Germany; [4]Institute for Nuclear Waste Disposal, Karlsruhe Institute of Technology, Germany

In certain cases [1], shell fitting of the EXAFS region has proved more sensitive to the presence of a more than one oxidation state than analysis of the XANES region. For Pu(III)–PuO$_2$ mixtures, we observe, however, that from shell fitting the Pu speciation in the sample cannot be derived correctly. In contrast, mathematical comparison of the normalized sample spectra to suitable references (e.g. by using an iterative target test (ITT) [2]) yields consistent results regarding Pu speciation. In addition, shell fitting behavior of mixed oxidation state samples could be reproduced by creating artificial sample spectra according to the Pu speciation derived by ITT.

EXPERIMENTAL. Mackinawite (FeS) [3] and siderite (FeCO$_3$) [4] were reacted under anoxic conditions for 40 days in 0.1 M NaCl with $1 \cdot 10^{-5}$ M Pu at approx. pH 8 (3.4 g/L FeS, 2.0 g/L FeCO$_3$). ^{242}Pu was added as electrolytically prepared Pu(V) after confirmation of the initial oxidation state by UV-vis spectrometry. Pu-L$_{III}$-edge XANES and EXAFS spectra of wet pastes were collected in fluorescence mode at 15 K at the ROBL beamline. Reference spectra of aqueous Pu(III) (at RT) and PuO$_2$(cr) (15 K) had been collected previously.

RESULTS. Reaction of Pu(V) with mackinawite and siderite results in PuO$_2$-like XANES and EXAFS spectra (Fig. 1). However, in the XANES region a 1.4 eV low energy shift of the Pu(V)-siderite spectrum compared to PuO$_2$(cr) indicates the presence of Pu(III). In addition, the Pu(V)-siderite sample shows significant differences to the other two spectra in the lower k-range (arrows in Fig. 1c). If the Pu(V)-siderite spectrum is fitted with a single oxygen shell, a Pu–O distance of 2.32 Å is found and the σ^2 value of 0.015 Å^2 is indicative of high structural disorder or the presence of multiple oxygen distances. A fit with two oxygen shells results in Pu–O distances of 2.27 Å and 2.43 Å, which according to $\Delta R = \pi / (2 \times \Delta k)$ is below the resolution limit (0.17 Å) for the given k-range ($3 \leq k \leq 12.3$ Å^{-1}) (Tab. 1). In both cases, the mean distance (2.32 Å for the single or 2.34 Å for the two shell fit) coincides with the Pu–O distance of PuO$_2$(cr) (2.33 Å). Shell fitting therefore provides no clear indication for the presence of Pu(III), which is characterized by a significantly longer Pu–O distance (2.49 Å). In contrast, analysis of the normalized spectra in the XANES and EXAFS regions using an Iterative Target Test (ITT) [2] with (Pu^{III})$_{aq}$ and
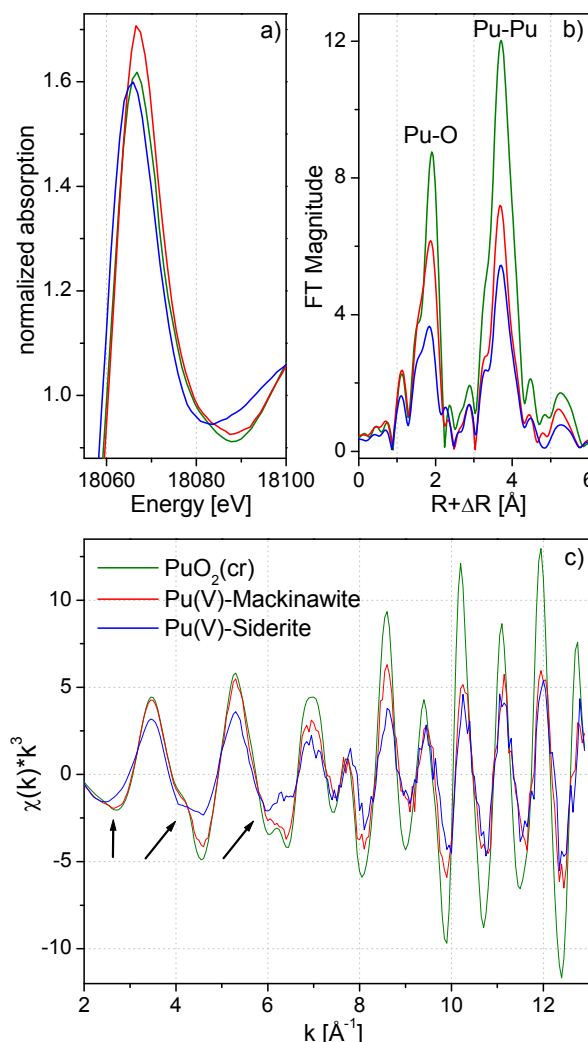
Fig. 1: Experimental Pu-L$_{III}$ spectra of PuO$_2$ (green) and Pu(V) reacted at pH 8 with mackinawite (red) and siderite (blue); a) XANES, b) Fourier Transform (3.0 < k < 12.6 Å^{-1}), c) χ(k) × k^3.

PuO$_2$ reference spectra yields a Pu(III) content of 33%. Applying shell fitting to artificial mixture spectra, obtained from (Pu^{III})$_{aq}$ and PuO$_2$ (crystalline or formed in the presence of mackinawite (red spectrum in Fig. 1), supports the ITT result as the fitting behavior of the Pu(V)-siderite spectrum is closely reproduced by the 33% (Pu^{III})$_{aq}$ − 67% PuO$_2$(mackinawite) spectrum (for more details see supporting information of [5]). For mixed Pu(III)-PuO$_2$ samples, structural analysis of the oxygen coordination shell by shell fitting is therefore clearly compromised and care must be taken not to over-interpret fit data.

[1] Denecke, M. et al. (2005) *Talanta* **65,** 1008-1014.
[2] Rossberg, A. et al. (2003) *Anal. Bioanal. Chem.* **376,** 631-638.
[3] Rickard, D. (1969) *Stockholm Cont. Geol.* **20,** 67-95.
[4] Thamdrup, B. et al. (1993) *Appl. Environ. Microbiol.* **59**, 101-108.
[5] Kirsch, R. et al. (2011) *Environ. Sci. Technol.*, in preparation.

Tab. 1: Shell fit comparison between Pu(V)-siderite and theoretical PuO$_2$-Pu(III) mixture spectra. Mixture spectra were created from normalized files according to:
y = x · PuO$_2$(cr or Mack) + (1−x) · (Pu^{III})$_{aq}$.

Paths	Pu(V)-siderite			66% PuO$_2$(cr) − 34% (Pu^{III})$_{aq}$			67% PuO$_2$(Mack) − 33% (Pu^{III})$_{aq}$		
	CN	R [Å]	σ^2 [Å^2]	CN	R [Å]	σ^2 [Å^2]	CN	R [Å]	σ^2 [Å^2]
Pu–O	3.6	2.27	0.0041^c	6.1	2.33	0.0084	3.8	2.27	0.0058^c
Pu–O	2.9	2.43	0.0041^c				2.9	2.43	0.0058^c
Pu–Pu	6.0	3.80	0.0043	5.9	3.81	0.0019	6.6	3.80	0.0053
Pu–O	10.4	4.42	0.0041^c	14.7	4.44	0.006^f	11.1	4.41	0.006^f

c – correlated, f – fixed.

Influence of reduced sulfur functionalities of humic acids on the Np(V) reduction

K. Schmeide, S. Sachs

The influence of reduced sulfur functional groups of humic acids (HA) on their capability to reduce Np(V) to Np(IV) in aqueous solution has been studied at pH 5.0, 7.0 and 9.0 under anaerobic conditions in dependence on time. Sulfur functional groups of HA were found to contribute to the Np(V) reduction in the slightly acidic pH range.

The migration behavior of actinide contaminants is influenced by humic substances (fulvic acids and humic acids (HA)) due to their complexing and redox properties and their ability to form colloids.

In the literature, the redox activity of humic substances is widely attributed to the reversible hydroquinone/quinone redox couple with semiquinone-type free radicals as significant electron donor/acceptor intermediate species [1] and furthermore, to the oxidation of phenolic OH groups to phenoxy radicals. The role of phenolic OH groups for the Np(V), U(VI) and Fe(III) reduction by HA has been studied in [2,3].

Also nitrogen and sulfur containing functional groups of HA are discussed as redox-active groups [4]. While sulfur functional groups of HA have not been studied as reducing agents toward actinides like U, Np or Pu so far, simpler organic compounds containing sulfur in the reduced form as thiol groups (R-SH) were found to reduce Np(VI) [5].

In this study, HA model substances type M1-S with different sulfur contents (1.9, 3.9, 6.9 wt.%) [6] were applied. Reduced sulfur species, such as thiols, dialkylsulfides and/or disulfides, were determined as the dominating sulfur functionalities in the HA by X-ray photoelectron spectroscopy. In this work, their Np(V) reduction behavior is studied in comparison to that of the sulfur-free HA type M1 and furthermore, compared to that of HA type Hyd-Glu [3], which was already shown to stabilize Np(IV) in sorption experiments [7].

EXPERIMENTAL. The HA model substances M1, M1-S-1, M1-S-2, M1-S-3 contain 0, 1.9, 3.9, 6.9 wt.% sulfur, respectively. The content of phenolic/acidic OH groups of these HA is nearly the same (cf. inset Fig. 1b). Conditions of reduction experiments: $[Np]_{tot} = 5\ \mu M$, $[HA] = 100\ mg/L$, $I = 0.1\ M$ ($NaClO_4$), pH 5.0, 7.0, 9.0, N_2 atmosphere, exclusion of light, room temperature.

RESULTS. At pH 5.0, the Np(V) reduction, determined by solvent extraction with 2-thenoyltrifluoroacetone [2], strongly increases with increasing sulfur contents of the HA (0 to 6.9 wt.%) (cf. Fig. 1a). That means that the reduced sulfur functional groups of HA contribute to the reduction capability of HA at pH 5.0. In contrast to this, at pH 7.0, the sulfur functionalities of HA have only a slight influence on the Np(V) reduction (cf. Fig. 1b). Also at pH 9.0, no significant influence of the sulfur functionalities on the reduction behavior of HA toward Np(V) was found (data not shown). This implies that the contribution of the sulfur functionalities to the Np(V) reduction capability of HA depends on pH value.

For comparison, the Np(V) reduction by the model HA type Hyd-Glu studied at pH 5.0 and 7.0 under identical experimental conditions [2] is shown in Fig. 1. Compared
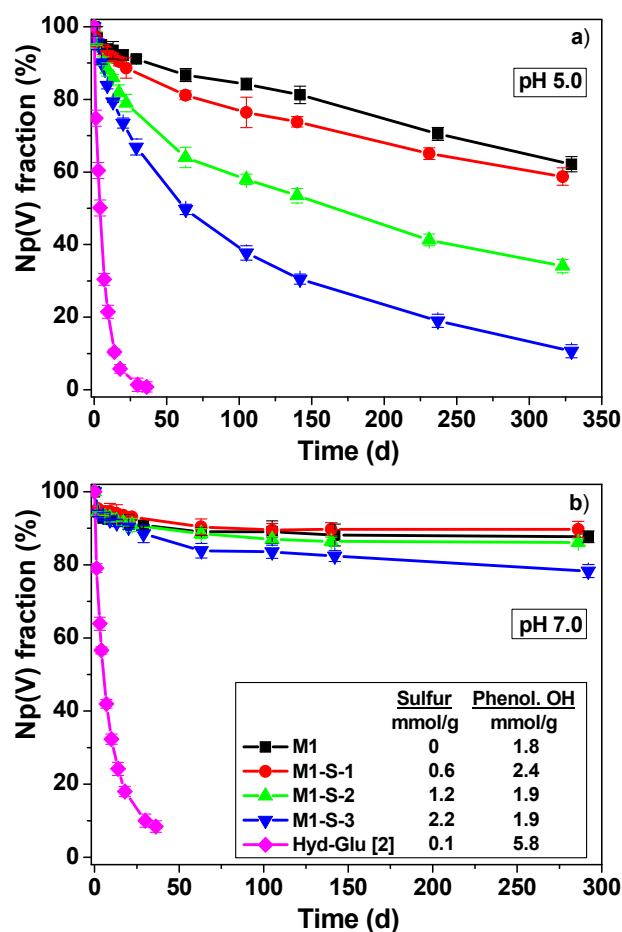
Fig. 1: Np(V) reduction by HA type M1(-S) at pH 5.0 and 7.0 as a function of sulfur content of HA and equilibration time. For comparison, the Np(V) reduction by HA type Hyd-Glu at pH 5.0 and 7.0 [2] is shown. The legend holds for both figures.

to the sulfur containing HA, HA type Hyd-Glu induces a faster Np(V) reduction and, finally, shows a higher Np(V) reducing capacity which can be attributed to its enhanced phenolic/acidic OH group content. This shows that phenolic OH groups contribute stronger to the total Np(V) reducing capacity of HA than sulfur functionalities. This effect becomes stronger with increasing pH value.

In this study, sulfur functional groups have been identified as redox-active functional units in HA in the slightly acidic pH range. Due to the low sulfur content of up to 2 wt.% in natural HA, however, their contribution to the total redox activity of HA toward Np(V) is small compared to hydroquinone-like moieties and non-quinoid phenols that dominate the redox behavior of humic substances.

[1] Nurmi, J.T. et al. (2002) *Environ. Sci. Technol.* **36**, 617-624.
[2] Schmeide, K. et al. (2009) *Radiochim. Acta* **97**, 603-611.
[3] Sachs, S. et al. (2011) *Geoderma*, accepted.
[4] Fimmen, R.L. et al. (2007) *Geochim. Cosmochim. Acta* **71**, 3003-3015.
[5] Weschler, C.J. et al. (1974) *Inorg. Chem.* **13**, 2360-2366.
[6] Sachs, S. et al. (2010) *Radiochim. Acta* **98**, 467-477.
[7] Schmeide, K. et al. (2010) *Appl. Geochem.* **25**, 1238-1247.

Comparative investigation of the solution species $[U(CO_3)_5]^{6-}$ and the crystal structure of $Na_6[U(CO_3)_5] \cdot 12H_2O$

C. Hennig, A. Ikeda-Ohno,[1] F. Emmerling,[2] W. Kraus,[2] G. Bernhard

[1]Japan Atomic Energy Agency, Synchrotron Radiation Research Center (Spring-8), Hyogo-ken, Japan; [2]BAM Federal Institute for Materials Research and Testing, Berlin, Germany

The limiting U(IV) carbonate species in aqueous solution was investigated by comparing its structure parameters with those of the complex preserved in a crystal structure [1].

To clarify the coordination of the limiting U(IV) carbonate complex, we investigated a crystal structure by X-ray diffraction, followed by a comparative investigation of the $[U(CO_3)_n]^{4-2n}$ complex in solid and solution state by U L_3–edge EXAFS spectroscopy. EXAFS is an appropriate method to test if the solution species is preserved in a crystal structure [2] or undergoes a ligand rearrangement [3] during crystallization. Because most of the authors mentioned difficulties to prevent the reoxidation of U(IV), we applied a new electrolysis route to obtain a pure U(IV) carbonate solution [1].

EXPERIMENTAL. Single crystals were obtained from 0.05 M U(IV) solution in 1 M $NaHCO_3$ after several weeks without evaporation of the solution (sample **A**). The U(IV) solution sample was prepared by bulk electrolysis of 0.05 M U(VI) carbonate in the 1.0 M $NaHCO_3$ solution at a constant potential of −1.45 V, using a 4.9 cm² Hg pool electrode, a Pt wire counter electrode, and a Ag/AgCl reference electrode (sample **B**).

RESULTS. The solid compound $Na_6[U(CO_3)_5] \cdot 12H_2O$ crystallizes in the triclinic space group with two $[U(CO_3)_5]^{6-}$ anions in the unit cell. The U(IV) atom is coordinated by five carbonate ligands resulting in a coordination number of 10. The carbonate ligands coordinate exclusively in bidentate mode as shown in Fig. 1. Figure 2 compares the crystalline $Na_6[U(CO_3)_5] \cdot 12H_2O$ with the solution of 0.05 M U(IV) in 1 M $NaHCO_3$. The structure parameters of $Na_6[U(CO_3)_5] \cdot 12H_2O$ were used

to calculate backscattering phase and amplitude functions of the individual neighboring atoms.

The carbonate coordination shows a linear arrangement of uranium, the carbon atoms C and the distal oxygen O_{dist} The bidentate-chelating coordination mode of the carbonate group is related with specific multiple scattering effects. The collinear arrangement of two ligand atoms C and O_{dist} with the absorbing atom results in strong multiple-scattering processes which usually increase the scattering power of a more distant atom like O_{dist} about several magnitudes. The clear U–C–O_{dist} multiple scattering peak is a sensitive indicator for the bidentate coordinating carbonates in the solid state and solution samples.
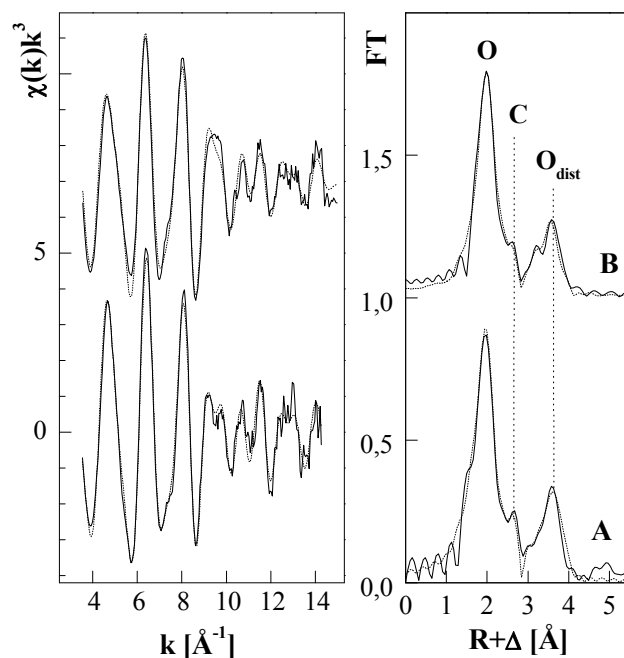
Fig. 2: U L_3-edge k^3-weighted EXAFS data and the Fourier transforms (FT) of $Na_6[U(CO_3)_5] \cdot 12H_2O$ (**A**) and the solution of 0.05 M U(IV) in 1 M $NaHCO_3$ (**B**). Experimental data – solid line, fit results – dotted line.

The data fit of the solution sample reveal within the typical error limits 5 bidentate coordinated carbonate ligands with distances similar to the ones observed in the solid state. This result corroborates the existence of the $[U(CO_3)_5]^{6-}$ anionic species in solution with the same coordination mode as the solid U(IV) carbonate complex. In comparison to the solid, the coordination number of the solution species is slightly reduced to N = 4.7 related with a marginal higher Debye-Waller factor. This may indicate the presence of a negligible amount of $[U(CO_3)_4]^{4-}$.

[1] Hennig, C. et al. (2010) *Dalton Transactions* (2010) **39**, 3774-3750.
[2] Hennig, C. et al. (2008) *Inorg. Chem.* **47**, 1634-1638.
[3] Hennig, C. et al. (2008) *Inorg. Chem.* **47**, 2987-2993.

Fig. 1: $[U(CO_3)_5]^{6-}$ anionic complex obtained from single crystal diffraction.

Complexation of U(VI) with lactate between 7 and 65 °C

R. Steudtner, K. Schmeide

The complexation between uranium(VI) and lactate (Lac) in 0.1 M NaClO$_4$ was studied at pH 3 in the temperature range from 7 to 65 °C. The formation constants of two complexes, UO$_2$Lac$^+$ and UO$_2$(Lac)$_2$, the molar enthalpy and the entropy of complexation were determined by UV-vis and time-resolved laser-induced fluorescence spectroscopy (TRLFS).

EXPERIMENTAL. The complexation experiments were performed at a fixed U(VI) concentration of $5 \cdot 10^{-4}$ M (UV-vis) or $5 \cdot 10^{-5}$ M (TRLFS). The lactate concentration was varied between 0 and 0.1 M (UV-vis) or 0 and 0.01 M (TRLFS). These measurements were carried out at an ionic strength of 0.1 M (NaClO$_4$) at pH 3 and at variable temperatures (7, 25, 45, 65 °C). The pH value was adjusted with HClO$_4$ or NaOH. The UV-vis measurements were performed using a CARY5G UV-vis-NIR Spectrometer (Varian Co.). The spectra were recorded between 375 and 500 nm. The luminescence of U(VI) was measured after excitation with laser pulses at 266 nm (Minilite laser system, Continuum) and an averaged pulse energy of 250 μJ. The emitted fluorescence light was detected using a spectrograph (iHR 550, HORIBA Jobin Yvon) and a ICCD camera (HORIBA Jobin Yvon). The TRLFS spectra were recorded from 450.0 nm to 649.9 nm by accumulating 50 laser pulses using a gate time of 20 μs.

RESULTS. The absorption spectra of the UV-vis spectrophotometric titration of the U(VI) solutions recorded at 25 °C are exemplarily shown in Fig. 1. An increase of the absorbance and a red shift of 10 nm of the absorption maxima in comparison to the bands of the free U(VI) ion indicate the formation of UO$_2^{2+}$-lactate species.

In addition, the TRLFS spectra (Fig. 2) show a strong decrease of the luminescence intensity of U(VI) with increasing ligand concentration at all temperatures studied. This is characteristic for static luminescence quenching due to complex formation. In some experiments, the lifetime of the free U(VI) decreases with increasing ligand concentration caused by an additional dynamic quenching process. The determined lifetimes could be used to calculate the luminescence intensities if no dynamic quenching occurs.

Fig. 2: Luminescence spectra of U(VI) solutions as a function of the lactate concentration ([U(VI)] = $5 \cdot 10^{-5}$ M, I = 0.1 M, pH 3, 25 °C).

For determination of the complex formation constant, the spectra were analyzed with SPECFIT (UV-vis) [1] or by an arithmetic procedure based on the mass action law (TRLFS). The complex formation reaction of U(VI) with lactate can be written in general as:

$$x \, UO_2^{2+} + y \, Lac^- \xrightarrow{\beta_{xy}} (UO_2)_x Lac^{(2x-y)}$$

Table 1 gives a summary of the determined complex formation constants and the calculated molar enthalpies and entropies. The thermodynamic data (enthalpy, entropy) were calculated graphically from the temperature-dependent stability constants by using the van´t Hoff equation in a modified linear form.

The complex formation constants of the 1 : 1 and 1 : 2 complexes increase by 3.9 and 17.4 times, respectively, as the temperature is increased from 7 °C to 65 °C. The complexation of U(VI) with lactate is endothermic (ΔH pos.) and entropy-driven (ΔS pos.). Similar thermodynamics has been observed for the complexation of U(VI) with other carboxylates (acetate, malonate) [2].

Tab. 1: Summary of complex stability constants log β, molar enthalpies and entropies of the identified U(VI) lactate complexes.

Complex	T [°C]	UV-vis log β_{11}	TRLFS log β_{11}	
UO$_2$Lac$^+$	7	2.75 ± 0.09	2.71 ± 0.08	ΔH = 18.7 ± 1.8 kJ·mol^{-1}
	25	2.94 ± 0.08	3.18 ± 0.08	
	45	3.19 ± 0.15	3.29 ± 0.21	ΔS = 119.2 ± 6.1 J·mol^{-1}·K^{-1}
	65	3.34 ± 0.07	3.70 ± 0.13	
		log β_{12}	log β_{12}	
UO$_2$(Lac)$_2$	7	4.40 ± 0.27	–	ΔH = 40.8 ± 7.0 kJ·mol^{-1}
	25	4.85 ± 0.19	–	
	45	5.55 ± 0.20	–	ΔS = 230.4 ± 22.5 J·mol^{-1}·K^{-1}
	65	5.64 ± 0.20	–	

[1] Binstead, R.A. et al. (2005) SPECFIT - Global analysis system, Version 3.0.37, Spectrum Software Associates, Marlborough, U.S.A.
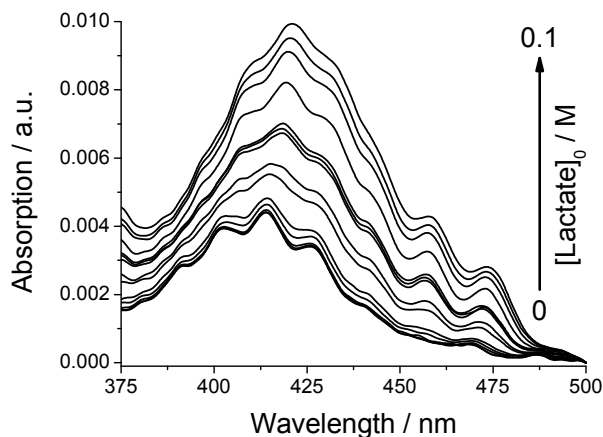[2] Rao, L.F. (2007) *Chem. Soc. Rev.* **36**, 881-892.

Fig. 1: Absorption spectra of U(VI) solutions as a function of the lactate concentration ([U(VI)] = $5 \cdot 10^{-4}$ M, I = 0.1 M, pH 3, 25 °C).
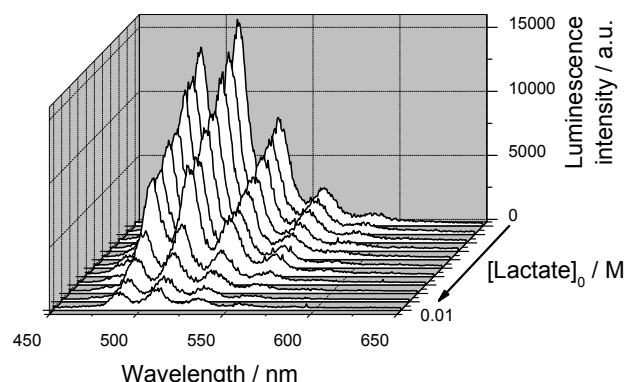
Luminescence quenching in uranyl(VI) complexes: a density functional theory study

S. Tsushima, C. Götz, K. Fahmy

The mechanism of luminescence quenching in uranyl(VI) halide complexes was studied by density functional theory calculations.

The quenching of uranium(VI) luminescence has been a subject of extensive experimental studies. Here, we focus on the uranium(VI) luminescence quenching by halide ions. In previous experimental studies, the quenching was interpreted as an electron transfer process involving the uranium(V)-radical pair. Five examples were examined by DFT calculations: the UO_2^{2+} aquo ion bound to F^-, Cl^-, Br^-, I^-, and methanol, which represent systems of UO_2^{2+} without (F^-) and with quenching (Cl^-, Br^-, I^-, methanol).

COMPUTATIONAL. The calculations on uranium halides were performed in the gas phase using the Gaussian 03 program employing the B3LYP method. The calculations on uranium in the presence of methanol were taken from a previous study [1]. In both halide and methanol systems, the first coordination sphere of U was saturated with solvent molecules. The small-core effective core potential (ECP) and the corresponding basis set as it was previously suggested [2,3] were used on U, I, Br, Cl, F, O, and C. For hydrogen, a 6-311++G** basis was used.

RESULTS. First, we studied the transition energies of the lowest-lying triplet states of four systems (F^-, Cl^-, Br^-, I^-). Vertical transition energy from the $^3B_2$ state to the $^1A_1$ state in the F^- system correspond to 2.12 eV (584 nm) in agreement with the luminescence emission in the presence of F^-. For Cl^- and Br^- systems, the calculated transition energies are red-shifted (1.87 and 1.35 eV, respectively) and, thus, comply with the lack of visible luminescence in the presence of these halides. In the case of I^-, the excited states most likely decays by non-radiative relaxation, because the transition energy is extremely low (0.02 eV). On the other hand, the lowest-lying triplet excited state $^3B_1$ of uranyl iodide has an equilibrium U–I distance of 3.78 Å which is sufficiently long to consider this complex already dissociated. This may explain why uranyl(VI) iodide is unstable especially under the influence of light although several U^{VI}–I compounds have been successfully isolated.

The Mulliken spin density α-β of the triplet states was calculated and is depicted in Fig. 1. There is a clear distinction in the spin density between the system with quenching (I^- and methanol) and without quenching (F^-). In the former systems, the spin density is localized on uranyl and on the ligand (I^- and methanol) to roughly equal extent. For example, in I^- system, the spin density is localized on UO_2 and on I by 0.98 and 1.00, respectively. This shows that in going from the ground state to the triplet excited state there is an electron transfer from iodine to the uranyl entity by nearly 1.0 e, and uranium in the $^3B_1$ state has uranium(V) character. In the F^- system (no quenching), spin density is localized almost exclusively on the uranyl unit (spin density 1.93 on UO_2) indicating that the singlet-to-triplet excitation occurs by excitation within the uranyl unit and the oxidation state remains uranium(VI). The Cl^- and Br^- system stay in between I^- and F^- systems. The spin density in $UO_2Cl(H_2O)_4^+$ is 1.55 and 0.46 for UO_2 and Cl entities, respectively. The spin den-

sity in $UO_2Br(H_2O)_4^+$ is 1.27 and 0.74 for UO_2 and Br entities, respectively. This trend may be predictable from the electronegativity of the halide ions, but the extension to organic compounds, such as methanol, requires a more detailed quantum chemical description as performed here based on DFT. In the methanol system, uranium(VI) is reduced to uranium(V) in the triplet state, and the triplet state is energetically highly stabilized by hydrogen atom abstraction and does not transfer back to the ground state. Therefore, the oxidation state of uranium remains V in the methanol system which is in agreement with experimental data.

The presented data confirm the quenching mechanism proposed by Burrows involving the uranium(V)-radical pair, $[UO_2^+X^\bullet]$ [4]. In combination with the previous DFT investigation on uranium(VI) photoreduction by alcohol [1], our results underscore that the analysis of the lowest-lying triplet state obtained by the single-determinant DFT method leads to a realistic representation of the state of interest. Obviously, the DFT method appears promising for exploring the uranium(VI) photochemistry.
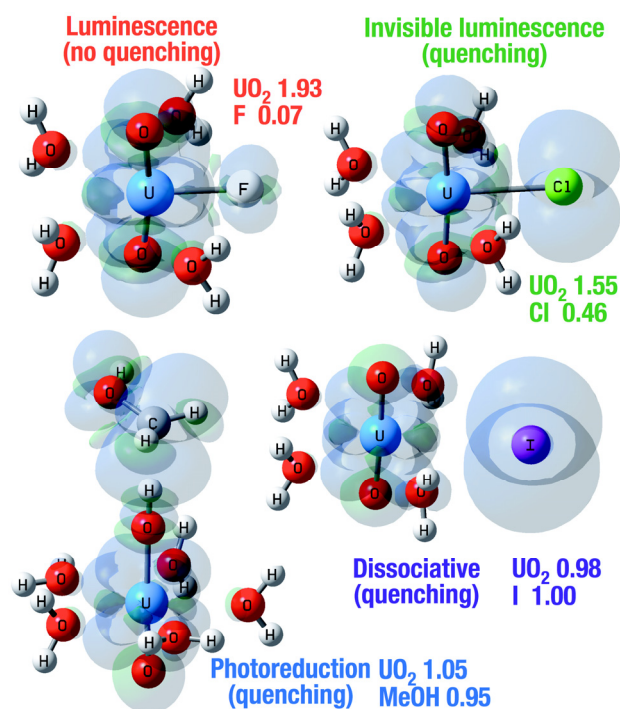
Fig. 1: Geometries and Mulliken spin densities α-β of the lowest-lying triplet states of UO_2^{2+} aquo ion associated with F^-, Cl^-, I^-, and methanol obtained by DFT calculations. Spin densities are given in numbers and in contour plot (isovalue of the plot is 0.0004 a.u.).

[1] Tsushima, S. (2009) *Inorg. Chem.* **48**, 4856-4862.
[2] Kuechle, W. et al. (1994) *J. Chem. Phys.* **100**, 7535-7542.
[3] Bergner, A. et al. (1993) *Mol. Phys.* **80**, 1431-1441.
[4] Burrows, H. D. (1990) *Inorg. Chem.* **29**, 1549-1554.

Spectroscopic confirmation and EXAFS structural characterization of thermodynamically predicted U(VI)-tartrate complexes: combining Factor Analysis with Landweber inversion method

A. Rossberg, C. Lucks, S. Tsushima, A. C. Scheinost

Common methods like the EXAFS shell fitting approach approximate the radial pair distribution function (PDF) by Gaussians functions. The Landweber iteration enables the inversion of the EXAFS equation solely on the basis of the FEFF scattering theory, hence, allows the direct calculation of the PDF without predefined assumptions about its shape [1]. Here we use the Landweber iteration to ascertain the structure of the mono-, bi- and trinuclear U(VI)-tartaric acid complexes which have been previously predicted by thermodynamic methods [2].

EXPERIMENTAL. Eight samples were prepared with 0.5 M U(VI) and 250 mM tartaric acid (tar) between pH 0.5 and pH 7.0. The X-ray absorption spectra were measured at room temperature at the ROBL Beamline.

RESULTS. The relative concentrations and the spectra of four complexes (Fig. 1a, I-IV) are isolated from the spectral mixtures by factor analysis [3]. For the Landweber iteration the theoretical U–O and U–U scattering functions are calculated in dependence of the radial distance r with FEFF 8.2. We used a step size of $\Delta r = 0.01$ Å. For the estimation of the necessary number of Landweber, iterations the L-curve concept are used [1]. The energy threshold shift ΔE_0 is determined by the Landweber iteration [1]. For all complexes, the calculated PDF's (Fig. 1c) yield a good reproduction of the isolated EXAFS spectra (Fig. 1a) and the corresponding Fourier transforms (Fig. 1b). All complexes show an asymmetric PDF of the equatorial O atoms (O_{eq}). Note that the U–O_{eq} PDF of the well known complex I, $UO_2(H_2O)_5^{2+}$, is also slightly asymmetric as observed here for the first time. In the case of complex III and IV the maximum of the PDF of the axial O atoms (O_{ax}) is shifted to higher distances (Fig. 1c). In addition, complex III and IV show a U–U interaction at 3.95 Å and at 3.81 Å (Fig. 1b). According to density functional theory (DFT) calculations (Fig. 2), the longer U–U distance can be explained by two U atoms which are bridged by two O atoms and the shorter one by three U atoms symmetrically bridged by three O atoms, hence, complex III is a dimeric and complex IV is a trimeric complex [4,5]. For the trimer, the DFT calculation predicts also the presence of a central μ_3-O atom in a radial U–O distance of 2.22 Å (Fig. 2, right) [4,5]. The presence of this μ_3-O is visible by the unusual asymmetry at the left side of the O_{eq} PDF (Fig. 1c). While complex II shows no special features, except for small contributions of C and O atoms beyond the first two oxygen shells, the U–O_{eq} PDF is strongly deformed (Fig. 1c). This deformation points to a strong distortion in the equatorial plane of U(VI). The structural reason for this distortion is recently investigated by DFT calculations. For complex II, no U–U interaction is observed, hence, this complex is in line with the thermodynamically predicted monomer.

CONCLUSIONS. We demonstrated that the Landweber iteration is well suited to derive the coordination structure of such complexes with asymmetric PDF shape. Depending on the pH, some of the complexes coexist and factor
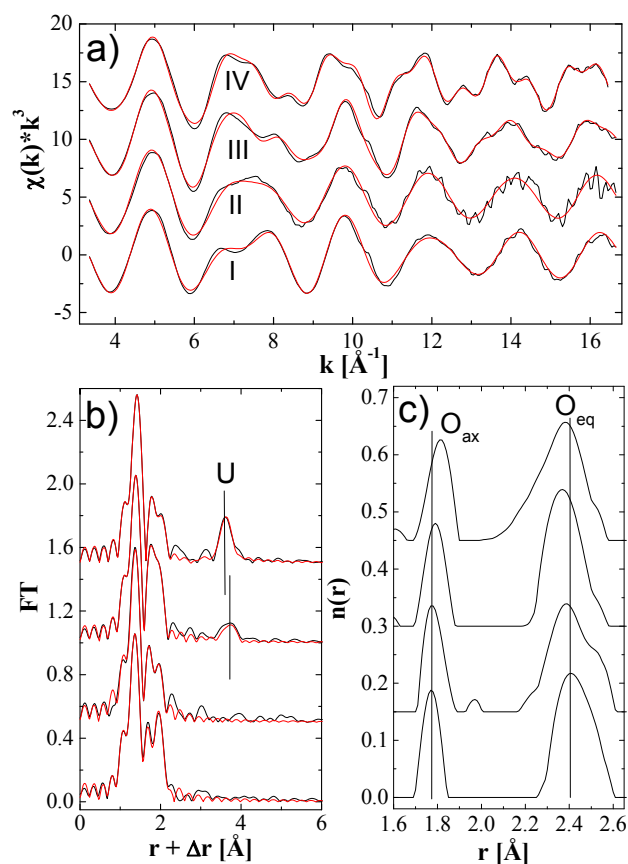
Fig. 1: a) EXAFS spectra of complexes I-IV isolated by factor analysis, b) corresponding Fourier transforms, c) U–O PDF's (U–U PDF's are not shown). Reproduction of the spectra by the calculated PDF's (red).
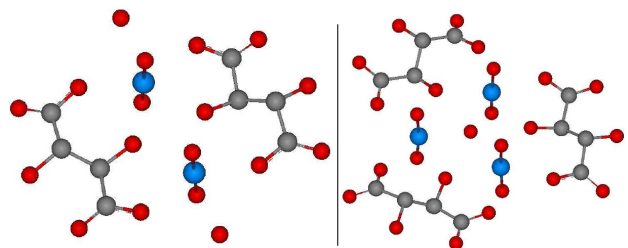
Fig. 2: DFT calculated structure of the dimeric (left) and the trimeric (right) U(VI)-tar complex. Blue – uranium, red – oxygen, grey – carbon. Hydrogen atoms are not shown.

analysis had to be applied to derive the spectra of the pure species before running the Landweber iteration.

[1] Rossberg, A. et al. (2010) *J. Synchrotron Radiat.* **11**, 280-288.
[2] Rajan, K. S. et al. (1964) *J. Inorg. Nucl. Chem.* **26**, 1927-1944.
[3] Rossberg, A., et al. (2003) *Anal. Bioanal. Chem.* **376**, 631-638.
[4] Tsushima, S. (2007) *Inorg. Chem.* **35**, 784-787.
[5] Rossberg, A. et al. (2010) *Report FZD-530*, p. 58.

Identification of photoreactive species of uranyl(VI) oxalate

S. Tsushima, V. Brendler, K. Fahmy

We found that the photoreactive uranyl(VI) oxalate species are trioxalate (1 : 3) and dimeric species (2 : 5).

In previous studies, we demonstrated that DFT calculations are capable of predicting photochemical properties of uranyl(VI) organic and inorganic complexes [1,2]. Here we revisited a classical problem of photochemical decomposition of uranyl(VI) oxalate.

THEORETICAL. All calculations were performed in the aqueous phase using the Gaussian 03 program employing the B3LYP method through the use of the conductor-like polarizable continuum model. The energy-consistent small-core effective core potential and the corresponding basis set as it was suggested in [3,4] were used for U, O, and C. For hydrogen, 6-311++G** basis was used.

RESULTS. We first studied the most stable structures of uranyl(VI) oxalate 1 : 1, 1 : 2, 1 : 3, and 2 : 5 complexes. For 1 : 1 and 1 : 2 complexes, it was found that chelate ring structures are most stable. In 1 : 3 and 2 : 5 complexes, each uranium has two chelate binding oxalate and one unidentately bound oxalate.

Next, we studied the photoreactivities of these complexes starting with 1 : 1 and 1 : 2 complexes. We found some of the 1 : 1 and 1 : 2 isomers are photochemically reactive. None of the photoreactive species, however, exhibits a ground state geometry, and the energy minimum of 1 : 1 and 1 : 2 were found to be photochemically unreactive. This implies that both uranyl(VI) oxalate 1 : 1 and 1 : 2 complexes are not photoreactive in practice, strongly arguing against the previously proposed photochemical reaction mechanism involving uranyl(VI) dioxalate by Brits et al. [5].

We have studied the photoreactivities of the uranyl(VI) oxalate 1 : 3 and 2 : 5 complexes. In the most stable structures of 1 : 3 and 2 : 5 complexes, there are one and two unidentately coordinated oxalate ligands, respectively. In the triplet states of these complexes, one unidentate oxalate was found to become decarboxylated accompanied by the reduction of U(VI) to U(V). In Fig. 1, the structure and major interatomic distances of the lowest lying triplet
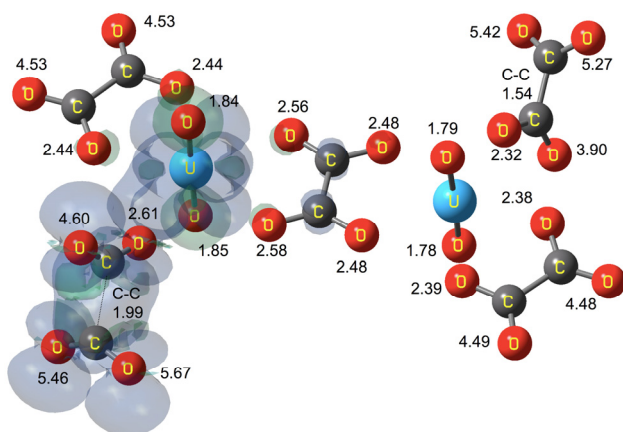
state of the 2 : 5 complex are given. The spin density of the complex is also shown in Fig. 1 which indicates a charge transfer from one of the unidentate oxalate to uranium. The calculated results demonstrate that both the 1 : 3 and 2 : 5 complexes are photochemically reactive species. Our results are consistent with the previous work by Görller-Walrand and Servaes who proposed a photochemical reaction mechanism involving a 2 : 5 complex although their study was performed in acetone and not in aqueous solution [6].

The previous studies on photochemistry of uranyl(VI) oxalate by Brits et al. [5] proposed the 1 : 2 complex as the main photoreactive species. From the $\log \beta_{25}$ value at I = 3.0 M $NaClO_4$ of Havel et al. [7], we have estimated the equilibrium constant of 2 : 5 complex at infinite dilution using two different approaches which gave $\log \beta^0$ values of -2.86 ± 0.76 and -2.16 ± 0.71. Computations with the geochemical speciation code EQ3/6 utilizing the average of the two $\log \beta^0$ (equalling -2.51) result in the uranyl(VI) oxalate speciation diagrams under the experimental conditions of Brits et al. (Fig. 2). In the experiments of Brits et al. which were done at pH 4.5 with $[UO_2^{2+}] = 4.0$ mM and $[ox^{2-}]/[UO_2^{2+}] = 0.0$ to 5.0, the 2 : 5 complex dominates for $2.8 > [ox^{2-}]/[UO_2^{2+}] > 2.3$ whereas the 1 : 3 complex becomes the dominating species at $[ox^{2-}]/[UO_2^{2+}] > 2.8$. Their claim that the 1 : 2 complex is the sole photoreactive species is, therefore, not justified, while their experimental data are consistent with our calculations suggesting the 1 : 3 and 2 : 5 complex as the photoreactive and the 1 : 2 complex as a non-photoreactive species.

Fig. 1: The structure of the lowest-lying triplet state of uranyl(VI) oxalate 2 : 5 complex. The distances are those between oxygen and the closest uranium (in Ångström) unless specified otherwise. The spin density is also given graphically with the isovalue of the plot of 0.0004 a.u.
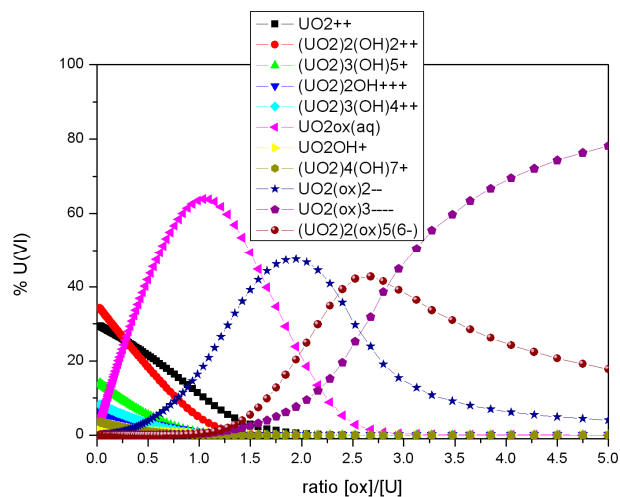
Fig. 2: Aqueous uranyl(VI) oxalate speciation under the experimental conditions of Brits et al. in reference [3].

[1] Tsushima, S. (2009) *Inorg. Chem.* **11**, 4856-4862.
[2] Tsushima, S. et al. (2010) *Chem. Eur. J.* **16**, 8029-8033.
[3] Kuechle, W. et al. (1994) *J. Chem. Phys.* **100**, 7535-7542.
[4] Bergner, A. et al. (1993) *Mol. Phys.* **80**, 1431-1441.
[5] Brits, A. G. et al. (1977) *J. Inorg. Nucl. Chem.* **39**, 1195-1199.
[6] Görller-Walrand, C. et al. (2009) *Helv. Chim. Acta* **92**, 2304-2312.
[7] Havel, J. et al. (2002) *Polyhedron* **21**, 1411-1420.

Structural investigation of aqueous, oligomeric uranium(VI) complexes with alpha-hydroxycarboxylic acids

C. Lucks, A. Rossberg, A. C. Scheinost

Using EXAFS and UV-vis spectroscopy, we have performed a systematic investigation of the speciation and structure of U(VI) complexes with lactic (lac), malic (mal), tartaric (tar), and citric (cit) acid. All ligands show trimer formation at near neutral pH. The presence of a second carboxylic group promotes the formation of dimeric complexes at slightly acidic pH.

EXPERIMENTAL. Solutions of 50 mM U(VI) in 0.25 mM solution of each ligand were prepared. After adjusting the pH to 7, a pH titration experiment was performed by adding small volumes of concentrated perchloric acid. UV-vis spectra were recorded simultaneously on a Cary 5G spectrophotometer in the spectral range from 700 to 350 nm. Uranium L_{III}-edge measurements were performed on selected samples in transmission mode at the Rossendorf Beamline BM20 (ROBL), ESRF.

RESULTS. The UV-vis pH titration data were analyzed using iterative target transform factor analyses (ITFA) [1] to identify the single components in the systems investigated. Figure 1 shows the UV-vis single component spectra of the oligomeric species. All investigated systems show a trimeric species at around pH 7 with a strong shift of the maximum from 414 nm (hydrated uranyl ion) to 440 nm and a ten times higher absorption. Except for the lactate system, all systems show in addition the formation of dimeric species around pH 3.5 with a strong shift of the maximum to 433-435 nm and a five times higher absorption. Because lactate does not form a dimer it can be concluded that a second carboxylic group is needed to stabilize the dimer. At more acidic pH, monomeric species co-exist with the dimer and the hydrated uranyl ion. These monomeric species (not shown here) give a slight shift of the maximum to 419-421 nm and a two times higher absorption.

Both dimers and trimers were accessible as nearly pure species at pH 3.5 and pH 7, respectively. Thus, the recorded EXAFS spectra (Fig. 2) represent the pure components.

The EXAFS spectra of the dimeric and trimeric species of the different systems are similar. For the trimeric complex
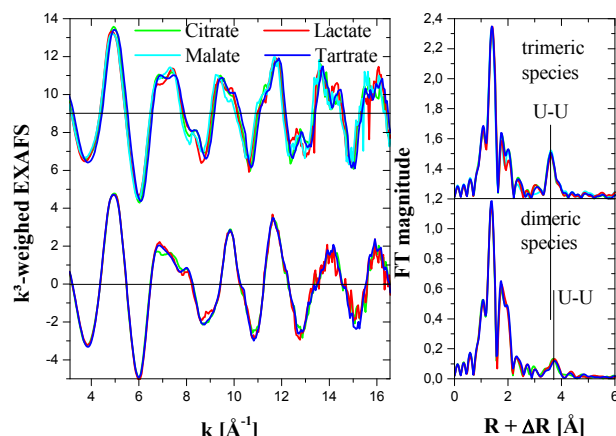
Fig. 3: k³-weighed EXAFS spectra and calculated Fourier transforms of the measured oligomeric species.

of tartaric acid, $(UO_2)_3(\mu_3\text{-}O)(H_{-1}tar)_3^{5-}$, it was shown previously by applying the Landweber iteration that a central oxygen atom (μ_3-O) is present [2]. Because of the similarity of the recorded EXAFS-spectra, one can deduce that the other complexes have also such a central oxygen atom.

Tab. 1 shows the main structural parameters that were calculated using the shell-fit procedure.

Tab. 1: EXAFS structural parameters for the dimeric (top) and trimeric (bottom) complexes.

Path	Tartrate R	Tartrate DW	Malate R	Malate DW	Citrate R	Citrate DW	Lactate R	Lactate DW	Average *M*	Average *SD*
O_{ax}	1.787	0.0012	1.789	0.0015	1.785	0.0014	n.a.	n.a.	*1.787*	*0.002*
O_{eq}	2.364	0.0056	2.356	0.0056	2.364	0.0062	n.a.	n.a.	*2.361*	*0.005*
C	3.28	0.0057	3.33	0.0090	3.39	0.0163	n.a.	n.a.	*3.33*	*0.06*
U	3.928	0.0063	3.932	0.0074	3.907	0.0074	n.a.	n.a.	*3.922*	*0.013*

Path	Tartrate R	Tartrate DW	Malate R	Malate DW	Citrate R	Citrate DW	Lactate R	Lactate DW	Average *M*	Average *SD*
O_{ax}	1.802	0.0014	1.807	0.0014	1.806	0.0016	1.796	0.0015	*1.803*	*0.005*
O_{cent}	2.205	0.0044	2.194	0.0039	2.205	0.0039	2.200	0.0041	*2.201*	*0.006*
O_{eq}	2.375	0.0071	2.363	0.0105	2.374	0.0069	2.382	0.0088	*2.373*	*0.008*
C	3.31	0.0116	3.36	0.0133	3.38	0.0155	3.31	0.0084	*3.34*	*0.03*
U	3.807	0.0050	3.816	0.0063	3.801	0.0052	3.816	0.0047	*3.810*	*0.007*
$O_{ax,dis}$	4.33	0.0061	4.37	0.0052	4.32	0.0069	4.32	0.0084	*4.33*	*0.02*

DW: Debye-Waller factor, *M*: Mean distance, *SD*: Standard deviation.

The distance of the equatorial oxygen in case of dimer (2.36 Å) and trimer (2.37 Å) formation is significantly shorter than that of the hydrated uranyl ion (2.40 Å). This is indicative for the formation of a tridentate chelate or bidentate chelate in case of lactic acid. Uranium is visible at a longer distance in case of dimer formation (3.92 Å) than in case of trimer formation (3.81 Å). This is in agreement with results of DFT calculation of dimeric and trimeric hydrolysis species in aqueous phase [3] that show a U–U distance of 3.87 Å (dimer) and 3.83 Å (trimer), respectively.

[1] Rossberg, A., et al. (2003) *Anal. Bioanal. Chem.* **376**, 631-638.
[2] Rossberg, A., et al. (2009) *Report FZD-530*, p. 58.
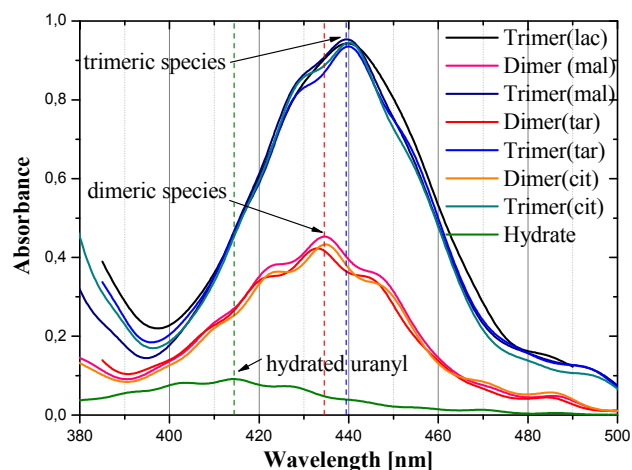[3] Tsushima, S. (2007) *Inorg. Chem.* **35**, 784-787.

Fig. 2: ITFA extracted UV-vis single component spectra of the systems investigated. The arrows and dashed lines indicate the absorption maxima of the individual species.

Spectroscopic characterization of the ternary U(VI) carbonato humate complex by cryo-TRLFS and ATR FT-IR spectroscopy

R. Steudtner, S. Sachs, K. Schmeide, K. Müller

For the first time, the complexation between U(VI) and humic acid (HA) in the presence of carbonate was studied applying time-resolved laser-induced fluorescence spectroscopy at low temperature (cryo-TRLFS) and attenuated total reflection Fourier-transform infrared (ATR FT-IR) spectroscopy. The formation of a ternary U(VI) carbonato humate complex of the type $UO_2(CO_3)_2HA(II)^{4-}$ was identified and a complex stability constant was determined.

EXPERIMENTAL. Complexation experiments were performed at a fixed U(VI) concentration of $1 \cdot 10^{-5}$ M (cryo-TRLFS) or $1 \cdot 10^{-3}$ M (ATR FT-IR). The HA concentration was varied between 0 and 100 mg/L (cryo-TRLFS) or kept constant at 1 g/L (ATR FT-IR). The measurements were carried out at an ionic strength of 0.1 M. The pH values of the solutions were adjusted to pH 8.5 (cryo-TRLFS) or titrated between pH 10 and 2 (ATR FT-IR) using diluted $HClO_4$ and NaOH solutions. For further experimental details see [1] for cryo-TRLFS and [2] for ATR FT-IR.

RESULTS. The luminescence spectra of U(VI) as a function of the HA concentration (Fig. 1) show a decrease of the U(VI) luminescence intensity with increasing HA concentration. No shift in the peak maxima of the fluorescence emission bands is detected. At low temperature ($T = 153$ K), fluorescence quenching effects are suppressed [3]. Thus, the decrease in the U(VI) luminescence intensity points to a complexation between $UO_2(CO_3)_3^{4-}$ and HA forming a U(VI) carbonato humate species. The U(VI) humate complex shows no individual fluorescence signal as already observed for the binary $UO_2HA(II)$ complex [4] and the ternary $UO_2(OH)HA(I)$ complex [5] at room temperature.

Based on the measured fluorescence spectra, the complex stability constant of the U(VI) carbonato humate complex is calculated applying the data analysis program SPECFIT [6,7]. The complex formation reaction of U(VI) carbonato humate complex can be written in general as:

$$UO_2^{2+} + 2\,CO_3^{2-} + HA(II) \rightarrow UO_2(CO_3)_2HA(II)^{4-}$$
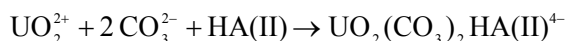
The complex stability constant for the $UO_2(CO_3)_2HA(II)^{4-}$
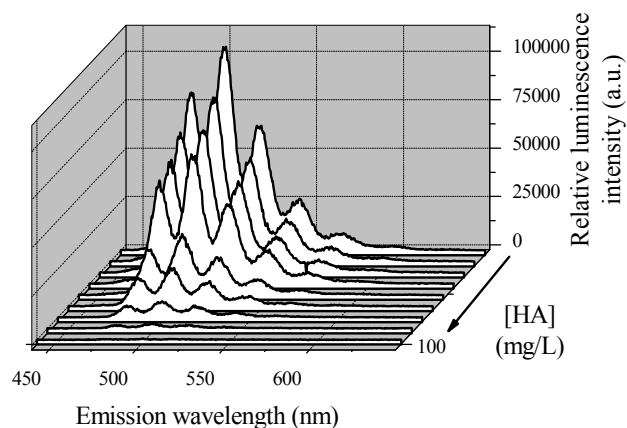
Fig. 1: U(VI) luminescence spectra ($t = t_0$) as a function of the HA concentration at pH 8.5 ($[U(VI)]_{tot} = 1 \cdot 10^{-5}$ M, $[HA]_{tot} = 0$-100 mg/L, 0.1 M NaClO$_4$, $T = 153$ K, $pCO_2 = 10^{-3.5}$ atm).
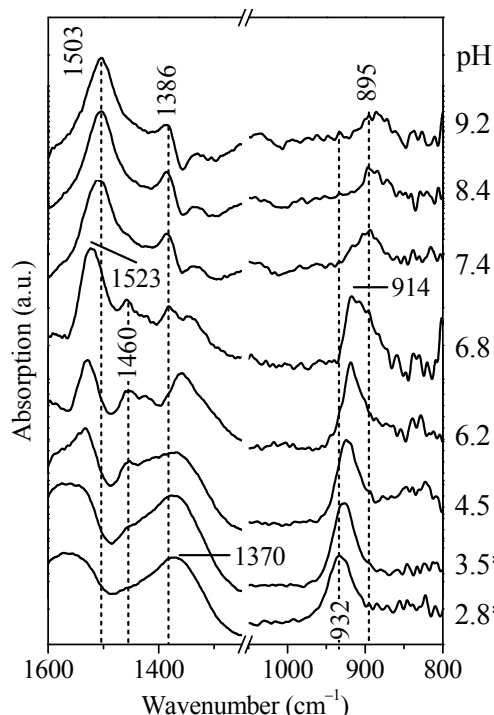
Fig. 2: Infrared spectra of U(VI) humate solutions as a function of the pH value ($[U(VI)] = 1$ mM, $[HA]_{tot} = 1$ g/L, 0.1 M NaCl, $T = 296$ K, $pCO_2 = 10^{-3.5}$ atm). *Spectra of suspended precipitates.

complex is calculated with $\log \beta_{I = 0.1\,M} = 24.57 \pm 0.17$ [1]. In addition, IR spectroscopy was used to validate the complex formation constant of the ternary U(VI) carbonato humate complex. The results of the spectrophotometric titrations of aqueous solutions of U(VI) in the presence of HA at ambient atmosphere are shown in Fig. 2.

From the variations in the IR spectra as a function of pH, stability constants for the U(VI) humate complexation were calculated. The obtained complex stability constant of $\log \beta_{I = 0.1\,M} = 24.47 \pm 0.70$ for the $UO_2(CO_3)_2HA(II)^{4-}$ complex validated the constant measured by cryo-TRLFS. In addition, the formation constants $\log \beta$ for aqueous $UO_2HA(II)$ and $UO_2(OH)HA(I)$ at an ionic strength of 0.1 M were calculated with 6.70 ± 0.25 and 15.14 ± 0.25, respectively. These values are in very good agreement with data determined by TRLFS [4,5] and by solubility measurements [8].

This study demonstrates the suitability of the cryo-TRLFS and of the ATR FT-IR method as new alternative techniques for the determination of complex formation constants. They thus promote an expansion of the existing thermodynamic data base.

[1] Steudtner, R. et al. (2011) *Radiochim. Acta*, submitted.
[2] Steudtner, R. et al. (2011) *Environ. Sci. Technol.*, submitted.
[3] Wang, Z. et al. (2008) *Radiochim. Acta* **96**, 591-598.
[4] Pompe, S. et al. (2000) *Radiochim. Acta* **88**, 553-558.
[5] Sachs, S. et al. (2007) *Radiochim. Acta* **95**, 103-110.
[6] Gampp, H. et al. (1985) *Talanta* **32**, 257-264.
[7] Binstead, R.A. et al. (2005) SPECFIT - Global analysis system, Version 3.0.37, Spectrum Software Associates, Marlborough, U.S.A.
[8] Pashalidis, I. et al. (2007) *J. Radioanal. Nucl. Chem.* **273**, 315-322.

Actinide(IV) oxyhydroxide colloids *vs.* actinide(IV)-silica colloids: their relevance for environmental conditions

H. Zänker, C. Hennig, S. Weiß

The likelihood of An(IV) oxyhydroxide colloid and An(IV)-silica colloid formation under the conditions of environmental waters is compared. It is concluded that the formation of An(IV)-silica colloids may well be more relevant in nature than the formation of An(IV)-oxyhydroxide colloids.

HITHERTO LABORATORY EXPERIMENTS. It is well known that in ultrapure water at very low pH the solubility of the tetravalent actinides is controlled by the extremely little soluble crystalline actinide dioxides, $An(IV)O_2(cr)$ [1]. At pH values above the onset of An^{4+} hydrolysis, amorphous actinide oxyhydroxide becomes solubility-limiting [1, 2]. Therefore, it has been emphasized in the literature that performance assessment calculations on the long-time behavior of actinides in the environment should not take into account the extremely low solubility resulting from the thermodynamic data of the crystalline An dioxides but should rather be based on the higher solubility values of amorphous An(IV) oxyhydroxide [3]. However, reliable concentration values of the dissolved actinides in the near-neutral range, $[An(OH)_4(aq)]$, were only obtained in solubility experiments if actinide colloids had thoroughly been removed from solution. If colloid removal (ultrafiltration, ultracentrifugation) is omitted, total actinide concentrations, $[An(IV)]_{tot}$, higher than those based on true solubility, $[An(OH)_4(aq)]$, by a factor of about 100 are found due to the presence of An(IV) colloids. Interestingly, the colloids of amorphous actinide oxyhydroxides responsible for these increased actinide(IV) concentrations seem to be in equilibrium with the truly dissolved actinide species [2-4]. They are hydrophilic and may be considered as large charged aqueous species that are comparable with ionic aqueous species. Altmaier et al. [3] determined equilibrium colloid saturation concentrations of $\log [Th(IV)]_{coll} = -6.3 \pm 0.5$ and $\log [Pu(IV)]_{coll} = -7.9 \pm 1.0$, i.e. these colloids are able to transform the "immobile" tetravalent actinides into an even more mobile form.

HITHERTO FIELD EXPERIENCE. Repeatedly there have been hypotheses that actinide behavior in geochemical field experiments or site-specific simulation experiments was influenced by actinide(IV) colloids. Efurd et al. [5] stated that Pu(IV) colloids may have interfered in their Pu solubility experiments with Yucca Mountain groundwater. Lieser et al. [6] found Th(IV), which had been added as mononuclear ions to Gorleben groundwaters, in a colloid-borne form. They attributed this to adsorption of Th onto colloids the main constituent of which was supposed to be silicic acid. In boom clay pore water, Delecaut et al. [7] found U concentrations three orders of magnitude higher than the literature data for U(IV) solubility. They interpreted this by the presence of U(IV) colloids.

A NEW TYPE OF ACTINIDE(IV) COLLOIDS. Some of the field experiment results are difficult to understand based solely on the above-mentioned equilibrium "saturation concentrations" of An(IV) oxyhydroxide colloids stated by Altmaier et al. [3]. In [8], we describe a type of An(IV) colloids which might explain this discrepancy: actinide(IV)-silica colloids. These colloids are formed in near-neutral solutions; concentrations of colloid-borne U(IV) of up to 10^{-3} M were observed. This is a U(IV) concentration of several orders of magnitude higher than any concentration of truly dissolved or colloidally suspended waterborne tetravalent actinide species hitherto reported for the near-neutral pH range. The vast majority of the particles had a size of < 20 nm. They were stable in the water-borne state over years. The internal structure of the particles was characterized by U–O–Si bonds that increasingly replace the U–O–U bonds of the uranium oxyhydroxide structure with increasing silicate concentration. We also found similar silicate-containing colloids for tetravalent thorium (publication in preparation).

GEOCHEMICAL IMPLICATIONS. So far, only the formation of actinide(IV) oxyhydroxide colloids in environmental waters has been discussed in the literature. How likely is it that actinide(IV)-silica colloids are generated in environmental scenarios? Both types of colloids have solely been observed in the laboratory till now. It is obvious that An(IV) oxyhydroxide colloids are the only type of colloids that can be formed in ultrapure water. However, real environmental waters are not ultrapure but contain, for instance, silicate concentrations of, roughly, 10^{-5} M to 10^{-3} M. Therefore, an influence of silicate should be surmised and a competition between the formation processes of the two types of colloids can be assumed. Note that the uranium and thorium concentrations of natural waters are in the range of only 10^{-10} M to 10^{-8} M which is much less than the above-mentioned silicate concentrations. Thus, it can not be ruled out that the formation of An(IV)-silica colloids is even much more probable than the formation of An(IV) oxyhydroxide colloids in natural waters.

From their studies on 10^{-10} M to 10^{-8} M Th(IV) traces added to real groundwaters Lieser et al. already concluded that "reaction of Th with silicate is by many orders of magnitude preferred over the interaction of the hydroxo complexes of Th with each other" [6]. Therefore,

(i) there is urgent need to investigate the An(IV)-silica colloids as thoroughly as the An(IV) oxyhydroxide colloids have already been investigated (cf. [1-4]), and

(ii) the assessment of actinide behavior in nature should take the possible existence of An(IV)-silica colloids, which are able to reach much higher concentrations than the An(IV) oxyhydroxide colloids, into account.

[1] Neck, V. et al. (2001) *Radiochim. Acta* **89**, 1-16.
[2] Neck, V. et al. (2002) *Radiochim. Acta* **90**, 485-494.
[3] Altmaier, M. (2004) *Radiochim. Acta* **92**, 537-543.
[4] Bitea, C. et al. (2003) *Colloids Surf. A* **217**, 63-70.
[5] Efurd, D. W. et al. (1998) *Environ. Sci. Technol.* **32**, 3893-3900.
[6] Lieser, K.H. et al.(1992) *Radiochim. Acta* **56**, 37-45.
[7] Delecaut, G. et al. (2004) *Radiochim. Acta* **92**, 545-550.
[8] Dreissig, I. et al. (2011) *Geochim. Cosmochim. Acta* **75**, 352-367.

Uranium(VI) sorption onto colloids produced by weathering: influence of complexants

H. Zänker, S. Weiß, T. Gensch

Colloids generated by the weathering of rock can adsorb significant amounts of uranyl(VI) which transforms the uranium into a colloid-borne form. Background solutes significantly reduce this effect if they form strong dissolved uranyl complexes which compete with surface complexation of U(VI) at the colloid interfaces.

EXPERIMENTAL. The weathering of phyllite from an abandoned uranium mine (for the chemical and mineralogical composition see [1]) was simulated. The phyllite was jaw-crushed, sieved and suspended in MilliQ water (40 g/L). By centrifugation and re-suspension, the material was "prewashed". For the "weathering" the suspension was shaken for 90 h during which period the colloids were formed (oxic conditions, pH 8.4). Thus, the ground phyllite was used as a "colloid generator". The bulk of the ground phyllite was separated from the colloids by centrifugation at 1000×g (particle size cut-off about 100 nm; cf. [1]). The centrifugate (supernatant; separation by pipetting) was used as the colloidal suspension for the sorption experiments. A uranium concentration of 50 µg/L and a series of pH values between 4.7 and 8.2 ($HClO_4$) were adjusted. The following background solutes were added: $NaHCO_3$, Na_2SO_4, $CaCO_3$ and $MgCO_3$. For three days, the samples were allowed to equilibrate. Finally, the major fraction of the colloids was removed by ultracentrifugation (170,000×g, separation by pipetting again). The maximum hydrodynamic diameter of the particles still present in the supernatant after this centrifugation is about 10 nm (cf. [2]). The supernatant solutions from the 1,000×g and 170,000×g centrifugations were analyzed by ICP-MS and/or AAS.

RESULTS. Information on the inventories of colloids of the size class 10 to 100 nm and the chemical composition of the colloids of this size class can be derived from the differences of the ICP-MS/AAS results after the 1,000×g and the 170,000×g centrifugations, $c_{1,000×g} − c_{170,000×g}$. It follows from these differences that the colloidal solution produced by the weathering of the phyllite contained a total of > 10 mg/L of colloids of the size class 10 to 100 nm. The colloids contained significant amounts of the secondary mineral ferrihydrite which is a very good sor-

Fig. 2: Fraction of centrifugable (colloid-borne) U as f(pH) in the presence of colloids from the "colloid generator" with/without the addition of background Na_2SO_4.

Fig. 3: Fraction of centrifugable (colloid-borne) U as f(pH) in the presence of colloids from the "colloid generator" with/without the addition of different alkaline and alkaline earth carbonates.

bent of U(VI).

The figures demonstrate the adsorption of uranium(VI) onto the colloids and the influence of background solutes on this adsorption. They show the colloid-borne U fraction (percentage of the total U) as determined by the differences $c_{1,000×g} − c_{170,000×g}$ for uranium in dependence on pH. Note that U(VI) is truly dissolved in these simulated natural waters in the absence of colloids [2]. However, the presence of the colloids makes much of the uranium colloid-borne at near-neutral pH.

CONCLUSIONS. Colloids produced by the weathering of phyllite are able to transfer large fractions of uranium(VI) into a colloid-borne form in the pH region of 5.0 to 8.5. Background solutes can significantly reduce this effect. This is due to the formation of dissolved uranyl complexes such as $UO_2(CO_3)_2^{2−}$, $UO_2(SO_4)^0(aq)$, $Ca_2UO_2(CO_3)_3^0(aq)$ etc. which show little adsorption and compete with the surface complexation of U(VI) at the colloid interfaces (see also [3]).

[1] Zänker, H. et al. (2006) *Aquatic Geochem.* **12**, 299-325.
[2] Zänker, H. et al. (2007) *Report FZD-459*, p. 62.
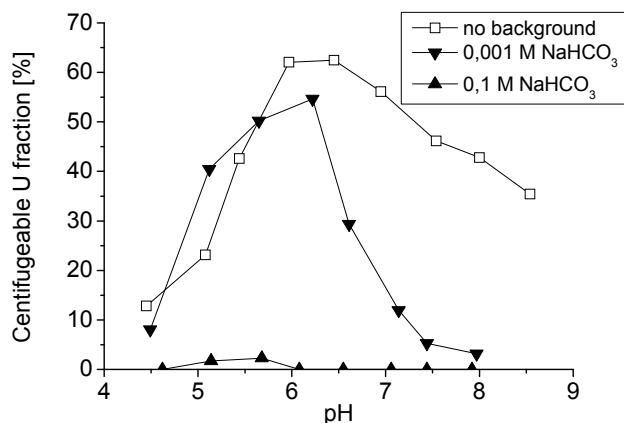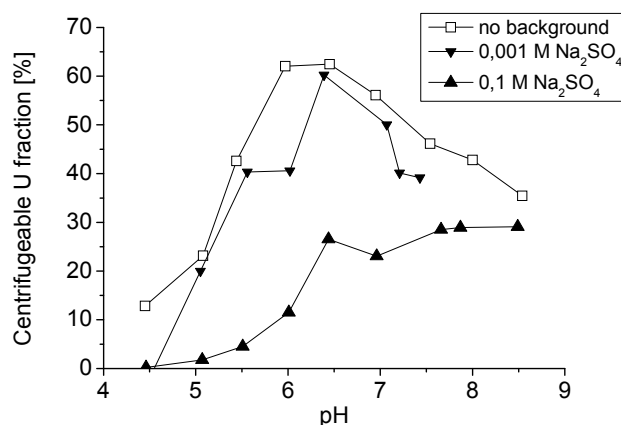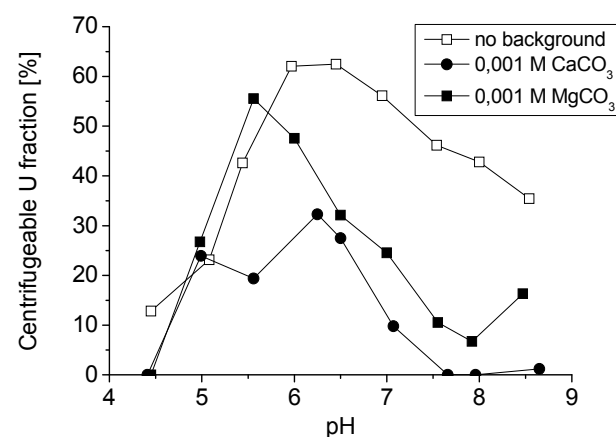[3] Fox, P.M. et al. (2006) *Geochim. Cosmochim. Acta* **70**, 1379-1389.

Fig. 1: Fraction of centrifugable (colloid-borne) U as f(pH) in the presence of colloids from the "colloid generator" with/without the addition of background $NaHCO_3$.

EXAFS investigations on uranium(IV)-silica colloids

S. Weiss, C. Hennig, I. Dreissig, H. Zänker

U(IV) forms mixed colloids with silicate by simultaneous precipitation at neutral pH [1]. The chemical composition of these colloids depends on the initial U(IV) und silicate concentrations in solution. Silicate stabilizes such colloidal U(IV) suspensions at neutral pH values. The question arises if and how the structure of the colloids might be modified. Uranium L_3 edge EXAFS spectroscopy was applied to gain information on the next-neighbor arrangement of uranium. We found that the characteristic U–O–U bonds of U(IV)-oxyhydroxide were replaced by U–O–Si bonds.

EXPERIMENTAL. The samples are listed in Tab. 1. Sample A is a U(IV)-oxyhydroxyde without silica. This sample was prepared according to a procedure described in [2] and measured as an aqueous colloidal suspension at room temperature. Samples B and C are U(IV)-silica colloids with different U/Si ratios. These samples were formed by mixing a solution of 1 mM U(IV) with 1-3 mM of tetramethyl orthosilicate (TMOS) according to a procedure described in [1] and flocculated at pH 4. The wet paste was stored in air-tight double-sealed cuvettes and measured by EXAFS spectroscopy at room temperature. The molar Si/U ratios of the formed solids were estimated by ultrafiltration. Coffinite, $USiO_4$, was used as a reference (sample D). It was synthesized by hydrothermal reaction [3] and measured as a dry powder at 15 K. The EXAFS spectra were collected in the transmission mode at the Rossendorf Beamline (ESRF, Grenoble). For more details of the instrumental setup and data extraction see [1].

RESULTS. The spectra are shown in Fig. 1. For sample A, the shell fit yielded a total of next neighbors of ~ 6 oxygen atoms with U–O distances of 2.34 and 2.52 Å. The next strong peak indicates a U–U distance of 3.85 Å. A reduced coordination number (crystalline UO_2 has 12 uranium next neighbors [4]) is the result of a strong structural disorder.

The next neighbors around uranium in the silica-containing samples B and C could be fitted with two contributions of oxygen at U–O distances of ~2.23 and 2.83 Å. It is obvious that the majority of the oxygen atoms is located at a distance of ~2.23 Å. A U–O distance of 2.83 Å is too long to be physically reasonable for a uranium-oxygen bond length. The scattering contribution of this shell is assumed to be mainly a contribution of silicon. The higher the silica content of the solids, the stronger is this contribution. The ionic radius of Si (0.26 Å) is far too small to replace U(IV). But SiO_4^{4-} tetrahedra may form a structure with U(IV) similar to that of coffinite. A similar U–Si distance of 3.1 Å can also be identified in the EXAFS spectrum of $USiO_4$ (sample D).

Another structural modification of the colloids was observed in the presence of silica: there is a significant weakening of the U–U backscattering signal with increasing silica content. This might be related to either increasing disorder of the structure which may result in destructive scattering effects on the EXAFS signal or to an increasing distance between the uranium atoms due to an increasingly growing silica network.
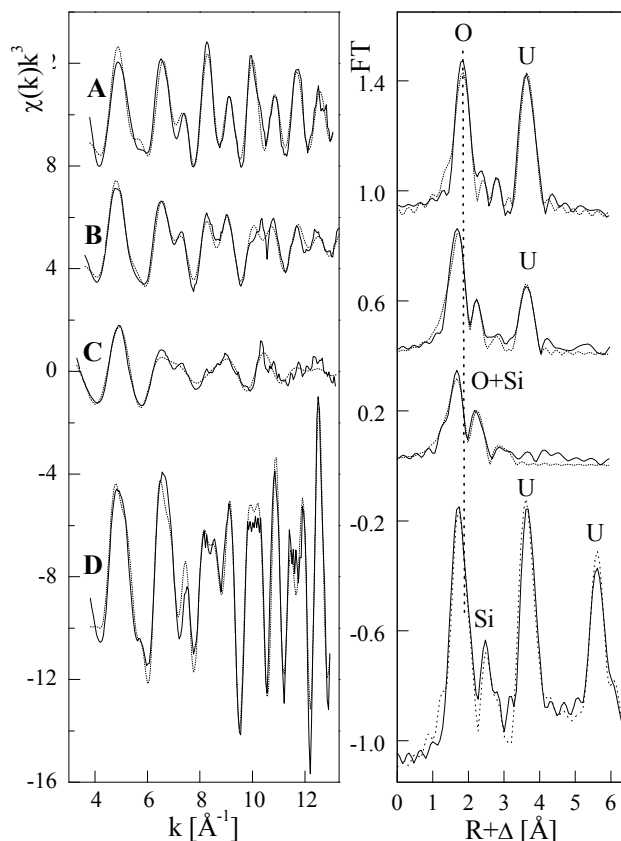
Fig. 1: Uranium L_3 edge EXAFS (left) and their corresponding Fourier transform (right) of samples A – D.

Tab. 1: Measured EXAFS-samples.

Sample	Description	Molar Si/U
A	U(IV)-oxyhydroxide (am.)	0
B	U(IV)-silica colloids	0.83
C	U(IV)-silica colloids	1.68
D	Coffinite ($USiO_4$(cr.))	1

A comparison between coffinite and the silicate-containing U(IV) colloids reveals similarities in the direct uranium coordination sphere but differences in the distant structure sequences. Both coffinite and the silicate-containing U(IV) colloids show that the maximum of the first U–O peak in the Fourier transform occurs at a lower distance R than that of the U(IV)-oxyhydroxide colloids. Furthermore, coffinite and the silicate-containing U(IV) colloids show a small peak resulting from the silicon backscattering signal. This is a strong indication that silicate coordinates directly with U(IV) in the U(IV)-silica colloids. However, this structural agreement between U(IV)-silica colloid samples and coffinite only concerns the first coordination sphere. The structure of the U(IV)-silica colloids appears to be highly disordered and is different from that of coffinite in this respect.

[1] Dreissig, I. et al. (2011) *Geochim. Cosmochim. Acta* **75**, 352-367
[2] Ikeda-Ohno, A. et al. (2009) *Inorg. Chem.* **48**, 7201-7210.
[3] Fuchs, L. H. et al. (1959) *Am. Mineral.* **44**, 1057-1063.
[4] Conradson, S. D. et al. (2004) *Inorg.Chem.* **43**, 6922-6935.

Vibrational spectroscopic characterization of U(VI) surface complexes on Al$_2$O$_3$

K. Müller, K. Stolze, H. Foerstendorf

The U(VI) sorption onto commercial γ-Al$_2$O$_3$ has been studied in-situ by application of ATR FT-IR spectroscopy. From time-resolved spectral data, the formation of three U(VI) species, namely a surface precipitate, an oligomeric and a monomeric sorption complex, as a function of different surface loadings is derived.

Aluminates contribute to the formation of clay minerals. They play a decisive role in regulating the mobility of contaminants, due to their widespread environmental presence and their contribution in rock and soil formation, and their tendency to form coatings on mineral surfaces [1]. In this work, U(VI) sorption on γ-Al$_2$O$_3$ is investigated as a function of different surface loadings.

EXPERIMENTAL. An Alfa Aesar γ-Al$_2$O$_3$ (No. 44931, 99.5%) was used. Particle size ranges between 40 and 50 nm and the BET specific surface area was determined to be 37 m²/g. For sorption experiments, U(VI) concentration was set to 20 μM at an ionic strength of 0.1 M adjusted by NaCl at pH 6 and normal atmosphere. The ATR FT-IR accessory and the procedure for the in-situ sorption measurement was described in detail previously [2].

RESULTS. The obtained ATR FT-IR spectra are shown in Fig. 1. Since no bands were observed in the difference spectrum of the conditioning stage (red trace), the stability of the prepared γ-Al$_2$O$_3$ film on the ATR crystal under the given conditions is confirmed.

Upon U(VI) sorption several bands increase in intensity with time. The bands at ~ 900 cm^{-1} are assigned to the antisymmetric stretching vibrational mode (ν$_3$) of the uranyl ion. At a lower U(VI) loading, the band is observed at 912 cm^{-1}. However, at an increased U(VI) level, the band shifts to 927 cm^{-1} and finally to 946 cm^{-1}. This spectroscopic observation must be correlated with a change in the surface speciation upon U(VI) accumulation on γ-Al$_2$O$_3$.

The ATR FT-IR spectrum obtained from an aqueous solution at 20 μM U(VI), ionic strength of 0.1 M at pH 5.5 shows the absorption band of ν$_3$(U^{VI}O$_2$) at 923 cm^{-1} The red shift of ν$_3$(U^{VI}O$_2$) to 912 cm^{-1} upon sorption can be assigned to an inner-sphere monomeric sorption complex, as previously reported for TiO$_2$ and ferrihydrite [3,4]. In contrast, the bands observed at an extended U(VI) accumulation at the γ-Al$_2$O$_3$ surface show a blue shift of ν$_3$(U^{VI}O$_2$). The band detected around 940 cm^{-1} is known from the spectrum of schoepite, freshly precipitated from a oversaturated U(VI) solution [5]. An intermediate step from sorption of monomeric species to surface precipitation would be oligomerization of U(VI) at the water-γ-Al$_2$O$_3$ interface. In fact, the peak position at 927 cm^{-1} fits well to spectra of oligomeric solution species, e.g. dimer and trimer hydroxo complexes in U(VI) solutions occurring at 940 and 925 cm^{-1} [6].

The band at 1044 cm^{-1} is probably due to rearrangement processes at the mineral oxide surface when U(VI) complexes. They are similarly observed for U(VI) sorption onto other sorbents, e.g. TiO$_2$ and also for interactions with Np(V), Mg(II) and Cs(I) [4,7].

The presence of bands between 1600 and 1300 cm^{-1} may indicate complexation of atmospheric carbonate with sur-
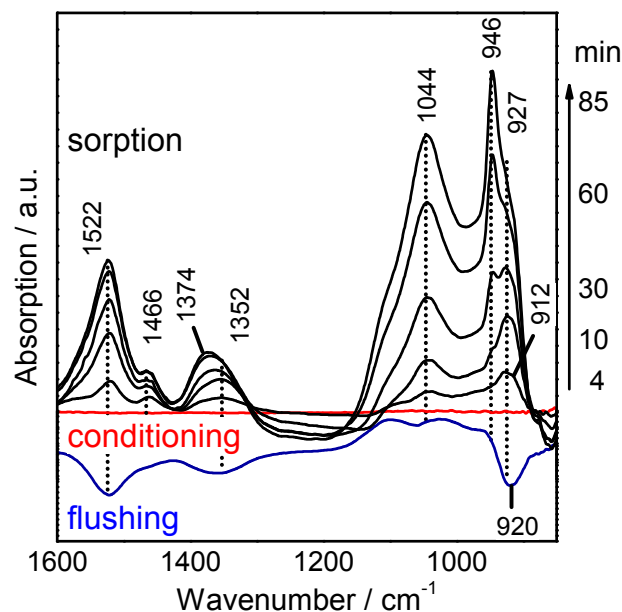
Fig. 1: ATR FT-IR spectra of 20 μM U(VI) sorbed onto γ-Al$_2$O$_3$ at pH 6, 0.1 M NaCl and under ambient atmosphere. Indicated values are in cm^{-1}.

face U(VI) species from the very beginning of sorption. Similar spectral contributions have been observed for the U(VI)-ferrihydrite system [3].

In the flushing stage a weakly bound species or an excess of sorption species are flushed out of the film pores. In the resulting spectrum (blue trace) an appropriate negative band at 920 cm^{-1} appears and possibly represents a mixture of monomeric and oligomeric species.

The spectra evidence the formation of energetically strong complexes, which remain stable during the whole sorption process. These results are confirmed by vibrational experiments performed at different flow rates, pH, ionic strength and U(VI) concentrations (data not shown) and by preliminary results of EXAFS experiments of batch samples showing different U(VI) surface loadings.

[1] Guillaumont, R. (1994) *Radiochimica Acta* **66**, 231-242.
[2] Müller, K. et al. (2009) *Environ. Sci. Technol.* **43**, 7665-7670.
[3] Foerstendorf, H. et al. (2009) *Report FZD-530*, p. 40.
[4] Müller, K. et al. (2009) *Report FZD-530*, p. 41.
[5] Duff, M.C. et al. (2002) *Geochim. Cosmochim. Acta* **66**, 3533-3547.
[6] Müller, K. et al. (2008) *Inorg. Chem.* **47**, 10127-10134.
[7] Meusel, T. et al. (2008) *Report FZD-511*, p. 48.

Uranium(VI) sorption on gibbsite studied by *in situ* ATR FT-IR

K. Gückel, H. Foerstendorf

The sorption of uranium(VI) on synthetic gibbsite (Al(OH)₃) was investigated in inert gas and ambient atmosphere by in situ attenuated total reflection FT-IR spectroscopy.

The retardation of uranium(VI) in groundwater aquifers is mainly controlled by sorption processes at mineral-water interfaces [1]. Hence, the identification of surface species formed and a rating of the binding strength of the respective complexes are needed.

Gibbsite is used in this study as a mineral model system because it is a common crystalline aluminum hydroxide and its sheets are part of the structure of important clays like kaolin [2].

EXPERIMENTAL. The synthetic gibbsite was prepared using the method described by Huittinen et al. [3] without dialysis. $AlCl_3 \cdot 6\,H_2O$ was dissolved in MilliQ-water and the amorphous $Al(OH)_3$ was precipitated by slowly adding 2 M NaOH to this solution until a pH value of 4.5 was reached. The produced $Al(OH)_3$ precipitate was freeze dried and the IEP and BET-surface were measured. A BET-surface of 2.6 m²/g and an IEP at pH 8.3 were determined.

The experimental setup, the preparation of the mineral film and parameter of the data acquisition we described elsewhere [4,5]. The U(VI) concentration was set to 20 μM at an ionic strength of 0.1 M adjusted by NaCl at pH 5.0. The anoxic solutions were prepared in a glove box under inert gas atmosphere.
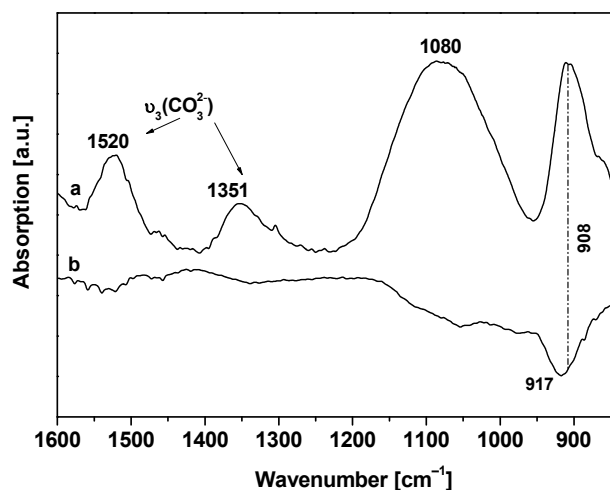

Fig. 1: *In situ* mid-IR spectra of 20 μM U (VI) sorption (a) on gibbsite and (b) after flushing with blank solution with 0.1 M NaCl in ambient atmosphere.

RESULTS. The IR spectrum of an aqueous U(VI) solution (20 μM UO_2^{2+}, pH 5.5) shows an absorption band of $\nu_3(UO_2)$ at 923 cm^{-1} [6]. Differences of the $\nu_3(UO_2)$ mode in spectra of sorption experiments potentially provide information about the species formed.

In the presence of atmospheric carbonate, the formation of an inner-sphere complex is proposed (Fig. 1) due to the significant red-shift of the $\nu_3 (UO_2)$ band (908 cm^{-1}) in comparison to aqueous species (923 cm^{-1}). Besides the inner-sphere complex, the formation of an outer-sphere complex is evidenced by means of the flushing with blank
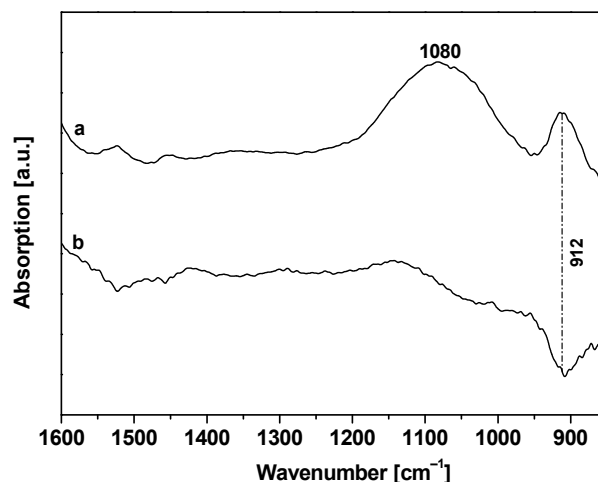
Fig. 2: *in situ* mid-IR spectra of 20 μM U (VI) sorption (a) on gibbsite and (b) after flushing with blank solution with 0.1 M NaCl in inert gas atmosphere.

solution (Fig. 1b) and peak fitting (data not shown). This weaker bound complex is reflected by a band at 917 cm^{-1} and is washed out during the flushing process. Because this outer-sphere complex is formed only to a small extent, no effect on the shape of the band at 908 cm^{-1} in the sorption spectrum is observed.

In the absence of atmospheric carbonate, verified by the lack of the $\nu_3(CO_3^{2-})$ band (Fig. 2), only one surface species is formed on the gibbsite surface showing an absorption maxima at 912 cm^{-1}. During the flushing step, this complex is removed from the mineral film (Fig. 2b).

In both sorption spectra (Fig. 1a, 2a), the broad band at 1080 cm^{-1}, representing vibrational modes of the solid phase, shows the same intensity. The comparison of the intensity ratios of this band and the band of the $\nu_3(UO_2)$ mode in the sorption spectra indicates an enhanced sorption of uranyl ions in the presence of atmospheric carbonate.

In conclusion, the spectra received under inert gas and ambient atmosphere illustrate the influence of atmospheric carbonate on the uranium(VI) sorption onto synthetic gibbsite. In the absence of carbonate weakly bound outer-sphere complexes are preferentially formed on the mineral surface, which are released during the flushing step. In the presence of carbonate, possibly two different surface species are formed and only the minor outer-sphere complex is washed out during the flushing step.

[1] Choppin, G.R. (2007) *J. Radioanal. Nucl. Chem.* **273**, 695-703
[2] Wu, T. et al. (2009) *Radiochim. Acta* **97**, 99-103
[3] Huittinen, N. et al. (2009) *J. Colloid Interface Sci.* **332**, 158-164
[4] Meusel, T. et al. (2009) *Report FZD-511*, p. 48.
[5] Müller, K. et al. (2009) *Environ. Sci. Technol.* **43**, 7665-7670.
[6] Müller, K. et al. (2008) *Inorg. Chem.* **47**, 10127-10134.

Stability of U(VI) in the Opalinus Clay/pore water system under anaerobic conditions

C. Joseph, K. Schmeide, S. Sachs, G. Bernhard

The U(VI) sorption onto Opalinus Clay (OPA) and FeS was investigated in pore water under anaerobic conditions and the reduction stability of U(VI) in these systems was followed. A reduction of U(VI) to U(IV) was not detectable in the supernatant.

Natural clay, like OPA, is discussed as possible host rock for a nuclear waste repository. Thus, it is of great interest to investigate the retention power of natural clay concerning radionuclides. Uranium can interact with the clay, e.g., by sorption but some of the natural clay mineral fractions can induce redox processes. U(VI) can be reduced to U(IV), for instance, by Fe(II) [1]. OPA contains 4.1% Fe(II) minerals (siderite, pyrite) [2]. Thus, U(VI) sorption experiments are performed with OPA and FeS under anaerobic conditions to investigate the reduction properties of the clay and especially, of its Fe(II) fraction.

EXPERIMENTAL. Two OPA batches (BHE-24/1, BLF-11/01) from the underground rock laboratory in Mont Terri, Switzerland and FeS (99%; Alfa Aesar) were applied. The U(VI) sorption was studied at pH 7.6 ([U(VI)]: $1 \cdot 10^{-6}$ M; I: 0.34 M OPA pore water [3]; S/L: 60 g/L (OPA), 2.46 g/L (FeS); $pCO_2 = 10^{-3.5}$ atm (OPA), inert gas atmosphere (OPA, FeS); room temperature). In the case of OPA, the suspensions were pre-equilibrated for 7 d. The contact time with U(VI) was 3 d. In the case of FeS, the suspension was pre-equilibrated for 1 d and the U(VI) sorption was investigated for 112 d, whereby aliquots of the suspensions were taken after different contact times. The redox speciation of uranium in both experiments was studied by solvent extraction using thenoyltrifluoroacetone (p.a., Fluka/Sigma-Aldrich) according to Bertrand and Choppin [4].

RESULTS. Previous studies showed that the dominant species in the U(VI) / OPA / pore water system under aerobic conditions is the $Ca_2UO_2(CO_3)_3(aq)$ complex [5]. This is due to calcite dissolution, which is a mineral fraction of OPA. Nearly the same amount of U(VI) is sorbed under aerobic (0.045 ± 0.003 µg/m²) and anaerobic (0.046 ± 0.002 µg/m²) conditions which can be explained by the constant composition of the initial pore water irrespective to the prevailing conditions. That means, because of the presence of dissolved carbonate ions in the background electrolyte, the U(VI) speciation is independent of CO_2 presence in the atmosphere. The $Ca_2UO_2(CO_3)_3(aq)$ complex is always the dominating species in solution. Thus, the CO_2 from the atmosphere has no significant influence on the U(VI) sorption onto OPA.

After the sorption experiment, the oxidation state of uranium in the supernatant was analyzed. No U(IV) was detectable. This might indicate that the $Ca_2UO_2(CO_3)_3(aq)$ complex is more stable against reduction in comparison to UO_2^{2+}, as already described by [6].

Furthermore, the sorption of U(VI) onto FeS in pore water under anaerobic conditions was investigated together with the redox speciation of uranium. The uranium sorption onto FeS and the respective fractions of U(VI) and U(IV) in the supernatant are shown in Fig. 1 as a function of time. For two days, the amount of sorbed uranium onto FeS remained nearly stable at a value of about 20%. Then,
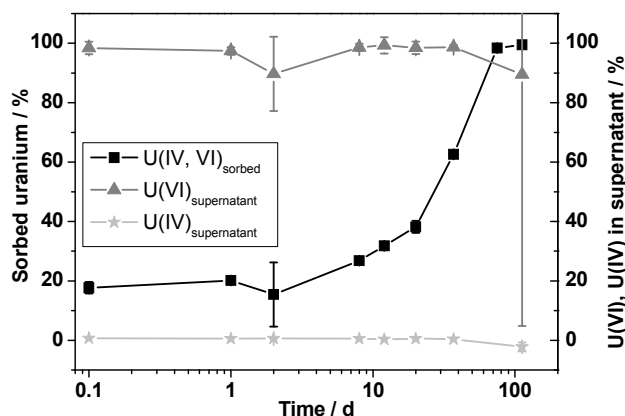

Fig. 1: Sorption of U(IV, VI) onto FeS under anaerobic conditions and fractions of U(VI) and U(IV) present in supernatant as a function of time.

the uranium sorption increased and reached its maximum with almost 100% after 112 d of contact time.

In the beginning of the experiment, the $Ca_2UO_2(CO_3)_3(aq)$ complex was the dominating species in solution. However, due to the loss of dissolved CO_2 into the surrounding inert gas atmosphere as shown in [7], and due to the lack of a carbon source in solution, the uranium speciation changed with time. The $(UO_2)_2CO_3(OH)_3^-$ complex became the dominant species in solution. This uranium species seems to have a higher affinity towards FeS than the $Ca_2UO_2(CO_3)_3(aq)$ complex.

In the studied systems, a reduction of U(VI) to U(IV) followed by precipitation of UO_2 might occur. However, because only the supernatant was investigated during the experiments and no U(IV) was detected. Nevertheless, the presence of U(IV) at the surface might be possible.

Eglizaud et al. [8] and Scott et al. [9] showed for pH 3, 4 and 6 and for pH 4.8, respectively, that there is only a partial reduction of U(VI) by pyrite (FeS_2). They observed that U(VI) and its reduced form coexist with a heterogeneous distribution on the pyrite surface. However, they performed their studies using inert background electrolytes. Thus, due to the absence of competing ions like calcium, the $Ca_2UO_2(CO_3)_3(aq)$ complex was not present in solution.

Within this study, it is demonstrated that the $Ca_2UO_2(CO_3)_3(aq)$ complex is the dominating U(VI) species under pore water conditions even in inert gas atmosphere. Without a carbon source in solution, the uranium speciation changes with time. A redox process was not observed, however, it can not be completely ruled out.

[1] Regenspurg, S. et al. (2009) *Appl. Geochem.* **24**, 1617-1625.
[2] Nagra (2002) *Nagra Technical Report NTB 02-03*, 230.
[3] Pearson, F.J. (1998) *PSI Internal report TM-44-98-07*, 1-5.
[4] Bertrand, P.A. et al. (1982) *Radiochim. Acta* **31**, 135-137.
[5] Joseph, C. et al. (2011) *Chem. Geol.*, accepted.
[6] Brooks, S.C. et al. (2003) *Environ. Sci. Technol.* **37**, 1850-1858.
[7] Joseph, C. et al. (2010) *Uranium(VI) diffusion in Opalinus Clay in the absence and presence of humic acid (Poster)*, Clays in Natural & Engineered Barriers for Radioactive Waste Confinement, March 29 – April 01, 2010, Nantes, France.
[8] Eglizaud, N. et al. (2006) *Radiochim. Acta* **94**, 651-656.
[9] Scott, T.B. et al. (2007) *Geochim. Cosmochim. Acta* **71**, 5044-5053.

Identification of the uranium speciation in the bulk solution of an underground AMD environment

T. Arnold, N. Baumann

The uranium speciation in underground AMD waters from Königstein flowing in mine galleries as well as dripping from the ceiling and forming stalactite-like dripstones were studied by Time Resolved Laser-Induced Fluorescence Spectroscopy (TRLFS). The fluorescence lifetime of uranium species in both AMD water environments were best described with a mono-exponential decay, indicating the presence of one major species only. The detected positions of the emission bands and by comparing it in a fingerprinting procedure with spectra obtained for acid sulfate reference solutions, in particular $Fe(III) - SO_4^{2-} - UO_2^{2+}$ reference solutions, indicated that the uranium speciation in the AMD environment of Königstein is dominated in the pH range of 2.5 to 3.0 by the highly mobile aquatic uranium sulfate species $UO_2SO_{4(aq)}$. The presence of iron in the AMD reduces the fluorescence lifetime of the $UO_2SO_{4(aq)}$ species from 4.3 μs found in iron-free uranium sulfate reference solutions to 0.7 μs in both AMD waters of Königstein and in iron containing uranium sulfate reference solutions, respectively.

EXPERIMENTAL. Water samples for TRLFS were collected during four sampling campaigns taking place in October 2008, June, July, and October 2009 in a gallery of pit 390 on level +50 m above sea level of the former uranium mine of the WISMUT GmbH near Königstein (Saxony, Germany). The water samples were collected in mine drainage channels operated with underground mine ventilation in which thick biofilms in form of filamentous and gelatinous streamers, also denoted as acid streamers, thrive. Additional water samples were collected in another parallel gallery from dripstone-like biofilms, so-called snottites. The water samples were collected in sterile glass bottles and subsequently transported to the laboratory for TRLFS analysis.
The TRLFS measurements are described in detail in [1].

RESULTS. The AMD drainage waters are characterized by high concentrations of Fe (47-381 mg/L) and SO_4^{2-} (700-2500 mg/L) and low pH values, whereby the dripstone waters show higher Fe and SO_4^{2-} concentrations and lower pH values. A pH value of 2.86 ± 0.05 in the flowing drainage channels and of 2.55 ± 0.05 in the dripping waters of the snottites, respectively were determined. In the drainage channels uranium concentrations ranging from $3 \cdot 10^{-5}$ M to $6 \cdot 10^{-5}$ M (mean $4.7 \cdot 10^{-5}$ M) were observed and in the dripping waters of the snottites higher uranium concentrations of $1.7 \cdot 10^{-4}$ M to $2.9 \cdot 10^{-4}$ M (mean $2.55 \cdot 10^{-4}$ M) were detected.
A time resolved fluorescence spectrum of a drainage water sample is shown in Fig. 1. These photoluminescence spectra are characteristic for all collected water samples representing both site types, i.e. the water of the drainage channels as well as the dripping water of the snottites, and were best described with a mono-exponential decay, indicating the presence of one species only. The emission spectra of drainage water and snottite water samples collected on two different sampling campaigns are shown in Fig. 1 together with emission spectra a uranium sulfate
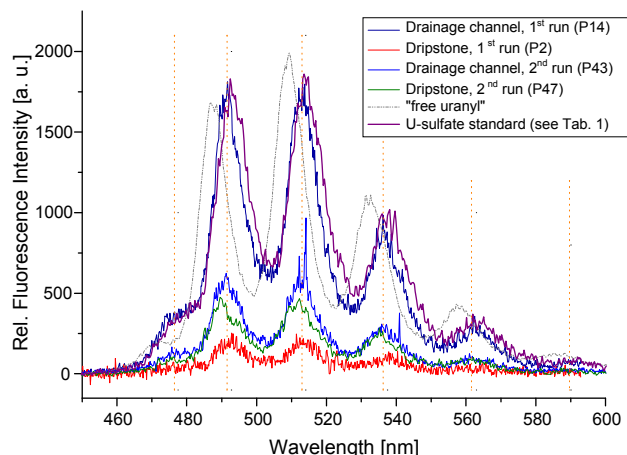

Fig. 1: Emission spectra of drainage and snottite water samples collected on two different sampling campaigns together with emission spectra of a U-sulfate standard and a free U(VI) standard solution. The dashed lines show the emission maxima of Königstein waters at 476.5, 491.5, 513.0, 536.3, 561.6, and 589.7 nm

standard and a free uranyl(VI) standard solution. Based on the detected positions of the emission bands and by comparing it in a fingerprinting procedure with spectra obtained for acid sulfate reference solutions prepared in the laboratory, i.e. simple two component systems [2-5], it was found that the uranium speciation in the complex solutions of the AMD environment of Königstein is dominated by one aquatic uranium sulfate species. The emission bands of the observed uranium species in Königstein were found at 476.5 ± 1.2, 491.5 ± 0.5, 513.0 ± 0.7, 536.3 ± 0.8, 561.6 ± 1.0, 589.7 ± 1.9 nm. The error corresponds to one standard deviation (1σ). These values represent mean values for altogether 19 samples collected on four different sampling campaigns of both dripstone water as well as water from the drainage channels, clearly showing that both water types are characterized by the same uranium speciation.
To study in more detail the uranium speciation in Königstein additional uranium sulfate reference solutions were prepared, representing uranium and sulfate concentrations of the drainage water and the dripstone waters, respectively and in addition one of the major eight cations, i.e., Mg, Na, Ca. K, Si, Al, Fe, and Zn in the respective mean Königstein concentrations found in the drainage waters and in the snottite waters, respectively. Here it was found that the fluorescence lifetime was significantly reduced by the presence of Fe in the $UO_2^{2+} - SO_4^{2-} - Fe$ reference samples to a fluorescence lifetime of 0.73 μs which represents an almost perfect match with the fluorescence lifetime obtained for the Königstein samples of 0.71 ± 0.19 μs (1σ). Obviously Fe, a well-known quencher (Meinrath, 1997) for the uranium photoluminescence in solution, quenches the fluorescence lifetime.

[1] Arnold, T. et al. (2011) *Geochim. Cosmochim. Acta*, submitted.
[2] Bernhard G. et al. (1996) *Radiochim. Acta* **74**, 87-91.
[3] Geipel, G. et al. (1996) *Radiochim. Acta* **75**, 199-204.
[4] Vercouter, T. et al. (2008) *Inorg. Chem.* **47**, 2180-2189.
[5] Vetešník et al. (2009) *Uranium, Mining and Hydrogeology*, p. 623-630, Springer, Berlin.
[6] Meinrath, G. (1997) *J. Radioanal. Nucl. Chem.* **224**, 119-126.

Speciation of uranium in soil water of heavy metal contaminated soil determined by TRLFS

N. Baumann, T. Arnold, M. Lonschinski[1]

[1]Institute of Earth Sciences, Friedrich-Schiller-University Jena, Germany

Time-resolved laser-induced fluorescence spectroscopy (TRLFS) has proved as a useful tool to determine the uranium speciation in soil waters from the former uranium leaching heap "Gessenhalde" (now Gessenbach grassland) close to Ronneburg (Eastern Thuringia). The uranium speciation in that soil water is dominated by the uranium (VI) sulphate species $UO_2SO_{4(aq)}$. The work presented here should contribute to the basement of further investigations concerning uranium speciation in plants which grow in association with that water at test site Gessenwiese.

Three soil water samples were investigated by TRLFS, subsequent to the investigations in surface water samples from the test field Gessenwiese [1]. All samples showed an evaluable fluorescence signal, despite of a high salinity in the water samples, with a high concentration of quenchers like manganese and iron (Tab. 1).

Tab. 1: Analytical results of the soil water samples SoilWtr1, SoilWtr2, and SoilWtr3 (contents in ppb).

	SoilWtr1	SoilWtr2	SoilWtr3
U	322	156	890
Mn	12000	1870	23700
Fe	2420	15500	18300
Cl^-	3.75	1.85	11.4
SO_4^{2-}	966	1010	2530
pH	4.02	3.40	3.27

The positions of the peak maxima from the fluorescence signals from soil water samples (Tab. 2) are all in concordance with data for uranium sulfate species published in the literature [2], [3].

The three most intensive spectra from the three soil water samples are shown in Fig. 1. The higher the uranium concentration (Tab. 1) the more intensive is the fluorescence intensity of the first spectrum.

The different lifetimes of the fluorescence signals from the three soil water samples are a consequence of the different concentration ratios of quenching substances and uranium in these samples. Life time t of the uranium fluorescence signal (Tab. 2) seems to be correlated with the iron concentration in the sample: The higher the Fe concentration in the soil water sample, the shorter is the life time from the uranium fluorescence signal (Tab. 1 and 2). Fluorescence signals from all three soil water samples show mono-exponential decay (Fig. 2).

Tab. 2: Positions of the peak maxima from the fluorescence signals of three pore water samples in nm, rounded in whole nm, compared with data measured for $UO_2SO_{4(aq)}$ in synthesized samples [3], and lifetime t of the signals in µs.

	SoilWtr1	SoilWtr2	SoilWtr3	[3]
1st peak	480	473	477	477.5
2nd peak	492	492	493	492.8
3rd peak	514	513	514	514.1
4th peak	537	535	538	537.5
5th peak	562	562	562	563.0
5th peak	590	–	590	590.1
t	2.6	1.7	1.0	4.72
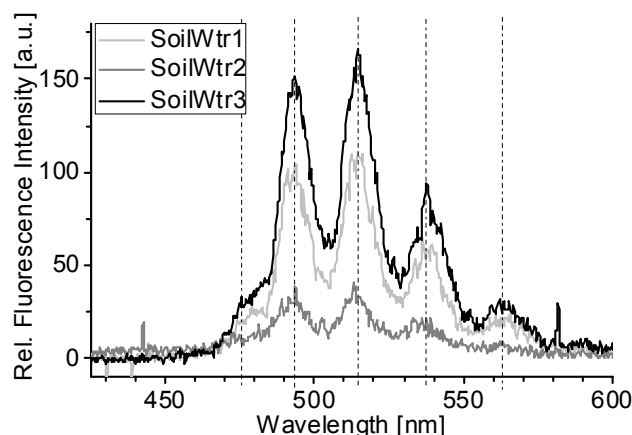
Fig. 1: Fluorescence signals of the three pore water samples, in comparison with positions of peak maxima published in [3] for $UO_2SO_{4(aq)}$ (dashed lines).
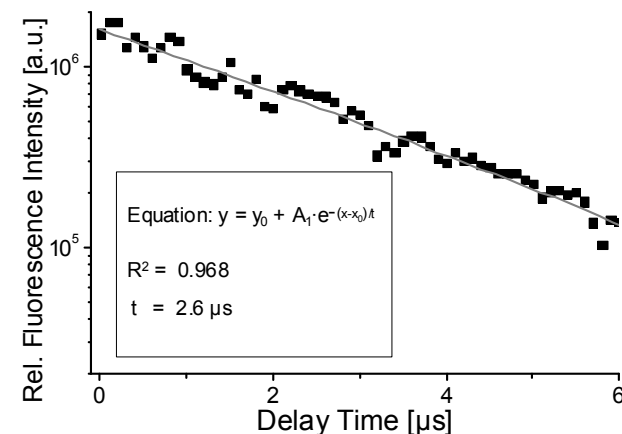
Fig. 2: Life time curve from the fluorescence signal sample SoilWtr1.

Equation: $y = y_0 + A_1 \cdot e^{-(x-x_0)/t}$

$R^2 = 0.968$

$t = 2.6$ µs

EXPERIMENTAL. Experimental conditions from the TRLFS measurements were the same described in [1].

RESULTS. These two characteristics, i.e. positions of peak maxima and the mono-exponential decay of the fluorescence signal revealed that the uranium speciation in the soil water is dominated by the $UO_2SO_{4(aq)}$ species.

Because uranium from water may enter economic plants and reach the human food chain, and the reactivity and toxicity of uranium depend on the speciation of heavy metals [4], uranium speciation in natural occurring waters has to be considered as a possible risk factor.

[1] Baumann, N. et al. (2009) *Report FZD-530*, p. 47.
[2] Geipel, G. et al. (1996) *Radiochim. Acta* **75**, 199-204.
[3] Arnold, T. et al. (2011) *Geochim. Cosmochim. Acta*, submitted.
[4] Carrière, M. et al. (2005) *Nucl. Instrum. & Methods Phys. Res. Sect. B* **231**, 268-273.

Adsorption of thallium(I) onto geological materials: influence of pH and humic matter

J. Liu,[1] H. Lippold, J. Wang,[1] J. Lippmann-Pipke, Y. Chen[1]
[1]Guangzhou University, Guangzhou, China

The adsorption behavior of the severely toxic heavy metal thallium onto goethite, pyrolusite and a natural sediment was examined as a function of pH in the absence and presence of two natural humic acids (HAs), using ^{204}Tl(I) as a radiotracer. Aiming at a prediction of the solid-liquid distribution based on a combined distribution model, adsorption of HAs and humate complexation of Tl(I) as a function of pH were investigated as well. In spite of a low degree of complexation, the presence of HAs resulted in obvious alterations of Tl(I) sorption onto pyrolusite and sediment. The model calculations were, however, unable to reproduce these effects.

Anthropogenic sources such as atmospheric emissions, wastewater discharges and solid wastes from coal combustion or mining/smelting activities generated high enrichments of Tl in some areas [1]. For long-term risk assessments, the mobility in geochemical systems is a topic of major interest. Adsorption onto mineral surfaces can be considerably affected by dissolved humic substances, e.g. HAs, which are ubiquitous in natural waters. By using radioactive tracers, we were able to investigate coadsorption of Tl and HAs at low concentration levels, in accordance with scenarios to be considered.

MATERIALS. Two natural HAs were extracted from river sediments collected in a contaminated mining area in South China (GZHA from Guangzhou, YFHA from Yunfu City). They were radiolabeled by an azo-coupling reaction with ^{14}C-aniline [2]. [^{204}Tl]Tl(I) was purchased from Polatom (Poland). Goethite and pyrolusite were supplied by Fluka (Germany), a natural sediment sample was taken in the region of Yunfu City.
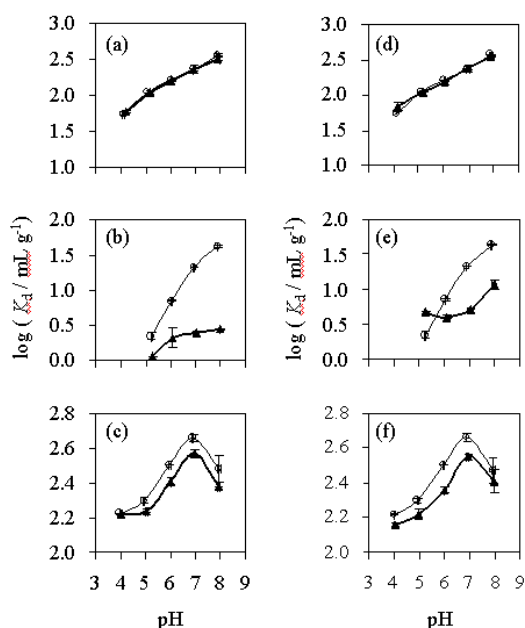
RESULTS. The effects of HAs on Tl(I) adsorption are shown in Fig. 1. Generally, metal adsorption is promoted with increasing pH since more binding sites are provided by deprotonation of surface hydroxyl groups. The decrease observed for the sediment at pH > 7 could be due to a release of negatively charged ligands from the solid material. Adsorption of HAs (not shown) was found to be counteracted with increasing pH, which is explained by increasing electrostatic repulsion as a consequence of deprotonation. As expected, the extent of Tl(I)-HA complexation turned out to be very low, with a slight increase at higher pH (not shown).

According to the Linear Additive Model [3, 4], the pH-dependent influence of humic substances on metal adsorption can be quantitatively predicted by combining the distribution data for the elementary processes discussed above, using the following equation:

$$K_d^{(M+M-HA)/S} = \frac{K_d^{M/S} + K_d^{HA/S}\, K_d^{M/HA}\, c_{HA}}{1 + K_d^{M/HA}\, c_{HA}} \qquad (1)$$

The distribution coefficient K_d is the ratio of the adsorbed amount per unit mass and the equilibrium concentration c. The indices M, M-HA and S stand for metal, metal-humic complex and surface, respectively. In Fig. 2, the modeling results are shown for the GZHA / pyrolusite system as an example, together with an illustration of the approach.
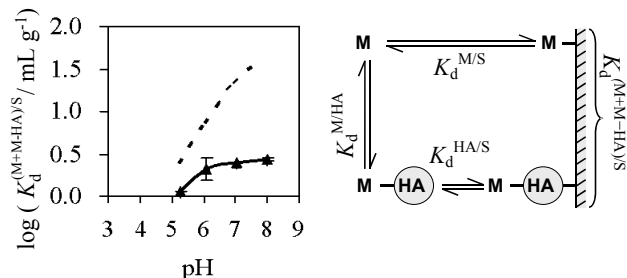
Fig. 2: Modeling results for Tl(I) adsorption onto pyrolusite in the presence of GZHA (dotted line), calculated according to the Linear Additive Model (Eq. (1)) schematically illustrated on the right.

Obviously, the model is not capable of reproducing the experimental data in this case. In view of the fact that the approach worked well in other studies, criteria for its applicability need to be identified. Selectivity within the multicomponent system of humic material, regarding adsorption as well as complexation, is one possible reason for a failure of the model. Investigations with fractionated humic substances might be helpful to substantiate this reasoning.

Fig. 1: Solid-liquid distribution coefficients of Tl(I) (10^{-7} M) in the absence (open circles) and presence (solid triangles) of 20 mg L^{-1} HA as a function of pH; (a) goethite / GZHA, (b) pyrolusite / GZHA, (c) sediment / GZHA, (d) goethite / YFHA, (e) pyrolusite / YFHA, (f) sediment / YFHA.

[1] Yang, C.X. et al. (2005) *Sci. Total Environ.* **341**, 159-172.
[2] Mansel, A. et al. (2007) *Appl. Radiat. Isot.* **65**, 793-797.
[3] Samadfam, M. et al. (1998) *Radiochim. Acta* **82**, 361-365.
[4] Lippold, H. et al. (2005) *Appl. Geochem.* **20**, 1209-1217.

Influence of temperature and organic ligands on Eu³⁺ sorption onto Opalinus Clay

J. Schott, M. Acker,[1] A. Barkleit, S. Taut,[1] G. Bernhard

[1]Central Radionuclide Laboratory, Dresden University of Technology, Dresden, Germany

The sorption of Eu³⁺ on Opalinus Clay (OPA) was investigated in presence of small organic ligands (tartaric acid, citric acid) at different temperatures (15…50 °C) under synthetic pore water conditions by batch sorption experiments and TRLFS spectroscopy. A significant temperature dependency and influence of organic matter on the sorption is observed.

Argillaceous rocks are possible host rocks for nuclear waste repositories; thus, radionuclide sorption experiments play an important role in the safety assessment. Although higher temperatures in repositories have to be expected, there is a lack of sorption data under such conditions. Therefore, the temperature dependency of sorption was investigated. Due to the fact that natural organic matter (NOM) was found in OPA formations [1] the influence of NOM on radionuclide sorption has to be investigated. In the experiments, small organic acids were chosen as model ligands for NOM.

EXPERIMENTAL. The sorption experiments were carried out between 15 °C and 50 °C at $p_{CO2} = 10^{-3.5}$ atm in 10 mL PE centrifuge tubes. OPA from the underground rock laboratory Mont Terri, Switzerland (sample BHE-241), and synthetic pore water [2] as medium were used. The solid-liquid-ratio was 2 g/L. Tartaric/citric acid concentrations were $0…5 \cdot 10^{-3}$ M. The total concentrations of Eu³⁺ were $2 \cdot 10^{-9}$ M, 10^{-6} M and 10^{-5} M (for TRLFS). ¹⁵²Eu was added for distribution analysis. The clay was preconditioned for 5 days and after addition of tartaric/citric acid and Eu³⁺ the suspensions were equilibrated for 7 days. During the conditioning and sorption, the samples were stored in a temperature adjustable shaker and the pH was adjusted to 7.6 for several times. After the contact time, the samples were centrifuged at the selected temperature at 40,000×g for 1 h and analyzed concerning ¹⁵²Eu activity by gamma counting (COBRA II, Canberra). For TRLFS measurements, a Nd:YAG-OPO laser (Continuum, USA) was used. Time-resolved spectra of the centrifugates and suspensions were recorded in the wavelength range 440-780 nm (delay times: 10…100 μs, pulse energy: 4 mJ, λ_{ex}: 395 nm).

RESULTS. Distribution coefficients R_d were calculated by eq. 1 (R_d: distribution coefficient [L/kg], c_{in}: added Eu(III) concentration [M], c_{eq}: equilibrium concentration [M], S/L: solid/liquid ratio [kg/L]) [3]:

$$R_d = \frac{c_{in} - c_{eq}}{c_{eq}} \cdot \frac{L}{S} \tag{1}$$

In presence of tartaric/citric acid, the Eu³⁺ sorption decreases with increasing ligand concentration (Fig. 1) because of the formation of aqueous Eu³⁺/tartaric/citric acid complexes. The influence of citric acid is greater than that of tartaric acid, because citric acid is a stronger complexing agent. In absence and presence of tartaric/citric acid, the sorption increases with increasing temperature. Thus, the sorption of Eu³⁺ on OPA is an endothermic reaction with ΔH of 40…60 kJ·mol⁻¹. Eu³⁺ sorption decreases with increasing Eu³⁺ concentration. It could be explained with a formation of a neutral Eu species ([Eu³⁺] < 10⁻⁷ M:
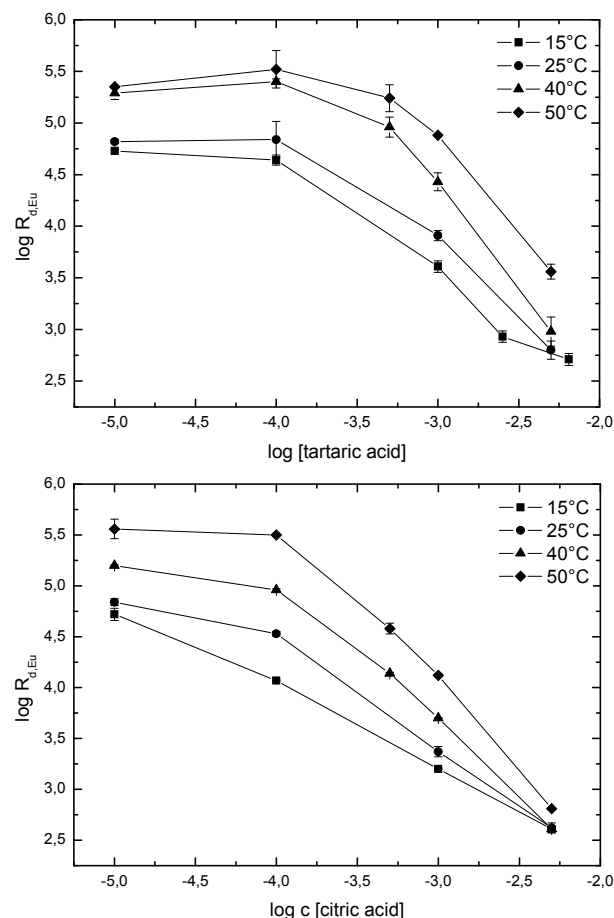
Fig. 1: Eu³⁺ sorption ([Eu³⁺] = 2·10⁻⁹ M) on OPA in dependence on tartaric/citric acid concentration and temperature.

EuCO₃⁺; [Eu³⁺] > 10⁻⁷ M: EuCO₃OH₍ₛ₎ [4]), which sorbs weaker on the clay surface.

Starting from a citric acid concentration of $5 \cdot 10^{-5}$ M, changes of TRLFS spectra and fluorescence emission lifetimes of Eu³⁺ are observed for the pore water samples (without clay) and for the centrifugates (with clay) in comparison with the same samples free of citric acid. Thus, the Eu³⁺ desorption from the clay surface correlates with the complexation of Eu³⁺ by citric acid in solution. The spectra and fluorescence lifetimes of the suspensions do not change below a citric acid concentration of 10^{-3} M and are similar to the spectrum of the sample without citric acid at pH 7.6. This result demonstrates that (1) there is no influence of citric acid on sorption mechanism and (2) there is no formation of a ternary surface complex with citric acid, contrary to the humic acid systems [5, 6]. The results of batch sorption experiments are consistent with those of TRLFS spectroscopy.

[1] Courdouan, A. et al. (2007) *Appl. Geochem.* **22**, 2926-2939.
[2] Van Loon, L.R. et al.(2003) *J. Contam. Hydrol.* **61**, 73-83.
[3] Lauber, M. et al. (2000) *Technical Report 00-11*, Nagra, PSI Villigen, Switzerland.
[4] Courdouan, A. et al. (2008) *Environ. Sci. Technol.* **42**, 5985-5991.
[5] Fairhurst, A.J. et al. (1995) *Colloids Surfaces A* **99**, 187-199.
[6] Wang, X.K. et al. (2004) *Radiochim. Acta* **92**, 691-695.

Luminescence and absorption spectroscopic study on the complexation of europium(III) with citric acid

A. Heller, A. Barkleit, H. Foerstendorf, G. Bernhard

The complexation of Eu(III) with citric acid in aqueous solution has been studied over a wide pH range and various metal to ligand ratios. TRLFS measurements led to the identification of five different complex species, namely EuCitH, $Eu(CitH)_2^{3-}$, $EuCit^-$, $EuCit_2^{5-}$ and $EuCitH_2CitH^{2-}$. ATR FT-IR measurements shed light on structural aspects of the complex species and revealed monodentate binding of the carboxyl groups in EuCitH as well as an additional participation of the hydroxyl group in $EuCit^-$.

Citric acid (CA) is an important intermediate of the tricarboxylic acid cycle and plays a key role in the metabolism of carbohydrates, fatty acids and amino acids in any organism. Hence, it occurs ubiquitously in biofluids and human body fluids, such as urine, in millimolar concentrations [1]. Therefore, CA has to be considered as a potential ligand for complexation of exogenous metals. Since one CA molecule has three carboxyl and one hydroxyl functionalities, the ligand is regarded as a four protonic acid ($CitH_4$). The carboxylic deprotonated citrate anion therefore refers to $CitH^{3-}$.

RESULTS. In the 570-640 nm range, the luminescence spectrum of $3 \cdot 10^{-5}$ M Eu(III) in water exhibits two maxima at 592 and 616 nm as well as a lifetime of 110 ± 10 μs [2]. Upon complexation with 10^{-5} to 10^{-1} M citric acid, the luminescence lifetime is prolonged and both emission maxima are split with the actual fine structure being different in each complex (see Fig. 1).
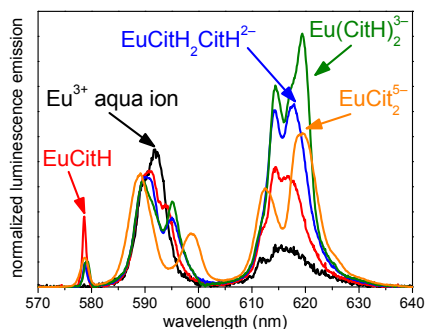

Fig. 1: Luminescence spectra of the single components in the system Eu(III) + CA as derived from peak deconvolution using Specfit.

At excess ligand concentrations, four species were identified in dependence on pH. In the acidic region, mainly the EuCitH species ($\tau = 165 \pm 10$ μs, $\log K_{111} = 7.5 \pm 0.2$) is formed. At pH 4-6, the mixed $EuCitH_2CitH^{2-}$ complex ($\tau = 255 \pm 5$ μs, $\log K_{123} = 10.8 \pm 0.5$) dominates. In the near neutral pH range, the $Eu(CitH)_2^{3-}$ species ($\tau = 485 \pm 20$ μs, $\log K_{122} = 11.4 \pm 0.4$) is formed and competes effectively with the metal ion hydrolysis. At basic pH, the hydroxyl group of the CA ligand is deprotonated and the $EuCit_2^{5-}$ species ($\tau = 675 \pm 3$ μs, $\log K_{120} = 21.0 \pm 0.2$) dominates. For Cm(III) analog complexes were found.

At equimolar metal to ligand ratio, only two complexes dominate the europium speciation. Over the wide range of pH 3-7 predominantly the EuCitH species is formed. At higher pH, another complex presumably the $EuCit^-$ spe-

cies dominates until hydrolysis of the metal ion occurs at basic pH > 10. Unfortunately, neither the luminescence spectrum nor the emission lifetime of the latter complex could be determined . Nevertheless, speciation calculation using the $\log K_{110}$ of the analog Am(III) complex [3] also predicts the dominance of this species.

Absorption and difference spectra of a complex solution at equimolar metal to ligand ratio were very similar at pH 2 and 4 as well as pH 8-12 (Fig. 2). At acidic pH predominantly EuCitH is formed. In this species, all carboxyl groups are deprotonated upon complexation as indicated by the $\nu_{as}(COO^-)$ and $\nu_s(COO^-)$ bands in the absorption spectra as well as the negative $\nu(COOH)$ and $\delta(COOH)$ bands in the difference spectra. Nevertheless, not all of the three carboxyl functionalities bind to the lanthanide in this complex. Furthermore, the hydroxyl group is not supposed to participate in the metal binding since the $\nu(COH) + \delta(COH)$ band shows no alteration upon complexation in this pH range.

At neutral to basic pH, the $EuCit^-$ species is predominantly formed. In this complex, the $\nu_{as}(COO^-)$ and $\nu_s(COO^-)$ bands indicate that all carboxylic functionalities are deprotonated and are coordinated to the metal ion. Furthermore, the absorption band referring to the $\nu(COH) + \delta(COH)$ vibration disappears in the absorption spectra and the corresponding negative band is observed in the difference spectra. This strongly suggests that the hydroxyl group is also deprotonated in this complex and participates in the binding of the lanthanide.

The binding mode of the carboxyl groups has been determined according to literature [4] from the spectral splitting of the $\nu_{as}(COO^-)$ and $\nu_s(COO^-)$ modes. In case of both complex species, the carboxyl groups obviously bind to the lanthanide in a monodentate fashion.
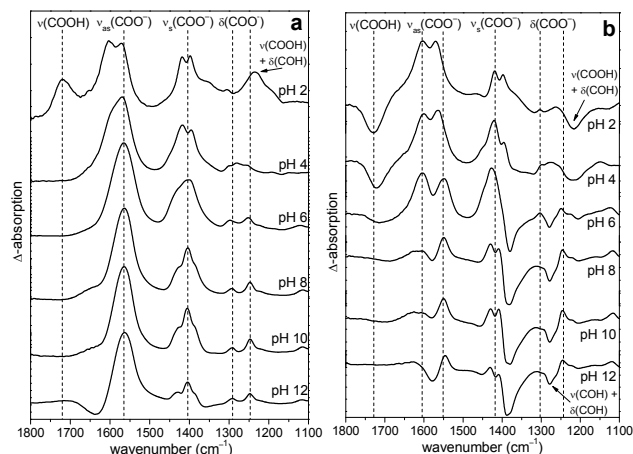
Fig. 2: Absorption (a) and difference (b) spectra of a 1:1 complex solution of Eu(III) + CA at I = 0.1 M.

[1] Renata, C. et al. (2003) *Front. Biosci.* **8**, S1084-S1106.
[2] Plancque, G. et al. (2003) *Anal. Chim. Acta* **478**, 11-22.
[3] Bouhlassa, S. et al. (1984) *J. Less Common Met.* **99**, 157-171.
[4] Kakihana, M. et al. (1987) *J. Phys. Chem.* **91**, 6128-6136.

Structural study on complex between $^{99}TcO_4^-$ and MIDOA by ATR FT-IR, EXAFS spectroscopy and DFT calculation

M. Saeki,[1] Y. Sasaki,[2] D. Banerjee, A. C. Scheinost, H. Foerstendorf

[1]Quantum Beam Science Directorate, Japan Atomic Energy Agency (JAEA), Japan, [2]Nuclear Science and Engineering Directorate, JAEA

Structures of complexes of TcO_4^- with MIDOA were investigated by IR and EXAFS spectroscopy. Analysis of observed spectra based on results of DFT calculation suggests that the complexes are stabilized by multiple hydrogen bonds.

Recently, a new extractant, 2,2'-(methylimino) bis(N,N-dioctyl-acetamide) (MIDOA; inset in Fig. 2) was synthesized. The MIDOA extractant has a high extraction ability for oxyanions, such as MO_4^- (M = ^{99}Tc and Re), in liquid-liquid extraction [1], although the mechanism remains unresolved. If we assume that (i) a $H^+MIDOA\cdots TcO_4^-$ complex, where the H^+MIDOA ion is created by attachment of H^+ to MIDOA, is formed in organic phase to keep the chemical system electronically neutral and (ii) the oxidation state of MO_4^- remains unaltered during the extraction process, we can derive the following equation of extraction equilibrium from the aqueous to the organic phase:

$$k\ MO_4^- + m\ MIDOA + k\ H^+$$
$$\rightarrow k\ [H^+MIDOA\cdots MO_4^-] + (m{-}k)\ MIDOA. \qquad (1)$$
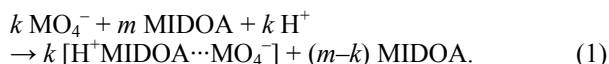
To examine the proposed process, we investigated the structure of the $^{99}TcO_4^-$ complex with MIDOA in organic solution by ATR FT-IR and Extended X-ray Absorption Fine Structure (EXAFS) spectroscopy and analyzed the spectra based on calculated structures and frequencies by density functional theory (DFT).

EXPERIMENTAL. Organic solutions of the complex of TcO_4^- with MIDOA were prepared by mixing the organic solution of 80–100 mM MIDOA with aqueous solutions of 200 mM HCl and 20 mM $KTcO_4$. The IR spectrum of the complex in the organic solution was measured with an FT-IR spectrometer (Spectrum 2000, Perkin Elmer) equipped with a mercury cadmium telluride (MCT) detector. For the spectral region between 1800 and 2800 cm^{-1} a ZnSe crystal was used whereas for the other spectral regions diamond was the internal reflecting element. EXAFS measurements were performed at the Tc K-edge (21.05 keV) in transmission mode at the Rossendorf Beamline.

RESULTS. Figure 1 shows observed spectra of the MIDOA molecule (a) and the $H^+MIDOA\cdots TcO_4^-$ complex in CCl_4 (b), respectively. The vibrational bands of CCl_4 and H_2O/CO_2 in air were subtracted. Both spectra show sharp bands at ~2900 and 1650 cm^{-1}, which are assigned to stretching modes of C–H and C=O, respectively. In addition to these vibrations, spectrum b shows a broad band centering at 3300 cm^{-1} and a sharp one at ~900 cm^{-1}. The broad band at 3300 cm^{-1} can be assigned to stretching modes of the $N–H^+$ or $O–H^+$ bonds of H^+MIDOA, because it was red-shifted by replacement of H^+ with D^+. The band at ~900 cm^{-1} is ascribed to the ν_2 mode of TcO_4^-.

By EXAFS spectroscopy we determined a Tc–O coordination number (CN) of 3.8 in H_2O and of 4.0 in the organic phase, both values correspond to a CN of four within the uncertainty of the method (± 0.5, data not shown). This confirms that Tc is dissolved in the HCl so-
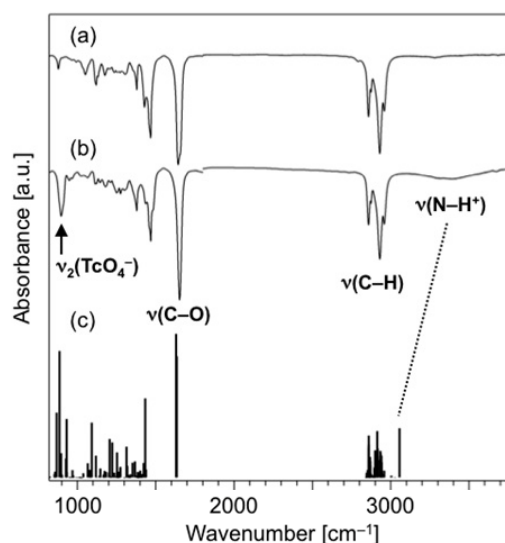
Fig. 1: Observed IR spectra of (a) MIDOA and (b) $H^+MIDOA\cdots TcO_4^-$ complex, and (c) simulated spectrum of $H^+MIDOA\cdots TcO_4^-$ complex.

lution as TcO_4^- and does not change its oxidation states during extraction into the organic phase.

Figure 2 shows the most stable structure of the $H^+MIDOA\cdots TcO_4^-$ complex derived by B3LYP/cc-pVDZ calculation. The MO_4^- anion interacts through three $O\cdots H–C$ hydrogen bonds with the H^+MIDOA ion, which is formed by attachment of a proton to the N moiety of MIDOA. In this structure, the proton pulls the electrons and increases positive charge on all H atoms in the $–CH_2–N(CH_3)–CH_2–$ moiety. The increase of positive charge is assumed to intensify the $O\cdots H–C$ hydrogen bonds. The simulated IR spectrum of $H^+MIDOA\cdots TcO_4^-$ is shown in Fig. 1 (c). The good agreement of the observed and simulated spectra strongly suggests the presence of the $H^+MIDOA\cdots TcO_4^-$ complex as shown in Fig. 2. Based on the structure, the broad band at 3300 cm^{-1} obviously represents the $N–H^+$ stretching mode.
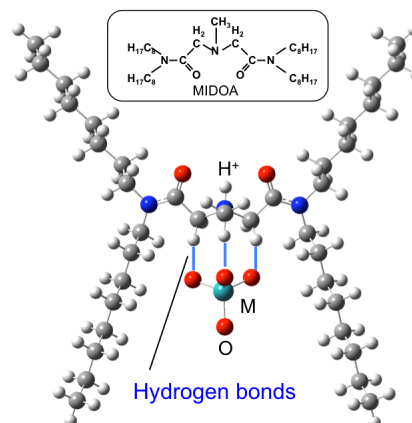
Fig. 2: Optimized structure of the $H^+MIDOA\cdots TcO_4^-$ complex in B3LYP/cc-pVDZ calculation. Chemical formula of MIDOA is shown in inset.

[1] Sasaki, Y. et al. (2007) *Chemistry Letters* **36**, 1394-1395.

EXAFS and XPS investigation of Sb(V) reduction on Mackinawite: effect of pH and surface loading

D. Banerjee, R. Kirsch, A. C. Scheinost

Reduction of Sb(V) at the surface of nanoparticulate mackinawite was studied using X-ray photoelectron spectroscopy (XPS) and extended X-ray absorption fine structure (EXAFS) spectroscopy. Two series of experiments, at pH 5 and pH 8 respectively, were conducted where four different Sb concentrations (0.1, 0.3, 0.6, 0.8 mM) were reacted with aqueous suspension of mackinawite under CO_2-free, anoxic conditions. XPS results demonstrate high surface loading and complete reduction of Sb(V) to Sb(III) at pH 5, whereas at pH 8 lower surface loading coupled with incomplete reduction of Sb(V) is observed. Presence of Fe(III)-O and S^0 as oxidation products were identified at the surface of reacted samples at both pH. Sb K-edge EXAFS results indicate that Sb(III) atoms form inner-sphere complex with three sulfur atoms at pH 5. At pH 8, however, only a small part of Sb(V) is reduced to Sb(III) which is most likely bound to S atoms, while the remaining Sb(V) atoms are in edge sharing and bidentate corner sharing linkages with Fe(O,OH)$_6$ octahedra which are formed as a reaction product.

EXPERIMENTAL. Nanoparticulate mackinawite samples were prepared and stored as suspensions under strictly anoxic conditions in a Jacomex glovebox. Sorption experiments at pH 5 and pH 8 with increasing Sb concentrations (0.1, 0.3, 0.6, 0.8 mM) were also conducted in the same glovebox under anoxic conditions. X-ray Photoelectron Spectroscopy (XPS) and X-ray Absorption Spectroscopy (XAS) measurements were conducted on frozen wet pastes of reacted mackinawite samples.

RESULTS. Sb3d XPS spectra of reacted sample series at pH 5 revealed presence of increasing amounts of Sb(III) at the surface suggesting that the rate of reduction of Sb(V) was directly proportional to surface loading (Fig. 1). Corresponding Fe 2p and S 2p spectra of the same samples showed significant increase in the proportion of Fe(III) species and presence of S^0 at the surface. However, the proportion of S^0 remained constant suggesting that Fe is the dominant redox partner in this system. At pH 8, presence of Sb(III) was only observed at higher surface loadings (Figure 1) indicating that adsorption and redox processes both occur at much slower rate compared to that at pH 5. In addition, increased contribution of surface monosulfide groups at pH 5 suggest that Sb is most likely coordinated to S atoms, which was confirmed by Sb K-edge EXAFS spectra. In contrast, at pH 8, such increase in surface monosulfide contributions is absent, suggesting Sb is most likely bound to O atoms at the surface. The EXAFS results from the sample series at pH 8 suggest that most of the Sb(V) atoms, are in edge sharing and bidentate corner sharing linkages with Fe(O,OH)$_6$ octahedral units, a bonding mechanisms observed fro Sb(V) under oxic conditions [1,2]. However, a small proportion of Sb atoms, most likely the reduced Sb species Sb(III), are also bound to sulfur atoms (Tab. 1).

The results further confirm our previous EXAFS study [3] where similar reaction products were also identified under different experimental conditions.
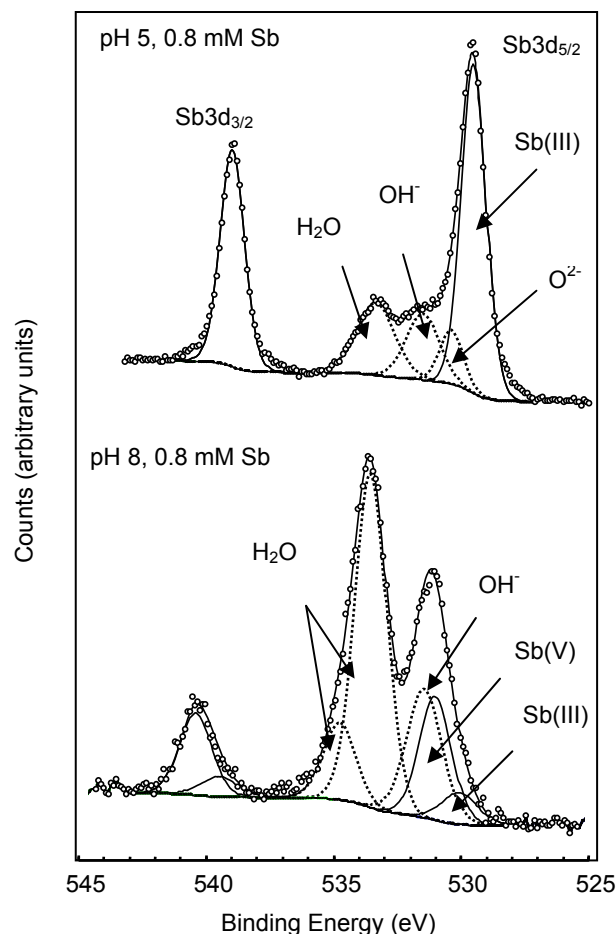
Fig. 1: Fitted Sb3d and O1s spectra for Sb-reacted mackinawite samples at pH 5 and pH 8.

Tab. 1: Fitting parameters for EXAFS spectra.

Sample	Shell	C.N.	Distance [Å]	σ^2
0.3 mM Sb, pH 5	Sb–S	3.0	2.48	0.0039
	Sb–Sb	0.6	3.81	0.0078
0.1 mM Sb, pH 8	Sb–O	3.7	1.98	0.0043
	Sb–S	1.0	2.44	0.0037
	Sb–Fe	1.0	3.12	0.0038
	Sb–Fe	2.0	3.55	0.0038
0.8 mM Sb, pH 8	Sb–O	4.8	1.97	0.0033
	Sb–S	0.2	2.46	0.0033
	Sb–Fe	1.0	3.09	0.0058
	Sb–Fe	2.3	3.55	0.0058

It is evident that Sb(III) has a higher affinity towards S coordination, while Sb(V) has a higher affinity towards O coordination, which – together with the pH effects – explains the observed differences in bonding and reduction.

[1] Mitsunobu et al. (2010) *Environ. Sci. & Technol.* **44**, 3712-3718.
[2] Scheinost, A.C. et al. (2006) *Geochim. Cosmochim. Acta* **70**, 3299-3312.
[3] Kirsch, R. et al. (2008) *Mineral. Mag.* **72**, 185-189.

Sorption of Se(VI) onto anatase

N. Jordan, H. Foerstendorf, S. Weiß, K. Heim, D. Schild,[1] V. Brendler

[1] Institute for Nuclear Waste Disposal, Karlsruhe Institute of Technology, Karlsruhe, Germany

The sorption processes of Se(VI) onto anatase have been investigated. The increase of pH and ionic strength led to a decrease of Se(VI) sorption. Zeta potential measurements showed that sorption of Se(VI) did not impact the pH_{IEP} of anatase, but involved a decrease of its net positive surface charge at $pH < pH_{IEP}$. Finally, *in situ* ATR FT-IR measurements revealed the formation of outer-sphere complexes during the sorption process.

In the context of nuclear waste management, [79]Se could be one of the major isotopes contributing to the global radioactivity potentially reaching the biosphere. Anatase (TiO_2 polymorph) is ubiquitous in the environment and is also present as an accessory mineral in many compounds (e.g. kaolinite). In addition, titanium oxide is very often used as a model oxide because of its high stability, low solubility over a wide pH range and its well-known structure. Thus, this study was aiming at characterizing at both macroscopic and microscopic levels the sorption process of Se(VI) onto anatase.

EXPERIMENTAL. Anatase (MTI Corporation, No. NP-TiO_2-A-10) is a polycrystalline powder with a high purity (99.99%) and a high specific surface area ($234 \ m^2 \ g^{-1}$). To avoid the activation of anatase photocatalytic properties, sorption experiments have been done under dark conditions. The effect of the pH and Se(VI) sorption onto anatase zeta potential was evaluated by using Laser-Doppler-Electrophoresis (nano-ZS, Malvern Instruments Ltd.). *In situ* ATR FT-IR spectra were recorded in the mid-IR region using a Bruker Vertex 80v instrument with a KRS5-diamond ATR accessory equipped with a flow cell. The detailed procedure of batch sorption studies, zeta potential measurements and *in situ* ATR FT-IR sorption experiments has been given elsewhere [1].

RESULTS. Se(VI) sorption onto anatase depends on both the pH and ionic strength (Fig. 1). Indeed, maximum sorption is achieved in the acidic pH range and decreases with increasing pH and ionic strength. XPS studies (data not shown) evidenced the absence of heterogeneous reduction of Se(VI) at the anatase surface. Thus, only sorption processes are responsible for the withdrawal of

Fig. 2: Zeta potential of anatase (open diamonds) and the effect of Se(VI) sorption (filled squares), $m/V = 0.1 \ g \ L^{-1}$, $[Se^{VI}]_{initial} = 5 \cdot 10^{-4} \ M$, 0.1 M NaCl, 3 days of stirring.
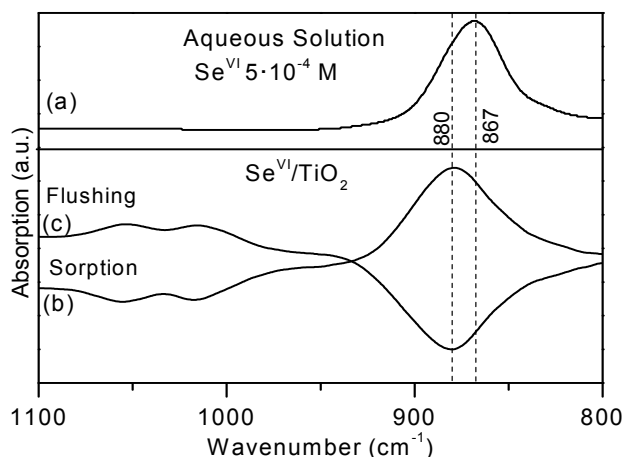
Fig. 3: *In situ* ATR FT-IR spectra of 500 μM Se(VI) (a) in aqueous solution, (b) sorbed on TiO_2 (c) desorbed from TiO_2 (D_2O, pD 3.6, 0.1 M NaCl, N_2). Indicated values are in cm^{-1}.

Se(VI) from the liquid phase to the solid phase.

The zeta potential is strongly dependent on the pH, ranging from ~ 26 mV at pH = 3.5 to ~ −29 mV at pH = 11.0 (Fig. 2). The net negative charge of anatase increases when pH increases. After addition of Se(VI), the pH_{IEP} of anatase is not affected. However, the net positive charge of anatase it decreased at pH < 5.5. These two observations are both strong indications of an electrostatic interaction process between the anatase surface and SeO_4^{2-} ions [2].

Finally, *in situ* ATR FT-IR measurements (Fig. 3) revealed the formation of outer-sphere complexes during Se(VI) sorption onto anatase. The asymmetric Se-O stretching vibration of SeO_4^{2-} ions is slightly blue shifted (867 to 880 cm^{-1}) upon sorption indicating that the tetrahedral symmetry (T_d) of Se(VI) ions cannot be significantly changed. Consequently, the formation of inner-sphere complexes with a completely different molecule symmetry is unlikely. Similar surface complexes were observed from experiments performed at higher pH, higher Se(VI) surface coverage and lower ionic strength (data not shown).

[1] Jordan, N. et al. (2011) *Geochim. Cosmochim. Acta,* accepted.
[2] Elzinga, E.J. et al. (2009) *J. Colloid Interf. Sci.* **340**, 153-159.
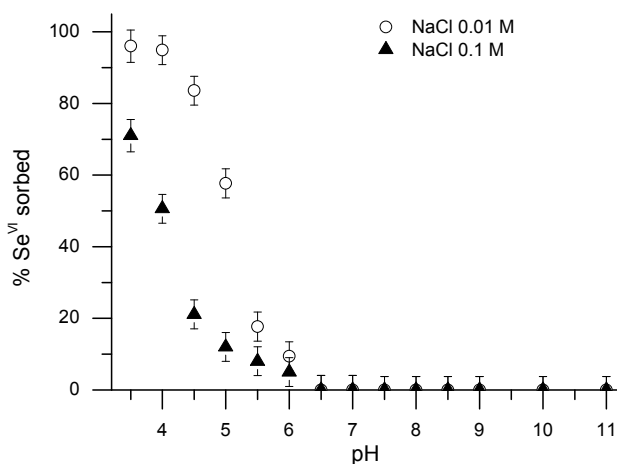
Fig. 1: Sorption edges of Se(VI) onto anatase. $m/V = 0.46 \ g \ L^{-1}$, 0.1 and 0.01 M NaCl, $[Se^{VI}]_{initial} = 1 \cdot 10^{-5} \ M$, 3 days of stirring.

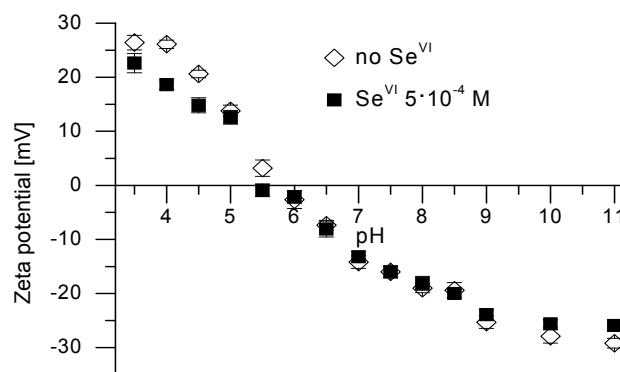# Sensitivity and uncertainty analysis applied to selenium sorption onto goethite

V. Brendler, C. Ekberg,[1] A. Ödegaard-Jensen[1]

[1]Department of Chemical and Biological Engineering, Chalmers University of Technology, Gothenburg, Sweden

One of the major contributors to the overall radiological risk of nuclear waste disposal is ^{79}Se. Sensitivity analysis of its sorption onto goethite revealed that namely the uncertainty of the unprotonated inner-sphere surface complexes affects the overall uncertainty of the distribution coefficient K_D, independent from the redox state. Moreover, the uncertainty of the computed K_D values is in the order of about 5-30%.

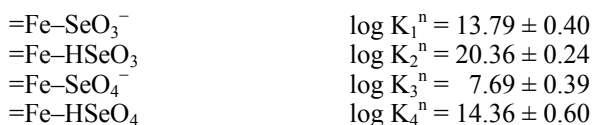**DATA & MODEL.** Quality-assurance of long-term safety assessment studies for nuclear waste repositories requires the identification of the most sensitive geochemical and thermodynamic model input parameters [1] by means of sensitivity analysis (SA) and uncertainty analysis (UA). Goethite is a well defined mineral and often used model substrate, thus 21 independently published surface protolysis data records [2] based on the Diffuse Double Layer Model could be averaged (after normalization to a reference site density of 2.31 sites/nm²), yielding $pK_1^n = 7.04 \pm 0.15$ and $pK_2^n = 9.41 \pm 0.24$. Based on the available literature, for both Se oxidation states a protonated and an unprotonated inner-sphere surface complex was selected as most probable species, with the following formation constants:

$=Fe–SeO_3^-$	$\log K_1^n = 13.79 \pm 0.40$
$=Fe–HSeO_3$	$\log K_2^n = 20.36 \pm 0.24$
$=Fe–SeO_4^-$	$\log K_3^n = 7.69 \pm 0.39$
$=Fe–HSeO_4$	$\log K_4^n = 14.36 \pm 0.60$

A specific surface area for goethite of 44.0 ± 2.8 m²/g was derived from the (log-normal) distribution of 124 published values [2]. The aqueous speciation of selenate and selenite (basically the hydrolysis steps of H_2SeO_4 and H_2SeO_3) is based on the NEA TDB review [3].

SA and UA tests for distribution coefficient K_D were performed on six different pH levels, for two different total selenium concentrations 10^{-4} M and 10^{-7} M), and for two different redox scenarios (300 mV and 800 mV), the solid-liquid ratio was set to 10 g/L, and atmospheric carbonate was excluded.

RESULTS. *A) Sensitivity analysis:* Whereas the right hand side of Fig. 1 summarized the ranking of the various input parameters as a function of the pH for an oxidizing environment (i.e. selenate as dominating Se oxidations state), the left hand side of Fig. 1 presents the results for a reducing environment, i.e. with selenite dominating. It is evident that the stability constants for the various Se surface complexes are the most sensitive input parameters. Independent from the Se oxidation state the respective protonated surface complex is ranked most sensitive for pH < 7 whereas the deprotonated one becomes most important above pH 7. At pH 7, the two surface complexes are equally important, and here even the protolysis constants of the goethite surface are similar in their sensitivity. In both cases the total selenium concentration has no measurable effect on the sensitivity ranking.

B) Uncertainty analysis: Concerning the case for reducing conditions i.e. selenite Se^{IV} (cf. Tab. 1), the values show the pH dependence typical for anions sorbing onto metal oxides. The uncertainty increases from about 5% under acidic conditions up to about 30% at pH 9. Note that for
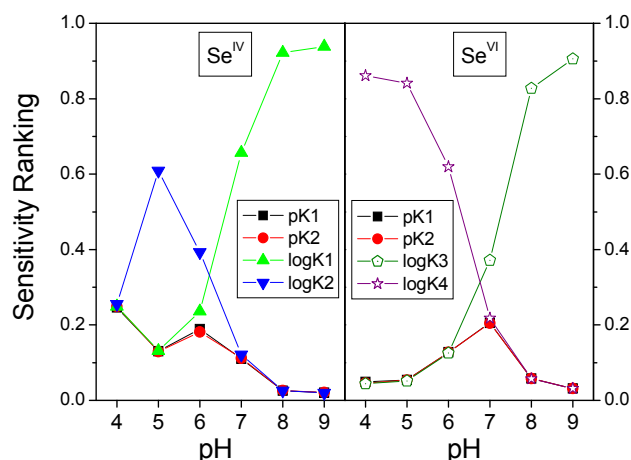

Fig. 1: Sensitivity ranking of reaction constant fro Se sorption onto goethite as a function of pH for two different redox states.

Tab. 1: K_D mean values and uncertainties for ^{79}Se as a function of pH and redox state. All K_D values are given in [L/g].

pH	4	5	6	7	8	9
Se(IV) @ 300 mV						
K_D mean	925	564	182	62.4	27.9	4.6
K_D uncertainty	41	71	49	14.0	7.4	1.3
Se(VI) @ 800 mV						
K_D mean	48.4	1.13	0.019	$5 \cdot 10^{-4}$	$4 \cdot 10^{-5}$	$4 \cdot 10^{-6}$
K_D uncertainty	14.7	0.34	0.005	$1 \cdot 10^{-4}$	$1 \cdot 10^{-5}$	$1 \cdot 10^{-6}$

pH 4 the Se sorption is computed to be nearly quantitative, with almost complete removal of Se from solution. Contrary to that, under oxidizing conditions (Se^{VI}) the computed K_D values are much lower than for the reducing conditions, with the difference becoming even larger when increasing pH. The associated uncertainty is consistently large around 30%.

For both redox scenarios, the total selenium concentration of course affects the size of K_D but only marginally (data not shown) and it does not alter the relative uncertainty.

With respect to the log K for the $=Fe–SeO_3^-$ formation (in the lower pH range) and for $=Fe–HSeO_3$ (for pH > 6), a reduction in uncertainty for these values will directly generate a higher confidence in the Se distribution coefficients. Similarly, assigning a smaller uncertainty on the complex formation constant log K for $=Fe–HSeO_4$ (the species $=Fe–SeO_4^-$ is here not relevant – despite its high uncertainty – as the K_D at pH above 6 is very small anyway) may considerably increase confidence in computed K_D values.

[1] Ochs, M. et al. (2011) *Thermodynamic Sorption Modeling in Support of Radioactive Waste Disposal Safety Cases*, NEA Report, Paris.
[2] Brendler, V. et al. (2003) *J. Contam. Hydrol.* **61**, 281-291.
[3] Olin, Å. et al. (2005) *Chemical Thermodynamics of Selenium. Chemical Thermodynamics Vol. 7*, Elsevier, Amsterdam.

ESTRAL – Conception and implementation of realistic geochemical parameters in the transport program r³t

M. Stockmann, V. Brendler, U. Noseck,[1] J. Flügge,[1] M. Lampe[2]

[1]Gesellschaft für Anlagen- und Reaktorsicherheit mbH, Braunschweig, Germany; [2]Steinbeis-Institut, Frankfurt a.M., Germany

In the framework of the ESTRAL project (Realistic Integration of Sorption Processes in Transport Programs for long-term Safety Analysis), the existing transport code r³t (radionuclide, reaction, retardation, and transport) [1] is modified to represent the sorption of repository-relevant elements under changing geochemical conditions more realistically.

This is done by implementing smart K_d values (computed distribution coefficients) which vary in time and space depending on the actual geochemical conditions [2]. The Gorleben site, a potential repository site in Germany has been selected as application case for a proof-of-concept. The most relevant environmental parameters in the overlying sedimentary rock there need to be identified and considered in the transport code r³t.

VARIATION OF INFLUENCE PARAMETERS. The sorption of radionuclides onto the relevant mineral phases is modelled in PhreeqC [3] as a function of important environmental parameters. Parameter variation and assembling of K_d matrices is performed by UCODE [4]. To keep the complexity and the calculation time at a minimum, the number of such parameters was limited and only those were selected having an important influence onto sorption processes. Following environmental parameters E1-E6 were selected:

- E1: pH value
- E2: DIC (dissolved inorganic carbon content)
- E3: Ionic strength I (salt concentration)
- E4: Total concentration of Al
- E5: Total concentration of Ca
- E6: Radionuclide total concentration

Figure 1 shows the interaction of these influencing parameters and their potential integration in r³t.
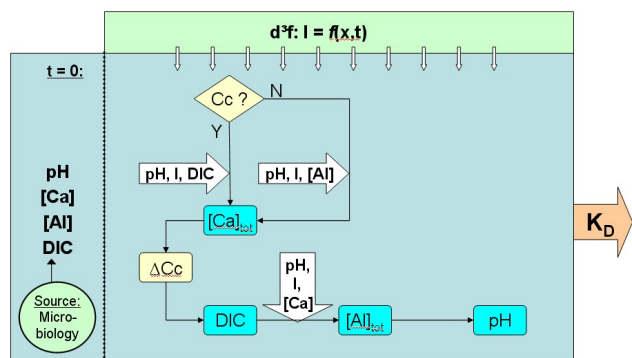

Fig. 1: Chemical influence parameters and their interaction.

CONCEPTIONAL MODEL. Most of these individual parameters E_i are not available in r³t so far. Therefore the code is to be modified by the Steinbeis-Institute. The following procedure is suggested for the coupling of transport and chemistry at each time-space point:

(i) Calculation of Al-, Ca-, DIC-concentration and pH based on the transport parameters: $[Al]^T$, $[Ca]^T$, DIC^T and pH^T.

(ii) Calculation of the equilibrium concentration for:

- **[Ca]:** $[Ca]^G = f([Al]^T, DIC^T, pH^T, I)$
  → Setting the new Ca-concentration $[Ca]^*$ as a mean of $[Ca]^T$ and $[Ca]^G$

- **DIC:** $DIC^G = DIC^T - \Delta Ca^{2+}$
  for solution / precipitation of the same amount of Ca and DIC (only done if calcite is oversaturated or already present)

- **[Al]:** $[Al]^G = f([Ca]^*, DIC^G, pH^T, I)$
  → Setting the new Al-concentration $[Al]^*$ as a mean of $[Al]^T$ and $[Al]^G$

- **pH:** $pH^G = f([Ca]^*, DIC^G, I)$, or
  $pH^G = f([Ca]^*, [Al]^*, DIC^G, I)$, if there is no calcite
  → Setting the new pH^* as a mean of pH^T and pH^G

The ionic strength (**I**) is derived from the distribution of relative NaCl concentrations provided by the code d³f (distributed density driven flow) [5]. The maximum concentrations of radionuclides **[RN]** were estimated from [6]. We assume that the radionuclides do not influence each other and neither (except uranium) the geochemical milieu.

For coupling the transport and chemistry, the calculated smart K_d values have to be acessible from within r³t at each time-space point for the correct geochemical conditions. The main challenge here is finding a fast and robust algorithm for search in multidimensional matrices. The simplest case (pursued at the moment) is an equidistant grid for each dimension. This, however, does not take into account that each environmental parameter is subject to a specific distribution function, which usually is not the uniform distribution. Thus, more realistic distributions have to be implemented later.

[1] Fein, E. (2004) *Report GRS-192*.
[2] Stockmann, M. et al. (2009) *Report FZD-530,* p. 33.
[3] Parkhurst, D.L. et al. (1999) *U.S.G.S. Report 99-425*.
[4] Poeter, E.P. et al. (2005) *U.S.G.S. Techniques and Methods 6-A11*, 283 p., Reston.
[5] Fein, E. et al. (1999) *Report GRS-139*.

▷ ARTICLES (PEER-REVIEWED)

▷ PROCEEDINGS, REPORTS, CONTRIBUTIONS

▷ LECTURES, ORAL PRESENTATIONS

▷ POSTERS

▷ THESES

▷ MASTER, DIPLOMA

▷ ARTICLES (PEER-REVIEWED)

Arnold, T.; Großmann, K.; Baumann, N.
Uranium speciation in biofilms studied by laser fluorescence techniques
Analytical and Bioanalytical Chemistry 396, 1641-1653 (2010).

Breynaert, E.; Scheinost, A.C.; Dom, D.; Rossberg, A.; Vancluysen, J.; Gobechiya, E.; Kirschhock, C.E.A.; Maes, A.
Reduction of Se(IV) with Boom clay: XAS solid phase speciation
Environmental Science & Technology 44, 6649-6655 (2010).

Brockmann, S.; Arnold, T.; Schweder, B.; Bernhard, G.
Visualizing acidophilic microorganisms in biofilm communities using acid stable fluorescence dyes
Journal of Fluorescence 20, 943-951 (2010).

Burkhardt, E.M.; Akob, D.M.; Bischoff, S.; Sitte, J.; Kostka, J.E.; Banerjee, D.; Scheinost, A.C.; Kuesel, K.
Impact of biostimulated redox processes on metal dynamics in an iron-rich creek soil of a former uranium mining area
Environmental Science & Technology 44, 177-183 (2010).

Chakraborty, S.; Boivin, F.; Banerjee, D.; Scheinost, A.; Mullet, M.; Ehrhardt, J.J.; Brendle, J.; Vidal, L.; Charlet, L.
U(VI) sorption and reduction by Fe(II) sorbed on montmorillonite
Environmental Science & Technology 44, 3779-3785 (2010).

Chave, T.; Nikitenko, S.I.; Scheinost, A.C.; Berthon, C.; Arab-Chapelet, B.; Moisy, P.
First synthesis of uranyl aluminate nanoparticles
Inorganic Chemistry 49, 6381-6383 (2010).

Conroy, D.J.R.; Millner, P.A.; Stewart, D.I.; Pollmann, K.
Biosensing for the environment and defence: aqueous uranyl detection using bacterial surface layer proteins
Sensors 10, 4739-4755 (2010).

Cotte, M.; Auffan, M.; Degruyter, W.; Fairchild, I.; Newton, M.; Morin, G.; Sarret, G.; Scheinost, A.C.
Environmental sciences at the ESRF
Synchrotron Radiation News 23, 28-35 (2010).

Franke, K.; Kupsch, H.
Radioiodination of humic substances
Radiochimica Acta 98, 333-339 (2010).

Gaillard, C.; Chaumont, A.; Billard, I.; Hennig, C.; Ouadi, A.; Georg, S.; Wipff, G.
Competitive complexation of nitrates and chlorides to uranyl in a room temperature ionic liquid
Inorganic Chemistry 49, 6484-6494 (2010).

Heller, A.; Rönitz, O.; Barkleit, A.; Bernhard, G.; Ackermann, J.U.
Complexation of europium(III) with the zwitterionic form of amino acids studied with UV/vis and time-resolved laser-induced fluorescence spectroscopy
Applied Spectroscopy 64, 930-935 (2010).

Hennig, C.; Ikeda-Ohno, A.; Emmerling, F.; Kraus, W.; Bernhard, G.
Comparative investigation of the limiting solution species $[U(CO_3)_5]^{6-}$ and the crystal structure of $Na_6[U(CO_3)_5] \cdot 12H_2O$
Dalton Transactions 39, 3744-3750 (2010).

Hennig, C.; Skanthakumar, S.; Soderholm, L.
Double photoexcitation of 2p and 4f electrons in curium
Journal of Electron Spectroscopy and Related Phenomena 180, 17-20 (2010).

Jankowski, U.; Merroun, M.L.; Selenska-Pobell, S.; Fahmy, K.
S-Layer protein from *Lysinibacillus Sphaericus* JG-A12 as matrix for Au(III) sorption and Au-nanoparticle formation
Spectroscopy 24, 177-181 (2010).

Jeanson, A.; Ferrand, M.; Funke, H.; Hennig, C.; Moisy, P.; Solari, P.L.; Vidaud, C.; Den Auwer, C.
The role of transferrin in actinide(IV) uptake: comparison with iron(III)
Chemistry - A European Journal 16, 1378-1387 (2010).

Kempe, U.; Thomas, S.M.; Geipel, G.; Thomas, R.; Plötze, M.; Böttcher, R.; Grambole, G.; Hoentsch, J.; Trinkler, M.
Optical absorption, luminescence, and electron paramagnetic resonance (EPR) spectroscopy of crystalline to metamict zircon: evidence for formation of uranyl, manganese, and other optically active centers
American Mineralogist 95, 335-347 (2010).

Kim, S.Y.; Takao, K.; Haga, Y.; Yamamoto, E.; Kawata, Y.; Morita, Y.; Nishimura, K.; Ikeda, Y.
Molecular and crystal structures of plutonyl(VI) nitrate complexes with N-alkylated 2-pyrrolidone derivatives: cocrystallization potentiality of U(VI) and Pu(VI) for uniform MOX fuel precursor
Crystal Growth & Design 10, 2033-2036 (2010).

Kristinsdóttir, L. H.; Flóvenza, O. G.; Árnasona, K.; Bruhn, D.; Milsch, H.; Spangenberg, E.; Kulenkampff, J.
Electrical conductivity and P-wave velocity in rock samples from high-temperature Icelandic geothermal fields
Geothermics, 39, 94–105 (2010).

Kubeil, M.; Stephan, H.; Pietzsch, H.J.; Geipel, G.; Appelhans, D.; Voit, B.; Hoffmann, J.; Brutschy, B.; Mironov, Y.V.; Brylev, K.A.; Fedorov, V.E.
Sugar-decorated dendritic nanocarriers: encapsulation and release of the octahedral rhenium cluster complex $[Re_6S_8(OH)_6]^{4-}$
Chemistry - An Asian Journal 5, 2507-2514 (2010).

Lederer, F.; Günther, T.; Flemming, K.; Raff, J.; Fahmy, K.; Springer, A.; Pollmann, K.
Heterologous expression of the S-layer-like protein SllB induces the formation of long filaments of *E. coli* consisting of protein stabilized outer membrane
Microbiology 156, 3584-3595 (2010).

Lehmann, S.; Geipel, G.; Grambole, G.; Bernhard, G.
Complexation of aqueous uranium(IV) with phosphate investigated using time-resolved laser-induced fluorescence spectroscopy (TRLFS)
Journal of Radioanalytical and Nuclear Chemistry 283, 395-401 (2010).

Li, B.; Barkleit, A.; Raff, J.; Bernhard, G.; Foerstendorf, H.
Complexation of U(VI) with highly phosphorylated protein, phosvitin. A vibrational spectroscopic approach
Journal of Inorganic Biochemistry 104, 718-725 (2010).

Liu, J.; Chen, Y.; Wang, J.; Qi, J.; Wang, C.; Lippold, H.; Lippmann-Pipke, J.
Factor analysis and sequential extraction unveil geochemical processes relevant for trace metal distributions in fluvial sediments of a pyrite mining area, China
Carbonates and Evaporites 25, 51-63 (2010).

Liu, J.; Wang, J.; Chen, Y.; Lippold, H.; Lippmann-Pipke, J.
Comparative characterization of two natural humic acids from the Pearl River Basin, China, and their environmental implications
Journal of Environmental Sciences - China 22, 1695-1702 (2010).

Liu, J.; Wang, J.; Chen, Y.; Qi, J.; Lippold, H.; Wang, C.
Thallium distribution in sediments from the Pearl River Basin, China
Clean - Soil, Air, Water 38, 909-915 (2010).

Mendes, M.; Hamadi, S.; Le Naour, C.; Roques, J.; Jeanson, A.; Den Auwer, C.; Moisy, P.; Topin, S.; Aupiais, J.; Hennig, C.; Di Giandomenico, M.V.
Thermodynamical and structural study of protactinium(V) oxalate complexes in solution
Inorganic Chemistry 49, 9962-9971 (2010).

Moll, H.; Johnsson, A.; Schäfer, M.; Glorius, M.; Pedersen, K.; Budzikiewicz, H.; Bernhard, G.
Neptunium(V) complexation by natural pyoverdins and related model compounds
Radiochimica Acta 98, 571-576 (2010).

Müller, M.; Acker, M.; Taut, S.; Bernhard, G.
Complex formation of trivalent americium with salicylic acid at very low concentrations
Journal of Radioanalytical and Nuclear Chemistry 286, 175-180 (2010).

Nebelung, C.; Brendler, V.
U(VI) sorption on granite: Prediction and experiments
Radiochimica Acta 98, 621-625 (2010).

Neu, M. P.; Boukhalfa, H.; Merroun, M. L.
Biomineralization and biotransformations of actinide materials.
MRS Bulletin 35, 849-857 (2010).

Planer-Friedrich, B.; Suess, E.; Scheinost, A.C.; Wallschläger, D.
Arsenic speciation in sulfidic waters: consolidation of contradictory spectroscopic and chromatographic evidence
Analytical Chemistry 82, 10228-10235 (2010).

Raditzky, B.; Schmeide, K.; Sachs, S.; Geipel, G.; Bernhard, G.
Interaction of uranium(VI) with nitrogen containing model ligands studied by laser-induced fluorescence spectroscopy
Polyhedron 29, 620-626 (2010).

Reitz, T.; Merroun, M.L.; Rossberg, A.; Selenska-Pobell, S.
Interactions of Sulfolobus acidocaldarius with uranium
Radiochimica Acta 98, 249-257 (2010).

Rossberg, A.; Funke, H.
Determining the radial pair distribution function from X-ray absorption spectra by use of the Landweber iteration method
Journal of Synchrotron Radiation 17, 280-288 (2010).

Sachs, S.; Reich, T.; Bernhard, G.
Study of the role of sulfur functionalities in humic acids for uranium(VI) complexation
Radiochimica Acta 98, 467-477 (2010).

Schmeide, K.; Bernhard, G.
Sorption of Np(V) and Np(IV) onto kaolinite: effects of pH, ionic strength, carbonate and humic acid
Applied Geochemistry 25, 1238-1247 (2010).

Sitte, J.; Akob, D.; Kaufmann, C.; Finster, K.; Banerjee, D.; Burkhardt, E.M.; Kostka, J.; Scheinost, A.; Büchel, G.; Küsel, K.
Microbial links between sulfate reduction and metal retention in uranium- and heavy metal-contaminated soil
Applied and Environmental Microbiology 76, 3143-3152 (2010).

Steudtner, R.; Arnold, T.; Geipel, G.; Bernhard, G.
Fluorescence spectroscopic study on complexation of uranium(VI) by glucose - A comparison of room and low temperature measurements
Journal of Radioanalytical and Nuclear Chemistry 284, 421-429 (2010).

Takao, K.; Ikeda, Y.
μ-η²: η²-Peroxo-bis[nitratobis(pyrrolidine-2-one)dioxouranium(VI)]
Acta Crystallographica Section E E66, m539-m540 (2010).

Takao, K.; Kato, M.; Takao, S.; Nagasawa, A.; Bernhard, G.; Hennig, C.; Ikeda, Y.
Molecular structure and electrochemical behavior of uranyl(VI) complex with pentadentate schiff base ligand: prevention of uranyl(V) cation-cation interaction by fully chelating equatorial coordination sites
Inorganic Chemistry 49, 2349-2359 (2010).

Takao, K.; Takao, S.; Scheinost, A.C.; Bernhard, G.; Hennig, C.
In situ spectroelectrochemical investigation of Pt(II/IV) oxidation in aqueous solution using X-ray absorption spectroscopy
Inorganica Chimica Acta 363, 802-806 (2010).

Tanh Jeazet, H.; Gloe, K.; Doert, T.; Kataeva, O.; Jaeger, A.; Geipel, G.; Bernhard, G.; Büchner, B.; Gloe, K.
Self-assembly of neutral hexanuclear circular copper(II) meso-helicates: topological control by sulfate ions
Chemical Communications 46, 2373-2375 (2010).

Tsushima, S.; Brendler, V.; Fahmy, K.
Aqueous coordination chemistry and photochemistry of uranyl(VI) oxalate revisited: a density functional theory study
Dalton Transactions 39, 10953-10958 (2010).

Tsushima, S.; Götz, C.; Fahmy, K.
Photoluminescence of uranium(VI): quenching mechanism and role of uranium(V)
Chemistry - A European Journal 16, 8029-8033 (2010).

Viehweger, K.; Geipel, G.
Uranium accumulation and tolerance in *Arabidopsis halleri* under native versus hydroponic conditions
Environmental and Experimental Botany 69, 39-46 (2010).

Vogel, M.; Günther, A.; Rossberg, A.; Li, B.; Bernhard, G.; Raff, J.
Biosorption of U(VI) by the green algae *Chlorella vulgaris* in dependence of pH value and cell activity
Science of the Total Environment 409, 384-395 (2010).

Vulpius, D.; Geipel, G.; Bernhard, G.
Excited-state proton transfer of 3-hydroxybenzoic acid and 4-hydroxybenzoic acid
Spectrochimica Acta Part A 75, 558-562 (2010).

Wiebke, J.; Weigand, A.; Weißmann, D.; Glorius, M.; Moll, H.; Bernhard, G.; Dolg, M.
Combined computational and experimental study of uranyl(VI) 1:2-complexation by aromatic acids
Inorganic Chemistry 49, 6428-6435 (2010).

Wittwer, D.; Abdullin, F.S.; Aksenov, N.V.;
Albin, Y.V.; Bozhikov, G.A.; Dmitriev, S.N.;
Dressler, R.; Eichler, R.; Gäggeler, H.W.;
Henderson, R.A.; Hübener, S.; Kenneally, J.M.;
Lebedev, V.Y.; Lobanov, Y.V.; Moody, K.J.;
Oganessian, Y.T.; Petrushkin, O.V.;
Polyakov, A.N.; Piguet, D.; Rasmussen, P.;
Sagaidak, R.N.; Serov, A.; Shirokovsky, I.V.;
Shaughnessy, D.A.; Shishkin, S.V.;
Sukhov, A.M.; Stoyer, M.A.; Stoyer, N.J.;
Tereshatov, E.E.; Tsyganov, Y.S.;
Utyonkov, V.K.; Vostokin, G.K.;
Wegrzecki, M.; Wilk, P.A.
**Gas phase chemical studies of superheavy
elements using the Dubna gas-filled recoil
separator – Stopping range determination**
*Nuclear Instruments and Methods in Physics
Research B 268, 28-35 (2010).*

Zänker, H.
**In-situ measurements on suspended
nanoparticles with visible laser light, infrared
light and X-rays**
*Nanoparticles in the Water Cycle. Properties,
Analysis and Environmental Relevance
(Nießner, R.; Frimmel, F.H eds.) Springer-
Verlag, Berlin, 117-138 (2010).*

Zänker, H.
Kohlenstoff-Nanoröhren und die Umwelt
GIT Labor-Fachzeitschrift 4, 310 (2010).

▷ PROCEEDINGS, REPORTS, CONTRIBUTIONS

Banerjee, D.; Kirsch, R.; Scheinost, A.C.
**XPS and XAS investigation of Sb(V)
reduction on mackinawite: effect of pH and
surface loading**
*Geochimica et Cosmochimica Acta 74, A47
(2010).*

Baumann, N.; Arnold, T.
**Investigations on seepage waters of the test
site Gessenwiese by TRLFS**
*RadChem 2010 – 16th Radiochemical
Conference, April 18-23, 2010, Mariánské
Lázně, Czech Republic – Chemické listy 104,
S190 (2010).*

Bernhard, G.; Geipel, G.
**Determination of uranium speciation in
aqueous samples by time-resolved laser-
induced fluorescence spectroscopy (TRLFS)**
*Advanced Trace Analysis (Lahiri, S. ed.) Narosa
Publishing House, New Delhi, 127-147 (2010).*

Breynaert, E.; Scheinost, A.; Dom, D.; Rossberg, A.;
Vancluysen, J.; Gobechiya, E.; Kirschhock, C.;
Maes, A.
**The geochemical fate of Se(IV) in the Boom
Clay system – XAS based solid phase speciation**
*Geochimica et Cosmochimica Acta 74, A122
(2010).*

González-Muñoz, M. T.; Rodriguez-Navarro, C.;
Martínez-Ruiz, F., Arias, J. M.; Merroun, M. L.;
Rodriguez-Gallego, M.
**Bacterial biomineralization: new insights
from *Myxococcus* induced mineral
precipitation**
*Tufas and Speleothems: Unravelling the
Microbial and Physical Controls (Pedley, H. M.;
Rogerson, M. eds.) Geological Society, London,
Special Publications, 336, 31-50 (2010).*

Geissler, A.; Selenska-Pobell, S.; Morris, K.;
Livens, F.R.; Lloyd, J.R.
**The microbial ecology of land and water
contaminated with radioactive waste;
towards the development of bioremediation
options for the nuclear industry**
*Ecology of Industrial Pollution (Batty, L.;
Hallberg, K. eds.) Cambridge University Press,
Cambridge, 226-241 (2010).*

Günther, T.; Weinert, U.; Raff, J.; Pollmann, K.
**Self assembling proteins as technology
platform for the development of new bio-
composite materials**
Biomaterialien S1, 35 (2010).

Hennig, C.
**Actinide redox speciation and structure
analysis in aqueous and nonaqueous solutions**
*APS users meeting 2010 – Celebrating 20 Years
of Groundbreaking Science, May 03-05, 2010,
Argonne, U.S.A., 48 (2010).*

Hennig, C.; Ikeda-Ohno, A.; Tsushima, S.; Scheinost, A.
Redox-dependent suphate coordination of neptunium in aqueous solutions
ESRF Highlights 2009 (Admans, G. ed.), European Synchrotron Radiatian Facility, Grenoble, 84-85 (2010).

Hennig, C.; Takao, K.; Takao, S.; Ikeda-Ohno, A.; Banerjee, D.; Weiss, S.; Zaenker, H.; Kraus, W.; Emmerling, F.; Scheinost, A.C.
Chemical bonds and formation process of actinide(IV) oligomers and colloids
Geochimica et Cosmochimica Acta 74, A400 (2010).

Jordan, N.; Foerstendorf, H.; Brendler, V.
Selenium(IV) retention onto ilite
RadChem 2010 – 16th Radiochemical Conference, April 18-23, 2010, Mariánské Lázně, Czech Republic – Chemické listy 104, S115 (2010).

Kirsch, R.; Fellhauer, D.; Altmaier, M.; Neck, V.; Rossberg, A.; Charlet, L.; Scheinost, A. C.
Reaction of Pu(III) and (V) with magnetite and mackinawite: a XANES/EXAFS investigation
Geochimica et Cosmochimica Acta 74, A520 (2010).

Krawczyk-Bärsch, E.
Second reporting of the scientific-technical outcome of WP 4.2: chemical and redox behavior of the investigated radionuclides in the different systems through microbial mediated processes
2nd Annual Workshop Proceedings of the Collaborative Project "Redox Phenomena Controlling Systems" (7th EC FP CP RECOSY), March 16-19, 2010, Larnaca, Cyprus, KIT Scientific Reports 7557, KIT Scientific Publishing, Karlsruhe, 51-54 (2010).

Krawczyk-Bärsch, E.; Steinbrück, D.; Arnold, T.; Schmälzlin, E.; Kumke, M.
Comparative studies on electrochemical and laser-based fiber-optic oxygen microsensors applied to uranium contaminated biofilms
2nd Annual Workshop Proceedings of the Collaborative Project "Redox Phenomena Controlling Systems" (7th EC FP CP RECOSY), March 16-19, 2010, Larnaca, Cyprus, KIT Scientific Reports 7557, KIT Scientific Publishing, Karlsruhe, 139-146 (2010).

Kulenkampff, J.; Wolf, M.; Gründig, M.; Mittmann, H.; Richter, M.
Tomographic investigations of transport processes with radiotracers in evaporitic rock and its hanging wall in Staßfurt
Exkursionsführer und Veröffentlichungen der Deutschen Gesellschaft für Geowissenschaften 242, 95-97 (2010).

Raff, J.
Schlussbericht zum BMBF-Vorhaben "Entwicklung und Erprobung neuer Instrumente zur Bildung von Verwertung- und Transfernetzen" NanoFoto - Neue Wege zur verwertungsorientierten Netzwerkbildung in der Nanobiotechnologie
Wissenschaftlich-Technische Berichte, FZD-529, Forschungszentrum Dresden-Rossendorf (2010).

Richter, A.; Altmaier, M.; Brendler, V.; Marquardt, C.; Moog, H.; Scharge, T.; Voigt, W.; Wilhelm, S.; Wollmann, G.
Further developments of the thermodynamic reference database THEREDA and the thermodynamic sorption database RES³T
Abstr. Pap. Am. Chem. Soc. 239, GEOC-112 (2010).

Rossberg, A.; Lucks, C.; Tsushima, S.; Scheinost, A. C.
Landweber-EXAFS structural analysis of aqueous polynuclear U(VI) complexes with tartaric acid
Geochimica et Cosmochimica Acta 74, A884 (2010).

Sachs, S.; Bernhard, G.
Influence of humic acids on the actinide migration in the environment: suitable humic acid model substances and their application
Application of Radiotracers in Chemical, Environmental and Biological Sciences, Vol. 3 (Lahiri, S.; Maiti, M.; Das, S.K. eds.), 286-288 (2010).

Selenska-Pobell, S.; Merroun, M.
Accumulation of heavy metals by microorganisms: biomineralization and nanocluster formation
Prokaryotic Cell Wall Components – Structure and Biochemistry (Claus, H.; König, H.; Varma, A. eds.) Springer Verlag, Heidelberg, 483-500 (2010).

Steinbrück, D.; Kumke, M.; Neck, V.; Fellhauer, D.;
  Runke, J.; Grambow, B.; Landesman, C.;
  Ribert, S.; Krawczyk-Bärsch, E.; Perdicakis, M.
  Development of redox determination methods
  *2nd Annual Workshop Proceedings of the
  Collaborative Project "Redox Phenomena
  Controlling Systems" (7th EC FP CP RECOSY),
  March 16-19, 2010, Larnaca, Cyprus, KIT
  Scientific Reports 7557, KIT Scientific
  Publishing, Karlsruhe, 11-26 (2010).*

Wolf, M.; Kulenkampff, J.; Enzmann, F.;
  Gründig, M.; Richter, M.; Lippmann-Pipke, J.;
  Mittmann, H.
  **3D-Visualisierung und Quantifizierung von
  Fluidströmungen in Salinargestein mittels
  Positronen-Emissions-Tomographie.**
  *Exkursionsführer und Veröffentlichungen der
  Deutschen Gesellschaft für Geowissenschaften,
  244, 200-212 (2010).*

▶ LECTURES, ORAL PRESENTATIONS

Banerjee, D.; Kirsch, R.; Scheinost, A.C.
  **XPS and XAS investigation of Sb(V)
  reduction on mackinawite: effect of pH and
  surface loading**
  *Goldschmidt 2010, Earth, Energy, and the
  Environment, June 13-18, 2010, Knoxville,
  U.S.A.*

Barkleit, A.; Li, B.; Foerstendorf, H.; Rossberg, A.;
  Moll, H.; Bernhard, G.
  **Structural aspects of uranyl complexes with
  lipopolysaccharide**
  *RadChem 2010 – 16th Radiochemical
  Conference, April 18-23, 2010, Mariánské
  Lázně, Czech Republic.*

Baumann, N.
  **Zeitaufgelöste, Laser-induzierte
  Fluoreszenzspektroskopie am Beispiel von
  Untersuchungen zur Sekundärphasenbildung
  auf Geschossprojektilen aus abgereichertem
  Uran**
  *Jahrestreffen des petrographischen
  Studienkreises, May 02, 2010, Kulmbach,
  Germany.*

Baumann, N.; Arnold, T.
  **Test site Gessenwiese: results in TRLFS
  investigations on surface water and pore
  waters, and preliminary results on plant saps
  concerning uranium speciation**
  *9th Symposium on remediation in Jena, "Jenaer
  Sanierungskolloquium", October 04-05, 2010,
  Jena, Germany.*

Bernhard, G.
  **Zur Bindungsform des Urans in
  Umweltkompartimenten**
  *GDCh-Kolloquien im Sommersemester 2010,
  June 03, 2010, Dresden, Germany.*

Brendler, V.; Altmaier, M.; Marquardt, C.;
  Moog, H.C.; Richter, A.; Scharge, T.; Voigt, W.;
  Wilhelm, S.; Wollmann, G.
  **THEREDA: providing quality-assured
  thermodynamic data for waste management
  assessment**
  *Volker Neck Memorial Session, May 20, 2010,
  Karlsruhe, Germany.*

Brendler, V.; Richter, A.
  Actinide Sorption Database
  *ABC-Salt – Actinide and Brine Chemistry in a
  Salt-Based Repository, September 15-17, 2010,
  Carlsbad, U.S.A.*

Eichler, S.; Fahmy, K.
  **Water repartitioning at the water lipid
  protein interface controls receptor activation
  in G-Protein coupled receptors**
  *Annual Meeting of the German Biophysical
  Society, October 03-06, 2010, Bochum,
  Germany.*

Fahmy, K.
  Infrared spectroscopy
  *BIOTEC Master Course, November 09, 2010,
  Dresden, Germany.*

Fahmy, K.
  **Was ist an der Chemie des Lebens so
  besonders?**
  *3. Tag der Wissenschaften, November 30, 2010,
  Dresden, Germany.*

Fellhauer, D.; Kirsch, R.; Altmaier, M.; Neck, V.;
  Scheinost, A.C.; Wiss, T.; Charlet, L.;
  Fanghänel, T.
  **Plutonium redox behavior in aqueous
  solutions and on nanocrystalline iron phases**
  *Plutonium Futures - The Science 2010,
  September 19-23, 2010, Keystone, U.S.A.
  (2010).*

Fellmer, F.
Geochemische Wechselwirkungen bei Anwesenheit von Huminstoffen in Untertagedeponien
GEOforum 2010, June 08, 2010, Leipzig, Germany.

Foerstendorf, H.; Müller, K.; Heim, K.
The sorption processes of Np(V) and U(VI) onto metal oxide phases. The formation of sorption complexes and mechanistic aspects studied by in situ ATR FT-IR spectroscopy
RadChem 2010 – 16th Radiochemical Conference, April 18-23, 2010, Mariánské Lázně, Czech Republic.

Frost, L.
Microorganisms relevant to nuclear waste repositories and their influence on radionuclide speciation – An exemplary investigation on an Äspö bacterium
Doktorandenseminar - Kompetenzzentrum Ost für Kerntechnik, December 16, 2010, Dresden, Germany.

Geipel, G.; Drewitz, S.; Viehweger, K.; Bernhard, G.; Henle, T.
Quercetin – A key substance in heavy metal uptake of plants?
Biometals 2010, July 25-30, 2010, Tucson, U.S.A.

Günther, A.; Roßberg, A.; Raff, J.; Bernhard, G.
Interaction of U(VI) with *Schizophyllum commune*
9th Symposium on remediation in Jena, "Jenaer Sanierungskolloquium", October 04-05, 2010, Jena, Germany.

Günther, T.; Weinert, U.; Raff, J.; Pollmann, K.
Self assembling proteins as technology platform for the development of new bio-composite materials
12th International and Interdisciplinary NRW Symposium; Biomaterials and Biomechanics, Fundamentals and Clinical Applications, March 17-19, 2010, Essen, Germany

Günther, T.; Weinert, U.; Raff, J.; Pollmann, K.
Self-assembling proteins as basis for new nano materials
International Conference on Functional Nanocoatings, March 28-31, 2010, Dresden, Germany.

Heller, A.; Barkleit, A.; Bernhard, G.
Speciation of curium(III) and europium(III) in human urine samples
RadChem 2010 – 16th Radiochemical Conference, April 18-23, 2010, Mariánské Lázně, Czech Republic.

Heller, A.; Barkleit, A.; Bernhard, G.; Ackermann, J.U.
Spektroskopische Bestimmung der Bindungsform von Europium(III) und Curium(III) im menschlichen Urin
Umweltkolloquium der HTW Dresden, April 01, 2010, Dresden, Germany.

Hennig, C.
Actinide redox speciation and structure analysis in aqueous and nonaqueous solutions
APS users meeting 2010 – - Celebrating 20 Years of Groundbreaking Science, May 03-05, 2010, Argonne, U.S.A., 48 (2010).

Hennig, C.
The use of EXAFS spectroscopy to determine metal coordination in solution
Institut de Chimie Moléculaire de l'Université de Bourgogne, January 08, 2010, Dijon, France.

Hennig, C.
XAS on actinides – Determining the coordination of solution species
XASs2010; X-ray Absorption Spectroscopy School January 14-15, 2010, Gent, Belgium.

Hennig, C.; Takao, K.; Takao, S.; Ikeda-Ohno, A.; Banerjee, D.; Weiss, S.; Zänker, H.; Kraus, W.; Emmerling, F.; Scheinost, A.C.
Chemical bonds and formation process of actinide(IV) oligomers and colloids
Goldschmidt 2010, Earth, Energy, and the Environment, June 13-18, 2010, Knoxville, U.S.A.

Joseph, C.; Schmeide, K.; Sachs, S.; Bernhard, G.
Effect of Ca^{2+} on the sorption of uranium(VI) and humic acid on natural clay
RadChem 2010 – 16th Radiochemical Conference, April 18-23, 2010, Mariánské Lázně, Czech Republic.

Joseph, C.; Schmeide, K.; Sachs, S.; Brendler, V.; Bernhard, G.
The ternary system U(VI) / humic acid / Opalinus Clay
Seminar at the Institute of Laboratory for Waste Management (LES) - Paul Scherrer Institut (PSI), June 28-30, 2010, Villigen, Switzerland.

Joseph, C.; Steudtner, R.; Schmeide, K.
Untersuchungen zur U(VI)-Komplexierung durch Milchsäure sowie zur U(VI)-Sorption an Opalinuston in Abwesenheit und Gegenwart von organischen Modellliganden in Abhängigkeit von der Temperatur
9. Workshop des Verbundprojekts "Wechselwirkung und Transport von Actiniden im natürlichen Tongestein unter Berücksichtigung von Huminstoffen und Tonorganika", October 05-06, 2010, Mainz, Germany.

Krawczyk-Bärsch, E.
Determination of redox processes in biofilms from acidic waters
2nd Annual Workshop of the Collaborative Project "Redox Phenomena Controlling Systems" (7th EC FP CP RECOSY), March 16-19, 2010, Larnaca, Cyprus (2010).

Krawczyk-Bärsch, E.; Arnold, T.; Steinbrück, D.; Kumke, M.
Electrochemical and fiber-optic oxygen sensor measurements in uranium contaminated biofilms - a collaboration with UPPC
2nd Annual Workshop of the Collaborative Project "Redox Phenomena Controlling Systems" (7th EC FP CP RECOSY), March 16-19, 2010, Larnaca, Cyprus (2010).

Kulenkampff, J.; Enzmann, F.
Anwendung von computertomographischen Methoden (Synchrotron-CT, Röntgen-CT, Neutronen-CT) sowie Radiotracer-Experimente (Positronen-Emission-Tomographie) zur mehrskaligen Beschreibung von Strukturen und Rissen in Gesteinen
Kolloquium, February 24, 2010, Hannover, Germany.

Kulenkampff, J.; Enzmann, F.; Gründig, M.; Mittmann, H.; Wolf, M.
Spatiotemporal observation of transport in fractured rocks
European Geosciences Union General Assembly May 02-07, 2010, Vienna, Austria.

Kulenkampff, J.; Gründig, M.; Lippmann-Pipke, J.; Zakhnini, A.; Enzmann, F.; Kersten, M.
Quantitative observation of transport processes in soils with high-resolution PET
Advanced Spectroscopy and Microscopic Characterisation Techniques - Tools to Enlighten Biogeochemical Interfaces in Soils, October 04-06, 2010, Jena, Germany.

Kulenkampff, J.; Gründig, M.; Wolf, M.; Lippmann-Pipke, J.; Richter, M.; Enzmann, F.
Direct quantitative observation of transport processes with Positron-Emission-Tomography
Transport in porous materials, Paul Scherrer Institut (PSI), August 19-20, 2010, Villigen, Switzerland.

Lederer, F.; Günther, T.; Raff, J.; Pollmann, K.
Heterologous expression of a surface layer-like protein in *E coli* causes a drastic morphological change of the cell
VAAM-Jahrestagung 2010, March 28-31, 2010, Hannover, Germany.

Lippold, H.; Lippmann-Pipke, J.
Radiotracer studies on interaction processes related to humic-bound transport of radionuclides
11th International Symposium on Environmental Radiochemical Analysis, September 15-17, 2010, Chester, United Kingdom.

Lippmann-Pipke, J.
Reactive transport investigations by means of radiotracer applications
Kolloquium, Friedrich-Schiller-Universität Jena, December 07, 2010, Jena, Germany.

Lucks, C.; Roßberg, A.; Scheinost, A.C.
Aqueous uranium(VI) complexes with tartaric acid: a combined UV-vis and EXAFS study
5th Graduate Students Seminar, September 22-24, 2010, Krögis, Germany.

Martin, P.; Belin, R.; Robisson, A.C.; Scheinost, A.C.
Study of americium and plutonium chemistry in Mixed OXide fuel
Plutonium Futures - The Science 2010, September 19-23, 2010, Keystone, U.S.A. (2010).

Moll, H.
Bakterielle Wechselwirkungen ausgewählter Actinide vor dem Hintergrund der Endlagerung von radioaktivem Abfall
Seminar für Kern- und Radiochemie am Institut für Kernchemie der Johannes Gutenberg-Universität Mainz, November 29, 2010, Mainz, Germany.

Moll, H.; Bernhard, G.
Actinide interactions with bacteria
Actinide and Brine Chemistry in a Salt-Based Repository (ABC-SALT) International Workshop, September 15-17, 2010, Carlsbad, U.S.A.

Moll, H.; Bernhard, G.
Complexation of curium(III) with pyoverdin-model compounds
RadChem 2010 – 16th Radiochemical Conference, April 18-23, 2010, Mariánské Lázně, Czech Republic.

Müller, K.
Speciation of actinyl ions in aqueous solution and at water-mineral interfaces. A vibrational spectroscopic approach.
Annual Seminar of the Graduiertenkolleg 826/3, Johannes Gutenberg University, Mainz, November 08, 2010, Oberwesel, Germany.

Müller, K.; Meusel, T.; Brendler, V.; Foerstendorf, H.; Bernhard, G.
The speciation of U(VI) in aqueous solution and sorbed onto TiO2 studied by in situ vibrational spectroscopy
Seminar at the Department of Nuclear Engineering, Kyoto University, June 29, 2010, Kyoto, Japan.

Müller, K.; Meusel, T.; Foerstendorf, H.; Brendler, V.; Bernhard, G.; Lefèvre, G.
The sorption of U(VI), Np(V) and Se(VI) onto surfaces of selected metal oxides studied by in situ vibrational spectroscopy
Seminar at the Institut de Physique Nucléaire, Division de Recherche Radiochemie,Université Paris-Sud, May 10, 2010, Orsay, France.

Müller, M.; Acker, M.; Schott, J.; Barkleit, A.; Taut, S.; Bernhard, G.
Neue Ergebnisse zur Komplexbildung und Sorption im System Am(III)/Eu(III)-Modellligand-Opalinuston
9. Workshop des Verbundprojekts "Wechselwirkung und Transport von Actiniden im natürlichen Tongestein unter Berücksichtigung von Huminstoffen und Tonorganika", October 05-06, 2010, Mainz, Germany.

Pieragnoli, A.; Belin, R.C.; Cécilia, G.; Léchelle, J.; Martin, P.M.; Valenza, P.J.; Richaud, J.C.; Reynaud, M.; Scheinost, A.C.
PuCrO$_3$ compound: synthesis, structural and thermodynamic studies
NuMat 2010 – The Nuclear Materials Conference, October 04-07, 2010, Karlsruhe, Germany.

Pollmann, K.
Bionik – Technische Erfindungen aus der Natur
Tag des offenen Labors, July 4, 2010, Dresden, Germany.

Pollmann, K.
Bionik – Umsetzung von Erfindungen der Natur in technische Innovationen
Lehrerfortbildung, November 05, 2010, Dresden, Germany.

Pollmann, K.
Self-assembling biomolecules as a tool kit for new nanomaterials
Zentrumskolloquium, FZD, January 04, 2010, Dresden, Germany.

Pollmann, K.
Von der Mikrobiologie zur Nanotechnologie – Nachwuchsforschergruppe NanoBio am FZD
Besuch von Herrn Gazlig, Pressesprecher der HGF, January 20, 2010, Dresden, Germany.

Pollmann, K.; Günther, T.; Weinert, U.; Marquard, A.; Raff, J.
Bacteria as natural resources for novel materials: bioinspired nanocomposites for environmental technology
Chemical Nanotechnology Talks X, January 26-27, 2010, Frankfurt, Germany.

Pollmann, K.; Raff, J.
Nano-Biotechnologie für den Umweltschutz: Neue photokatalytisch aktive Verbundmaterialien zur Eliminierung von pharmazeutischen Reststoffen (NanoPharm)
4. Mitteldeutsches Netzwerktreffen, November 30, 2010, Magdeburg, Germany.

Pollmann, K.; Raff, J.
Proteinbasierte Oberflächenfunktionalisierung für die Umwelttechnolgie
Ideas to market, January 15, 2010, Dresden, Germany.

Pollmann, K.; Rothenstein, D.
Rational design of nanoparticle arrays using bioinspired mineralisation mediated by peptide-modified bacterial S-layers
DFG-SPP 1569 "Generation of Multifunctional Inorganic Materials by Molecular Bionics", Kick-Off-Meeting, October 25, 2010, Stuttgart, Germany.

Raditzky, B.; Schmeide, K.; Sachs, S.; Bernhard, G.
Complexation of U(VI) with nitrogen and phosphorous containing ligands in aqueous solution
RadChem 2010 – 16th Radiochemical Conference, April 18-23, 2010, Mariánské Lázně, Czech Republic.

Raff, J.
  Bioinspired nanomaterials
  nanoSeminar des Instituts für Werkstoffwissen-schaft, Dresden University of Technology, November 11, 2010, Dresden, Germany.

Raff, J.
  Radioökologische Forschung als Basis zur Entwicklung neuer Materialien
  Visit of former IRC's staff members, November 19, 2010, Dresden, Germany.

Raff, J.
  Wie Bakterien einer Uranabfallhalde zur Entwicklung neuer Materialien beitragen können
  "Tage der Wissenschaften", June 16, 2010, Radebeul, Germany.

Raff, J.
  Wie die Natur die Forscher inspirieren kann
  Tag des offenen Labors 2010, FZD, July 04, 2010, Dresden, Germany.

Raff, J.; Weinert, U.; Günther, T.; Marquard, A.; Matys, S.; Kutschke, S.; Pollmann, K.
  Bioinspired nanocomposite materials for technical applications
  Materials Science and Engineering 2010, August 24-26, 2010, Darmstadt,Germany.

Raff, J.; Weinert, U.; Lehmann, F.; Günther, T.; Matys, S.; Kutschke, S.; Pollmann, K.
  Proteinbasierte Biokompositmaterialien zur Behandlung schadstoffhaltiger Wässer
  7. Max-Bergmann-Symposium, November 16, 2010, Dresden, Germany.

Richter, A.; Altmaier, M.; Brendler, V.; Marquardt, C.; Moog, H.; Scharge, T.; Voigt, W.; Wilhelm, S.; Wollmann, G.
  Further developments of the thermodynamic reference database THEREDA and the thermodynamic sorption database RES³T
  239th ACS National Meeting, March 21-25, 2010, San Francisco, U.S.A.

Richter, A.
  The Institute of Radiochemistry of the FZD: Molecular understanding and thermodynamics of actinides at the solid/liquid interface
  U.S. Geological Survey, March 18, 2010, Menlo Park, U.S.A.

Sachs, S.
  Untersuchungen zum Einfluss von Huminsäuren auf die Migration von Actiniden in der Umwelt
  Umwelttechnisches Fachseminar "Wissenschaft&Praxis" des Instituts für Verfahrensentwicklung, Torf- und Naturstoff-Forschung (iTN), March 31, 2010, Zittau, Germany (2010).

Sachs, S.; Bernhard, G.
  Influence of humic acids on the actinide migration in the environment: suitable humic acid model substances and their application
  ARCEBS-10; Second International Conference on Application of Radiotracers in Chemical, Environmental and Biological Sciences, November 07-13, 2010, Kolkata, India.

Scheinost, A.C.
  Probing redox reactions at the mineral/water interface by X-ray absorption spectroscopy: reduction of Se, Sb and Pu by Fe(II)-bearing minerals
  Graduiertenkolleg "Spurenanalytik von Elementspezies: Methodenentwicklungen und Anwendungen", March 23, 2010, Mainz, Germany.

Scheinost, A.C.
  The Rossendorf Beamline at ESRF - A unique facility to perform X-ray absorption spectroscopy of radionuclides
  Seminar des Instituts fuer Energie- und Klimaforschung, FZ Jülich, March 25, 2010, Jülich, Germany.

Sobolev, O.; Cuello, G.J.; Scheinost, A.C.; Johnson, M.R.; Nikitenko, S.; Le Forestier, L.; Brendle, J.; Charlet, L.
  The short range order of ions in clay minerals: Sm^{3+} coordination
  10th International Workshop on Non-Crystalline Solids, April 21-23, 2010, Barcelona, Spain.

Steudtner, R.; Günther, A.; Geipel, G.; Bernhard, G.; Brendler, V.
  Luminescence spectroscopy characterization of uranium(VI) at low temperature
  3rd EuCheMS Chemistry Congress, August 29-September 02, 2010, Nuremberg, Germany.

Tsushima, S.
  Application of computational chemistry and experimental spectroscopy to nuclear waste problem
  Ulsan National Institute of Science and Technology, March 09, 2010, Ulsan, South Korea.

Tsushima, S.
Exploring uranium chemistry with computational chemistry
User's meeting of Zentrum für Informationsdienste und Hochleistungsrechnen (ZIH), Dresden University of Technology, December 06-07, 2010, Dresden, Germany.

Tsushima, S.
Quantum chemical calculation for the nuclear safety research: complementary tool to spectroscopy and electrochemistry
Seminar at the Institute of Scientific and Industrial Research, Osaka University, December 28, 2010, Osaka, Japan.

Tsushima, S.; Fahmy, K.
Photochemistry of uranium(VI) revisited: A density functional theory study
239th ACS National Meeting, March 21-25, 2010, San Francisco, U.S.A.

Viehweger, K.; Geipel, G.; Bernhard, G.
Glutathione – An important intracellular chelator of uranium
Biometals 2010, July 25-30, 2010, Tucson, U.S.A.

Weinert, U.; Günther, T.; Raff, J.; Pollmann, K.
Self assembling proteins as matrix for the construction of optical devices
Design and Nature 2010 – Fifth International Conference on Comparing Design in Nature with Science and Engineering, June 28-30, 2010, Pisa, Italia.

Weiß, S.; Dreißig, I.; Hennig, C.; Bernhard, G.; Zänker, H.
Die Kolloidbildung von Uran(IV) in silikat-haltigen Systemen im nah-neutralen pH-Bereich.
6. Workshop Radiochemische Analytik bei Betrieb und Rückbau kerntechnischer Anlagen, der Deklaration von Abfällen und im Strahlenschutz (RCA) & 23. Seminar Aktivierungsanalyse und Gammaspektroskopie (SAAGAS), September 6-8, 2010, Dresden, Germany.

Wolf, M.
3D-observation of heterogeneous transport and comparison to Lattice-Boltzmann modelling
5th Graduate Students Seminar, September 22-24, 2010, Krögis, Germany.

Wolf, M.
Stofftransport bei Bergbaufolgeschäden und Altlastensanierung
GEOForum 2010, June 08, 2010, Leipzig, Germany.

Wolf, M.; Kulenkampff, J.; Enzmann, F.; Lippmann-Pipke, J.; Gründig, M.; Richter, M.
3D-Visualisierung von Fluidströmungen in Salinargestein mittels Positronen-Emissions-Tomographie
Staßfurt-Verbund Abschlusstagung 2010, November 18-20, 2010, Staßfurt, Germany.

Wolf, M.; Kulenkampff, J.; Lippmann-Pipke, J.; Gründig, M.; Richter, M.; Enzmann, F.
Fluid flow in geological material: GeoPET observation in comparison with Lattice-Boltzmann simulation
Bodenphysik-Seminar, October 14, 2010, Halle, Germany.

▷ POSTERS

Barkleit, A.; Heller, A.; Baraniak, L.; Bernhard, G.
Comparison of spectroscopic investigation and computer modelling of lanthanide(III) and actinide(III) speciation in human biological fluids
Third European IRPA Congress, June 14-18, 2010, Helsinki, Finland.

Dreissig, I.; Weiß, S.; Zänker, H.; Hennig, C.; Brendler, E.; Bernhard, G.
Investigation on stability and structure of thorium colloids
RadChem 2010 – 16th Radiochemical Conference, April 18-23, 2010, Mariánské Lázně, Czech Republic.

Frost, L.; Moll, H.; Krawczyk-Bärsch, E.
Interaction of selected actinides with microorganisms relevant to nuclear waste disposal
5th Graduate Students Seminar, September 22-24, 2010, Krögis, Germany.

Gückel, K.
Vibrational spectroscopy of actinyl sorption complexes
5th Graduate Students Seminar, September 22-24, 2010, Krögis, Germany.

Gückel, K.; Foerstendorf, H.; Brendler, V.
Sorption of U(VI) onto mineral model systems -An in situ ATR FT-IR spectroscopic study
Doktorandenseminar - Kompetenzzentrum Ost für Kerntechnik, December 16, 2010, Dresden, Germany.

Günther, T.; Weinert, U.; Raff, J.; Pollmann, K.
Self assembling proteins as technology platform for the development of new bio-composite materials
12th International and Interdisciplinary NRW Symposium Biomaterials and Biomechanics, Fundamentals and Clinical Applications, March 17-19, 2010, Essen, Germany

Günther, T.; Weinert, U.; Raff, J.; Pollmann, K.
Surface functionalization with bacterial surface layer proteins
5th Graduate Students Seminar, September 22-24, 2010, Krögis, Germany.

Jordan, N.; Weiß, S.; Brendler, V.
Retention of selenium oxyanions on kaolinite
Clays in Natural & Engineered Barriers for Radioactive Waste Confinement, March 29-April 01, 2010, Nantes, France.

Joseph, C.; Schmeide, K.; Sachs, S.; Bernhard, G.
Uranium(VI) diffusion in Opalinus Clay in the absence and presence of humic acid
Clays in Natural & Engineered Barriers for Radioactive Waste Confinement, March 29-April 01, 2010, Nantes, France.

Kuhlmann, M.; Stephan, H.; Geipel, G.; Appelhans, D.
Dendrimer-encapsulated rhenium cluster complexes
3rd EuCheMS Chemistry Congress, August 29-September 02, 2010, Nuremberg, Germany.

Kulenkampff, J.; Wolf, M.; Enzmann, F.; Gründig, M.; Richter, M.; Lippmann-Pipke, J.
Matching of fluid flow observations in geological material (GeoPET, mm3 resolution) with lattice Boltzmann simulations in μm resolved structures
AGU 2010 Fall Meeting, December 13-17, 2010, San Francisco, U.S.A.

Lederer, F.; Günther, T.; Raff, J.; Pollmann, K.
Filamentous *E. coli* induced by heterologous expression of surface layer proteins
Bacterial Cell Surfaces, June 27 - July 2, 2010, New London, U.S.A.

Lippold, H.
Combined effects of humic matter and surfactants on PAH solubility: is there a mixed micellization?
IHSS 15 – 15th Meeting of the International Humic Substances Society, June 27 – July 02, 2010, Tenerife, Spain.

Lucks, C.; Roßberg, A.; Scheinost, A.C.
Structural investigation on the complexation of uranium(VI) with simple, aliphatic, carboxylic acids in aqueous solution
Doktorandenseminar - Kompetenzzentrum Ost für Kerntechnik, December 16, 2010, Dresden, Germany.

Müller, M.; Acker, M.; Bernhard, G.
Spectroscopic characterization of Am(III)-complexes with small organic acids
5th Graduate Students Seminar, September 22-24, 2010, Krögis, Germany.

Pollmann, K.; Günther, T.; Weinert, U.; Marquard, A.; Raff, J.
Bacteria as natural resources for novel materials: bioinspired nanocomposites for environmental technology.
Chemical Nanotechnology Talks X, January 26-27, 2010, Frankfurt, Germany.

Pollmann, K.; Weinert, U.; Günther, T.; Raff, J.
Novel biosensors based on aptamer functionalized bacterial surface layers (S-layers)
Biosensors 2010, May 26-28, 2010, Glasgow, United Kingdom.

Raff, J.; Pollmann, K.
Advanced bio-composite materials for water treatment
POLEKO 2010, International Trade Fair of Environmental Protection, November 23-26, 2010, Poznań, Poland.

Raff, J.; Weinert, U.; Günther, T.; Matys, S.; Kutschke, S.; Pollmann, K.
From nature for nature – Bioinsipred nanocomposite materials for environmental technology
nano tech 2010 – International Nanotechnology Exhibition and Conference "Green Nanotechnology", February 17-19, 2010, Tokyo, Japan.

Raff, J.; Weinert, U.; Günther, T.; Matys, S.; Kutschke, S.; Pollmann, K.
From nature for nature – Bioinsipred nanocomposite materials for environmental technology
VAAM-Jahrestagung 2010, March 28-31, 2010, Hannover, Germany.

Schmeide, K.; Sachs, S.; Bernhard, G.
Np(V) reduction by humic acids – Impact of sulfur functionalities of humic acids
Plutonium Futures - The Science 2010, September 19-23, 2010, Keystone, U.S.A.

Weinert, U.; Günther, T.; Pollmann, K.; Raff, J.
Entwicklung von sensorischen Schichten auf Basis bakterieller Hüllproteine
7. Max-Bergmann-Symposium, November 16, 2010, Dresden, Germany.

Weinert, U.; Günther, T.; Pollmann, K.; Raff, J.
Novel biosensors by combining bacterial S-layers, fluorescent dyes and aptamers
Nanocoatings – International Conference on Functional Nanocoatings, March 28-31, 2010, Dresden, Germany.

Weinert, U.; Günther, T.; Pollmann, K.; Raff, J.
S-layer based concept for the development of nano-structured biosensors
Nanofair 2010 – 8th International Nanotechnology Symposium, July 06-07, 2010, Dresden, Germany.

Zirnstein, I.; Krawczyk-Bärsch, E.; Arnold, T.; Röske, I.
Molecular and microscopical characterization of the algae mat from the „Gessenhalde" (Ronneburg/Eastern Thuringia) and the proof of the retention of uranium
9th Symposium on remediation in Jena, "Jenaer Sanierungskolloquium", October 04-05, 2010, Jena, Germany.

▷ Theses

Glorius, M.
Zum Komplexbildungsverhalten ausgewählter Actiniden (U, Np, Cm) mit mikrobiellen Bioliganden
Dresden University of Technology, Dresden, Germany (2010).

Lehmann, S.
Zur Komplexchemie des Uran(IV) – Fluoreszenz- und absorptionsspektroskopische Untersuchungen
Dresden University of Technology, Dresden, Germany (2010).

Madathil, S.
Modular switches in protein function: a spectroscopic approach
Dresden University of Technology, Dresden, Germany (2010).

Müller, K.
The sorption of uranium(VI) and neptunium(V) onto surfaces of selected metal oxides and alumosilicates studied by *in situ* vibrational spectroscopy
Dresden University of Technology, Dresden, Germany (2010).

Steudtner, R.
Zur Wechselwirkung von Uran mit den Bioliganden Citronensäure und Glucose
Dresden University of Technology, Dresden, Germany (2010).

Tanh Jaezet, H.B.
Neue multifunktionelle Komplexbildner mit N,O,S-Donorfunktionen für Aktinoidelemente: Synthese, Komplexbildung und Struktur
Dresden University of Technology, Dresden, Germany (2010).

▷ MASTER, DIPLOMA

Drewitz, S.
Untersuchung von Redoxprozessen von Uranyl-Verbindungen mit Flavonoiden
Dresden University of Technology, Dresden, Germany (2010).

Fajardo Uribe, C. H.
Charakterisierung der Wechselwirkung von U(VI) mit *Desmodesmus subspicatus*
Dresden University of Technology, Dresden, Germany (2010).

Groß, M.
Spektroskopische Untersuchungen zur Struktur und Funktion der Kupfer-ATPase CopB von *E. hirae*
Dresden University of Technology, Dresden, Germany (2010).

Hilsberg, M.
Ermittlung von Gleichgewichtsdaten und kinetischen Parametern für die Verteilung von ausgewählten Wasserinhaltsstoffen an Kunstharzionenaustauschern
University of Applied Sciences, Zittau-Görlitz, Germany (2010).

Leske, S.
Konzeption und prototypische Realisierung von Schnittstellen für heterogene Zugangssysteme zu einer SQL-basierten chemischen Stoffdatenbank
University of Applied Sciences, Dresden, Germany (2010).

Richter, K.
Protein basierte Herstellung von Fotokatalysatoren zur Eliminierung von Arzneimittelrückständen aus Wasser
University of Applied Sciences, Dresden, Germany (2010).

Schott, J.
Untersuchungen zum Einfluss der Temperatur und kleiner organischer Liganden auf die Sorption von Eu(III) am Opalinuston
Dresden University of Technology, Dresden, Germany (2010).

Zirnstein, I.
Bestimmung der mikrobiellen Diversität von Biofilmen mit Schwerpunkt des Nachweises von Eukaryonten Mikroorganismen in Uran kontaminierten Milieus
Dresden University of Technology, Dresden, Germany (2010).

▷ SEMINARS (TALKS OF VISITORS)

▷ WORKSHOPS

▷ TEACHING ACTIVITIES

▷ SEMINARS

Dr. Barbora Dousova
The Institute of Chemical Technology, Dept. of Solid State Chemistry, Prague, Czech Republic
Introduction to the Institute of Chemical Technology Prague
April 28, 2010

Lenka Herzogova
The Institute of Chemical Technology, Dept. of Solid State Chemistry, Prague, Czech Republic
The use of modified aluminosilicates as selective anionic sorbents"
April 28, 2010

Stanislava Krejčová
The Institute of Chemical Technology, Dept. of Solid State Chemistry, Prague, Czech Republic
Geochemical processes of As and Se in soils
April 28, 2010

Bohumila Jakubikova
The Institute of Chemical Technology, Dept. of Solid State Chemistry, Prague, Czech Republic
The environmental impact of waste drugs
April 28, 2010

Dr. Dirk Rothenstein
Institute of Materials Science, University Stuttgart, Germany
Phage display: identification of peptide-interactions with inorganic materials
May 06, 2010

Dr. Ulf Kempe
Institut für Mineralogie, Technische Universität Bergakademie Freiberg, Germany
Warum wird Zirkon metamikt?
May 27, 2010

Prof. Dr. Susanta Lahiri
Saha Institute of Nuclear Physics, Kolkata, India
Role and responsibilites of radiochemists to develop green chemistry
June 14, 2010

Dr. Moumita Maiti
Saha Institute of Nuclear Physics, Kolkata, India
Recent nuclear and chemical data on accelerator produced Tc and At radionuclides
June 14, 2010

Dr. Hildegarde Vandenhove
Belgian Nuclear Research Centre, Environment Health and Safety, Radiological Impact and Performance Assessment, Biosphere Impact Studies, Mol, Belgium
Biosphere impact studies at the Belgian Nuclear Research Centre
October 07, 2010

Dr. Catherine Van den Hoof
Belgian Nuclear Research Centre, Environment Health and Safety, Radiological Impact and Performance Assessment, Biosphere Impact Studies, Mol, Belgium
Evaluation of the suitability of the Land Surface Model JULES for long term safety assessments in Belgium
October 07, 2010

Prof. Dr. Tobias Reich
Institut für Kernchemie, Johannes Gutenberg-Universität Mainz, Germany
EXAFS-Untersuchungen zur Sorption von Neptunium und Plutonium an Tonmineralien
October 21, 2010

▷ WORKSHOPS (ORGANIZED BY THE IRC)

Workshop "Nanostructured biocomposites – Chances and perspectives for water management"

Stadtentwässerung Dresden-Kaditz, Dresden, Germany, February 02, 2010.

Debeaumont, J.-L.
A new vertical photoreactor design

Dziubek, J.
Arsenic removal from industrial wastewater

Hambach, B.
Trace substances in drinking water – Application potential for nano particles?

Lippok, D.
Innovations of technologies for purification of water – Management issues and challenges of upscaling

Raff, J.
Nanostructured biocomposites – Chances and perspectives for water treatment

Rohde, S.
Stand und Perspektiven im Hinblick auf Umweltnormen nach der Wasserrahmenrichtlinie nach WRRL

8. Workshop des Verbundprojekts: "Wechselwirkung und Transport von Actiniden im natürlichen Tongestein unter Berücksichtigung von Huminstoffen und Tonorganika"

FZD, Dresden, Germany, April 13-14, 2010.

Fröhlich, D.
Sorptions- und Diffusionsuntersuchungen mit Neptunium

Krüger, S.
Adsorption von Uranyl an Kantenflächen von Kaolinit und Pyrophyllit

Kumke, M.
Speziation des Europium-Aquo-Ions

Lippold, H.
Neue fluoreszenzspektroskopische Untersuchungen zur Huminstoff-Komplexbildung konkurrierender Metalle und aktuelle Ergebnisse von Transportstudien mittels PET

Möser, C.
Beiträge zur Metall-Speziation in Porenwasser und erste Ergebnisse zur Tonalterung durch hohe Temperaturen

Müller, M.
Temperaturabhängigkeit der Komplexbildung und Sorption von Am(III)/Eu(III) im System Actinid-NOM-Opalinuston

Raditzky, B.
Untersuchungen zur Am(III)-Komplexierung durch Modellliganden, zur Np(V)-Reduktion durch schwefelhaltige Huminsäuren sowie zur pH-abhängigen U(VI)-Sorption an Opalinuston unter aeroben und anaeroben Bedingungen

Skerencak, A.
Spektroskopische und thermodynamische Untersuchungen zur Komplexierung von trivalentem Curium mit anorganischen Liganden bei erhöhten Temperaturen

Steudtner, R.
Spektroskopische Charakterisierung eines ternären U(VI)-Carbonato-Humat-Komplexes mittels ATR FT-IR und cryo-TRLFS

Workshop of the Paul Scherrer Institute (PSI), Villigen, Switzerland, and the Institute of Radiochemistry (IRC)
FZD, Dresden, Germany, September 27-28, 2010.

Arnold, T.
Anwendungen der Konfokalen Laser Raster Mikrokopie (CLSM) an umweltrelevanten Proben

Brendler, V.
Radioisotope speciation in geothermal waters: data acquisition and modelling

Curti, E.
Experimente und Modellierung zum Ra/Ba Sulfat Projekt

Frost, L.
U(VI) interactions with the Äspö-bacterium *Pseudomonas fluorescens*

Geißler, A.
Bacterial diversity in Opalinus Clay samples.

Hingerl, F.
Influence of thermodynamic data and activity models on calculated properties of enhanced geothermal systems

Jordan, N.
Retention of selenium onto anatase: macroscopic and microscopic characterization.

Kosakowski, G.
Gekoppelte reaktive Modellierung im Rahmen Sachplan geologische Tiefenlagerung

Lippmann-Pipke, J.
Reactive transport division: scope and aims

Wolf, M.
Fluid flow in geological material: GeoPET observation in comparison with Lattice-Boltzmann simulation

Helmholtz Meeting "Research on Waste Repositories", Institute for Waste Disposal (INE), KIT, Karlsruhe, Institute of Radiochemistry (IRC), FZD, Dresden, and Institute of Energy and Climate Research (IEK), FZJ, Jülich, Germany
FZJ, Jülich, Germany November 23-24, 2010.

Bach, D.
TEM for nanoscale analysis of radioactive materials – First results on green rust interacted with neptunyl

Bachvarova, V.
Bacterial diversity in unpertubed and R2A medium treated Opalinus Clay samples from the Mont Terri Rock Laboratory

Brendler, V.
Weiterentwicklungen der thermodynamischen Referenzdatenbasis THEREDA und der thermodynamischen Sorptionsdatenbank RES³T

Bukaemskiy, A.
Fundamental research on ceramic materials for actinide conditioning

Foerstendorf, H.
Vibrational spectroscopic identification of binary and ternary surface complexes of U(VI) on TiO_2 and ferrihydrite

Holliday, K.
Time Resolved Laser Fluorescence of Eu and Cm doped $LaPO_4$

Kaden, P.
NMR-investigations at KIT-INE

Klinkenberg, M.
Elektronenmikroskopie im IEK-6 – SEM, FIB, TEM

Labs, S.
Synthese und Stabilität von Uranmineralen Coffinit, Thorit

Lucks, C.
Aqueous uranium(VI) complexes with acetic and succinic acid: combining multi-spectroscopic methods with factor analysis and quantum chemical calculations

Ruff, C.
Neue Strategien im Partitioning: Wasserlösliche Komplexbildner für den i-SANEX-Prozess

Schlenz, H.
Strukturforschung im FZJ-IEK – Raman, XRD

Viehweger, K.
Redox status of uranium in the cytoplasm of plant cells

Wilden, A.
Direkte Actiniden(III) Abtrennung aus PUREX-Raffinaten

Status-Seminar 2010:
„Long-lived radionuclides in the environment"
FZD, Dresden, Germany, December 15-16, 2010.

Auerhammer, J.
Low-level alpha spectroscopy for determining intrinsic alpha particles of process relevant materials for the microelectronics

Bachvarova, V.
Progress in bacterial diversity investigations of Opalinus Clay samples from the Mont Terri Rock Laboratory

Banerjee, D.
XPS and EXAFS investigation of Sb(V) reduction on mackinawite: effects of pH and surface loading

Barkleit, A.
Spectroscopic characterization of Eu(III) and Am(III) complexes with small organic molecules at elevated temperatures

Dulnee, S.
Redox reactions of Sn(II) with magnetite and goethite: Preliminary XAFS results

Eichler, S.
Lipid protein interactions underlie an evolutionary conserved proton switch in a transmembrane peptide derived from helix-3 of class-1 GPCRs

Frost, L.
Interaction of selected actinides with microorganisms relevant to nuclear waste disposal – Preliminary investigations

Gaona, X.
Chemistry of neptunium in cementitious environments: An EXAFS study

Günther, A.
***Schizophyllum commune* – U(VI) binding experiments combined with TRLFS and EXAFS studies**

Günther, T.
Atomic Force Microscopy – Possibilities and limitations

Hennig, C.
The special case of actinide(IV) complexation by the carboxylic function of small and large organic ligands

Joseph, C.
Sorption of U(VI) onto FeS in Opalinus Clay pore water

Krawczyk-Bärsch, E.
The influence of biofilms on the mobilization of uranium in contaminated AMD waters

Kulenkampff, J.
Advancements of GeoPET image quality as prerequisite for comparison of observation and simulation

Lucks, C.
Structural investigations on the complexation of uranium(VI) with simple, aliphatic carboxylic acids in aqueous solution

Moll, H.
Planned XAS investigations within the microbial diversity in clay project

Müller, K.
Comparative investigation of the uranium complexation onto γ-Al_2O_3 by means of FT-IR and EXAFS spectroscopy

Rossberg, A.
Spectroscopic confirmation and structural characterization of thermodynamically predicted U(VI)-tartrate complexes by using multianalytical techniques

Saeki, M.
Structural study on complex between $^{99}T_cO_4^{-}$ and an organic extractant by ATR FT-IR and EXAFS spectroscopies and DFT calculation

Scheinost, A.C.
Redox-reactions of plutonium with iron-(II)-minerals under anoxic conditions: a XANES and EXAFS study

Schmeide, K.
Influence of small organic model ligands on U(VI) sorption onto Opalinus Clay between 10 and 60°C

Steudtner, R.
Spectroscopic characterization of the ternary U(VI) carbonato humate complex by using ATR FT-IR and cryo-TRLFS

Viehweger, K.
Redox status of uranium in the cytoplasm of plant cells

Vogel, M.
Effect of cell viability on the biosorption of U(VI) by *Chlorella vulgaris*

▷ TEACHING ACTIVITIES

Lectures

Bernhard, G.
> **Radiochemistry – Radiochemical methods**
> *Dresden University of Technology*
> *Summer term 2010*

> **Environmental analysis (Trace analysis)**
> *Dresden University of Technology*
> *Summer term 2010*

> **Environmental chemistry (Environment – Substance – Energy)**
> *Dresden University of Technology*
> *Winter term 2010/2011*

Fahmy, K.
> **Biophysics**
> *1. Dresden-International-PhD-Programme (DIPP), Dresden University of Technology,*
> *Winter term 2010/2011*

> **Infrared spectroscopy**
> *2. BIOTEC-Master-Course, Dresden University of Technology,*
> *Winter term 2010/2011*

Lippold, H.
> **Radiochemistry and radiopharmacology – Part II: origin, properties and applications of ionising radiation**
> *University of Leipzig*
> *Summer term 2010*

> **Radioanalytics**
> *Lecture within the post-graduate course "Analytics and spectroscopy", University of Leipzig, Summer term 2010*

> **Radiochemical analytical methods**
> *Lecture within the post-graduate course "Toxicology and environmental protection", University of Leipzig, Winter term 2010/2011*

Courses

▷ The laboratory course "Radiochemistry" was provided from August 9th to 12th and from 23rd to 26th, 2010, as a part of a module of the chemistry master degree program at the Dresden University of Technology.

Advisers:

Bachvarova, V.	Heller, A.	Müller, M.
Dr. Barkleit, A.	Joseph, C.	Weinert, U.
Frost, L.	Lederer, F.	Weiß, S.
Gückel, K.	Li, B.	
Günther, T.	Lucks, C.	

▷ The IRC provided one experiment "Alpha spectrometric isotope dilution analysis of uranium" of the laboratory course "Instrumental Analysis" held by the Institute for Analytical Chemistry, Dresden University of Technology, during winter term

Adviser:
Dr. Foerstendorf, H.

Teaching Assistants:

WT 09/10	*WT 10/11*
Frost, L.	Gückel, K.
Lederer, F.	Lucks, C.
Müller, M.	Müller, M.
Raditzky, B.	Weinert, U,
Weiß, S.	Weiß, S.

Institute of Radiochemistry

Helmholtz-Zentrum Dresden-Rossendorf e.V.

- **Biogeochemistry**
- **Biophysics**
- **Molecular Structures**
- **Reactive Transport**
- **Surface Processes**
- **Administration**
- **Radiation Protection Techniques**

Prof. Dr. habil. G. Bernhard (Director)

Administration
Kirmes, Claudia; Kovács, Jenny; Glückert, Marion (ESRF); Gerstner, Katrin (FS Leipzig)

Radiation Protection Techniques
Heim, Heidemarie; Falkenberg, Dirk; Henke, Steffen; Hiller, Bernd; Rumpel, Annette

D I V I S I O N S

BIOGEO-CHEMISTRY

Dr. Geipel, Gerhard

Dr. Arnold, Thuro
Bacharova, Velina
Dr. Baumann, Nils
Dudek, Monika
Eilzer, Manuela
Flemming, Katrin
Förtsch, Gerd
Frost, Laura
Dr. Geißler, Andrea
Dr. Glorius, Maja
Götz, Christian
Grambole, Genia
Dr. Günther, Alix
Gürtler, Sylvia
Heller, Anne
Heller, Sylvia
Dr. Krawczyk-Bärsch, Evelyn
Dr. Lehmann, Sandra
Lindner, Katja
Dr. Moll, Henry
Müller, Christian
Raditzky, Bianca
Dr. Raff, Johannes
Reitz, Thomas
Dr. Sachs, Susanne
Seibt, Jana
Dr. Selenska-Pobell, Sonja
Dr. Tanh Jeazet, Harold B.
Dr. Viehweger, Katrin
Vogel, Manja
Zirnstein, Isabel

BIOPHYSICS

Dr. habil. Fahmy, Karim

Eichler, Stefanie
Khesbak, Hassan
Kummer, Ulrike
Dr. Madathil, Sineej
Dr. Oertel, Jana
Philipp, Jenny
Dr. Savchuk, Olesya
Sayed, Ahmed
Dr. Tsushima, Satoru

Junior Research Group
Dr. Pollmann, Katrin
Günther, Tobias
Hauptmann, Tobias
Dr. Kutschke, Sabine
Lederer, Franziska
Lehmann, Falk
Marquard, André
Suhr, Matthias
Weinert, Ulrike

EXIST – Fellowship for business start up / ForMaT Project Mangement Jülich
NANOLAB/Kryofluor.
Dr. Großmann, Kay
Sobirai, Dirk
Trepte, Paul

MOLECULAR STRUCTURES

Dr. habil. Scheinost, Andreas C.

Dr. Banerjee, Dipanjan
Dulnee, Siriwan
Exner, Jörg
Fengler, Matthias
Dr. Hennig, Christoph
Hesse, Marco
Kirsch, Regina
Lucks, Christian
Dr. Roßberg, André
Dr. Takao, Koichiro
Dr. Takao, Shinobu

REACTIVE TRANSPORT

Dr. Lippmann-Pipke, Johanna

Bütow, Claudia
Fellmer, Friederike
Dr. Franke, Karsten
Gruhne, Stefan
Gründig, Marion
Dr. Hildebrand, Heike
Dr. Kulenkampff, Johannes
Dr. Lippold, Holger
Dr. Mansel, Alexander
Mittmann, Helmut
Dr. habil. Richter, Michael
Schößler, Claudia
Willnow, Nicole
Wolf, Martin
Zakhnini, Abdelhamid

SURFACE PROCESSES

Dr. Brendler, Vinzenz

Dr. Auerhammer, Jutta
Dr. Barkleit, Astrid
Dreissig, Isabell
Eckardt, Carola
Dr. Foerstendorf, Harald
Fröhlich, Christine
Gester, Sven
Gückel, Katharina
Heim, Karsten
Heine, Katja
Dr. Jordan, Norbert
Joseph, Claudia
Li, Bo
Müller, Christa
Dr. Müller, Katharina
Nebelung, Cordula
Neubert, Heidrun
Dr. Richter, Anke
Ritter, Aline
Schaefer, Ursula
Dr. Schmeide, Katja
Schott, Juliane
Dr. Steudtner, Robin
Dr. Stockmann, Madlen
Weiß, Stephan
Dr. Zänker, Harald

External Ph. D. students
Brockmann, Sina
Ilyashuk, Alina
Müller, Melanie
Osman, Ahmed. A

GUEST SCIENTISTS

Dr. Comarmond, M. Josick	*Institute for Environmental Research, Australian Nuclear Science and Technology Organisation, Menai, Australia*
Dr. Merroun, Mohamed L.	*Department of Microbiology, Universidad de Granada, Spain*
Dr. Saeki, Morihisa	*Quantum Beam Science Directorate, Japan Atomic Energy Agency, Naka-gun, Ibaraki, Japan*

MASTER/DIPLOMA/BACHELOR

Brüning, Sebastian	Groß, Magdalena	Münch, Robert	Wimmer, Christin
Drewitz, Susanne	Hilsberg, Mathias	Richter, Katrin	
Fajardo Uribe, Carlos H.	Husar, Richard	Schott, Juliane	
Funke, Franziska	Leske, Steffen	Steiniger, Claudia	

GRADUATE ASSISTANTS, STUDENT ASSISTANTS, TRAINEES

Abt, Marvin	Heller, Tina	Nahum, Oz	Thode, Janek
Aliyeva, Lala	Hilprecht, Diana	Naumann, Sylvia	Vogel, Tobias
Eisbein, Emanuel	Höppner, Nadine	Obermann, Benjamin	Wahl, Anne
Gensch, Tobias	Kissauer, Frances	Patzig, Ramona	Weißpflog, Maria
Hagemann, Bettina	Klemm, Katja	Schikora, Johannes	Wiedmer, Robert
Hamann, Diana	Küchler, Stefanie	Seidel, Peggy	Zachmann, Tilo
Han, Wenbo	Müller, Nico	Smidt, Marco	Zegke, Markus

ACKNOWLEDGEMENTS

The Institute of Radiochemistry is part of the Helmholtz-Zentrum Dresden-Rossendorf e.V. (HZDR). In 2010, it was part of the Forschungszentrum Dresden-Rossendorf e. V. (FZD) which was financed in equal parts by the *Federal Republic of Germany* and the *Free State of Saxony*.

The Commission of the European Communities (EU) supported the following projects:

- ACTINET Integrated Infrastructure Initiative (ACTINET-I3)
  Contract No.: 232631

- HEXANE
  Heavy Elements X-ray Absorption Spectroscopies Network
  Contract No.: 230807

- Redox phenomena controlling systems (RECOSY)
  Contract No.: 212287

- UMBRELLA
  Using microbes for the regulation of heavy metal mobility at ecosystem and landscape scale: An integrative approach for soil remediation by geobiological processes
  Contract No.: 226870

Ten projects were supported by the *Bundesministerium für Wirtschaft und Technologie (BMWi)* and by the *Bundesministerium für Bildung und Forschung (BMBF)*:

- Mikrobielle Diversität im Tongestein (Opalinus-Ton) und Wechselwirkung dominanter Mikroorganismen mit Actiniden
  Contract No.: BMWi 02E10618

- NanoAqua ZIM – Kooperationsprojekt: Entwicklung von neuen Nano-Biokomposit-Materialien und Verfahren zur photokatalytischen Wasseraufbereitung
  Contract No: BMWi KF2306401

- Thermodynamische Referenzdatenbasis THEREDA, Teilvorhaben FZR, gefördert durch das BMBF bzw. BMWi
  Contract No.: BMBF 02C1436
  Contract No.: BMWi 02E10136

- Verbundprojekt: Actinidenmigration im natürlichen Tongestein:
  Charakterisierung und Quantifizierung des Einflusses von Tonorganika auf die Wechselwirkung von U und Am im Ton
  Contract No.: BMWi 02E10156

  Beiträge zur Modellierung des Actinidentransports in potentiellen Wirtsgesteinsformationen
  Contract No.: BMWi 02E10176

- Verbundprojekt: Dynamik abgesoffener oder gefluteter Salzbergwerke und ihres Deckgebirgsstockwerkes; TV 8 (IIF): Tomographische Radiotraceruntersuchungen und Fluoreszenztraceruntersuchungen
  Contract No.: BMBF-FZK 02C1536

- Verbundprojekt: Realitätsnahe Einbindung von Sorptionsprozessen in Transportprogramme für die Langzeitsicherheitsanalyse (ESTRAL)-TV2
  Contract No.: BMWi 02E10528

- Verbundprojekt Strahlung und Umwelt II: Radionuklide in der Umwelt, ihr Transport in die Nahrungsketten zum und im Menschen, Teilprojekt F
  Contract No.: BMBF-FZK 02NUK015F

- Verbundprojekt: Verhalten langlebiger Spalt- und Aktivierungsprodukte im Nahfeld eines Endlagers und Möglichkeiten ihrer Rückhaltung (VESPA)
  Contract No.: FZK-BMWi 02E10790

- Verbundprojekt Partitioning II: Multifunktionelle Komplexbildner mit N, O, S-Donorfunktionen für d- und f-Elemente
  Contract No.: BMBF-FZK 02NUK014B

- NanoTrack – Untersuchung des Lebenszyklus von Nanopartikeln anhand von $[^{45}Ti]TiO_2$ und $[^{105}Ag]Ag0$
  Contract-No.: 03X0078A

Six projects were supported by the *Deutsche Forschungsgemeinschaft (DFG)*:

- Bindungsform von Cm(III) und Eu(III) in menschlichen Biofluiden (Speichel, Urin)
  Contract No.: BE 2234/10-2

- Imaging and image simulation of organic target compound migration between different biogeochemical interfaces of a soil horizon using position emission tomography and the lattice Boltzmann equation approach (BIG)
  Contract No.: LI 872/5-1

- In-situ Speziation von Uran in Biofilmen
  Contract No.: AR 584/1-1

- Sorptionsprozesse von Np(V) an Alumosilikaten. Schwingungsspektroskopische Untersuchungen
  Contract No.: FO 619/1-2

- Sorptions- und Redoxreaktionen von SN II und Sn IV an der Magnetite/Wasser-Grenzfläche in An- und Abwesenheit organischer Liganden (Zinn-Redox)
  Contract No.: SCHE 509/3-1

- Strukturbestimmung von ternären aquatischen U(VI)-Sorptionskomplexen mittels neuester entwickelter kombinierter EXAFS-Auswertemethoden (ITFA, MCTFA) (STAUME II)
  Contract No.: RO 2254/3-2

INDEX OF AUTHORS